Hydroxamic Acids and Their Porous Materials

Hayley Rebecca Green

A thesis submitted for the Degree of Doctor of Philosophy.

School of Engineering and Physical Sciences.

Heriot-Watt University.

January 2018

Abstract

This thesis aims to provide better understand of the supramolecular synthons of hydroxamic acids and the design rules associated with the porous materials based on hydroxamic acids. Also studied was how synthesis routes influcence the self-assembaly process and the properties of the materials produced.

Using a range of analytical techniques, including thermogravimetric analysis, pair distribution function and X-ray diffraction, the structure, design and supramolecular synthons of hydroxamic acids have been studied. By determining the supramolecular synthons of hydroxamic acids the successful production of cocrystals was accomplished. By better understanding the coordination of hydroxamates to metals we have formed two solvates of an eight coordinate $Zirconium_1[hydroxamate]_4$ complex. The design rules for the formation of intrinsically and extrinsically porous $M_4[hydroxamate]_6$ tetrahedra have also been explored. Using crystal engineering principles it has been possible to produce a series of materials with increasing amounts of extrinsic porosity.The host:guest chemistry of the M_4L_6 tetrahdera has been studied. The host:guest properties of a family of coordination polymers and macrocycles were also studied. The materials were synthesised via mechanochemical synthesis and solution state crystallisation, with the aim of understanding how the synthetic method affects the host:guest properties of the material.

For my Family

"No, no! The adventures first, explanations take such a dreadful time." Gryphon, in Lewis Carrol's, Alice's Adventure in Wonderland.

Acknowledgements

Firstly, I would like to thank Dr Gareth Lloyd, my supervisor, for giving me the opportunity to work in his group and for all the wonderful opportunities, this has provided me. A special thank you must be extended to Profs. Catharine Esterhuysen and Len Barbour at Stellenbosch University, South Africa, where I spent three very happy months of my PhD under their guidance. I would also like to thank Dr Helena Shepherd, Dr Phil Chater, Dr Kathi Edkins, Dr Ross Forgan and Oxford Rigaku Diffraction for their contributions, allowing me to complete this work.

A big thank you to the supramolecular group at Stellenbosch University who made me feel so welcome and at home. Closer to home I must thank the Lloyd group past and present and the materials office.

Finally, I would like to thank my friends and family for their support, patience and understanding throughout my studies, especially my parents, for encouraging me to carry on and reminding me that I can achieve whatever I set my mind too.

Contents

Chapter 1 - Introduction

Chapter 2 – Hydroxamic Acids

Chapter 3 – Molecular Cages

Chapter 4 – Co-ordination Polymers

Chapter 5 – Overview and Future Work

Appendix A

List of Tables

List of Figures

List of Abbreviations

Δ - Delta

Λ - Lambda

AHA - 5-Amino-isophthaloyl Hydroxamic Acid

AHPs - Adsorption Heat Pumps

API – Active Pharmacuetical Ingredient

ASU – Asymmetric Unit

BCC – Body Centred Cubic

BET - Brunauer-Emmet-Teller

Cage 1 - $Fe_4(C_8H_6N_2O_4)_6.m(H_2O).n(DMF)$

Cage 2 - $Fe_4(C_8H_7N_3O_4)_6.m(H_2O).n(DMF)$

Cage 3 - $Fe_4(C_8H_6N_2O_5)_6.m(H_2O).n(DMF)$

Cage 4 - $Fe_4(C_8H_6N_2O_4)_6.m(H_2O).n(DMF)$

Cage 5 - $Ga_4(C_8H_6N_2O_4)_6.m(H_2O).n(DMF)$

Cage 6 - $Ga_4(C_8H_7N_3O_4)_6.m(H_2O).n(DMF$

Cage 7 - $Al_4(C_8H_6N_2O_4)_6.m(H_2O).n(DMF)$

Cage 8 - $In_4(C_8H_6N_2O_4)_6.m(H_2O).n(DMF)$

CDI – 1,1’-carbonyl diimidazole

COFs – Covalent Organic Frameworks

CP1 - $Co(H_2O)_2$-μ-$(C_{18}H_{14}N_4O_2)_2$

CP2 – $[Cd(NO_3)_2$-μ-$(C_{18}H_{14}N_4O_2)_2]_n$,

CP3 - $[Co(I)_2$-μ-$(C_{18}H_{14}N_4O_2)_2]_n$,

CPs – Coordination Polymers

D(r) – Pair Distribution Function

DEF – Diethylformamide

DMA - Dimethylacetamide

DMF – Dimethylformamide

DMSO – Dimethyl sulfoxide

DSC – Differential Scanning Calorimetry

EI – Electron Ionization

Fac – Facial

FCC – Face centred cubic

HCP – Hexagonal Close Packed

I_2 – Iodine

IHA – Isophthaloyl Hydroxamic Acid

IUPAC – International Union of Pure and Applied Chemistry

LAG – Liquid Assisted Grinding

Ligand 1 - 1,2-bis(Isonicotinoylamino)benzene

Mer – Meridonial

MOF - Metal Organic Framework

MOPs – Metal Organic Polyhedra

MS – Mass Spectroscopy

NMR – Nuclear Magnetic Resonance

P_4 – White Phosphours

PDF – Pair Distribution Function

PPM – Parts Per Million

pXRD - Powder X-ray Diffraction

RH – Relative Humidity

SBU – Secondary Building Unit

SCC - Supramolecular Coordination Complexes

$ScCO_2$ – Super Critical Carbon dioxide

ScXRD - Single Crystal X-ray Diffraction

SD – Standard Deviation

STP – Standard Temperature Pressure

TDCs - Thermally Driven Adsorption Chillers

TGA – Thermogravimetric Analysis

THF – Tetrahydrofuran

VT-PDF – Variable Temperature Pair Distribution Function

VT-pXRD – Variable Temperature Powder X-ray Diffraction

WAG –Water Assisted Grinding

xPDF – X-ray Pair Distribution Function

XRD – X-ray Diffraction

List of Publications

H. R. Green and G. O. Lloyd, in *Chapter 9. Porous Metal Organic Polygons and Polyhedra - Intrinsic vs. Extrinsic Porosity in Functional Supramolecular Materials : From Surfaces to MOFs*, ed. R. Banerjee, The Royal Society of Chemistry, Cambridge, 1st edn., 2017, pp. 297–324.

S. Ramalhete, J. S. Foster, H. R. Green, K. P. Nartowski, M. Heinrich, P. Martin, Y. Z. Khimyak and G. O. Lloyd, *Faraday Discuss.*, 2017, 423-439

K. P. Nartowski, S. M. Ramalhete, P. C. Martin, J. S. Foster, M. Heinrich, M. D. Eddleston, H. R. Green, G. M. Day, Y. Z. Khimyak and G. O. Lloyd, *Cryst. Growth Des.*, 2017, 4100-4109.

Chapter 1 – Introduction

'If opportunity doesn't knock, build a door.' Milton Berle.

Foreword

The majority of this chapter is based on the published work written by Hayley Green and Gareth Lloyd. This work was published as Chapter 9. Porous Metal Organic Polygons and Polyhedra - Intrinsic vs. Extrinsic Porosity in Functional Supramolecular Materials: From Surfaces to MOFs, The Royal Society of Chemistry, Cambridge, 2017, 297-324.[1] All CSD references were correct as of July 2017, using the CSD version 5.38 (November 2016) + 3 updates.[2] Six figure CSD refcodes for single crystal structures are included within the figure captions.

1.0 Introduction

Porous materials encompass a range of species from the crystalline materials such as zeolites, Metal Organic Frameworks (MOFs) and Covalent Organic Frameworks (COFs), to amorphous species such as Porous Organic Polymers and Porous Carbons. These materials are rapidly growing areas of research that typically display good stability, diversity, designability and are significantly important industrial materials. Due to their high chemical stabilities, they are insoluble making them incongruous for solution processing. However, porous molecular solids, by their nature, are generally more soluble than the former examples meaning solution processing is possible.[3] This thesis will focus on the suitability of hydroxamic acids in porous molecular materials. By discussing the synthesis, characterisation and supramolecular synthons of hydroxamic acids and the design and synthesis of porous Metal Organic Polyhedra (MOPs) based on them. Finally, the design and synthesis of metal organic polygons based on a diamide linker will be discussed.

Over the last century, since the awarding of the Noble prize in 1913 to the "father of coordination chemistry", Alfred Werner. Coordination chemistry has grown extensively through better understanding of the coordination geometries of metal ions and the dynamics of coordination based supramolecular assembly. This understanding established rules by which scientists could create rational synthetic methodologies for the incorporation of ligands and metals together to give pre-designed structures. Within the field of coordination chemistry, the last decade has seen a divergence, resulting in two recognisable branches: Metal Organic Frameworks (MOFs) and Supramolecular Coordination Complexes (SCCs). SCCs have also been known as MOPs. Midway through the 20th century, it was established that complementary small molecules could exhibit intermolecular recognition using noncovalent interactions, such as van der Waal's, hydrogen bonding and Pi-Pi stacking. These rules were then applied to build larger more complex entities from molecular species that again are held through supramolecular interactions.[4,5]

This can manifest as crystalline materials which show solid-state host:guest chemistry. This is historically described as inclusion chemistry and/or clathrate chemistry, which has a very rich history in purely organic phases, as well as coordination complexes such as Hofmann and Werner complex clathrates.[6–8] An excellent description/summary of the potential of inclusion chemistry to show porosity was produced by Nassimbeni[9] over a decade ago. The production of a potentially porous crystalline material from a *molecular* building component requires some form of crystallisation process (Figure 1.1). As nature has an aversion to a vacuum/empty void, this often results in the "inclusion" of a guest molecular species resulting in a multi-component material and/or a "close-packed" phase. This close-packed solid form is described as the apohost. Apo- meaning furthest point from (the host structure). The apohost structure has been shown through computational work and crystal structure prediction (CSP) to be isostructural to the solvated or guest included materials in some examples, e.g. Dianin's compound.[9–11] An apohost lattice is "close-packed" and normally exhibits the most stable lattice energy for the host building molecule and is referred to as the α phase.

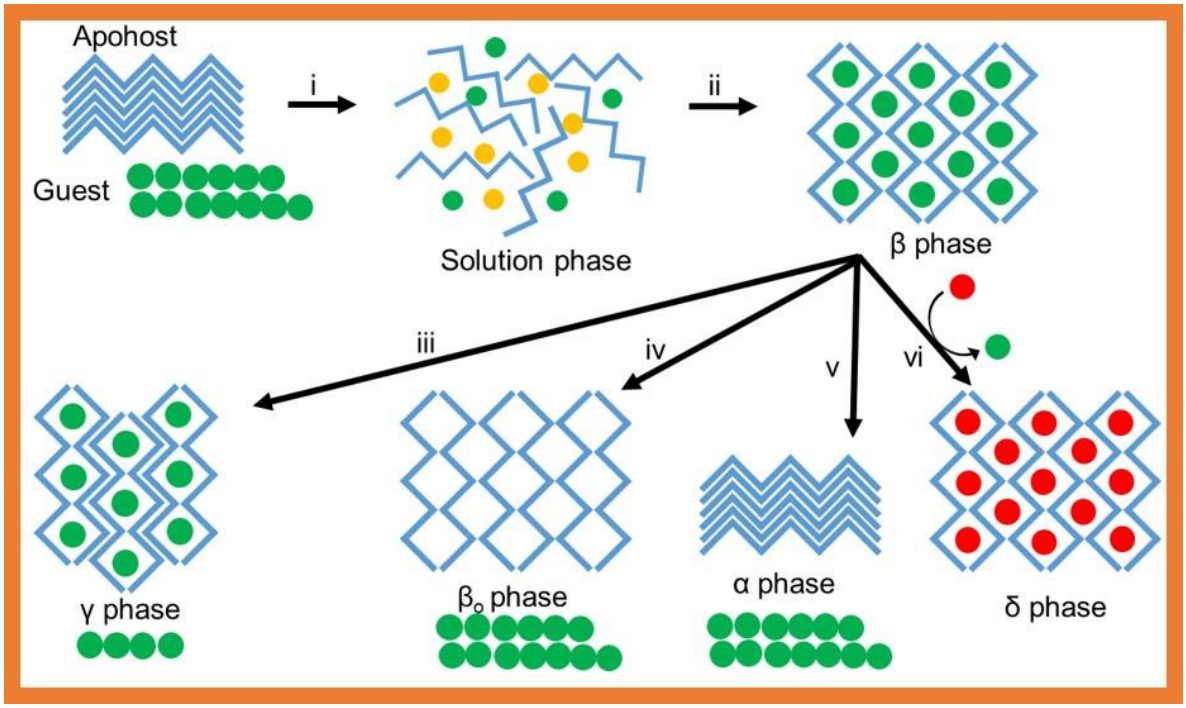

Figure 1.1 show a schematic of the formation and decomposition of inclusion compounds. ***i)*** *The "close-packed" apohost lattice α phase is dissolved into a solution that may contain potential guest molecules (green dots),* ***ii)*** *Recrystallisation results in an inclusion complex (β phase) with guests.* ***iii)*** *Partial decomplexation can occur, resulting in a new lattice (γ phase). There can be a number of γ phases, i.e. stepped decomplexation. iv) Complete decomplexation but retention of the host lattice structure (β_o phase).* ***v)*** *Collapse of the host lattice reforming the α phase.* ***vi)*** *Post-assembly modification through guest exchange resulting in a δ phase. Reprinted (adapted) with permission from (L. R. Nassimbeni, Acc. Chem. Res., 2003, 36, 631–637.). Copyright (2003) American Chemical Society.*

Recrystallisation, of the apohost, from the dissolved molecules in a solution that may contain potential guest molecules can result in an inclusion complex (β phase). Ibragimov has formulated a set of general rules for which topology, for the β phase, is likely to arise from crystallisation at different temperatures.[12] These may be summarised as follows:

(i) The guest/host ratio decreases as the crystallisation temperature increases.

(ii) The topology change from low temperature to high temperature is intercalate - tubulate - cryptate - apohost.[13]

There can be a number of β phases based upon different guests where the host framework/lattice is different. When materials are obtained with the same lattice composed of the complexes with different guest forms, then these forms are all the same β phase. "Isoskeletal" has been suggested by Barbour to describe this phenomenon.[13,14] Partial decomplexation can occur resulting in a different host:guest ratio and expulsion of guests giving a new lattice (γ phase). There can be a number of γ phases. Complete decomplexation can result in total loss of the guests but retention of the host lattice structure, resulting in a β_o phase. Conversely, complete loss of the guests normally results in the collapse of the host lattice, resulting in the reformation of the α phase (apohost) and occasionally a close-packed polymorph of the α phase. Post-assembly modification (also referred to as post-synthetic modification) can be made of the host:guest complex phase, e.g. β phase, through guest exchange resulting in a δ phase. This transformation must occur through a crystal-to-crystal mechanism and must not be able to form through crystallisation from solution. If it forms through solution crystallisation then it is simply another β phase. A δ phase may show its own versions of the γ and β_o phases but will also be able to revert to the α phase. In terms of porosity, this represents the different thermodynamic and kinetic routes to getting a potentially porous phase. For example, the β_o phase and δ_o phases normally represent kinetically trapped porous phases and pathway complexity arises through the use of the intermediate phases. These phases may not be accessible directly from solution. This description of inclusion solid: state chemistry allows for design of a porous material, a subset of the general field of crystal engineering.

Porous molecules can be classified as either intrinsically and/or extrinsically porous (Figure 1.2). Intrinsic porosity is defined as porosity that is already inherent in the molecular structure when viewed as a discrete molecule, i.e. a concave cavity within the host that can fit a convex guest to form a molecular complex.[15] For example, shape-persistent voids, clefts, or cavities, traditionally found in purely organic materials such as calixarenes, cyclodextrins, molecular cages and cucurbiturils are viewed as intrinsically porous.[5,16] Extrinsic porosity is where the molecules pack together inefficiently forming a porous structure, i.e. the molecules form a lattice inclusion compound that has cavities, channels,

or layers which can accommodate guest molecules (i.e. form intercalates, tabulates and cryptates). Molecules within molecular solids tend to pack together as closely as possible to maximise intermolecular contacts, meaning that finding a molecular crystal with open channels or discrete lattice voids of more than 25 $Å^3$ is rare.[17]

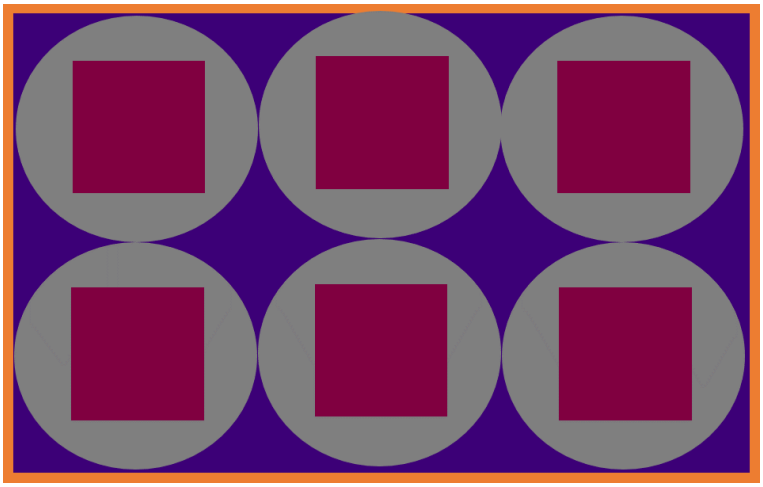

Figure 1.2 shows intrinsic (maroon square) and extrinsic (indigo between spherical molecules) pore spaces formed by molecular species (grey circle) in a periodic assembly.

Examples of purely organic compounds that show extrinsic porosity due to inefficient packing in the solid-state are 4-phenoxyphenol[18] and Dianin's compound.[19] Day and co-workers report the use of energy-structure-function (ESF) crystal structure prediction to predict low-density crystal forms of organic compounds.[20] Molecular crystals cannot be easily predicted, because they assemble using weak intermolecular interactions such as hydrogen bonds, instead of strong predictable bonding pattern used with MOP prediction.[20,21] Day combines computational studies with real life crystallisation, they ultimately prove that obtained structure and gas sorption of the compound is the same as those they predicted. One of the predicted and subsequently crystallised structures also has the largest pore size observed for any molecular organic crystal, even exceeding the intrinsically mesoporous organic cages reported by Masterlez.[16,22] The Werner complexes, such as [Ni(4-methylpyridine)$_4$(NCS)$_2$], as coordination examples, also show extrinsic porosity. Although the intrinsic/extrinsic porosity is a useful set of definitions, they should be viewed as being a grey scale, i.e. nearly all molecular porous materials will have some

pore volume that can be viewed as intrinsic and some that is extrinsic. The definitions can aid the production of a porous material through design of the crystalline lattice's molecular building blocks by utilising intrinsic and extrinsic porosity and their connectivity, in conjugation with crystal engineering concepts.

Intrinsically porous molecules can be utilised in host:guest chemistry and are synonymous with the development of supramolecular chemistry. The 1987 Nobel Prize for Chemistry was awarded to Donald Cram, Jean-Marie Lehn and Charles Pedersen for the discovery of cryptands and crown ethers, in part. Cryptands can be simplistically described as three-dimensional crown ethers (Figure 1.3) that are suited to the selection and binding of certain cations.[23] The binding of metals within the "intrinsic pore space" of these hosts is the analogue utilised for describing the development of metal organic porous molecular materials in the form of metal organic polygons (metallocycles) to metal organic polyhedra (metallocryptands).

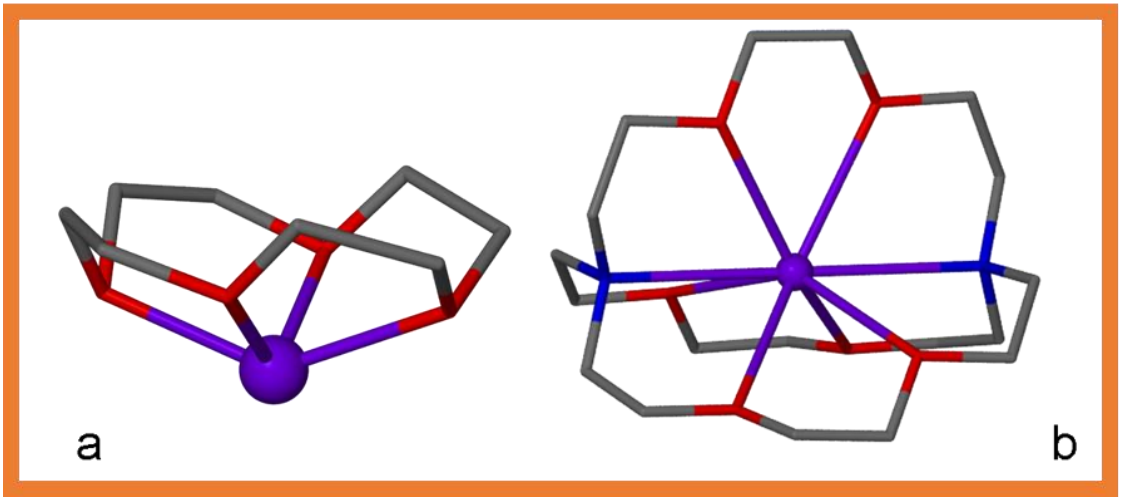

Figure 1.3 ***a*** *shows a metal complexed crown ether (CSD REFcode - BARVOF)* ***b*** *is a complexed cryptand (NAYSIQ). The cation is displayed in purple, O in red, N in blue and C in grey. The figure also represents the design principle of a simple polygon-shaped molecule to a polyhedral-shaped molecule.*

1.1 Polygons

The simplest of all the intrinsically porous metal organic compounds to make are the metal organic polygons (metallocycles) (e.g. M_2L_2, M_3L_3 etc., where M refers to the metal and L

the organic ligand). The rational design of these complexes can be simple, as all that is normally needed is complementarity between a convergent or divergent ligand (e.g. C-shaped) and a functionality match with the convergent or divergent coordination species of the metal arising in a macrocycle formation.[24] Note that when both species are divergent in a two-component system, a polymer must result. Therefore metallocycles form with convergent:convergent, convergent:divergent and divergent:convergent combinations of metal and ligand. Further detail of rational design in MOPs can be found in the next section on polyhedra. This type of chemistry can result in a dynamic mixture of macrocycles and oligomers. Preferential crystallisation from the solution-based mixture of species through constitutional dynamic chemistry concepts is important and allows for design of preferential crystallisation from the mixture.[25] The development of metallocycles is as old as the development of coordination chemistry, but it is only really in the last two decades that the porosity of the solid materials has been studied.

To understand the assembly processes of such complexes, the chemist needs to have some understanding of the mathematics of polygons. In geometry, a polygon is a plane figure that is bounded by a finite chain of straight line segments closing in a loop to form a closed chain or circuit (e.g. macrocycle). These straight line segments are called edges and the points where two edges meet are the polygon's vertices. The interior of the polygon is called its body and often describes the intrinsic porosity of a molecular host. An *n*-gon is a polygon with *n* sides, so for example when *n* = 3 you have a triangle (trigon), *n* = 4 quadrilateral (tetragons like squares and rectangles) and *n* = 5 is a pentagon, etc. Regular convex simple polygons such as squares and equilateral triangles, are defined by Euclidean geometry, having equal angles between sides (equiangular) and equal lengths of sides (equilateral). Most people are familiar with the regular convex polygons, the nonconvex regular polygons are the regular star polygons. A polygon is a two-dimensional example of the general polytopes which mathematically can be of any dimension. The three-dimensional versions are polyhedra (polyhedrons) and are described in the next section on metal organic polyhedra.[24]

An early example of the applicability of these intrinsically porous metal organic polygons is by Hupp and coworkers.[26,27] By utilising divergent, rigid dipyridyl ligands and coordination sites that are 90° to each other, the researchers showed the regular assembly of a series of Re squares (Figure 1.4).

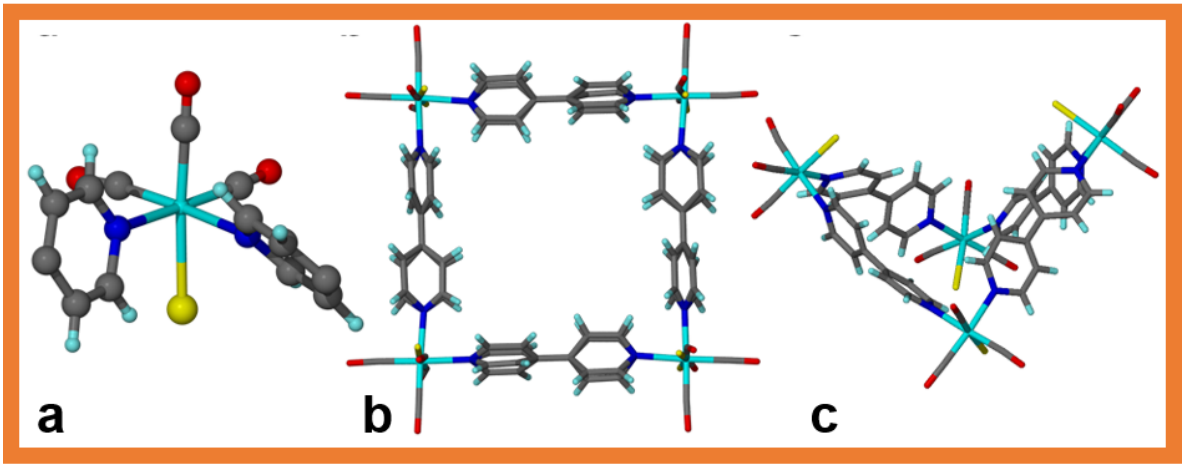

Figure 1.4 ***a*** *shows the coordination sphere of the Re complex meaning connectivity is effectively 90° and planar (TEZHIP).* ***b*** *"Ideal" square complex (regular convex simple polygon - square with equal lengths and angles) (TEZHIP).* ***c*** *Folded form of the same complex in different solvate material (JOQBAS).*

The applications of these assemblies are described in section 1.4. This particular assembly is also a useful example of the dynamics of both the conformational and configurational space available for large coordination assemblies and how the different solvates and inclusion compounds (β, δ or γ phases) can result in remarkably different properties for essentially the same complex.[28] An "ideal" square conformation of the complex (Figure 1.4b), with positions of the coordinated chloride relative to each other undetermined due to disorder in the crystal, results from the crystallisation of a 3:1 host-to-guest ratio material (the guest, in this case, is acetone). "Ideal" refers here to a regular convex simple polygon (square with equal lengths and angles). The opposing crystal form, a 2:1 host-to-guest ratio material, has the coordinated chloride ordered in an up-down alternating pattern. However, the assembly is far from "ideal" square with the conformation in a folded form (Figure 1.4c). This example of the structure illustrates how different phases can have very different packing efficiencies. The 2:1 ratio material is less well packed (38 % void space of

the unit cell volume calculated using Mercury, 1.2 Å probe over a 0.7 Å grid), and potentially more porous, than the 3:1 ratio material (22 % void space of the unit cell volume).

As mentioned in the introduction, one issue of the crystal engineering of molecular porous materials is the connectivity of the pore spaces (the extrinsic porosity). This was highlighted through the work on an M_2L_2 metallocycle consisting of tetrahedral M^{2+} dihalide coordination spheres with a dipyridyl diamide ligand.[29] Work originally published by Puddephett showed the metallocycles could be produced as a number of solvates.[30–33] However, the solvent occupied voids space (intrinsic porosity) is not connected. By changing the solvent form (ethanol or methanol inclusion phases) the intrinsic porosity is linked together into one-dimensional channels (tubulate) (Figure 1.5).[29]

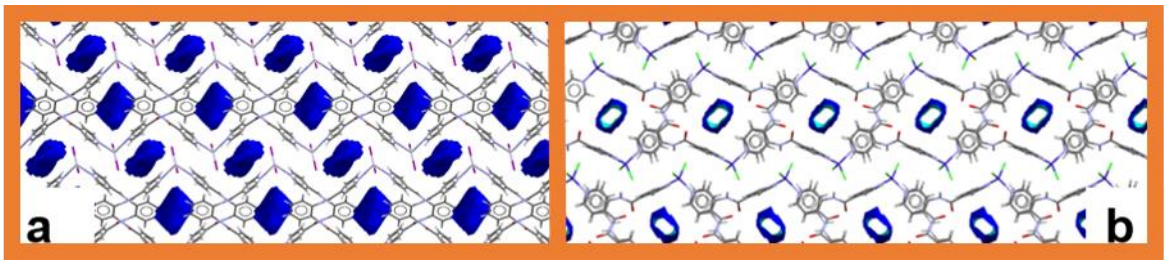

Figure 1.5 ***a*** *showing a discrete intrinsically porous form (XAHSEF), the dark blue area represents the outside of the void space which highlights the fact that the void is discrete.* ***b*** *showing the tubulate form (KATHEU), clear channels can be seen through the macrocycles, with the light blue colour highlighting the inside of the channel. Images created using solvent free crystal structures utilising the voids function within Mercury.*

This phase can be easily desorbed through a single-crystal-to-single-crystal transformation resulting in a porous material, as shown through I_2 sorption experiments and standard gas isotherm determination. See section 1.4 for characterisation techniques for porous MOP materials.

Non-porous porosity refers to a crystalline material in which the static crystallographic structure shows no sign of porosity, yet the material clearly shows porous behaviour during experimental tests.[34–38] The characterisation of pore volumes and connectivity is described later in the section on characterisation and involves studying the crystal structures. The non-porous porosity behaviour is related to the gating phenomena found in some porous

MOFs and zeolites. The thermally induced dynamics of the crystalline material results in transient porosity or the pressure (chemical activity) of the guests can force a transient opening of the material at a specific gate opening pressure. This behaviour often requires cooperative events between close neighbours within a porous framework.

Cooperativity between molecules within materials built from molecular entities can be utilised to control properties and functions. This was particularly well characterised in the example from Barbour and coworkers.[34] In this M_2L_2 metallocycle the intrinsic void can hold two relatively small guests (e.g. two MeOH molecules or two gas molecules). This material shows non-porous porosity as mapping of the static crystal structure only shows discrete void spaces (Figure 1.6). Through careful experimental work utilising gas sorption isotherms, computational/physical theory work involving statistic mechanics and in situ gas crystallography, they have shown how the deformation of the macrocycles, induced by the inclusion of two guests in the intrinsic void of the macrocycle material, enhances the probability of the neighbouring macrocycles deforming. This makes the neighbouring macrocycles become energetically more likely to absorb two guests. This particular example occurs when the gas being sorbed into the material is acetylene. This gives rise to a type VI gas isotherm (stepped isotherm) which has a noticeable inflection half way through the full saturation of the material with the guest. This saturation occurs at a 1:2 host-to-guest ratio, with the inflection occurring at half loading (1:1 ratio). This acetylene guest uptake is in strong contrast to that of CO_2, where the uptake shows a typical type I isotherm. The reasoning behind this difference can clearly be seen when the host:guest crystalline structure is determined under in situ crystallographic conditions (Figure 1.6). The binding of CO_2 occurs in an orientation that means that no structural rearrangement in the host framework needs to occur as the void space can easily accommodate two CO_2 guests.

However, in the case of acetylene, the interaction of the acetylene with the host, and its resultant orientation results in a lack of space for two guests, with the void large enough to contain one guest with no deformation. Therefore, the framework deforms to fit the two guests. This deformation must occur through a cooperative effect resulting from the elastic coupling between host macrocycles, i.e. deformation of one host macrocycle “pressures”

the neighbouring macrocycles to “conform”, resulting in their transformation being energetically more favourable.

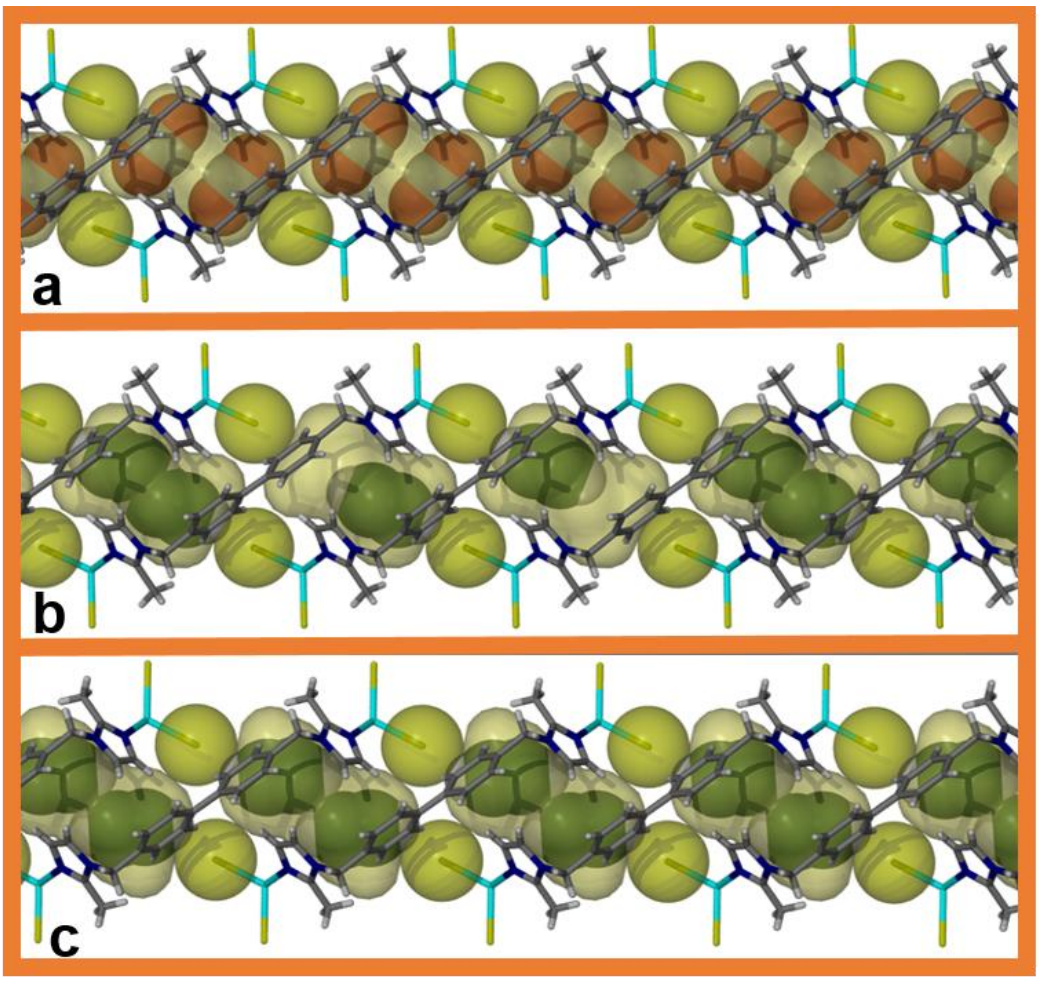

Figure 1.6 crystal structures of a non-porous metal organic polygon under in situ gas pressure. The void spaces (semi-transparent yellow surfaces) can be occupied by two guest molecules of CO_2 or C_2H_2. ***a*** *In the case of CO_2, there is ample room for both molecules within the void space. (WEZRIE -40 10 bar).* ***b*** *However, in the case of C_2H_2, the void is too small for two guest molecules as shown from the crystal structure at only one occupancy ((16 bar WESTOM)).* ***c****. The structure therefore deforms, resulting in an increase in void space and a reorientation of the interactions of the guest C_2H_2 molecules within the void. This rearrangement occurs in a cooperative manner.*

In summary, metal organic polygons are the simplest of the MOP materials that can be constructed. However, this does not mean they show uncomplicated behaviour. Crystal engineering of the void space is still required and careful attention must always be paid to

selecting the correct host:guest system to get to a porous material. The simple building blocks and structures mean that complex behaviour relating to porosity, such as non-porous porosity and cooperativity, can be studied in great detail.

1.2 Polyhedra

Metal organic polyhedra are discrete molecular complexes assembled from a combination of metals coordinating to organic ligands which can be defined as having a particular solid topology. Their well-defined "cage-like" structures and confined cavities allow for guests such as solvent molecules, dissolved species or counter-ions to reside within the structure.[39] The polyhedra topologies, like most three-dimensional solids, can be mathematically categorised as Platonic solids, Archimedean solids, Johnson solids, faceted polyhedra or stellated polyhedra. This is analogous to the concept of there being only 230 space groups in crystallography. Platonic and Archimedean solids are simpler, high symmetry and familiar three-dimensional shapes that are closely related to each other.[24,40] The five platonic solids (Figure 1.7) are polyhedra created from one regular polygon, they are the tetrahedron, hexahedron (cube), octahedron, icosahedron and dodecahedron.

Meanwhile, Archimedean solids are semi-regular solids that contain at least two different regular polygons to create the faces. The dodecahedron, truncated tetrahedra and snub cube are three examples of the fifteen possible Archimedean solids.[41] The nine faceted polyhedra are derived from the Archimedean solids but share vertices as opposed to edges as seen with the Platonic and Archimedean solids. Stellated polyhedra are rarely seen in MOP structures, they are star-shaped polyhedra formed from elongating the polyhedron in three dimensions. The Johnson solids are non-uniform and convex polyhedra, where each face is a regular polygon but there are no rules regarding how the polygons join around vertices or that each face must be the same, allowing for ninety-two polyhedra to be formed. It is very rare to see MOP materials that can be clearly described as Johnson solids.[42,43] It must be noted that whilst the majority of compounds will be Archimedean or Platonic in nature, due to the majority of assemblies being highly symmetric, some will fail to crystallise as any of these 'regular' polyhedra.

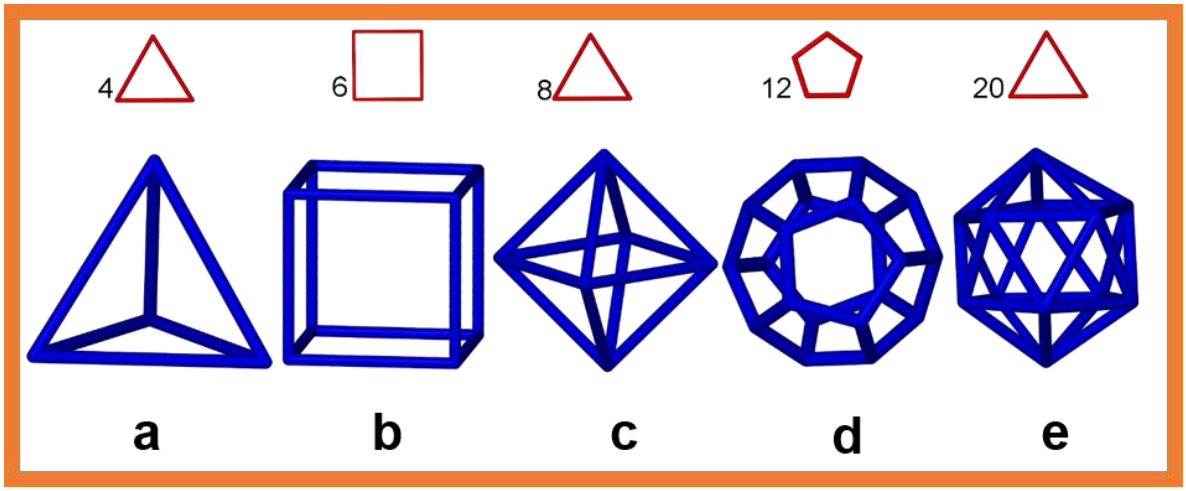

Figure 1.7 the five Platonic solids. ***a*** *represents the tetrahedron (IRADEK),* ***b****, cube (ELUGIB),* ***c****, octahedron (PUZMAZ),* ***d,*** *dodecahedron (DOPSIK) and* ***e****, icosahedron (DATMOD) shown. Shown above the blue solids are the number of regular polygon from which each of the Platonic solids is formed. Each of the shapes is a representation of an experimentally determined crystal structure, showing that molecular structures can exhibit these solid forms.*

Rational design of metal organic polyhedra has been utilised by many researchers over the years to produce complexes of a predetermined shape.[4,41,44,45] This rational design can be split into two principles, although in truth they are similar and should always be considered in conjunction:

-the symmetry interaction model,

-the molecular library model, alternatively named the directional bonding model.

The metal organic polyhedral structures can be simplified by viewing them in terms of nodes and spacers, as described by Wells in the 1950's.[4,40] All linear ligands/connections are termed spacers, while nodes are viewed as anything that diverges from linear. From this, it is then possible to determine which net the structure belongs to using the (*n*,*p*) parameters, for example.[4] However, this simplistic methodology does not cover all possible polyhedral and polygons and therefore more complex methods have been developed to create uniform symbols, for example, Schläfli- and Delaney-symbols.[46] In the 1990's the foundation stones of node and spacer were fully utilised in the development of methods that would allow for

the rational design and construction of discrete self-assembled complexes. Stang coined the term "directional bonding" to describe the self-assembly process.[4,45] This is also known as the "symmetry interaction model". This process began with the formation of 2D macrocycles, in the shape of a regular polygon, by designing both the organic ligand and the metal occupying the edges and vertices of the target shape. To do this, the polygon is broken along its edges to provide sections with no more than a 2-fold symmetry axis, the angles of these pieces can then be equated to those that the linkers and nodes will be required to take on. For example, a square is broken into four 90° nodes (these can also be referred to as acceptors) and four 180° spacers (donors); this means four ditopic ligands are required to link four ditopic metal centres (Figure 1.8).

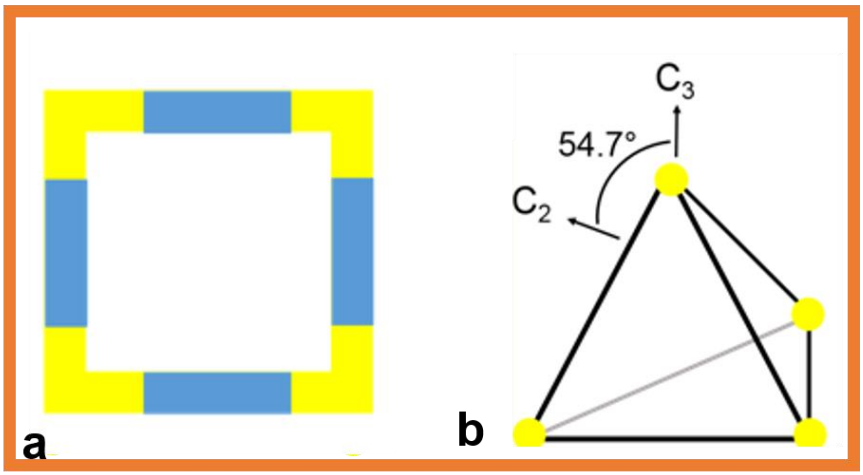

*Figure 1.8 shows **a** molecular library model shows the formation of a square through ditopic nodes (yellow 90° sections) and spacers (blue 180° sections) and **b** the "symmetry interaction model" shown with a tetrahedron.*

By the same approach, a triangle can be broken into three 60° nodes and three 180° spacers. Fujita reported taking a 180° dipyridyl spacer and an ethylenediamine palladium nitrate node which allows the self-assembly of molecular squares and triangles based on the above principles.[47–49] By incorporating higher symmetry tritopic linkers with the ditopic species, it becomes possible to design cages/polyhedra. The formation of higher symmetry linkers can

be accomplished through adding additional binding sites on the donor, increasing the amount of labile coordination sites or the number of metals in an organometallic acceptor.

The "molecular library model" described as "directional bonding" was proposed in 2008 by Yaghi and co-workers to aid the reticular synthesis of a family of MOPs.[39] This family of materials is described in the section 1.3.2 – Tetrahedral MOPs. Reticular chemistry is the process of assembling rationally designed rigid molecular building blocks into predetermined ordered structures (networks). Reticular chemistry can be used in the design and synthesis of compounds built from chemically bonded secondary building units (SBU).[39] A SBU is best described as a molecular complex or cluster. They can be connected by polytopic ligands to form a closed discrete MOP or network.[39,50]

Finally, the "symmetry interaction model" is based upon controlling the bonding vector direction between the symmetry building units. More simply put, this method relies on knowledge of the ligands favoured geometry when chelated to metals, based upon binding energies. Further understanding of the symmetry laws required to make the desired polyhedra, and the geometric relationship between the ligand and the metal, allows for the construction of the MOP.[44] Both models are represented in Figure 1.8.

There can be a number of general approaches to the formation of these MOP assemblies, most commonly utilising edge directed and face directed assembly of a particular solid form. As implied by the name, edge directed assembly uses the organic linker to define the edges of the MOP/polyhedron, whilst face directed means that the linker covers some, or all, of the faces of the MOP/polyhedron. This self-assembly process is maybe best visualised in terms of a cube (Figure 1.9). An edge directed cube can be formed from eight 90° tritopic linkers connected to twelve linear ditopic linkers [M_8L_{12}]. A face directed cage requires twelve 90° ditopic linkers connected to six tetratopic planar 90° faces [M_6L_{12}].[51,52] The design of polyhedra allows for applications in material porosity. The majority of the MOP materials published in the literature to date are charged or only studied in solution. Presented in the next section are examples of polyhedra that have been successfully shown to be porous within crystalline phases.

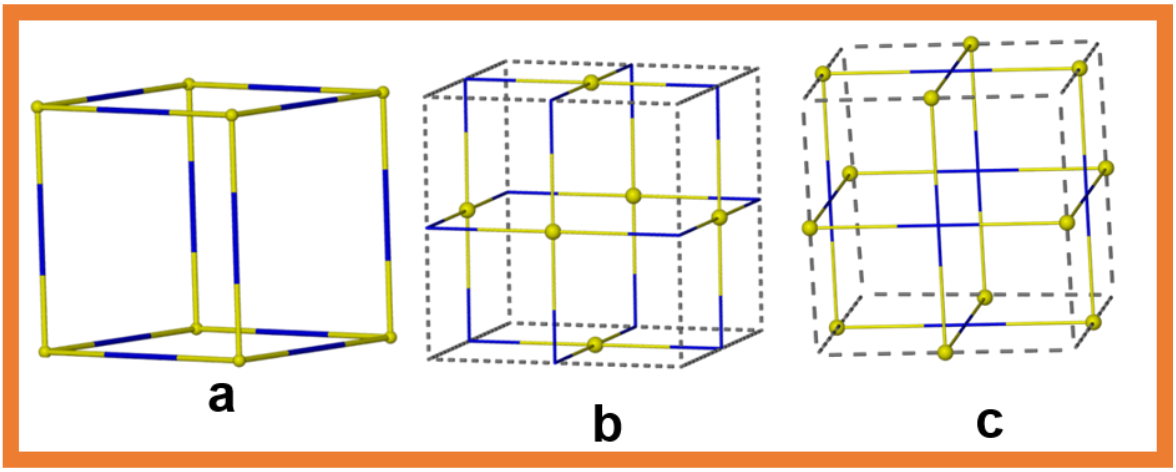

Figure 1.9 shows the assembly of cubic cage MOP materials can use one of three design configurations. ***a*** *an* M_8L_{12} *stoichiometry (ELUGIB) where the cubes vertex points* (C_3 *symmetry connected metal centres, yellow spheres) are connected through the edges (effectively linear ditopic ligands, blue).* ***b*** *Four-coordinate metal centres at the faces connected by right-angled ditopic ligands giving an* M_6L_{12} *cube (COWBIA).* ***c*** *two-coordinate metal centres at the edge of a cube connected by* C_4 *symmetry ligands positioned on the faces of a cube to give an* $M_{12}L_6$ *stoichiometry.*

1.3 Materials and their properties

Presented are two case studies of two families of polyhedra, the copper nanoball and tetrahedral MOPs. These two classes of materials are presented as they represent two well-studied materials and they give good descriptions of much of the complex understanding that is required to truly make these materials applicable and useful.

1.3.1 Copper nanoball

Within the literature, there is an identifiable family of MOPs containing the paddle wheel secondary building unit.[53–63] This paddle wheel motif, commonly seen in MOF synthesis, is constructed of four carboxylate linkers coordinated to two metal atoms, typically copper, as shown in Figure 1.10. The metal atoms have an additional ligand bonded to them, providing square pyramidal coordination. These ligands are typically neutral nitrogen and oxygen donors, such as solvent, which can be subsequently removed creating open coordination metal sites.

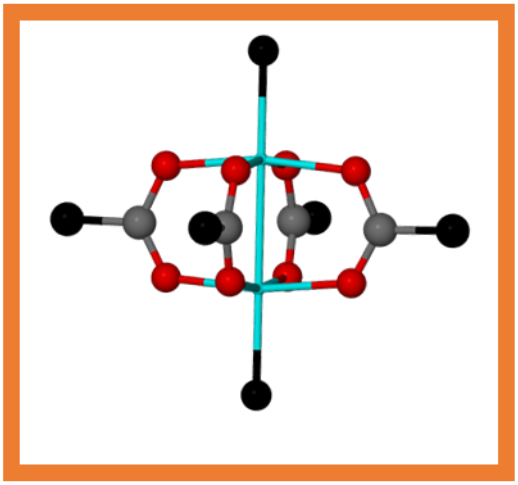

Figure 1.10 shows the copper paddle wheel (DIZQEK) secondary building unit where the aqua points are Cu, red spheres are O, grey spheres are C and black spheres are neutral donor groups.

There are two descriptions when it comes to the naming of polyhedra built from this copper paddle wheel and isophthalate ligands. These are the small rhombihexahedron and the cuboctahedron. The small rhombihexahedron is an example of a faceted polyhedron; with 48 edges, 24 vertices and displays two fold symmetry. The small rhombihexahedron is very similar to the solid rhombicuboctahedron, which is the dual of a cuboctahedron. The cuboctahedron is an Archimedean solid displaying 12 vertices, 24 edges and four fold symmetry. The two solid forms are closely related to each other, and a copper nanoball structure can be viewed in both ways. The point of four fold symmetry within the cuboctahedron is the paddle wheel building unit, which can be located within the centre of the coloured squares of the diagram of the small rhombihexahedron shown in Figure 1.11. Faceted polyhedra, contain both concave and convex faces, are often excellent descriptions of the MOPs. This particular MOP discussed here, generated from reacting copper nitrate with isophthalic acid in methanol in the presence of a templating agent such as nitrobenzene, is often described by both methods in the literature.[55] The intrinsic pore of one such cage is approximately 1nm^3 in volume and is large enough to encapsulate a C_{60} molecule.[55]

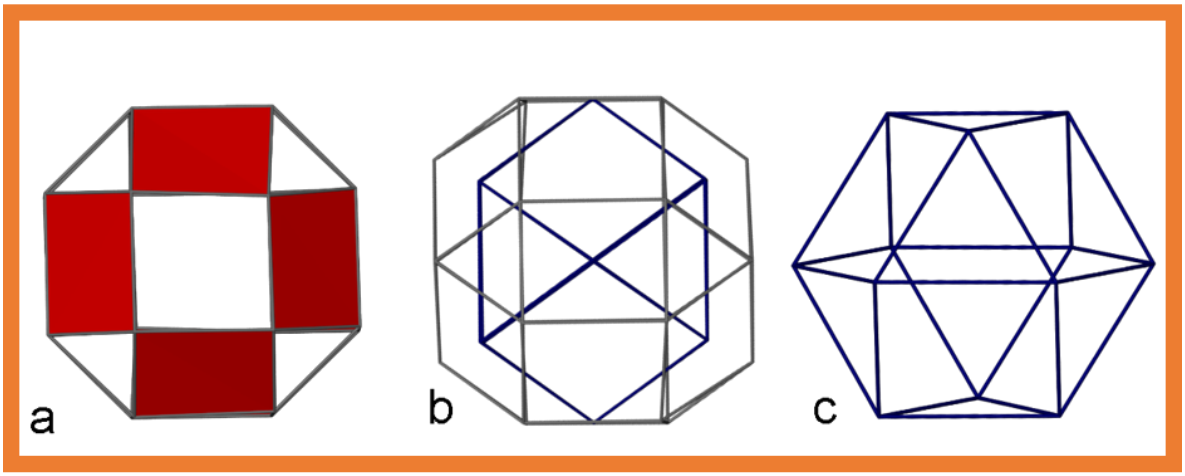

Figure 1.11 ***a*** *shows a representation of the rhombihexahedron where the red squares are the paddlewheel SBU, the white spaces (triangles and squares) are the facets within the polyhedron* ***b*** *Shows an overlay of the rhombihexahedron (grey) and the cuboctahedron (blue), where the blue 4 fold symmetry points correspond to the red square in part a.* ***c*** *Displays the cuboctahedron where the points/vertices of four fold symmetry are the paddle wheel SBU. These shapes are generated from a single crystal structure of the copper paddle wheel isophthalate "nanoball" (XEXZUV).*

Paddle wheel formation is not strictly limited to using copper as its metal source. Zhou and co-workers[57] have shown that it is possible to use molybdenum in the formation of the paddle wheel building unit. This slight difference in metal provided some interesting results in terms of the structure of the polyhedra formed. They recognised that by slightly varying the organic linker used it was possible to form both a cuboctahedron and an anticuboctahedron.

As already mentioned, the cuboctahedron is an Archimedean solid that contains eight triangular faces and six square faces and displays the O_h point group symmetry, while the anticuboctahedron is an isomer of the cuboctahedron. Whilst it still contains six square faces and eight triangular faces, it displays D_{3h} point group symmetry and is one of the Johnson solids, of which there are ninety-two.[57] Zhou and co-workers give an elegant description of the assembly of the anticuboctahedral structure. The paddle wheel contains four dicarboxylic acid linkers and one Mo-Mo unit. These linkers, however, can be orientated to provided four geometric isomers, with the point group symmetries C_{4v}, C_s, C_{2h}

and D_{2d}. Due to their energetic similarities, they are all equally likely to be formed but only the C_{4v} is capable of forming a closed polyhedron (Figure 1.12).[57]

The C_{4v} paddlewheel templates the formation of the *cis* triangles, which in turn form halves of the polyhedra, referred to as a triangular cupola. Depending upon how the two halves align, a cuboctahedron or anticuboctahedron is formed. If the triangles align to the squares, a cuboctahedron is formed (Figure 1.13**a**). Meanwhile, if the triangles align with each other the anticuboctahedron (Figure 1.13**b**) results.[57]

In 2010 Li and Zhou[56] reported the use of a bridging ligand substitution reaction for the synthesis and isolation of a number of MOPs containing the copper paddle wheel secondary building unit linked by a range of different carboxylate ligands. They initially created three MOPs which displayed cuboctahedral geometries. The MOPs were then soaked in solvents containing an excess of an additional carboxylate ligand. This allowed for the exchange of ligands and the formation of new polyhedra.

In some cases, the new polyhedra contained both of the organic linkers and formed a new geometry, whilst in other cases, the original linker was substituted entirely resulting in polyhedra containing just the new ligand. This post synthetic modification, or post assembly modification, produced cages of different geometries (octahedral opposed to cuboctahedral) determined by the ligand species and the conditions used. Aside from the isolation of new structures, the variation in the cages alters both the packing of the solids within the crystalline materials, ultimately altering the extrinsic porosity of the materials. The variation in the ligands functionality causes changes in the intermolecular interactions experienced between the cages, which therefore alter the extrinsic porosity.

As a good example of this extrinsic porosity crystal engineering, Li and coworkers reported the formation of two cuboctahedral cages synthesised from isophthalic acid and 5-hydroxyisophthalic acid.[56] Both cages display the same cuboctahedral topology and will have similar intrinsic porosities; however, their extrinsic porosity is different.

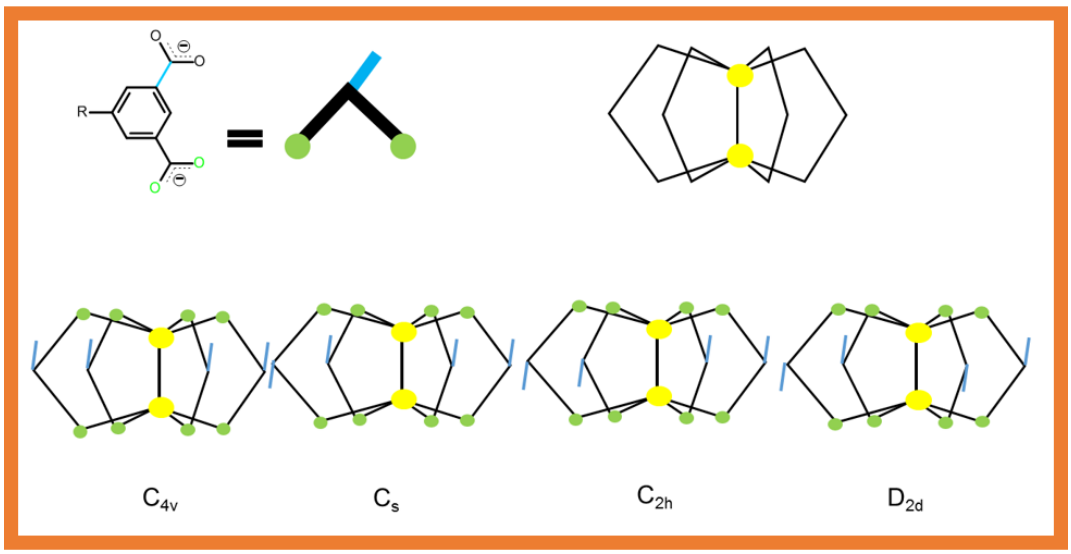

Figure 1.12 shows the four geometric isomers of the paddle wheel structure which orientates the functionality up or down relative to the plane of the carbon centres of the carboxylate groups bound to the metals, as shown. Yellow represents the metal centres and green the single set of oxygens of a carboxylate within an isophthalate ligand.

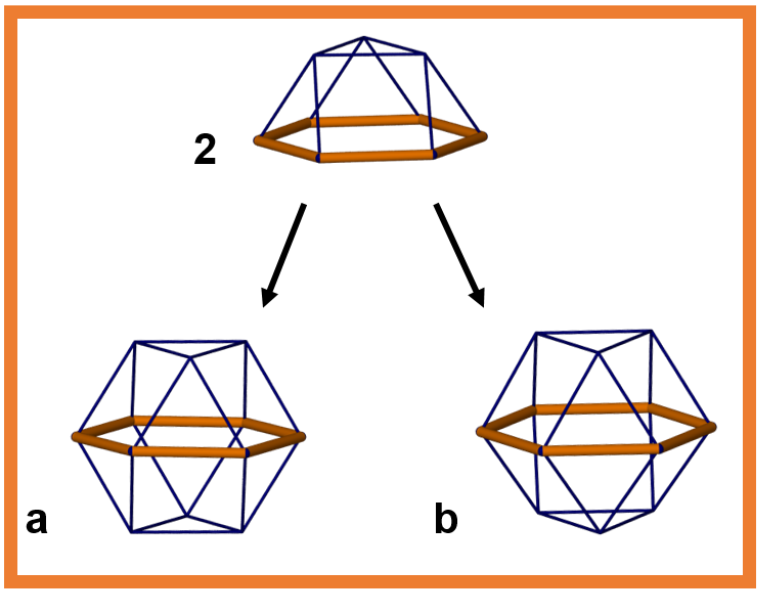

Figure 1.13 ***a*** *shows the formation of a cuboctahedron from two triangular cupola (MAQPOK).* ***b*** *shows the anticuboctahedron (MAQPEA). They form dependent upon how the two triangular cupola are orientated relative to each other.*

The bulkier 5-hydroxyisopthalate actually shows the greater amount of void space per unit cell, at 66.3%, whilst the less bulky isophthalate cage shows 63.2% void space per unit cell. This shows that intermolecular forces between the cages are of significant importance, where controlling extrinsic porosity is concerned.[5,64,65]

1.3.2 Tetrahedral MOPs

Another family of porous MOPs identified from the literature are those based around the tetrahedral structure. The tetrahedron is a Platonic solid formed of four triangular faces. The tetrahedron can be produced by three different assemblies; M_4L_6, M_4L_4 and M_6L_4. The former two assemblies are most commonly seen providing the edge and face form of the tetrahedron, respectively. The M_4L_6 tetrahedron is formed from six ditopic linker and four metal centres. The M_4L_4 requires four tripodal linkers connected to four metal centres whilst the M_6L_4 connects six metal centres with four tripodal ligands. Figure 1.14 displays these three stoichiometries of tetrahedra.

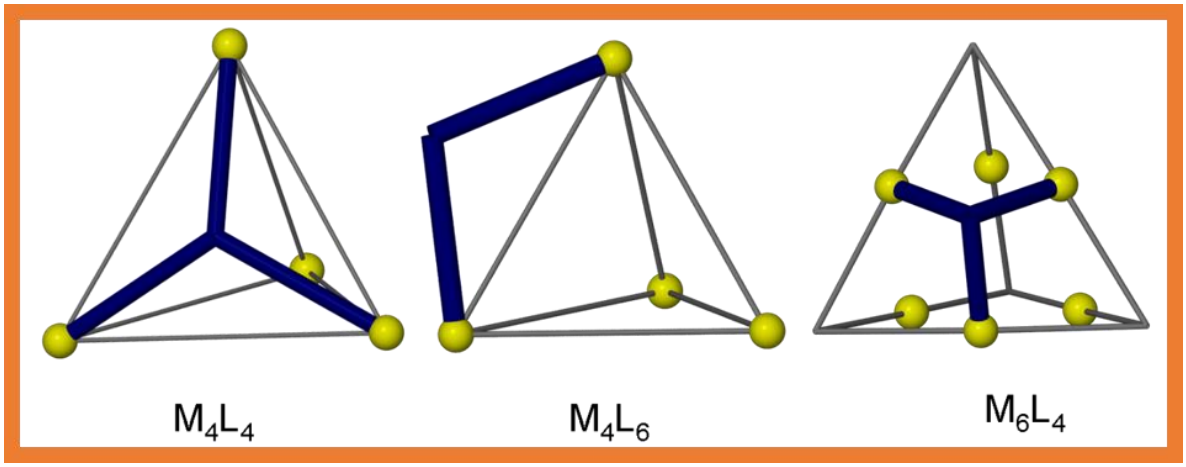

Figure 1.14 Three possible assemblies of tetrahedra through use of face connectivity with vertices (M_4L_4) (IMIHER), edge connectivity with vertices (M_4L_6) (IRADEK) and face connectivity with edges (M_6L_4). These are schematics of real crystal structures. The three tetrahedral assemblies are represented in grey, where the yellow spheres represent the metal atoms and the blue represents a single ligand.

In 2005 Yaghi and coworkers reported a family of M_4L_6 truncated tetrahedra based on a derivative of the basic iron acetate secondary building unit (SBU).[66] The SBU is based on the

well-known basic chromium acetate SBU where the chromium is substituted with iron and three of the acetates are replaced by sulphate anions. The three equivalent octahedrally bound iron atoms connect through three bridging carboxylate ligands and three bridging sulphate ligands. A triply coordinated oxide at the centre of the SBU connects the three metal centres together. Finally, a neutral donor atom, typically from a solvent atom such as water or pyridine, completes each of the iron's coordination spheres. This leads to a C_3 symmetric SBU. The iron acetate SBU (Figure 1.15) is connected with a set of ditopic or tritopic carboxylate ligands which ultimately lead to the formation of the polyhedra. By systematically increasing the length of the ligand (Reticular chemistry), the formation of a family of tetrahedra with an increasingly large pore volume was formed. The isoreticular system formed showed some interesting features in terms of its porosity. Using the "calc solv" algorithm in Platon the intrinsic pore volume increased from 7.1 % up to 26.7 %, as a result of the larger ligand being incorporated into the structure. Whilst the extrinsic porosity is dependent on the packing of the polyhedra, this value varied from 27.2 % to 62.7 % again calculated using calc solv.[66]

Yaghi established that both the intrinsic and extrinsic pores are interconnected via the open faces of the tetrahedra, showing it would be possible for guest species to move through the material. Upon desolvation, the material experiences a loss of crystallinity due to loss of the weak forces between the tetrahedra, resulting in the collapse of the framework.[66] Yaghi went on to establish whether the material maintained permanent porosity. By using gas sorption isotherms it was established that the materials show a reversible type 1 isotherm. So, whilst the materials have lost long range order, they likely maintained their intrinsic pore, whilst the extrinsic porosity has been altered. This work showed that MOPs have surface areas comparable to other porous materials such as zeolites and MOFs.[66] One other example of a porous tetrahedron was reported in 2004 by Bai *et al.*[67] This neutral tetrahedron is based on the M_4L_6 structure with four iron centres connected by six ditopic hydroxamic acid ligands. The four windows of the cage contain dimethylformamide (DMF) solvent and as yet no work has been published on the gas sorption or permanent porosity

of this material. These finding will be discussed more throughout the thesis as this research formed the basis of the project.

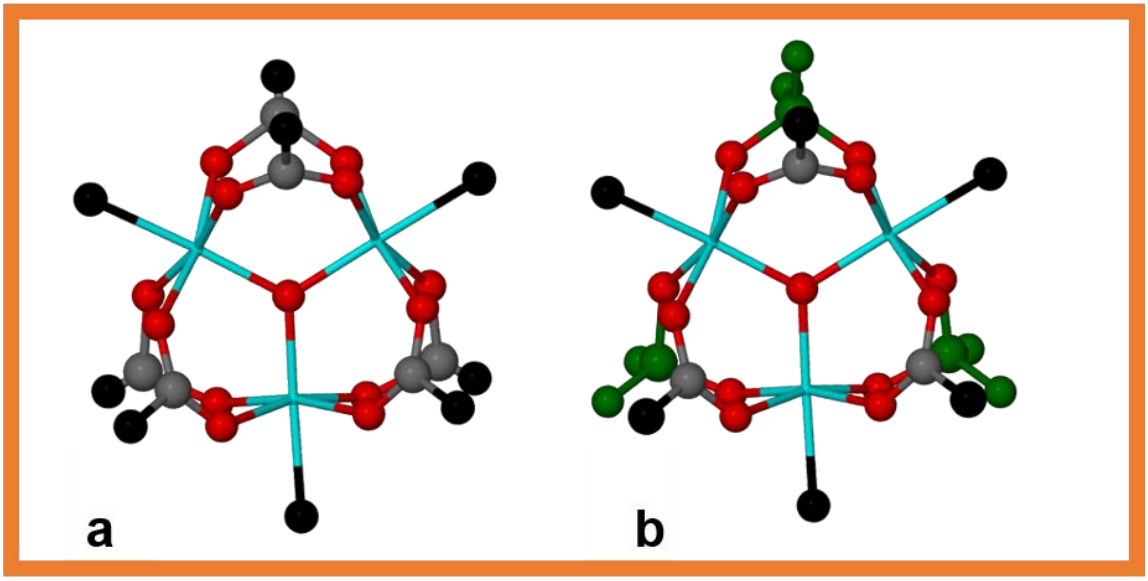

Figure 1.15 ***a*** *shows the basic iron/chromium acetate SBU (ADAZAH). In the design of the Yaghi tetrahedral SBU, half the carboxylates are replaced with sulphates resulting in a* C_3 *symmetric secondary building unit* ***b*** *(JANZII). Within this figure the iron is coloured aqua, oxygen is red, carbon is grey and R groups are black.*

1.4 Applications and characterisations

Due to the varied chemical and material properties of these porous MOP materials, porosity can be targeted towards a wide variety of applications. Catalysis, separation and adsorption are all common target uses for materials of a porous nature and MOPs are no exception. Possibly the most conventional application for porous MOPs are those pertaining to gas separation and storage. This is not only due to the potential applications of this gas sorption but also as it is a key characterisation tool of the porosity. This section aims to describe both characterisation routes and processes required to understand the material properties and potential applications. To begin with, a collective set of procedures to ensure the complete characterisation of the material properties are presented. Each step necessarily requires feedback to others, which results in a dynamic process. This process can be broken down to structural determination, determination of host:guest chemistry (can include gas

sorption isotherms), guest removal characterisation and finally porosity testing (Figure 1.16).

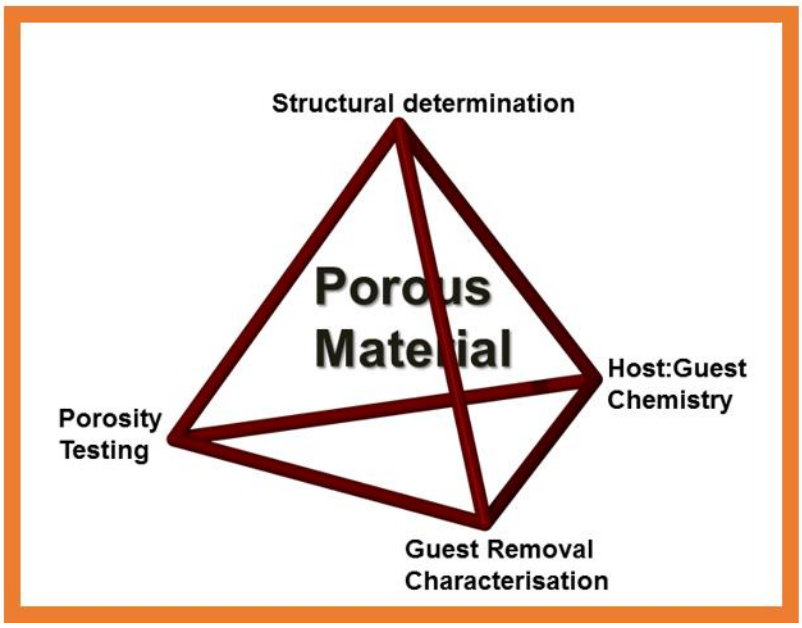

Figure 1.16 characterisation of a porous material. The tetrahedron represents the feedback from several characterisation techniques. This allows for the determination of the structure of the material, its lattice and host:guest chemistry, how to remove the included guests, and testing of the resultant porosity.

Characterising molecular materials is of great importance in terms of understanding the porosity of the materials created, their properties and potential applications. Initially, single crystal X-ray crystallography (ScXRD) is often utilised to determine the structure of the material. Powder X-ray crystallography (pXRD) can subsequently or separately be used to determine bulk phase purity or structural information when ScXRD is not possible. From this data, it is possible to quantify some measure of the porosity of the material. By using pore mapping software (for example, as found in the Mercury, Platon, XSeed and Olex2 single crystal crystallography programs) it is possible to calculate the free volume within the material when a clear host framework can be defined. The majority of these utilise the "rolling ball" algorithm originally developed to map enzyme surfaces and the accessible surface area or solvent-accessible area.[68–73]

By using a probe, a sphere with a radius typically between 1.2 – 1.7 Å (selection of sphere is crucial and should always be stated in the analysis) the program of choice maps the volume that the probe can sweep out within a molecular void or channel. The vast majority of the materials produced contain guest species within the pores of the molecules, to determine the porosity of the materials using this procedure these guests need to be removed; this can be done virtually by removing the guest species from the asymmetric unit within the crystallography software being used prior to the pore mapping regime.[17] This "virtually" empty structure is packed to show any channels or cavities formed, but it should be noted that this may not provide the most accurate representation because removal of the guest within molecular species can often cause the system to rearrange or collapse leading to less porous systems (as described in section 1.2 and Figure 1.1). The connectivity/topology of the pore space, as well as the framework built from the molecular species, can be determined as it is sometimes important in understanding the properties but more importantly, the design of the material(s). Programs such as Topos allows for this analysis, although experience is often required as the "connectivity" interactions are not as directional as those seen in MOFs.[17] Ideally, the host species should be removed and the crystal structure re-determined as the solvent free materials and mapping done on this structure. The process of the removal of the guests is not trivial.

Once the material has been structurally mapped and there is confidence that the system displays cavities or channels that could be potentially porous, the guest can be removed utilising heat and chemical potential.[74,75] Heating is often combined with dynamic vacuum to remove mobile guests from hypothetically porous materials. To circumvent the possible collapse of the materials to a more thermodynamically stable α phase, techniques such as freeze drying and supercritical drying have been utilised to trap intermediate, metastable states. Thermogravimetric analysis and differential scanning calorimetry (TGA and DSC, respectively) are crucial analytical steps in determining this "emptying" of materials. TGA accurately records the weight of the material as it is heated at a specific rate, or held at a constant temperature, under a specific atmosphere. Using TGA, it is possible to accurately determine the amount of included guest within the material[29,76] and gauge the temperature

at which the material can be completely desolvated or dehydrated. The amount of guest shown within the crystallographic structure should tally with the TGA data, helping to confirm the material is desolvated and thus giving definitive structural characterisation.[77] DSC works simply by recording the difference in the amount of energy required to heat the reference and the sample to the same temperature and rate. DSC can provide information on phase changes and enthalpies due to changes in the materials' heat capacity. Understanding whether the materials undergo phase transitions upon desorption of guests can be useful in determining amorphous and crystalline phases produced as part of "processing" the materials for porosity. Clearly, after characterisation and emptying of the material, pXRD and ScXRD need to be repeated to confirm structural coordinates.

The standard measurement for porosity requires the determination of gas sorption isotherms for a variety of gases. There are many isotherms types and models for their interpretation. IUPAC categorise isotherms as one of six types, Types I – VI. One of the most common models utilised for quantifying porosity between materials is Brunauer-Emmet-Teller model (BET).[78] BET values are referred to as surface areas, typically as cm^2g^{-1} or m^2g^1, however, care should be always taken to ensure the theory still holds and the other representations of the isotherm data is not more appropriate. For example, the materials discussed here are discrete molecular species which will show absolute host:guest ratios. Therefore it is recommended, when possible, that the host:guest ratios at specific pressures or vapour pressures be reported, with typical mg/g given for CO_2 sorption isotherms being easily converted in molar quantities and reported. One very simple method for testing porosity is simply to absorb a guest. Iodine (I_2) represents an easy method for testing porosity as it changes the colour of the material, although some care must be taken to ensure that the I_2 is not just bound to the surface of the crystals.[29,35,79] Tests such as elemental analysis and TGA can also confirm sorption of I_2. There has been much interest in I_2 sorption into porous materials, mostly due to interest in radioactive I_2 produced from nuclear reactors.[79,80] Related to that is the interest in porous materials that absorb dyes out of solution.[79] This has been shown to occur in MOP materials as well.[79]

In situ crystallography,[81,82] where the structure of the crystals are determined in the presence of the guest in the form of liquid, vapour pressure or gas pressure under controlled experimental values, allows for determination of not only the binding positions of the guests (if possible) but also host:guest inclusion properties. This technique requires the use of a capillary/sealed vessel loaded with gas/vapour at a desired pressure, at which the data collection is performed. This can allow for refinement of crystal structures in which the location of the gas molecules trapped within the pores of the material can be determined. This, of course, can be complemented by the many computational techniques available for determining gas sorption and the gas binding sites.[83]

Due to the control that can be exerted over these materials in terms of their pore shape, size, and chemical functionality, they are an obvious choice when dealing with gas separation and storage. The intrinsic cavity of the cage can be designed with properties idealised to capturing and trapping molecules of the desired gas. Due to the environmentally harmful effects of greenhouse gases such as CH_4, CO_2 and N_xO_x, they have become common targets for gas separation and storage across the field of porous materials, with MOPs being no exception. One such example is the selective separation of CO_2 from multi-gas systems. Zhou and co-workers[84] developed a MOP cavity to specifically capture a single CO_2 molecule. The intrinsic porosity of the cage was designed to contain one molecule of CO_2. The cavity is designed to optimise the interactions between the cavity and the CO_2 molecule, therefore increasing its selectivity towards CO_2 and limiting the adsorption of other gases within a gas mixture.[84] More specifically the angle and length of the ligands optimise the metal – metal length and orientation to allow the CO_2 to anchor between the metals within the MOP. When separation is the targeted properly there are other analyses that can be utilised to quantify the materials' efficiencies. These are the calculation of a separation factor from the isotherms of different gases and the use of break-through experiments.[85] Separation of other gaseous compounds is possible with MOPs, for example, the separation of alkane, alkene and aromatic organic compounds is important industrially. A Johnson-solid based material has been shown to have selectivity towards larger C_2H_6 and C_3H_8 over methane.[42] Designed to produce an asymmetric MOP by utilising the organic

building blocks in the form of a calixarene and 5-(pyridin-4-yl) isophthalate, this example shows how complex the MOP designs can become. Crowley and co-workers[86] produced a series of lantern shaped coordination cages with the general formula $[Pd_2(L)_4]^{4+}$. Despite these cages being a charged species, the counterions are not located within the intrinsic pore, probably due to the lone pair-lone pair repulsion. This leaves the intrinsic pore free for the adsorption of CO_2 gas. They report that the cages have little affinity for N_2 but CO_2 binds favourably due to a number of electrostatic interactions between the CO_2 molecules and the pyridyl ligand used to form the MOP.

Sensing based on a colorimetric change in a material is an important methodology for the development of sensors. There are a number of MOP examples shown in the literature,[26,28,87] especially based on solution sensing, but the examples of solid materials that are porous in nature are scarcer. A good example to show the potential of these materials for applications is given of a metal organic polygon based on a colorimetric sensing group and platinum-based assembly (Figure 1.17).[87] This material is constructed from a Pt-based assembly of a metallocycle with a C-shaped organic ligand, which contains a reporting colorimetric group. Upon desolvation, the empty material can phase change upon exposure to CH_2Cl_2 vapours within minutes. This new phase is not only metastable, i.e. can maintain its phase upon CH_2Cl_2 removal, it is also a different colour. The material converts from yellow to orange. To reform the yellow phase the orange material needs to be mechanically ground.

MOPs have a clear future in membrane development as they have an advantage over many porous materials due to their processability. This processability is due to their solubility, as they are molecular species.[21,88,89] Membrane technologies are seen as a low cost, energy efficient solution to the problem of separation.[89] Within the literature, there are examples of MOPs being combined with a variety of polymers to form a material suited to separation.[88,89] The separation of methane from carbon dioxide is vital in industry due to the harmful effects of carbon dioxide and the improvement in the combustion of the methane. The incorporation of MOPs into polymer membranes can significantly improve both the permeability and the separation factors of the material.[89]

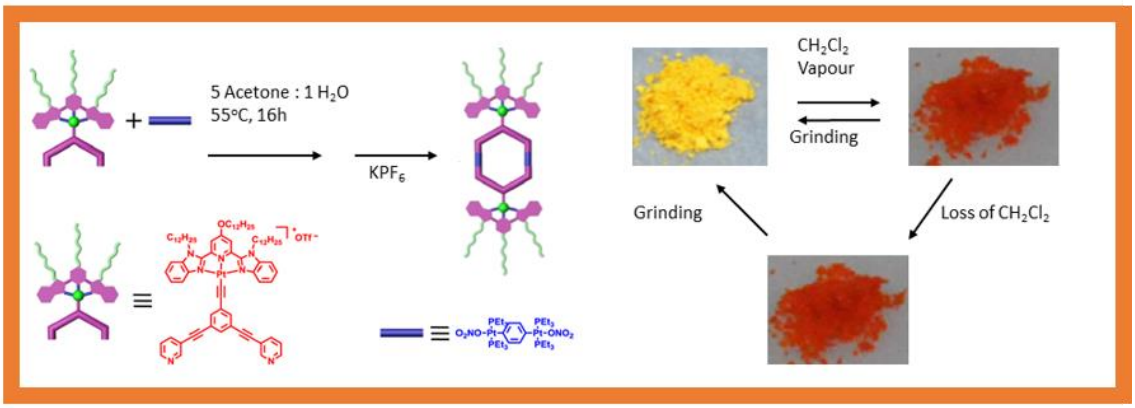

Figure 1.17 colour change material. ***a*** *Assembly of the Pt-based metal organic polygon incorporating a colorimetric sensing group.* ***b*** *The empty material changes from yellow to red within minutes of being exposed to CH_2Cl_2 vapours. Even on loss of the CH_2Cl_2, the material maintains this colour. It is only through a mechanochemical induced phase change that the material can be returned to its original yellow form. Reprinted (adapted) with permission from (B. Jiang, J. Zhang, J. Q. Ma, W. Zheng, L. J. Chen, B. Sun, C. Li, B. W. Hu, H. Tan, X. Li, and H. B. Yang, J. Am. Chem. Soc., 2016, 138, 738-741). Copyright (2016) American Chemical Society.*

The post synthetic modification of these MOPs also plays a role in altering the separation and selectivity of the materials. Due to the high solubilities displayed by the MOPs, they display excellent adhesion and dispersion properties within the polymers. This is shown to improve permeability and the separation factors by up to 81% and 60%, respectively.[89] Conventional polymer membranes have a trade-off between selectivity and permeability so by incorporating MOPs there is potential to create a highly selective and controlled permeability in a material. Due to the high solubility of MOPs, it is thought that they can be better dispersed throughout the material thus avoiding aggregation problems seen with other additives in mixed membrane systems.[89] Another example shows the separation of liquids and uses a soluble copper-based MOP with its organic linker functionalised to improve solubility and functionality when incorporated into a highly branched polymer solution.[88] It forms a material capable of separating a 1:1 toluene, *n*-heptane solution, with a separation factor of 19. The material can also enrich benzene from a 50% benzene/cyclohexane solution, with a separation factor of 15.4 towards benzene.[88] The final example given here is the Hupp Re square described earlier in section 1.2.1.[21] By

incorporating the square into a membrane, they were able to show a stable porous material with good selectivity.

MOP materials are also being developed for use within pharmaceutical delivery. The aim is to develop new routes for drug delivery due to the size of discrete MOP being analogous to that of enzymes.[90] MOPs can be seen to be favourable over other potential carriers as they are easily functionalised and decorated upon their surface, thus allowing for biocompatibility. They can selectively encapsulate the target drug molecule, store and transport it to the target site before controlling the release of the drug at a specific site within the body. By controlling the design of the cavity, the encapsulation of the drug can be controlled and by controlling the composition of both the ligand and the metal used within the cage, it is possible to control biocompatibility or even use metals as part of the treatment. For example, Ruthenium (II) complexes are used as anti-cancer agents and building blocks of the MOPs.[90] As a potential drug formulation, the crystalline phase of these materials will be important.

Given the importance of porous materials within industrial heterogeneous catalysis, for example, the use of zeolite ZSM-5 for the cracking of long chain hydrocarbons, it is surprising that no crystalline porous molecular material has yet been utilised as a heterogeneous catalyst. A particular advantage over traditional inorganic solid material catalysts that the MOP materials could potentially have is their high processability due to their solubility. This makes their separation from products or regeneration processes much easier. Within the literature, there are many examples of homogeneous supramolecular catalysis; one example of many within the literature is the Nazarov cyclisation within a catechol-based tetrahedral cage.[91] The field is continuously developing and there are many exciting opportunities for stereo- and enantio-selective synthesis mimicking biological enzymes. These catalysts are often described as being biomimetic as the intrinsic pore space of the MOPs acts as a controlling environment reminiscent of those found in enzymes. One major difference between heterogeneous and homogeneous supramolecular catalysis is that in the solid-state it is required that there be extrinsic porosity to allow for the diffusion of the products and reactants through the material and into the intrinsic pore where the

catalysis takes place. This makes the crystal engineering of such materials incredibly difficult and the stability of such materials can be compromised through decreases in mechanical and chemical stabilities. The mechanical properties of the MOP crystalline family of materials has not been investigated in depth, which is in contrast to most other materials.[92]

1.5 Hydroxamic acids

1.5.1 An introduction

Hydroxamic acids can be simply viewed as a hydroxy-amide. A hydroxyl group is attached to the nitrogen of the amide as shown in Figure 1.18a. The hydroxamic acid functionality is a group that plays its most significant role within the field of medicinal chemistry. Hydroxamic acids have a high binding affinity towards trivalent metal ions (M^{3+}) and in particular Fe^{3+}. Sources of Fe^{3+} tend to be insoluble at physiological conditions.[93] Iron is essential for life sustaining processing many species including bacteria, plants and octopus use Fe chelating compounds called siderophores, molecules that sometimes contain the hydroxamate functionality, to bypass the Fe solubility problem.[94–96]

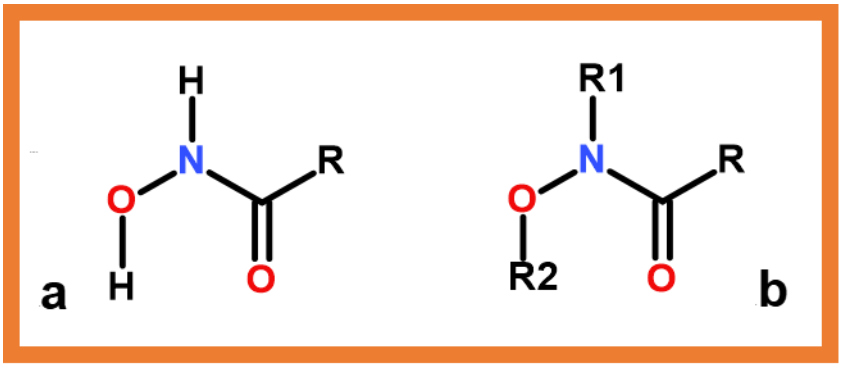

Figure 1.18 ***a*** *shows the structure of a primary hydroxamic acid, within the CSD the majority of conformers show the cisoid conformation. This is where the carbonyl O is cis to the other O.* ***b*** *Potential derivatives of a hydroxamic acid R, R1, R2, can be H, alkyl, or aryl providing many possible structures using the same functional group.*

Due to their affinity for M^{3+}, hydroxamic acid based medications such as Deferoxamine are licensed for use in chelation therapy,[97,98] which is used in conjunction with dialysis

treatment to remove excess Al^{3+} and Fe^{3+} from the blood.[99–102] Other disorders that cause an overload of iron in the blood, such as thalassemia and hemochromatosis, are also treated with Deferoxamine.[100,102] Hydroxamic acids have also been shown, to act as histone deacetylase inhibitors, which work by disrupting normal DNA replication resulting in death of the cell.[93,94,97,98,103,104] There is currently much research being conducted on their potential as treatments for HIV, cancer and neurological diseases such as Huntington's and Alzheimers.[103–105] They also show promise as antibacterial, antifungal, enzyme and metalloprotein inhibiting drugs.[93,95,98,106,107] There are already examples of licensed hydroxamic acid medication on the market for the treatment of cancers; Panobinostat and Vorinostat are used in the treatment of multiple myeloma and T-Cell lymphoma.[98,100,108,109]

The most typical chelation mode of the hydroxamic acid is through the two oxygens.[96] Hydroxamic acids can be deprotonated in two ways, the singly deprotonated 'hydroxamato' species, shows loss of the hydroxyl hydrogen, or they can be doubly deprotonated forming the 'hydroximato' species (loss of the proton from both the N and the O), both species are depicted in Figure 1.19.[95,96]

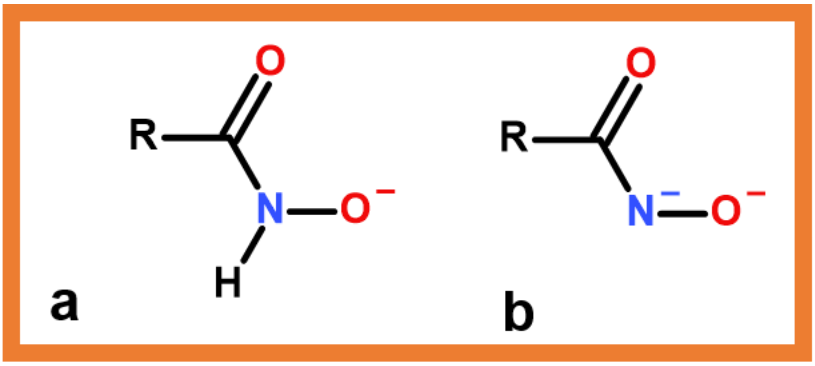

Figure 1.19 ***a*** *the singly deprotonated hydroxamato species and* ***b*** *the doubly deprotonated hydroximato species.*

Within the CSD (Cambridge Structural Database) there are around a 100 primary hydroxamic acids (where both the N and O have H's) and around 240 structures of their metal complexes. Which provides users with a database of typical bond lengths and angles for these compounds when both complexed and uncomplexed.

Hydroxamic acids can be synthesised using a plethora of techniques including biological synthesis from bacteria.[106,110–112] Alternatively, there are many chemically synthetic ways to produce hydroxamic acids using different functional groups, including aldehydes via the Angeli-Rimini reaction,[113] the most common synthesis method is the nucleophilic hydroxylamine reaction.[114] Hydroxylamine substitution can occur with esters,[96] carboxylic acids,[115] acid chlorides,[95,116] and acid anhydrides.[114] The synthesis of hydroxamic acids shall be discussed in greater detail in chapter 2. The coordination of Fe^{3+} with the hydroxamic acid provides a distinct purple colour which is used to help confirm the conversion to the hydroxamic acid.[96]

1.5.2 Materials of hydroxamic acids.

Hydroxamic acid coordination with metals is primarily bidentate, through the two oxygens. Within the CSD, there are 825 hydroxamic acid containing metal complexes. The coordination sphere of these is dependent upon the oxidation state of the metal. When chelated to metals such as In^{3+}, Fe^{3+}, Al^{3+} and Ga^{3+} form octahedral complexes involving three ligands. Zn^{2+} also forms an octahedral complex but in all the reported cases one of the three ligands is not a hydroxamic acid.[67,117–120] Of the 825 examples, 31 are of eight coordinate complexes. This is four ligands coordinated to a single metal atom of Zr^{4+}, Hf^{4+}, Ce^{4+}, Sm^{4+} and U^{4+}.[121,122] Cu^{2+} forms square planar complexes involving just two ligands.[117] Figure 1.20 shows examples of these coordination spheres. Copper has been reported to form metallacrowns.[123,124] The metallacrowns are cyclic structures, like the molecular square reported earlier, are another member of the polygon family.

1.5.2.1 Metallacrowns

The first hydroxamic acid metallacrown was reported by Pecoraro in 1989.[123] Metallacrowns (Figure 1.21) are a self-assembling macrocyclic compound, sometimes described as the inorganic version of a crown ether.[123,124]

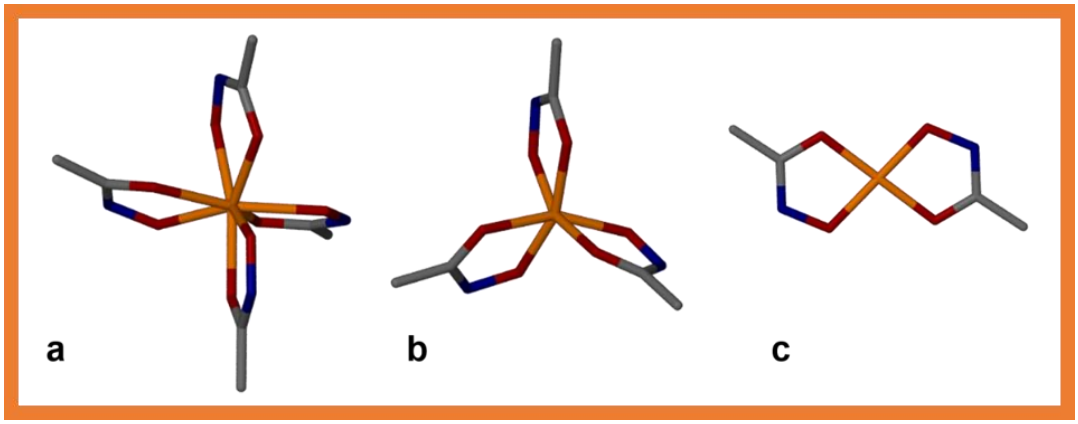

*Figure 1.20 capped stick images of **a** coordination sphere of an ocadentate hydroxamic acid metal complex. (TEQSAL. **b** distorted octahedral hydroxamic acid coordination sphere (IRADEK). **c** square planar hydroxamic acid complex (QOFKAX). Where the metal centre is coloured orange and CPK colours are used for other elements, oxygen in red, nitrogen in blue and carbon in grey.*

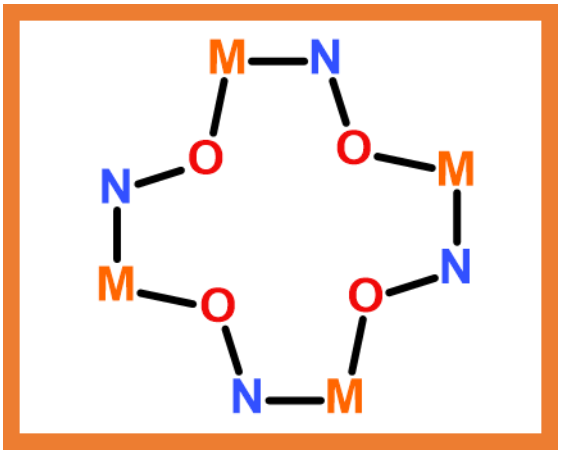

Figure 1.21 shows the 12-metallacrown-4 structure. Displaying the typical M-O-N repeat unit. Where M (orange) is a metal, O (red) is oxygen and N (blue) is nitrogen.

They comprise of metal and heteroatoms commonly with an (M-O-N) repeat unit.[123–127] Like molecular squares, their intrinsic pore makes them highly suited to the encapsulation of di and trivalent ions. Their host:guest chemistry is being investigated for use in molecular recognition and in the separation of lanthanides.[124,126] Other research utilises their magnetic properties for use as single molecule magnets.[127,128]

Pecoraro and co-workers have reported several examples of phenylalanine hydroxamic acid coordinating to Zn or Cu forming metallacrowns.[124,125,129,125] They also report that these metallacrowns can be connected to form frameworks by incorporating metal bridges such as the copper paddlewheel. It is possible to control the framework structure formed by selecting metals that favour certain coordination geometries. For example silver favours linear coordination, this forms more open frameworks, whilst the likes of Cu form more compact structures due to their square planar coordination.[124] The framework species produced display chiral channels suitable for the separation of chiral molecules and substrate recognition.[124]

1.5.2.2 MOPs of hydroxamic acids

As well as the polygons mentioned above, there are literature examples of hydroxamic acids forming MOPs. Hydroxamates chelate to metals through two oxygens, as seen with carboxylates, this suggests that hydroxamates should be suitable for the formation of porous materials including MOFs and cages.[67,119,130–132] The literature is limited on hydroxamic acid based cages but there are some interesting examples of neutral M_4L_6 tetrahedra presented by Raymond and Bai.[67,119,132] In both cases the hydroxamic acid cages are chiral in nature, due to the asymmetric nature of the five member ring formed by the chelation of the hydroxamate to Fe^{3+} or Ga^{3+}. The octahedral vertex is distorted, leading to lambda (Λ) or delta (Δ) chirality. The propeller type vertex will display rotation either right (Δ) or left (Λ) (Figure 1.22). Both Bai and Raymond[132,119] report the tetrahedra displaying four chiral metal vertices (Λ/Δ) connected by six hydroxamic acid ligands. Raymond uses Ga^{3+}, enabling solution state ^{1}H-NMR (Nuclear Magnetic Resonance) studies on the cages. They establish that the cages are dynamic in solution and readily convert between five isomers on the NMR timescale. The isomers of the cage are dependent on their chiral vertices, where there are two T type cages that display ΛΛΛΛ or ΔΔΔΔ vertices. Two C_3 cages, where one vertex is of the alternate chirality *(*ΛΛΛΔ, ΔΔΔΛ*)* and finally one S_4 cage where there are two vertices of each chirality *(*ΛΛΔΔ*).*[119] The isomers are pictorially represented in Figure 1.22. The isomer names represent the point group symmetries of the vertex. Within the solid state Bai reports the cages to show racemic T type symmetry; the

crystal contains cages of both T symmetries. Raymond's cages are also racemic with the S_4 symmetry.

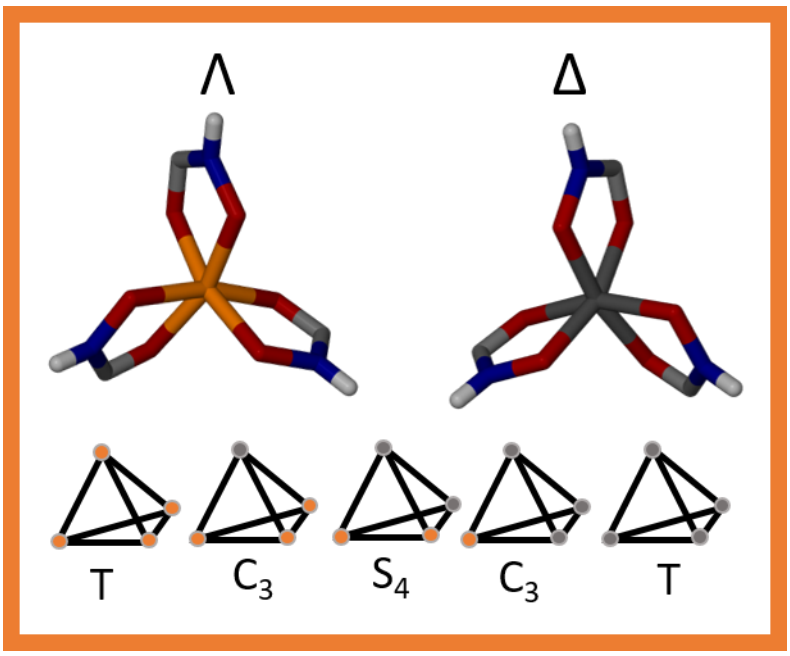

Figure 1.22 shows the Fe^{3+} hydroxamate propeller coordination. Lambda (Λ) isomer has its Fe centre coloured orange. The delta (Δ) isomer has its centre in dark grey (IRADEK). The five cage isomers are also represented below where each circle represent the chirality at that vertex.

The majority of cages reported by the likes of Fujita[133–135], Nitschke[136–138] and Raymond[91,139,140] are charged species and as such require charge-balancing ions to be incorporated into the void space of the structure and can only be substituted, not removed. The Raymond and Bai cages crystallise as the DMF solvate due to the cages being neutral species, they do not require a counter ion. Upon removal of the DMF solvent, both the intrinsic and extrinsic void of the cage will be empty, therefore, the void space available to guest molecules is larger and more accessible than that of the charged cages.

Raymond also reports M_2L_3 helices formed from rhodotorulic acid (Figure 1.23a); a siderophore isolated from yeast.[141–143] This cyclic dipeptide contains two hydroxamate groups and produces M_2L_3 helices when complexed to Fe, Al and Cr.[142] The chiral nature of the vertex gives rise to three potential helicate isomers (ΔΛ, ΔΔ, ΛΛ).

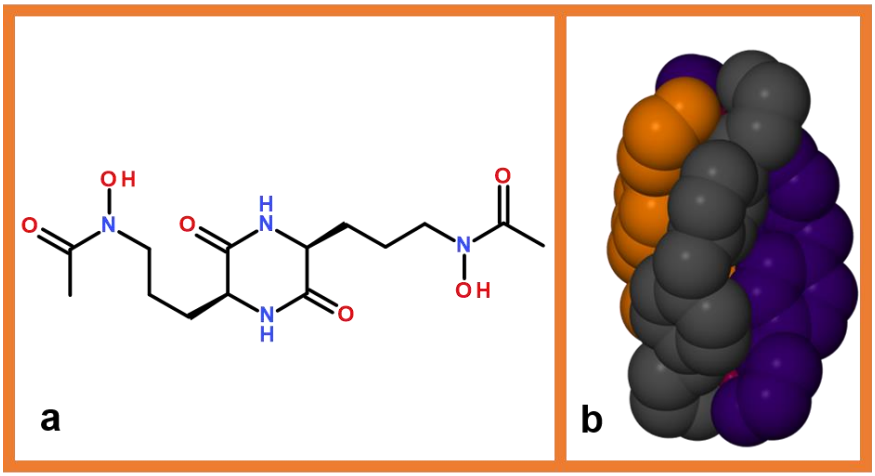

Figure 1.23 ***a*** *showing the structure of rhodotorulic acid.* ***b*** *space filled structure of an M_2L_3 helicate (EGUWAE, tris(μ_2-bis(4-((Pyrid-2-yl)methyleneamino)phenyl)methane)-di-copper(ii)). The three ligands have been coloured differently to highlight the D_3 symmetry of the complex.*

In the case of rhodotorulic acid, the first reported naturally occurring example of a triple helicate, only the ΔΔ isomer was found.[141–143] An analogue of rhodotorulic acid was shown to form a racemic mixture of the ΔΔ/ΛΛ triple helicates, and encapsulates a molecule of water within it.[144] Triple helicates are defined as a complex comprised of three identical C_2 symmetric ligands complexed to two metal centres, both with the same chirality. They typically display idealized D_3 point group symme try where the C_3 axis is coincident with, and the three C_2 axes are perpendicular to, the helical axis of the complex (Figure 1.23b).[141]

1.5.2.4 MOFs

There are a small number of reported hydroxamic acid frameworks. One example by Tezcan discusses the rational synthesis of a 3D framework incorporating spherical proteins.[131] They report that by understanding and controlling the symmetry elements of the metal nodes and organic struts it is possible to design a framework. In this case, they selected a spherical Zn ferritin protein with octahedral symmetry. Essentially a spherical cage to act as the node. Linear, rigid and ditopic ligands in the form of 1,4-benzene dicarboxylate (terephthalic acid) and 1,4-benzene dihydroxamate, were selected to connect the spheres, which was predicted to form a body centred cubic (bcc) lattice. They go on to show that the strong

coordination of hydroxamic acids is essential to form the predicted bcc lattice and that hydroxamic acids can be used in the design of modular frameworks, due to their predictable bidentate coordination with metals. Farah utilises post synthetic modification to incorporate hydroxamic acid linkers into the Zr-UiO-66 MOF.[145] Using solvent assisted ligand exchange they substituted terephthalic acid for 1,4-benzene dihydroxamate. This produces a MOF with the same topology but with different functionality. With the hydroxamate Zr interaction being stronger than that of the Zr carboxylate interaction, it offers the advantages of increased framework stability and bond strength. They report a 60% ligand conversion after six days and go on to show that the hydroxamic acid seals defects within the frameworks which contributes towards the increase in framework stability. Farah also states:

"Given the strength of Zr–hydroxamate bonds, it is expected to be very difficult to obtain a porous, crystalline material by de novo synthesis using a Zr precursor and hydroxamic acid linkers."[145]

Which when thought about in conjunction with the dynamic nature of the hydroxamic acid coordination to metals, this goes some way to explaining the lack of porous hydroxamic acid materials reported in the literature.

1.6 Conclusion

Crystal engineering and material characterisation of molecular porous materials constructed from discrete metal organic polygons and polyhedra represent a growing applicable class of materials for deployment in porous applications within industry and academia. Even with this progress, there are still a significant number of challenges to overcome. To design the materials, capable of solving societal and industrial problems such as renewable and sustainable energy, and anthropometric induced climate change, they need to be designed. The design of cage structures is still fraught with difficulties, mostly due to the lack of easy to use software and theory tools.[146] Even if you can make the cage compounds, crystallisation and the crystal structure are still difficult to predict, despite

significant advancements regarding prediction of structure in cages from the Day and Cooper groups.[20] This means that over the coming decades, there will be significant developments on this front.[20]

Crystal engineering tools are available, and persistent intrinsic porosity of the MOPs means that obtaining porous materials is likely whatever crystalline or amorphous phase is obtained. Crystal structure prediction is not universally accurate for all molecule types and when kinetics dominate the assembly process, even more so. The material properties need to be better characterised, especially that of the mechanical properties, as is happening in the literature at the moment with MOFs.[92] Molecular porous compounds can display porosity with BET surface areas of up to 2000 m^2g^{-1}, which is comparable to nearly all other classes of materials.[16,22] It is the host:guest chemistry of the intrinsic and extrinsic porosity that truly differentiates these materials from their more illustrious cousins. The well-establish supramolecular chemistry of host:guest chemistry means that scientists have an excellent opportunity to design, tune and eventually make applicable materials for specific tasks.[3] This is not the only advantage over other classes of materials. The solubility of the molecular entities means that processability of the materials should be significantly easier, cost affordable and flexible meaning that the engineering of the applications should be possible.[3,21,147] This could be no truer than when discussing the production of membranes for separation technologies.[88,90,147,148]

In summary, metal organic polygons and polyhedra are a rapidly expanding field of porous material research. Due to their rational synthesis, high selectivity, display of both intrinsic and extrinsic porosity, and high solubility they are a fascinating area of research which encompasses many different techniques in understanding their structure and potential applications. The use of hydroxamic acids to form these materials is an area that provides lots of potential for expansion due to their ready chelation to a variety of metals, and the limited literature on the coordination and structure of hydroxamic acid based porous materials.

1.7 Thesis overview

The aim of this PhD was to understand the synthesis and host:guest chemistry of porous molecular solid-state materials that incorporate hydroxamic acids. By understanding the connectivity, coordination and supramolecular synthons of hydroxamic acids, it will be possible to design materials of specific geometries utilising design rules and crystal engineering principles. By exploiting a range of analytical techniques including pXRD, ScXRD and Pair Distribution Function (PDF) the aim is to show how design rules and crystal engineering can be utilised in forming more porous, low symmetry molecular cages.

Chapter 2 discusses the synthesis of hydroxamic acids from the solution state through to the solid-state synthesis. Co-crystal design and the supramolecular synthons seen within the solid state were also studied.

A number of previously unreported hydroxamic acids were synthesised in the solid state. By removing the solublity barrier, mechanochemistry allows formation of previously unaccessible compounds. Hydroxamic acids are commonly seen in medicinal chemistry, however their poor thermal stability and solublity limits their uses. By forming cocrystals of hydroxamic acids the aim was to improve their physical properties. Two solvates of a zirconium-hydroxamate complex were also studied. The increased number of hydroxamic acids, their cocrystals and metal complexes has allowed for a better understanding of the supramolecular synthons favoured by hydroxamic acids.

The hypothesis of this chapter was to understand the synthesis and supramolecular synthons of hydroxamic acids.

Chapter 3 discusses the synthesis, crystallisation and host:guest chemistry of a family of potentially porous M_4L_6 tetrahedra based on hydroxamic acids. This chapter utilises a range of crystallographic techniques and PDF to understand the chemistry of these materials.

By better understanding the synthons hydroxamic acids favour, it is possible to understand their favoured interactions and how to incorporate them into porous materials. Hydroxamic

acids have been shown to form molecular cages. Molecular cages are processable and are throught to be promising in the area of molecular separation, with their intrinsic and extrinsic void spaces.[3] The intrinsic void can be used for guest separation and storage based on size and chemistry. With the extrinisic void allowing the guest access to the intrinsic void space. Using crystal engineering principle it has been possible to form more extrinsically porous molecular cages, whilst maintaining a fixed intrinsic void.

The hypothesis of this chapter was to produce more extrinsically porous materials whilst maintaining the same intrinsic pore space and to understand the host:guest chemistry of the materials.

Chapter 4 discusses the synthesis and host:guest chemistry of a range of coordination polymers and macrocycles based on the, 1,2-bis(isonicotinoylamino)benzene ligand.

Discussed is the synthesis and host:guest chemistry of a family of macrocycles and coordination polymers formed via mechanochemical synthesis. Solvent crystallisation of these compounds has produced a rich landscape of macrocycles and coordination polymers, dependent upon the included solvent and anion. The aim is to understand if the synthesis route plays a role in determining the structure of the complex formed. The affect of the synthesis route upon the host:guest chemistry was also studied. The bulk samples formed via mechanochemical synthesis was compared to the samples produced from standard solution-based crystallisations.

The hypothesis of this chapter was to understand the effect that synthesis route plays on a family of dynamic self assemballing macrocycles and coordination polymers. In terms of their structure and material properties.

1.8 References

1 H. R. Green and G. O. Lloyd, in *Chapter 9. Porous Metal Organic Polygons and Polyhedra - Intrinsic vs. Extrinsic Porosity in Functional Supramolecular Materials : From Surfaces to MOFs*, ed. R. Banerjee, The Royal Society of Chemistry, Cambridge,

1st edn., 2017, pp. 297–324.

2 C. R. Groom, I. J. Bruno, M. P. Lightfoot, S. C. Ward, R. Taylor, M. Towler, J. van de Streek, P. A. Wood and A. G. Orpen, *Acta Crystallogr. Sect. B*, 2016, **72**, 171–179.

3 A. G. Slater and A. I. Cooper, *Science*, 2015, **348**, 988.

4 T. R. Cook, Y. R. Zheng and P. J. Stang, *Chem. Rev.*, 2013, **113**, 734–777.

5 S. Jiang, J. T. A. Jones, T. Hasell, C. E. Blythe, D. J. Adams, A. Trewin and A. I. Cooper, *Nat. Commun.*, 2011, **2**, 207.

6 J. L. Atwood, J. E. D. Davies and D. D. MacNicol, *J. Lipkowski, Inclusion compounds formed by Werner MX_2A_4 Coordination Complexes*, Academic Press, London, 1st edn., 1984.

7 J. L. Atwood and J. W. Steed, *Encyclopedia of Supramolecular Chemistry, Volume 2*, CRC Press, New York, 2004.

8 D. V. Soldatov, G. D. Enright and J. A. Ripmeester, *Cryst. Growth Des.*, 2004, **4**, 1185–1194.

9 L. R. Nassimbeni, *Acc. Chem. Res.*, 2003, **36**, 631–637.

10 A. J. Cruz-Cabeza, G. M. Day and W. Jones, *Chem. - A Eur. J.*, 2009, **15**, 13033–13040.

11 A. J. Cruz-Cabeza, S. Karki, L. Fábián, T. Friscić, G. M. Day and W. Jones, *Chem. Commun.*, 2010, **46**, 2224–2226.

12 B. Ibragimov, *J. Incl. Phenom. Macrocycl. Chem.*, 1999, **34**, 345–353.

13 L. J. Barbour, D. Das, T. Jacobs, G. O. Lloyd and V. J. Smith, in *Supramolecular Chemistry*, John Wiley & Sons Ltd, 2012.

14 G. O. Lloyd, J. Alen, M. W. Bredenkamp, E. J. C. de Vries, C. Esterhuysen and L. J.

Barbour, *Angew. Chem. Int. Ed.*, 2006, **45**, 5354–5358.

15 D. J. Cram, *Nobelprize.org*, 1987, 420–436. accessed October 2016.

16 M. Mastalerz and I. M. Oppel, *Angew. Chem. Int. Ed.*, 2012, **51**, 5252–5255.

17 L. J. Barbour, *Chem. Commun.*, 2006, 1163–1168.

18 T. Jacobs, V. J. Smith, L. H. Thomas and L. J. Barbour, *Chem. Commun.*, 2014, **50**, 85–87.

19 R. M. Barrer and V. H. Shanson, *Chem. Commun.*, 1976, 333.

20 A. Pulido, L. Chen, T. Kaczorowski, D. Holden, M. A. Little, S. Y. Chong, B. J. Slater, D. P. McMahon, B. Bonillo, C. J. Stackhouse, A. Stephenson, C. M. Kane, R. Clowes, T. Hasell, A. I. Cooper and G. M. Day, *Nature*, 2017, **543**, 657–664.

21 A. G. Slater, M. A. Little, A. Pulido, S. Y. Chong, D. Holden, L. Chen, C. Morgan, X. Wu, G. Cheng, R. Clowes, M. E. Briggs, T. Hasell, K. E. Jelfs, G. M. Day and A. I. Cooper, *Nature Chem.*, 2016, **9**, 1–9.

22 G. Zhang, O. Presly, F. White, I. M. Oppel and M. Mastalerz, *Angew. Chem. Int. Ed.*, 2014, **53**, 1516–1520.

23 J. P. Konopelski, F. Kotzyba-Hibert, J. M. Lehn, J. P. Desvergne, F. Fages, A. Castellan and H. Bouas-Laurent, *Chem. Commun.*, 1985, **7**, 433.

24 H. S. M. Coxter, *Regular Polytopes*, Dover publications Inc, New York, 3rd edn., 1973.

25 M. Barboiu, Ed., *Constitutional Dynamic Chemistry*, Springer-Verlag, Berlin Heidelberg, 2012.

26 S. Bélanger, J. T. Hupp, C. L. Stern, R. V. Slone, D. F. Watson and T. G. Carrell, *J. Am. Chem. Soc.*, 1999, **121**, 557–563.

27 R. V. Slone, J. T. Hupp, C. L. Stern and T. E. Albrecht-Schmitt, *Inorg. Chem.*, 1996, **35**, 4096–4097.

28 L. Dobrzańska, G. O. Lloyd, C. Esterhuysen and L. J. Barbour, *Angew. Chem. Int. Ed.*, 2006, **45**, 5856–5859.

29 C. D. Jones, J. C. Tan and G. O. Lloyd, *Chem. Commun.*, 2012, **48**, 2110–2112.

30 T. J. Burchell, D. J. Eisler and R. J. Puddephatt, *Inorg. Chem.*, 2004, **43**, 5550–5557.

31 T. J. Burchell, D. J. Eisler and R. J. Puddephatt, *Chem. Commun.*, 2004, **788**, 944–945.

32 T. J. Burchell, D. J. Eisler, M. C. Jennings and R. J. Puddephatt, *Chem. Commun.*, 2003, 2228–2229.

33 T. J. Burchell, D. J. Eisler and R. J. Puddephatt, *Cryst. Growth Des.*, 2006, **6**, 974–982.

34 T. Jacobs, G. O. Lloyd, J. A. Gertenbach, K. K. Müller-Nedebock, C. Esterhuysen and L. J. Barbour, *Angew. Chem. Int. Ed.*, 2012, **51**, 4913–4916.

35 L. Dobrzańska, G. O. Lloyd, H. G. Raubenheimer and L. J. Barbour, *J. Am. Chem. Soc.*, 2006, **128**, 698–699.

36 J. L. Atwood, L. J. Barbour, A. Jerga and B. L. Schottel, *Science*, 2002, **298**, 1000–1002.

37 G. M. Espallargas, M. Hippler, A. J. Florence, P. Fernandes, J. van de Streek, M. Brunelli, W. I. F. David, K. Shankland and L. Brammer, *J. Am. Chem. Soc.*, 2007, **129**, 15606–15614.

38 S. B. Baek, D. Moon, R. Graf, W. J. Cho, S. W. Park, T. U. Yoon, S. J. Cho, I. C. Hwang, Y. sang Bae, H. W. Spiess, H. C. Lee and K. S. Kim, *Proc. Natl. Acad. Sci. U. S. A.*, 2015, **112**, 14156–14161.

39 D. J. Tranchemontagne, Z. Ni, M. O'Keeffe and O. M. Yaghi, *Angew. Chem. Int. Ed.*,

2008, **47**, 5136–5147.

40 A. F. Wells and R. R. Sharpe, *Acta Crystallogr.*, 1963, **216**, 857.

41 J. J. Perry, J. A. Perman and M. J. Zaworotko, *Chem. Soc. Rev.*, 2009, **38**, 1400–1417.

42 X. Hang, B. Liu, X. Zhu, S. Wang, H. Han, W. Liao, Y. Liu and C. Hu, *J. Am. Chem. Soc.*, 2016, **138**, 2969–2971.

43 D. Fujita, Y. Ueda, S. Sato, N. Mizuno, T. Kumasaka and M. Fujita, *Nature*, 2016, **540**, 563–566.

44 G. Seeber, B. E. F. Tiedemann and K. N. Raymond, *Top. Curr. Chem.*, 2006, **265**, 147–183.

45 S. Leininger, B. Olenyuk and P. J. Stang, *Chem. Rev.*, 2000, **100**, 853–907.

46 V. A. Blatov, M. O'Keeffe and D. M. Proserpio, *CrystEngComm*, 2010, **12**, 44–48.

47 M. Fujita, M. Aoyagi and K. Ogura, *Inorganica Chim. Acta*, 1996, **246**, 53–57.

48 M. Fujita, O. Sasaki, T. Mitsuhashi, T. Fujita, J. Yazaki, K. Yamaguchi and K. Ogura, *Chem. Commun.*, 1996, **20**, 1535–1536.

49 M. Fujita, J. Yazaki and K. Ogura, *J. Am. Chem. Soc.*, 1990, **112**, 5645–5647.

50 M. Eddaoudi, D. B. Moler, H. Li, B. Chen, T. M. Reineke, M. O'Keeffe and O. M. Yaghi, *Acc. Chem. Res.*, 2001, **34**, 319–330.

51 S. R. Seidel and P. J. Stang, *Acc. Chem. Res.*, 2002, **35**, 972–983.

52 P. J. Stang and B. Olenyuk, *Acc. Chem. Res.*, 1997, **30**, 502–518.

53 M. Tonigold, J. Hitzbleck, S. Bahnmüller, G. Langstein and D. Volkmer, *Dalton Trans.*, 2009, **114**, 1363–1371.

54 J. Yang, M. Lutz, A. Grzech, F. M. Mulder and T. J. Dingemans, *CrystEngComm*, 2014, **16**, 5121.

55 B. Moulton, J. Lu, A. Mondal and M. J. Zaworotko, *Chem. Commun.*, 2001, **2**, 863–864.

56 J. R. Li and H. C. J. Zhou, *Nature Chem.*, 2010, **2**, 893–898.

57 Y. Ke, D. J. Collins and H. C. J. Zhou, *Inorg. Chem.*, 2005, **44**, 4154–4156.

58 H. Kim, M. Oh, D. Kim, J. Park, J. Seong, S. K. Kwak and M. S. Lah, *Chem. Commun.*, 2015, **51**, 3678–3681.

59 C. D. Ene, A. M. Madalan, C. Maxim, B. Jurca, N. Avarvari and M. Andruh, *J. Am. Chem. Soc.*, 2009, **131**, 4586–4587.

60 A. D. Burrows, C. G. Frost, M. F. Mahon, M. Winsper, C. Richardson, J. P. Attfield and J. a Rodgers, *Dalton Trans.*, 2008, **2**, 6788–6795.

61 H. Abourahma, B. Moulton, V. Kravtsov and M. J. Zaworotko, *J. Am. Chem. Soc.*, 2002, **124**, 9990–9991.

62 M. Eddaoudi, J. Kim, J. B. Wachter, H. K. Chae, M. O'Keeffe and O. M. Yaghi, *J. Am. Chem. Soc.*, 2001, **123**, 4368–4369.

63 Z. Ni, A. Yassar, T. Antoun and O. M. Yaghi, *J. Am. Chem. Soc.*, 2005, **127**, 12752–12753.

64 M. J. Bojdys, M. E. Briggs, J. T. A. Jones, D. J. Adams, S. Y. Chong, M. Schmidtmann and A. I. Cooper, *J. Am. Chem. Soc.*, 2011, **133**, 16566–16571.

65 J. R. Holst, A. Trewin and A. I. Cooper, *Nature Chem.*, 2010, **2**, 915–920.

66 C. Sudik, R. Millward, N. W. Ockwig, P. Cote, J. Kim and O. M. Yaghi, *J. Am. Chem. Soc.*,

2005, **127**, 7110–7118.

67 Y. Bai, D. Guo, C. Y. Duan, D. Bin Dang, K. L. Pang and Q. J. Meng, *Chem. Commun.*, 2004, 186–187.

68 B. Lee and F. M. Richards, *J. Mol. Biol.*, 1971, **55**, 379–384.

69 A. Shrake and J. A. Rupley, *J. Mol. Biol.*, 1973, **79**, 351–371.

70 M. L. Connolly, *J. Appl. Crystallogr.*, 1983, **16**, 548–558.

71 T. J. Richmond, *J. Mol. Biol.*, 1984, **178**, 63–89.

72 M. L. Connolly, *J. Mol. Graph.*, 1993, **11**, 139–141.

73 M. L. Connolly, *Science*, 1983, **221**, 709–713.

74 L. Ma, A. Jin, Z. Xie and W. Lin, *Angew. Chem. Int. Ed.*, 2009, **48**, 9905–9908.

75 A. P. Nelson, O. K. Farha, K. L. Mulfort and J. T. Hupp, *J. Am. Chem. Soc.*, 2009, **131**, 458–460.

76 J. B. DeCoste and G. W. Peterson, *Chem. Rev.*, 2014, **114**, 5695–5727.

77 E. J. Carrington, I. J. Vitórica-Yrezábal and L. Brammer, *Acta Crystallogr. Sect. B*, 2014, **70**, 404–422.

78 S. Brunauer, P. H. Emmett and E. Teller, *J. Am. Chem. Soc.*, 1938, **60**, 309–319.

79 E. Amayuelas, A. Fidalgo-Marijuán, B. Bazán, M. K. Urtiaga, G. Barandika and M. I. Arriortua, *CrystEngComm*, 2016, **18**, 1709–1712.

80 B. J. Riley, J. D. Vienna, D. M. Strachan, J. S. McCloy and J. L. Jerden, *J. Nucl. Mater.*, 2015, **470**, 307–326.

81 L. J. Barbour, *Acta Crystallogr. Sect. B*, 2014, **70**, 403.

82 S. A. Moggach, S. Parsons and P. A. Wood, *Crystallogr. Rev.*, 2008, **14**, 143–184.

83 C. E. Wilmer, M. Leaf, C. Y. Lee, O. K. Farha, B. G. Hauser, J. T. Hupp and R. Q. Snurr, *Nature Chem.*, 2011, **4**, 83–89.

84 J. R. Li, J. Yu, W. Lu, L. B. Sun, J. Sculley, P. B. Balbuena and H. C. J. Zhou, *Nat. Commun.*, 2013, **4**, 1538.

85 D. Peralta, G. Chaplais, A. Simon-Masseron, K. Barthelet, C. Chizallet, A. A. Quoineaud and G. D. Pirngruber, *J. Am. Chem. Soc.*, 2012, **134**, 8115–8126.

86 J. D. Crowley, D. Preston, R. A. S. Vasdev, K. F. White, J. E. M. Lewis and B. F. Abrahams, *Chem. - A Eur. J.*, 2017, **23**, 10559–10567.

87 B. Jiang, J. Zhang, J. Q. Ma, W. Zheng, L. J. Chen, B. Sun, C. Li, B. W. Hu, H. Tan, X. Li and H. B. Yang, *J. Am. Chem. Soc.*, 2016, **138**, 738–741.

88 C. Zhao, N. Wang, L. Wang, H. Huang, R. Zhang, F. Yang, Y. Xie, S. Ji and J. R. Li, *Chem. Commun.*, 2014, **50**, 13921–13923.

89 J. Ma, Y. Ying, Q. Yang, Y. Ban, H. Huang, X. Guo, Y. Xiao, D. Liu, Y. Li, W. Yang and C. Zhong, *Chem. Commun.*, 2015, **51**, 4249–4251.

90 N. Ahmad, H. A. Younus, A. H. Chughtai and F. Verpoort, *Chem. Soc. Rev.*, 2015, **44**, 9–25.

91 C. J. Hastings, M. D. Pluth, R. G. Bergman and K. N. Raymond, *J. Am. Chem. Soc.*, 2010, **132**, 6938–6940.

92 J. C. Tan and A. K. Cheetham, *Chem. Soc. Rev.*, 2011, **40**, 1059–1080.

93 M. J. Miller, *Chem. Rev.*, 1989, **89**, 1563–1579.

94 T. W. Giessen, K. B. Franke, T. A. Knappe, F. I. Kraas, M. Bosello, X. Xie, U. Linne and M. A. Marahiel, *J. Nat. Prod.*, 2012, **75**, 905–914.

95 H. L. Yale, *Chem. Rev.*, 1943, **33**, 209–256.

96 R. Codd, *Coord. Chem. Rev.*, 2008, **252**, 1387–1408.

97 H. J. Kim and S. C. Bae, *Am. J. Transl. Res.*, 2011, **3**, 166–79.

98 A. K. Bubna, *Indian J. Dermatol.*, 2015, **60**, 419.

99 A. J. Felsenfeld, *Semin. Dial.*, 1990, **3**, 8–20.

100 W. P. Baldus, V. F. Fairbanks, E. R. Dickson and A. H. Baggenstoss, *Mayo Clin. Proc.*, 1978, **53**, 157–165.

101 C. Canavese, L. Gurioli, M. D'Amicone, R. Cardelli, F. Caligaris, P. Bongiorno, A. Arnaud, G. Mattiello and M. Marchiori, *Nephron*, 1992, **60**, 411–417.

102 J. Stivelman, G. Schulman, M. Fosburg, J. M. Lazarus and R. M. Hakim, *Kidney Int.*, 1989, **36**, 1125–1132.

103 M. B. Lucera, C. A. Tilton, H. Mao, C. Dobrowolski, C. O. Tabler, A. A. Haqqani, J. Karn and J. C. Tilton, *J. Virol.*, 2014, **88**, 10803–12.

104 E. Hockly, V. M. Richon, B. Woodman, D. L. Smith, X. Zhou, E. Rosa, K. Sathasivam, S. Ghazi-Noori, A. Mahal, P. A. S. Lowden, J. S. Steffan, J. L. Marsh, L. M. Thompson, C. M. Lewis, P. A. Marks and G. P. Bates, *Proc. Natl. Acad. Sci.*, 2003, **100**, 2041–2046.

105 S. Parvathy, I. Hussain, E. H. Karran, A. J. Turner and N. M. Hooper, *Biochemistry*, 1998, **37**, 1680–1685.

106 H. R. Bravo and W. Lazo, *J. Agric. Food Chem*, 1996, **44**, 1569–1571.

107 S. Pepeljnjak, B. Zorc and I. Butula, *Acta Pharm.*, 2005, **55**, 401–408.

108 A. Winston, D. V Varaprasad, J. J. Metterville and H. Rosenkrantz, *J. Pharmacol. Exp. Ther.*, 1985, **232**, 644–649.

109 C. Schneider, A. Bierwisch, M. Koller, F. Worek and S. Kubik, *Angew. Chem. Int. Ed.*, 2016, **55**, 12668–12672.

110 A. Yekkour, A. Meklat, C. Bijani, O. Toumatia, R. Errakhi, A. Lebrihi, F. Mathieu, A. Zitouni and N. Sabaou, *Lett. Appl. Microbiol.*, 2015, **60**, 589–596.

111 J. B. Neilands, *Science*, 1967, **156**, 1443–1447.

112 T. Emery, *Adv. Enzymol. Relat. Areas Mol. Biol.*, 1971, **35**, 135–85.

113 A. Porcheddu and G. Giacomelli, *J. Org. Chem.*, 2006, **71**, 7057–7059.

114 A. S. Reddy, M. S. Kumar and G. R. Reddy, *Tetrahedron Lett.*, 2000, **41**, 6285–6288.

115 N. Usachova, G. Leitis, A. Jirgensons and I. Kalvinsh, *Synth. Commun.*, 2010, **40**, 927–935.

116 Z. Rappoport and J. F. Liebman, *The Chemistry of Hydroxylamines, Oximes and Hydroxamic Acids*, John Wiley & Sons, Chichester, 1st edn., 2009.

117 M. C. M. M. Fernandes, E. B. Paniago and S. Carvalho, *J. Braz. Chem. Soc.*, 1997, **8**, 537–548.

118 C. A. Matsuba, S. J. Rettig and C. Orvig, *Can. J. Chem.*, 1988, **66**, 1809–1813.

119 T. Beissel, R. E. Powers, T. N. Parac and K. N. Raymond, *J. Am. Chem. Soc.*, 1999, **121**, 4200–4206.

120 Z. Ma, R. Hopson, C. Cai, S. Han and B. Moulton, *Cryst. Growth Des.*, 2010, **10**, 2376–2381.

121 P. Jewula, J. C. Berthet, J. C. Chambron, Y. Rousselin, P. Thuéry and M. Meyer, *Eur. J.*

Inorg. Chem., 2015, **2015**, 1529–1541.

122 D. Tranqui, J. Laugier, P. Boyer and P. Vulliet, *Acta Crystallogr. Sect. B*, 1978, **34**, 767–773.

123 M. S. Lah and V. L. Pecoraro, *J. Am. Chem. Soc.*, 1989, **111**, 7258–7259.

124 J. J. Bodwin, A. D. Cutland, R. G. Malkani and V. L. Pecoraro, *Coord. Chem. Rev.*, 2001, **216**–**217**, 489–512.

125 J. Jankolovits, J. W. Kampf and V. L. Pecoraro, *Chinese Chem. Lett.*, 2015, **26**, 444–448.

126 M. Tegoni, M. Tropiano, L. Marchiò, U. K. Haering, R. Malini-Balakrishnan, V. L. Pecoraro and A. Barwinski, *Dalton Trans.*, 2009, **152**, 6705.

127 C. M. Zaleski, E. C. Depperman, J. W. Kampf, M. L. Kirk and V. L. Pecoraro, *Angew. Chem. Int. Ed.*, 2004, **43**, 3912–3914.

128 E. Gumienna-Kontecka, I. A. Golenya, N. M. Dudarenko, A. Dobosz, M. Haukka, I. O. Fritsky and J. Swiatek-Kozlowska, *New J. Chem.*, 2007, **31**, 1798.

129 G. Mezei, C. M. Zaleski and V. L. Pecoraro, *Biomed. Res.*, 2007, **107**, 4933–5003.

130 E. Gumienna-Kontecka, I. A. Golenya, A. Szebesczyk, M. Haukka, R. Krämer and I. O. Fritsky, *Inorg. Chem.*, 2013, **52**, 7633–7644.

131 P. A. Sontz, J. B. Bailey, S. Ahn and F. A. Tezcan, *J. Am. Chem. Soc.*, 2015, **137**, 11598–11601.

132 T. Beissel, R. E. Powers and K. N. Raymond, *Angew. Chem. Int. Ed. Engl.*, 1996, **35**, 1084–1085.

133 Q. F. Sun, S. Sato and M. Fujita, *Nature Chem.*, 2012, **4**, 330–333.

134 Y. Fang, T. Murase, S. Sato and M. Fujita, *J. Am. Chem. Soc.*, 2013, **135**, 613–615.

135 Y. Nishioka, T. Yamaguchi, M. Kawano and M. Fujita, *J. Am. Chem. Soc.*, 2008, **130**, 8160–8161.

136 T. K. Ronson, W. Meng and J. R. Nitschke, *J. Am. Chem. Soc.*, 2017, **139**, 9698–9707.

137 T. K. Ronson, S. Zarra, S. P. Black and J. R. Nitschke, *Chem. Commun.*, 2013, **49**, 2476–2490.

138 A. M. Castilla, W. J. Ramsay and J. R. Nitschke, *Acc. Chem. Res.*, 2014, **47**, 2063–2073.

139 Z. J. Wang, C. J. Brown, R. G. Bergman, K. N. Raymond and F. D. Toste, *J. Am. Chem. Soc.*, 2011, **133**, 7358–7360.

140 A. V. Davis, D. Fiedler, G. Seeber, A. Zahl, R. Van Eldik and K. N. Raymond, *J. Am. Chem. Soc.*, 2006, **128**, 1324–1333.

141 D. L. Caulder and K. N. Raymond, *J. Chem. Soc. Dalt. Trans.*, 1999, 1185–1200.

142 C. J. Carrano and K. N. Raymond, *J. Chem. Soc. Chem. Commun.*, 1978, **129**, 501–502.

143 C. J. Carrano, S. R. Cooper and K. N. Raymond, *J. Am. Chem. Soc.*, 1978, **101**, 599–604.

144 R. C. Scarrow, D. L. White and K. N. Raymond, *J. Am. Chem. Soc.*, 1985, **107**, 6540–6546.

145 C. F. Pereira, A. J. Howarth, N. A. Vermeulen, F. A. Almeida Paz, J. P. C. Tomé, J. T. Hupp, O. K. Farha, G. W. Brudvig, V. S. Batista, M. Peräkylä, C. Ballatore and C. A. Schmuttenmaer, *Mater. Chem. Front.*, 2017, **1**, 1194–1199.

146 B. P. Hay and T. K. Firman, *Inorg. Chem.*, 2002, **41**, 5502–5512.

147 E. V. Perez, K. J. Balkus, J. P. Ferraris and I. H. Musselman, *J. Memb. Sci.*, 2014, **463**, 82–93.

148 W. Cao, Y. Mao and X. Peng, *CrystEngComm*, 2014, **16**, 10916–10920.

Chapter 2 – Hydroxamic Acids

"It doesn't matter what it is. What matters is what it will become." Dr. Seuss

Foreword

Dr Jamie Foster initially performed the growth of the 4-aminobenzohydroxamic acid crystal and the IHA synthesis. Mechanochemical synthesis was performed in collaboration with the Friščić group at McGill University. Francesca Cutolo and Gemma McMurdo conducted preliminary co-crystal work. Gemma McMurdo established the initial synthesis of the 4,4'-dipyridyl, 4-bromobenzohydroxamic acid co-crystal. Unless stated otherwise all crystallographic images were created in X-Seed with CPK colours used were nitrogen in blue, oxygen in red, carbon in grey and hydrogens in white. Lambda (Λ) and delta (Δ) are represented by orange and grey respectively throughout. Where CCDC structures are used, the six-letter reference code is provided.

2.0 Introduction

Hydroxamic acids can be viewed as an amide with an additional hydroxyl group off the nitrogen (Figure 2.1).[1,2] They are commonly seen in medicinal chemistry[3] and due to their high affinity for chelating metals, they are an obvious choice as ligands for coordination materials.[1,2,4](see chapter 1.5.1). To date, there is limited literature about the supramolecular synthons,[5,6] coordination[7,8] and connectivity[9–12] of hydroxamic acids. This chapter will discuss the synthesis of these compounds from a range of synthetic methods.[4,13,14] The supramolecular synthons of hydroxamic acids from pure compounds and their multi-component crystals will also be analysed. There are examples of patents and patent applications for co-crystals including hydroxamic acids within them.[15] This signifies the belief that they will be suitable for the formation of multicomponent crystals, however, published work on hydroxamic acids co-crystals is much less substantial. The number of reported hydroxamic acid multi-component crystals at present is limited to one, Vorinostat (suberanilohydroxamic acid) with ammonia[9]. Forming a 2:1 Vorinostat to ammonia

composition.[9] Prohens and co-workers, claim that due to the Vorinostat being a weak acid it would be unlikely for it to form a salt.[9] If the structures were a salt, formed of the hydroxamate anion and the ammonium cation, it could not be considered a co-crystal under the definition of a pharmaceutical co-crystal.

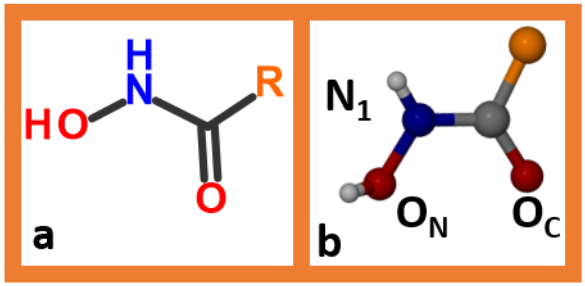

Figure 2.1 ***a*** *shows the structure of the hydroxamic acid as a drawn 2D representation.* ***b*** *shows a ball and stick representation of a hydroxamic acid crystal structure, where the orange R group can be alkyl or aryl in nature.*

2.0.1 Multi-component crystals

Multi-component crystals are composed of two or more components, these materials have no covalent bonds and are therefore held together by intermolecular interactions, such as hydrogen-bonds, halogen-bonds, dispersion interactions or π-π interactions.[5,6,16–18] Multi-component crystals encompass a range of compounds; common ones include solvates, salts and co-crystals.[19] The term co-crystal is sometimes, wrongly, used synonymously with multicomponent crystals.[20] Whilst all co-crystals are examples of a multi-component crystal, not all multicomponent crystals are co-crystals. The exact definition of a co-crystal is of great debate but the generally regarded rules state that a co-crystal can only be produced from neutral molecular species, that are solids under ambient conditions and that a stoichiometric amount of each component is required.[20]

Pharmaceutical co-crystals have become a large area of research in recent times.[15,21–23] By incorporating a co-former with the active pharmaceutical ingredient (API), the resulting product can provide favourable properties such as increased solubility, improved stability and dissolution rate, essentially making drugs that were once unusable, a successful pharmaceutical agent.[23–25] Studying the hydrogen-bond interactions seen within

hydroxamic acids you begin to see hydrogen-bond motifs that are repeated or common to other functional groups; such as the amide tape motif, and the homodimer motif commonly seen with carboxylic acids (Figure 2.2). By understanding these interactions, it becomes possible to predict the synthons that will be seen when two functional groups are incorporated together.[15,26]

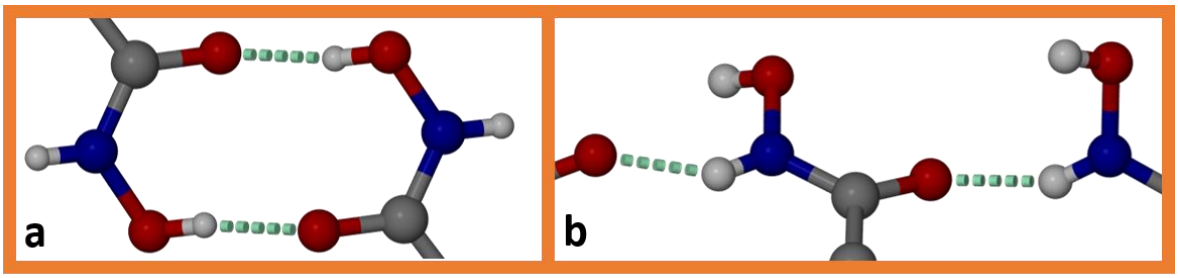

*Figure 2.2 shows ball and stick images of hydroxamic acid functionalities showing hydrogen-bond synthons seen within one crystal structure. Where **a** shows a homodimer motif and **b** shows an amide tape style motif*

Hydroxamic acids are commonly seen within medicinal chemistry and are of pharmaceutical importance.[27–29] One drug based on hydroxamic acids is Vorinostat, it was initially used in the treatment of T-cell lymphoma,[29–31] and more recently in the treatment of HIV.[29] Hydroxamic acids show poor thermal stability and low solubility in water and many organic solvents. It is thought that co-crystals may be a way of altering the solid state structure of hydroxamic acids and providing them with more favourable properties.

By looking at the crystal structure of pure hydroxamic acids, it is clear to see that each compound interacts through a unique hydrogen-bond system, however, upon closer inspection, there are a number similarities that tie these structures together. This includes the fact that many of the hydroxamic acids form amide style tapes, this suggests that amides may be a suitable conformer. The AHA structure also shows the homo acid dimer motif, reminiscent of that seen with carboxylic acids. Hydroxamic acids show potential to interact with many functionalities. Even aided by computational methods there is just not the background on the likely synthons of these structures to predict likely co-formers, as seen with more established synthons like primary amides.[26,32]

Once suitable co-formers have been selected, there are three common ways of producing co-crystals. Melt synthesis, is where the two components are melted together followed by crystallisation via cooling.[24,33] Solution state synthesis, where the two components are dissolved in a mutually miscible solvent and allowed to crystallise.[24,34] Solid state synthesis, where the two components are ground together using mechanical force.[24,25] Initially, the components were ground in a mortar and pestle; however, the rise of ball milling and mechanochemistry removed the need for manual labour, making solid-state co-crystal synthesis a popular technique.[35] The co-former solubility is typically different from those of the API; this makes solvent-based crystallisation difficult to perform. Melting and mechanochemistry removes the phase diagram issue, making them favourable techniques. Hydroxamic acids decompose when heated rather than melting which makes forming co-crystals from melt synthesis unfavourable. Mechanochemistry has shown itself to be the most effective way of producing co-crystals in this project.

The characterisation of co-crystals,[23] in the first instance, is via powder X-ray diffraction (pXRD); pXRD patterns should be collected for both the starting materials and the final compound. If new peaks appear in the final compound pattern, it can indicate the formation of a new material. The diffraction pattern alone, however, is rarely enough evidence to confirm the formation of a multi-component crystal. Co-crystals should also show a melting point that is different from its starting materials, so a melting point for the sample should also be determined and compared to those of its starting components.[36] Differential Scanning Calorimetry (DSC) allows accurate determination of any phase changes that occur. This includes the melting point of the material, also allowing the study of polymorph changes, solvent loss and decomposition. Single crystal determination of the co-crystal structure would provide conclusive evidence that a co-crystal has been formed. Comparing the calculated pXRD pattern from the single crystal structure to the pXRD pattern obtained from the bulk milling experiment would confirm that the bulk phase is the same as the phase determined via single crystal.

This chapter aims to discuss the synthesis and supramolecular synthons of hydroxamic acids, their coordination chemistry and their co-crystals. All focused towards better understanding the supramolecular aggregation of hydroxamic acids. Also studied were

awkwardly shaped molecular coordination complexes as inclusion compounds focusing on Ti and Zr. This will further our understanding of the design of coordination polymer and MOF materials, from hydroxamic acids.

2.1 Hydroxamic acid synthesis

Hydroxamic acid synthesis is commonly conducted in solution; there are a number of methods used to create them, with a vast array of starting materials from the reaction of hydroxylamine with esters,[1] aldehydes,[37] carboxylic acids[38] and acid chlorides.[39] Here the solution state synthesis of a range of hydroxamic acid ligands shall be discussed, a general method is provided. The main issue regarding solution state synthesis is the solubility of hydroxylamine. Hydroxylammonium sulphate and hydroxylamine hydrochloride are two commercially available hydroxylamine sources. Both salts have low solubility in most organic solvents, leaving alcohol and water as the best medium for dissolution of the hydroxylamine salt. Due to water being poorly miscible with the vast majority of organic solvents, this limits solution state synthesis to compounds that are soluble in alcohols such as ethanol and methanol. Another issue with solution state synthesis hydroxamic acids is with their purification, which commonly require column chromatography.[37,39]

The initial hydroxamic acid syntheses were performed using solution state chemistry with esters. Once the conditions were optimised the synthesis was high yielding. This methodology was limited by the solubility of the starting materials. A mechanochemical methodology was developed in collaboration with McGill University. A publication by Mocci[40] on the mechanochemical synthesis of hydroxamic acids was published, this utilised a variation of the methodology developed but unfortunately made it difficult to publish just the methodology.

2.1.1 Solution state synthesis

A typical solution state synthesis requires the formation of a miscible water:methanol solution, where all the reagents are solubilised. Within the literature, a number of variations on this simple methodology are cited, many involve the use of increased time, temperature or different starting materials.[1,13,39,41] Having established that esters appear to provide the

best conversion of reagent to product, in terms of both yield and purity, a typical reaction is stated below.

An aqueous solution (45 mL) of sodium hydroxide (6 equivalents per ester), and hydroxylamine hydrochloride (3 equivalents per ester) is added to one equivalent of methyl ester dissolved in methanol (50 mL). The sodium hydroxide is essential to activate the hydroxylamine. The reaction mixture is heated at 40 ˚C for 17 hours before the highly basic pH 13 solution is acidified to pH 6.5 using 10% hydrochloric acid. The solid product precipitates out of the solution, if this is not the case reducing the solution volume under vacuum causes the precipitation of the pure hydroxamic acid product.

By exploiting the high pK_a of the hydroxamic acids and precipitating the pure product, removes the need for column chromatography to purify the product. Hydroxamic acids have a pK_a of 8, compared to the carboxylic acid pK_a of 4. By lowering the pH to 6.5 the majority of the hydroxamate initially dissolved at the high pH is protonated and is therefore insoluble. This means that the by-products including carboxylates and salts stay solubilised in the predominately water solvent, as seen at the start of the reaction. From experimental experience, the reaction is highly sensitive to the variance of both time and temperature. Increasing either of these factors significantly decreases the yield of the final product. The procedure above yields the product in both high purity and quantity, on average greater than 90 % yield was obtained with no further purification required.

There are a great number of commercially available esters and many of these are methyl ester but there is also a large range of ethyl esters. Attempts at converting them to hydroxamic acids also proved successful when a 25:25:50 ethanol:methanol:water ratio was used. A pure ethanol solution can be used, however; the yield of the product is seen to decrease by around 50%. Despite the reaction providing a high yield of a pure product one problem with the synthesis remains, the use of the methanol:water solvent system, the polar nature of the solution means it is not suitable for many of the desired aromatic compounds. These problems with solubility have severely limited the number of hydroxamic acids that can be produced by conventional solution state chemistry.

Mechanochemical synthesis was used to produce hydroxamic acids, whose starting materials were not suitable for the alcohol:water mixture.

2.1.2 Mechanochemical synthesis

The standard synthesis for the hydroxamic acids via mechanochemistry utilises CDI (1,1'-carbonyl diimidazole), imidazole and hydroxylamine sulphate. The generalised procedure, of the one pot two-step synthesis, is outlined in Figure 2.3.

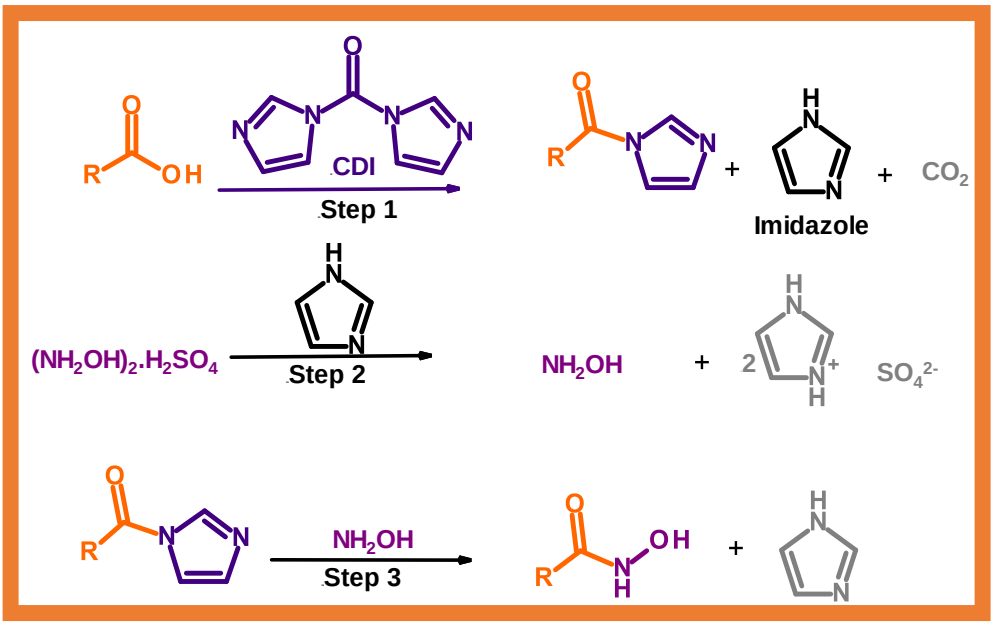

Figure 2.3 shows a schematic diagram of the generalised one pot two-step mechanochemical synthesis of hydroxamic acids. Key reagents are coloured in orange, purple, indigo and black whilst by-products of the reaction are shown in grey. Step 1 shows the activation of the carboxylic acid (orange) where R can be alkyl or aryl, using CDI (indigo), forming imidazole (black) and CO_2 as by-products. The imidazole formed is used in step 2, the activation of the hydroxylamine sulphate (purple). Additional imidazole is added at step 2 along with the hydroxylamine sulphate species to ensure complete activation. Imidazole sulphate is formed as a by-product of this step. In step 3, the activated hydroxylamine species formed in-situ reacts with the previously activated carboxylic acid forming the hydroxamic acid product and imidazole.

In the stainless-steel milling cup, one equivalent of the carboxylic acid starting material is added to nitromethane (40 µL) and 1.3 equivalents of CDI, the mixture is milled for 10 minutes at 25 Hz. After which time 1.5 equivalents of both imidazole and hydroxylamine sulphate are added to the mixture and milled at 25 Hz for 60 minutes. The reaction mixture is then washed with basic water at pH 10, causing any residual starting materials and by

products to dissolve, purifying the insoluble product. The product, usually obtained in quantitative yield is then filtered and dried.

The formation of hydroxamic acids from CDI activated carboxylic acids was initially reported as a solution state reaction; however, the reaction required dry conditions and the carboxylic acid to be soluble in THF.[41] Mechanochemical synthesis removes the solubility issues of the system and the requirement for an inert atmosphere. The reaction goes simply by grinding the carboxylic acid starting material with CDI, this activates the carboxylic acid, also formed are gaseous CO_2 and imidazole, which is further utilised, in the second step. The CO_2 causes a build-up of pressure inside the milling cup, which is realised when the reagents of the second step are added. The addition of hydroxylamine sulphate and imidazole allows conversion of the activated carboxylic acid to the hydroxamic acid.

The imidazole activates the hydroxylamine by removal of the proton, forming imidazolium sulphate and hydroxylamine. The hydroxylamine species reacts via nucleophilic substitution at the activated carboxylic acid forming the hydroxamic acid product with imidazole as a by-product. The by-products of the reaction are gaseous CO_2, imidazole and imidazolium sulphate; both imidazole species are highly water soluble to purify the water insoluble hydroxamic acid, washing with pH 10 water to ensure the full removal of imidazole compounds.

Mocci[40] has also reported the formation of hydroxamic acids utilising CDI activated carboxylic acids using mechanochemical synthesis. They use hydroxylamine hydrochloride typically yielding between 70-80 % product.[40] The synthesis using hydroxylamine sulphate, typically yields above 90%.

The mechanochemical synthesis has shown that is possible to produce a wide range of monotopic primary hydroxamic acids. Whilst performed on a much smaller scale (mg) compared to the gram scale used in solution state chemistry, the reaction is much quicker so this is not of real concern. Mechanochemistry can be scaled, allowing for greater quantities to be produced.[42] This also significantly widened the range of possible starting reagents, with a large number of commercially available carboxylic acid compounds on the market and the issues regarding the solubility of starting materials removed. The next step

in the process is to synthesise ditopic hydroxamic acids via mechanochemistry, within this it will be possible to produce asymmetric ligands. The ligands can have different functionalities at each end, including primary and secondary hydroxamic acids; the variance in hydroxamic acid can be controlled by the hydroxylamine used. Primary hydroxamic acids have a hydrogen at the *N* position, they are conventionally synthesised using hydroxylamine purchased as NH_2OH·salts. A secondary hydroxamic acid is one where a hydrogen is replaced with an alkyl and aryl functionality is bound to the *N*. A variety of *N* substituted hydroxylamines, including *N*-Phenyl and *N*-Methyl hydroxylamine, are available for purchase. The incorporation of this additional functionality would give the hydroxamic acids very different properties, including their solubility and could even incorporate chirality into the ligand. Hydroxylamine can also be synthesised via a number of synthetic pathways.[43,44] It would be possible to produce the hydroxylamine and then use mechanochemical synthesis to produce hydroxamic acids with unique functionality at the *N* position.

2.1.3 Hydroxylamine formation

The formation of secondary hydroxamic acids, hydroxamic acids that do not have a hydrogen bound to the nitrogen, is one of great interest. Raymond[14] produced a secondary hydroxamic acid by the partial reduction of nitrotoluene with ammonium chloride and Zn, forming a hydroxylamine species. This is further reacted with an acyl chloride to yield the secondary hydroxamic acid.[14] Secondary hydroxamic acids also show different solubility properties, to their primary counterparts. Raymond reports that the ditopic *N-tolyl* hydroxamic acid is soluble in chloroform.[14] The ligand produces an M_4L_6 tetrahedral cage when complexed with iron and gallium in acetone. The most common way to produce a secondary (*N*-substituted) hydroxylamine is via the partial reduction of the nitro species.[14,43] Following the same procedure, *N*-substituted hydroxylamine was produced via the partial reduction of nitrobenzene, which was further reacted with isophthaloyl dichloride, forming a secondary hydroxamic acid, suitable for cage synthesis.

Preventing the reduction going to completion and forming the amine is essential. Metals in acidic conditions do not allow for the controlled reduction to the hydroxylamine instead they cause reduction straight to the amine.[14,43] Zinc with ammonium chloride is the most

commonly cited literature method but other variations are possible including SmI_2.[43] The reduction of nitro compounds is not the only way to access hydroxylamine, the partial oxidation of amines can also provide the desired species.[44] The literature reports the use of sodium tungstate with a hydrogen peroxide urea to oxidise chiral primary amines forming chiral *N*-substituted hydroxylamines.[44]

2.1.4 Synthesis summary

In summary hydroxamic acids can be synthesised via a variety of synthetic methods,[1,40] the nature of the hydroxamic acid you wish to produce will dictate the synthetic method you use and ultimately the starting materials you select. Solution state hydroxamic acid synthesis requires alcohol:water soluble starting reagents. Mechanochemical synthesis has provided an efficient and simple route to the synthesis of hydroxamic acids. The previous issues regarding solubility have been sidestepped by removing the need for the starting reagents to be soluble in organic solvents. Primary and secondary hydroxamic acids previously unexplored and inaccessible due to competing functionalities can be synthesised, and their structures and properties determined.

2.2 Hydroxamic acids synthons

Within the CSD there are 91 uncomplexed hydroxamic acid containing crystals structures, these are including alkyl and aromatic compounds that can be salts, di or monotopic hydroxamic acids and many of the structures include a variety of additional functionalities. There are 38 hydroxamic acid functionalised aryl and pyridyl compounds. Just one of these 38 is a ditopic species, 2,6-pyridinedihydroxamic acid (DOMQUS). The limited number of hydroxamic acid crystal structures means little is known about hydroxamic acids interactions and the synthons they favour. Single crystals of four hydroxamic acid compounds were successfully grown in addition to the 38 structures in the CSD. Graph set terminology is used to describe and compare the hydrogen-bond synthons of the 42 hydroxamic acids.[45,46]

The main interactions will be discussed for each structure. This will then be used to relate the discussion of synthons within the structure of hydroxamic acids. 4-amino-

benzohydroxamic acid (Figure 2.4) is packed into the *Pna2₁* space group, each molecule is hydrogen-bonded to seven other molecules. There are no π-π interactions between the molecules. Three of the hydrogen-bond interactions occur incorporating the amino group (N1), these weaker interactions occur between (N1···N1= 3.362 (2) Å, graph set notation,[6-8] $C2$). Hydrogen-bonds also occur between (N1···O11= 3.179 (2) Å, D) and (N1···O9= 3.318 (2) Å, D). Where O11 is the OH of the hydroxamic acid and O9 is the carbonyl oxygen. A pseudo-amide tape conformation, described as $R_3^2(10)$, incorporates three molecules via the N10···O9= 2.888 (2) Å and O11···O9= 2.6472 (19) Å interactions.

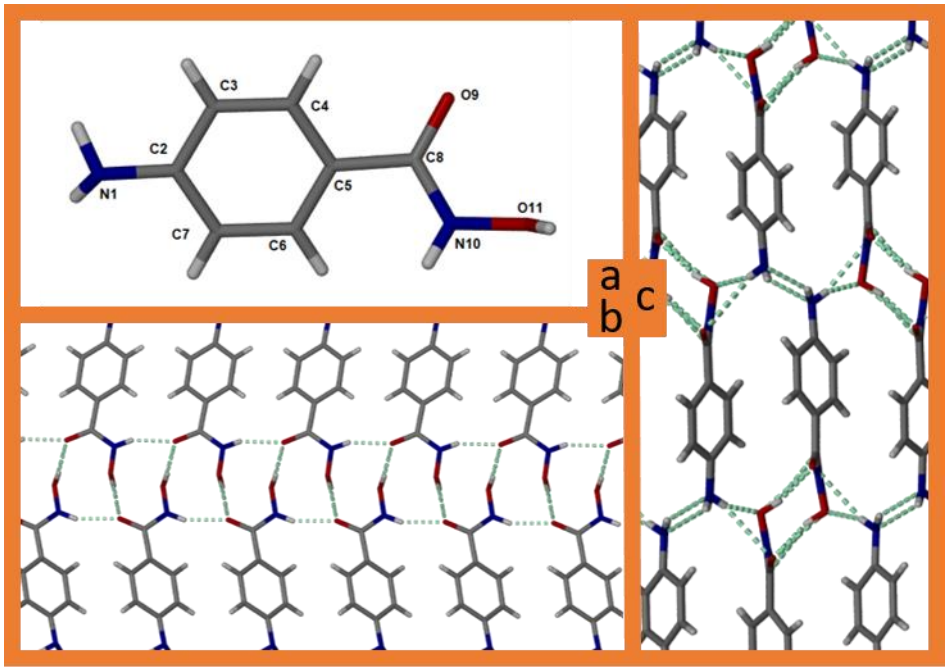

*Figure 2.4 shows **a** the crystallographically labelled molecule of 4-amino-benzohydroxamic acid. **b** shows the pseudo-amide tape conformation ($R_3^2(10)$) viewed down the a axis. **c** shows all the hydrogen-bond interactions of the molecule viewed down the c axis. Hydrogen-bond interaction shown as green broken bond.*

The 4-bromo-benzohydroxamic acid (Figure 2.5) are packed into the chiral *P2₁* space group, whilst the molecule is achiral itself, the molecules are packed chirally. The molecules show a 2D hydrogen-bonding pattern whereby each molecule forms hydrogen-bonds to three other molecules through two types of hydrogen-bond. Giving a graph set analysis of N_1 = $C_3^4(14)$ [$R_2^2(10)$] N_2=$R_1^1(6)$. The $R_2^2(6)$ is formed through donation of N10···O11 2.862 (10) Å. The $R_2^2(10)$ is from the O11···O9 2.581 (10) Å. Type 1 halogen-bonds are also present within

the structure with a Br···Br interaction distance is 3.7028 (19) Å, and the angle of donation, 70.66 (3) ˚, is not linear indicating a type 1 interaction.[34,47] The molecules are planar in nature, the hydrogen of the O11, the hydroxyl group is the only atom out of the plane of the benzene moiety. The molecules show dispersion forces and π-π between atoms C7-C3 of the benzene ring, with an interaction distance of 3.3 Å.

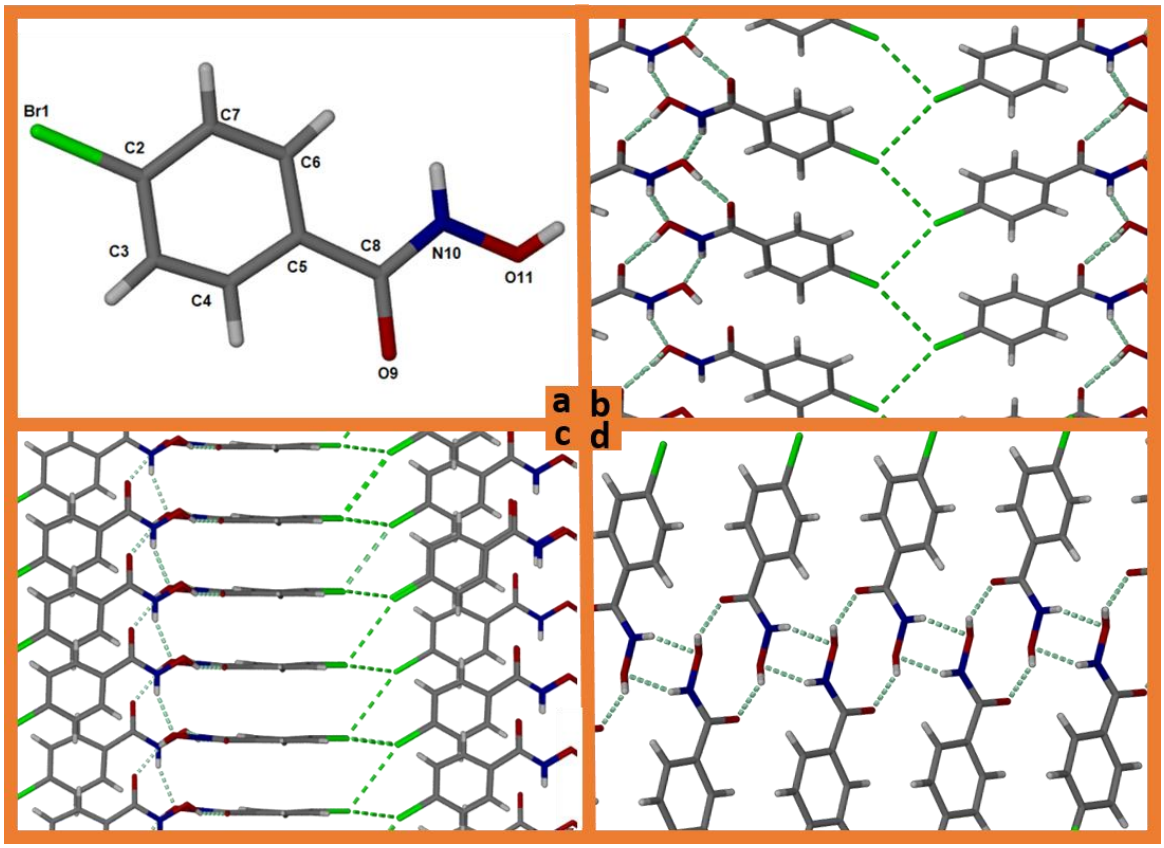

Figure 2.5 ***a*** *shows a crystallographically labelled molecule of 4-bromo-benzohydroxamic acid.* ***b*** *shows halogen-bond interactions and the hydrogen-bonds viewed down the a axis.* ***c*** *shows the flat π-π stacking of the molecules and the halogen-bond interactions of the molecule viewed down the (1 1 0) plane.* ***d*** *shows the hydrogen-bond interactions down the b axis. Hydrogen-bond interaction shown as pale green broken bond, halogen-bond interaction shown in lime green.*

AHA (5-Amino-isophthaloyl hydroxamic acid) (Figure 2.6) is a ditopic hydroxamic acid packed in the *P2₁/c* space group. It shows a 3D hydrogen-bonding system with each molecule hydrogen-bonded to six molecules through five types of bonds. With no π-π interactions between the benzene rings. The structure shows two ring type hydrogen-bond systems; a homo dimer (O15···O13 = 2.677(2) Å, 2.723 (2) Å. $R_2^2(10)$) (Figure 2.2a), and a

$R_2^2(8)$ is formed between N14···O4, 3.075 (2) Å and O1···O15 3.062 (2) Å. There are also three direct molecule to molecule hydrogen-bonds; (N8···O13, 2.954 (2) Å, D), (O1···N8, 2.723 (2) Å, D) and (N2···O4 3.043 (2) Å, D).

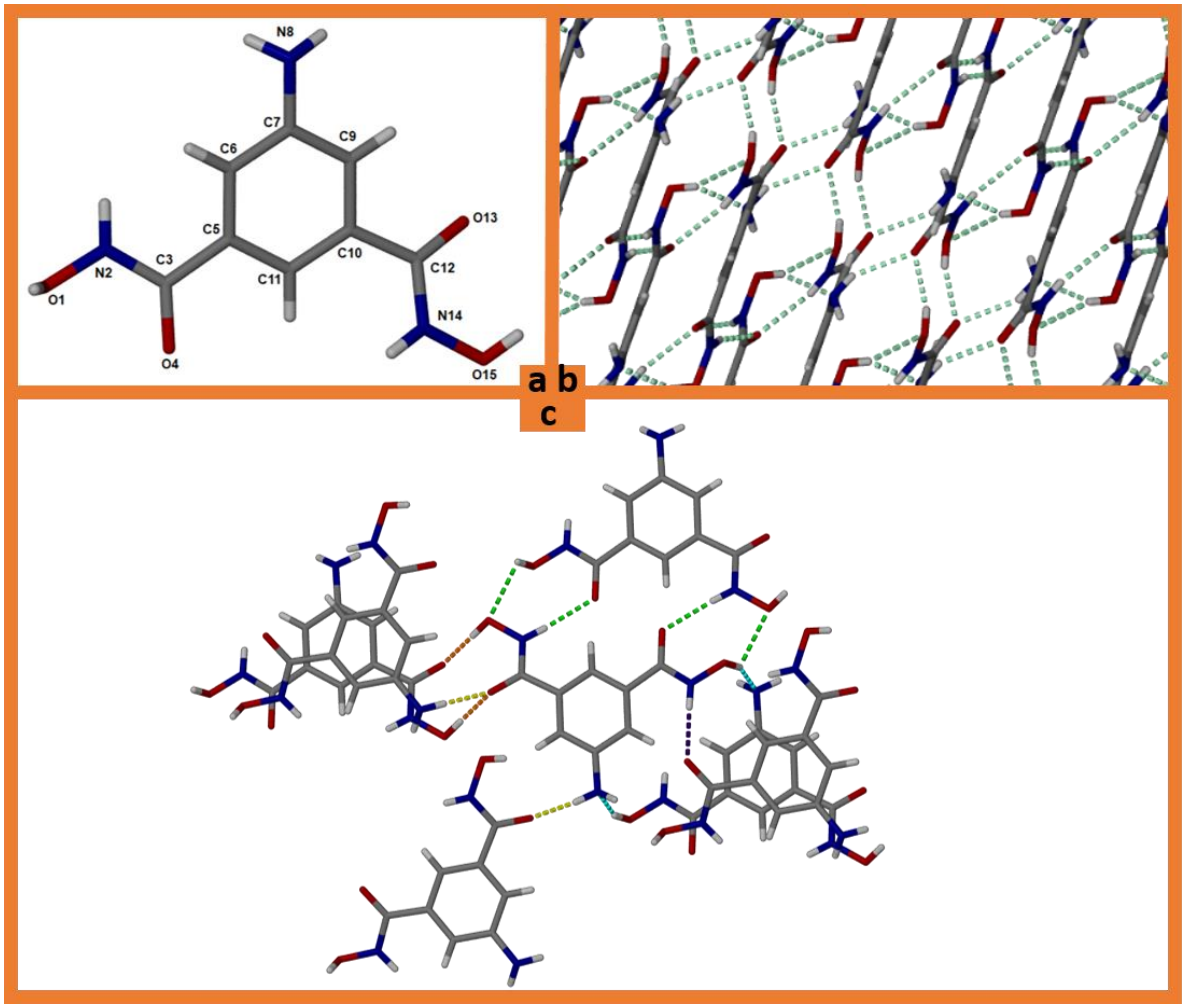

Figure 2.6 ***a*** *shows the crystallographically labelled 5-Amino-isophthaloyl hydroxamic acid structure,* ***b*** *shows the packed unit cell down the [0 1 0] plane and* ***c*** *shows the five hydrogen-bond interactions type, where the broken bond represents the hydroge-bond.* $R_2^2(10)$ *in orange,* ($R_2^2(8)$) *in green. The direct interactions are in yellow (N8···O13), aqua (O1···N8) and purple (N2···O4).*

3-amino-benzohydroxamic acid shows a monohydrate structure, also in the *Pna2₁* space group (Figure 2.7). The placement of the hydrogen on the water and the NH group in this structure appears to be disordered. There is residual electron density occurring around the OH position of the hydroxamic acid. This provides the potential for a second, different hydrogen-bonded networks to be formed. The Cahn-Ingold-Prelog (CIP) priority rules were used to describe the priority of hydrogen-bonds in the network.[48]

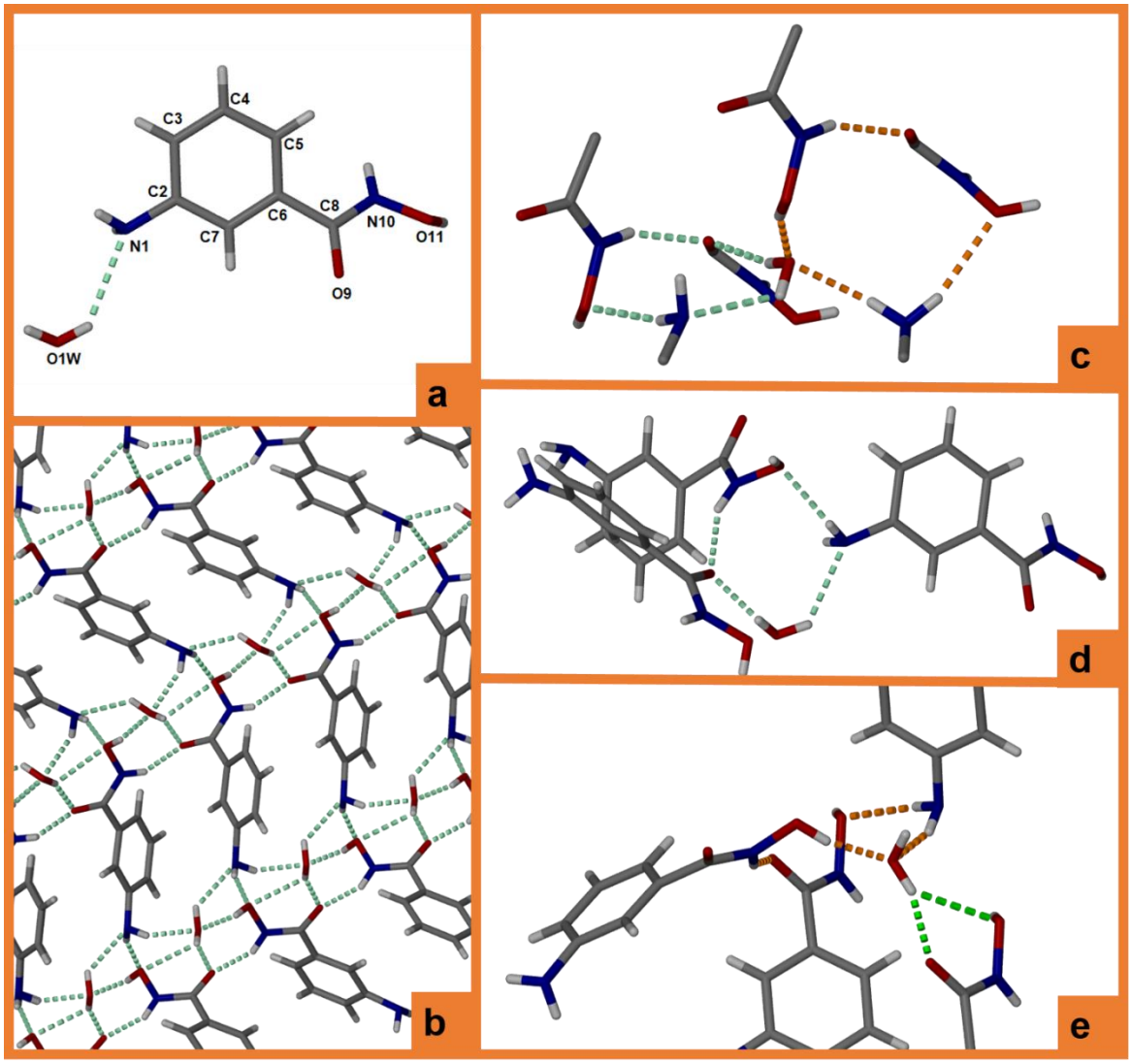

Figure 2.7 ***a*** *shows the capped stick, crystallographically labelled 3-amino-benzohydroxamic acid structure,* ***b*** *shows the packed unit cell down the b axis.* ***c*** *shows the relationship between the* $R_4^3(9)$ *(pale green) and* $R_4^3(12)$ *(orange) hydrogen-bond interactions.* ***d*** *The* $R_4^3(9)$ *shown in pale green.* ***e*** *The bifurcated* $R_1^2(5)$ *in lime green and the* $R_4^3(12)$ *interaction in orange.*

Each 3-amino-benzohydroxamic acid is hydrogen-bonded to four other molecules of 3-amino-benzohydroxamic acid and four molecules of water. The hydrogen (H1W) of the water forms a bifurcated $R_1^2(5)$ hydrogen-bond motif with O9 and O11, (O1W ···O9 = 2.7382 (10) Å / O1W ···O11 = 3.2088 (10) Å, $R_1^2(5)$. The 3-amino-benzohydroxamic acid form molecule to molecule hydrogen-bond interactions between the hydrogen of the NH group and the carbonyl of the hydroxamic acid (N10···O9 = 2.7428 (10) Å, C4), this is the amide

tape motif. The other molecule to molecule hydrogen-bond interaction occurs between the nitrogen of NH_2 group and the hydroxyl oxygen O11, (N1···O11 = 3.1278 (14) Å, C8). A secondary hydrogen-bonded network can be defined, formed of an $R_4^3(12)$ hydrogen-bond motif and a $R_4^3(9)$ hydrogen-bond motif. The $R_4^3(12)$ hydrogen-bond motif occurs between N1···O11= 3.1278 (14) Å, N10 ··· O9 = 2.7428 (13) Å, N1···O1W = 2.8902 (14) Å, O11··O1W = 2.6099 (13) Å. The $R_4^3(9)$ occurs between O1W···N1 = 3.1574 (15) Å, O1W ··· O9 = 2.7382 (13) Å, N10 ···O9 = 2.7428 (13) Å, N1··· O11 = 2.8902 (14) Å, (Figure 2.7c).

Within the collated data 20 % of the structures are hydrates and a further 5 % are solvates. When looking at all hydrogen-bonding interactions, 31 % of structures show only one type of hydrogen-bonding pattern. Of the remaining 69 % of structures 80 % show both $O_N\cdots O_c$ and NH···O interactions. 19 % of structures show the homo dimer motif, $R_2^2(10)$. The $R_2^2(6)$ motif occurs in 9.5 % of structures. The $R_3^2(10)$ amide tape motif appears in 7 % of structures, it occurs in half of the determined structures. Direct or chain interactions between the $NH\cdots O_c$ occur in 57 % of structures, 9 % of structures show $NH\cdots O_H$ (hydroxyl oxygen) and 78 % of structures show $O_N\cdots O_c$ interactions.

The interaction described for the four collected structures can be defined as synthons as they are also represented in the published CSD structures. Although the amide interactions are fairly common in the structures, the other hydrogen-bond patterns are highly variable. This is most likely due to the key flexible torsion angle of the hydroxamic acid.

Overlaying the five hydroxamic acid moieties from the four collected structures (Figure 2.8), there is an evident variation in the torsion angle of the hydrogen of the OH group. To gain a better understanding of the rigid character of the hydroxamic acid moiety, two torsion angles of the hydroxamic acids were measured and analysed against the published data in the CSD (Table 2.1). These are the C-N-O-H torsion angle and the R-C-N-O_N torsion angle of the hydroxamic acid, where R is the carbon of the phenyl ring in these structures. The C-N-O-H torsion angle measured in the four new datasets show large variation, which is in agreement with the statistics of the published crystal structures. The R-C-N-O_N torsion angle is much more ridged at near 180 ° as commonly seen with amides.

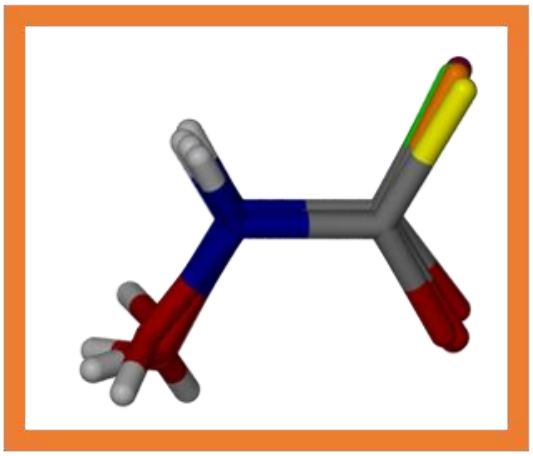

Figure 2.8 shows the variance in the hydroxamic acid OH hydrogen position. The five hydroxamic acid functionalities are overlaid in the following order. 4-amino-benzohydroxamic acid (yellow), 3-amino-benzohydroxamic acid (orange), AHA, which has two hydrogen positions (maroon), and 4-bromo-benzohydroxamic acid (green).

Table 2.1 shows the calculated torsion angles for the crystal structures and the CSD structures.

	R-C-N_1-O_N torsion angle (˚)	C-N-O-H torsion angle (˚)
CSD average*	170(8)	97 (90)
3-amino-benzohydroxamic acid	169.59 (7)	129.26 (13)
AHA – 1	178.25 (14)	99.13 (19)
AHA – 2	177.82 (3)	40.20 (19)
4-bromo-benzohydroxamic acid	176.1 (8)	136.0 (9)
4-amino-benzohydroxamic	168.47 (14)	108.16 (18)

**The CSD error is the standard deviation not the ESD as reported for the other crystal structures.*

An additional aspect to complete this analysis is to determine the strength of interaction possible with these groups. The electrostatic potential maps of the Hirshfeld surface,[49] (Figure 2.9), were calculated for each structure using CrystalExplorer.[49]

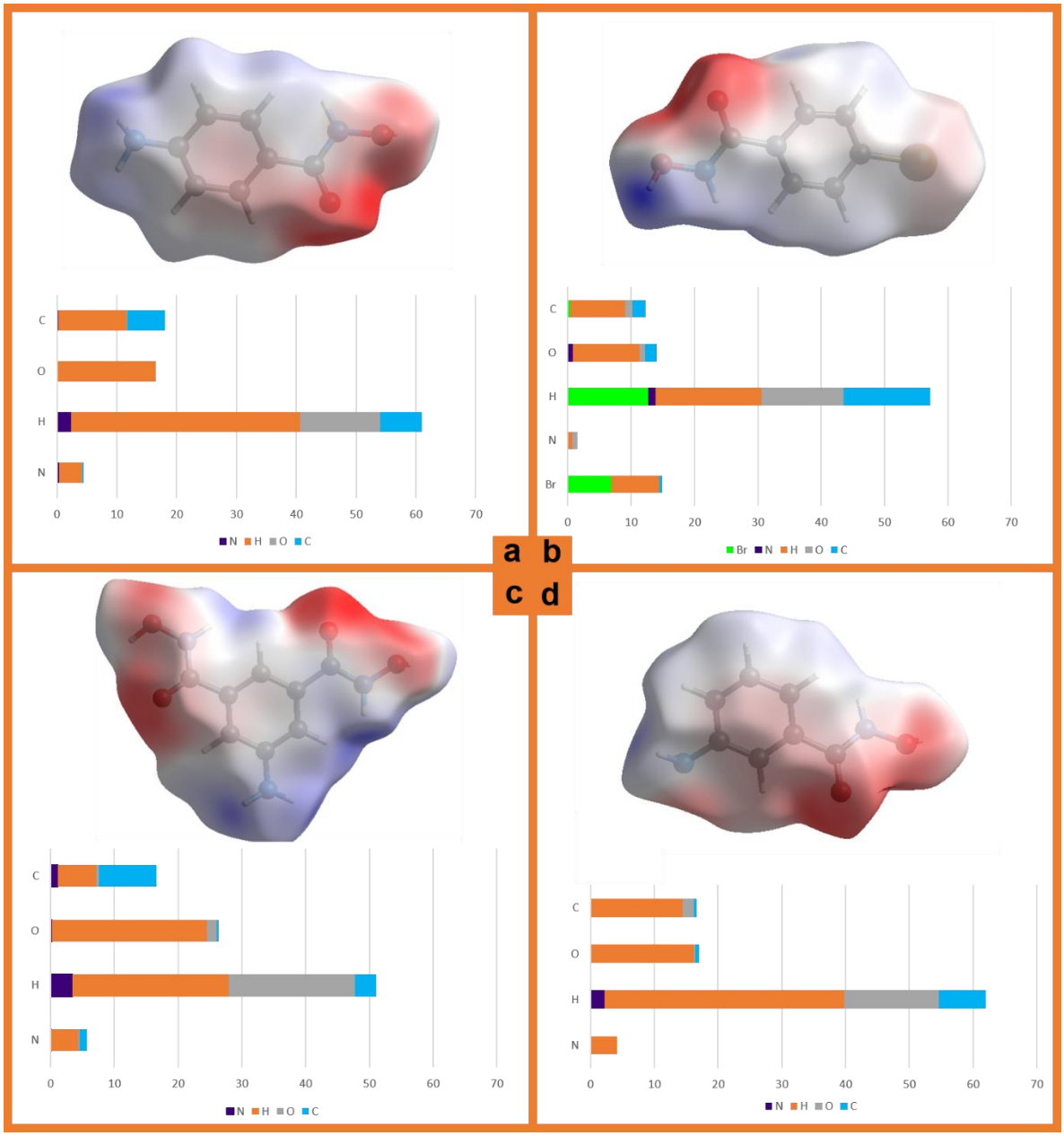

Figure 2.9 shows the electrostatic potential maps of the Hirshfeld surface of ***a*** *4-amino-benzohydroxamic acid,* ***b*** *4-bromo-benzohydroxamic acid,* ***c*** *5-amino-isophthalic hydroxamic acid, and* ***d*** *3-amino-benzohydroxamic acid. Where the blue areas show areas of positive electrostatic potential, the white areas showing the mid-potential, and finally areas of negative electrostatic potential shown in red. The "sigma" hole of the bromine can be seen as the white area on the side the red bromine. Below each electrostatic potential map is a composite bar chart showing the intermolecular contacts contributing to the Hirshfeld surface for each element as a percentage. In all cases, the hydrogen-oxygen interaction nominates the surface, consistent with a hydrogen-bonded networks. Electrostatic potential maps and intermolecular contacts were created in CrystalExplorer, the composite bar charts created in Microsoft Excel.*

The electrostatic potentials show the hydroxamic acid functionality of all four structures have positive electrostatic interactions, in blue, at the hydrogens of the N and O_N of the hydroxamic acid. The negative regions of the electrostatic potential are shown in red. These regions include both oxygens of the hydroxamic acid.[49,50]

The four structures show that the carbonyl oxygen is a more intense red in colour, than the neighbouring hydroxyl oxygen. Indicating that the electrostatic potential of the carbonyl oxygen is more negative. The two oxygens are in close proximity, which provides the molecules with a region of negative electrostatic potential. The nitrogen of the NH groups show approximately the same amount of electrostatic potential (red colour) as that seen for the aromatic π cloud. The 4-bromo-benzohydroxamic acid structure shows a "sigma" hole at the bromine. This is the circular "white" region of the top of the red area of the bromo group.[47] The Hirschfeld surface can be used to determine the intermolecular interactions occurring between molecules. The composite bar charts in Figure 2.9 show intermolecular contacts contributing to the Hirshfeld surface for each element as a percentage. The hydrogen-oxygen interactions form the majority of the interaction within all the molecules, which is consistent with the hydrogen-bonded networks formed.

2.3 Multicomponent crystals of hydroxamic acids

2.3.1 Results and Discussion

The lack of literature regarding the likely synthons of hydroxamic acids provided many different avenues of exploration. Initially, simple unfunctionalised hydroxamic acids in the form of benzohydroxamic acid, isophthaloyl dihydroxamic, acid and terephthaloyl dihydroxamic acid were selected. Having seen that hydroxamic acids form amide tape style interactions and the homodimers, chosen co-formers included other hydroxamic acids, carboxylic acids and amides, that gave the potential to form these interactions.[6,32] A variety of functionalities were investigated because it is difficult to predict the likely interactions given the current lack of knowledge regarding the synthons of hydroxamic acids. A typical co-crystal screening synthesis has many variables; in this case these included reagents and the stoichiometric ratio. The API (hydroxamic acid) and co-former ratio were varied from

1:1, 2:1 and 1:2, and the mixture ground for 20 minutes and 20 Hz. The pXRDs obtained were of unreacted mixtures of the starting reagents, suggesting dry grinding does not yield the formation of a new species. Liquid Assisted Grinding (LAG) was attempted, 20 µl and 50 µl aliquots of solvent including ethanol, methanol, chloroform, THF and nitromethane were added to the reaction mixture, and they were ground under the same conditions. Again, conversion only yielded a mixture of unreacted starting materials. Varying both the time (15 mins – 60 mins) and the frequency (15Hz - 30 Hz) of the reaction continued to give a mixture of reagents and not a new species.

Hydroxamic acids containing additional functionality were then selected. The mechanochemical synthesis of hydroxamic acids provided a wide range of functionalised hydroxamic acids that were suited to co-crystal screening. These include 4-bromo-benzohydroxamic acid, 4-chloro-benzohydroxamic acid, 3-pyridyl-hydroxamic acid, 4-amino-benzohydroxamic acid, and 4-carboxy-benzohydroxamic acid. Again, a variety of co-formers including pyridyls, halogens, carboxylic acids and amides co-formers were selected (Figure 2.10).

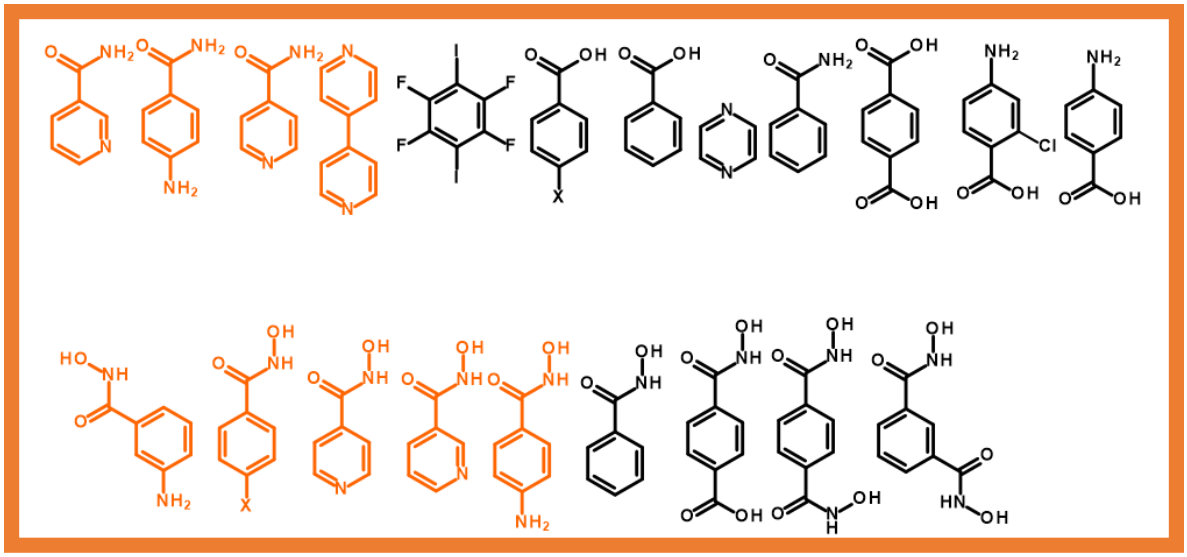

Figure 2.10 shows the structure of the selected hydroxamic acids along the bottom row and top row showing some of the selected co-formers. The orange structures are those to have provided promising results. X denotes the halogen series, where F, Cl, Br and I were all produced.

In some cases, the co-former was selected based on the additional functionality, for example, halogen-bonding between halogens and pyridyl functionalities are well known in the literature.[17,18,23,51] Diiodo-tetrafluoro-benzene was used as a co-former with the pyridyl hydroxamic acid and the 4-halogen-benzohydroxamic acid series to maximise the likelihood of forming a halogen-bond.[52,53] Frequency, time, stoichiometry and solvent was again varied alongside the starting reagents, produced five pXRD patterns that showed potential as co-crystals.

Of the five co-crystals formed (Figure 2.11), three had a stoichiometric ratio of 1:1. This includes the 4-bromo-benzohydroxamic acid with 4,4' dipyridyl, 4-pyridyl-hydroxamic acid with isonicotinamide, and 4-amino-benzohydroxamic acid with 4-amino-benzamide. The final two co-crystals, 3-amino-benzohydroxamic acid with 4-amino-benzamide, and 3-pyridyl-hydroxamic acid with nicotinamide were formed from a 1:2 stoichiometry. All five were produced using 20 µL of nitromethane as a solvent at a frequency of 20 Hz for 20 minutes. The time and frequency were optimal at this point because it allowed for the conversion to the co-crystal, whilst minimising the amount of peak broadening. The nitromethane, however, is essential for conversion to the co-crystal, removal or substitution of the 20 µL of nitromethane causes the formation of a mixture of starting materials. Additional nitromethane does not improve the conversion or the pXRD pattern obtained.

The powder patterns of the starting materials have been milled under the same conditions as the product, to negate the preferred orientation and peak broadening. In all five patterns, the pXRD pattern of the final product is different to its starting materials. The majority of the peaks with a high intensity in the starting materials are lost in the co-crystal and new peaks that are unique to the product appear. This is indicative of the formation of a new phase.

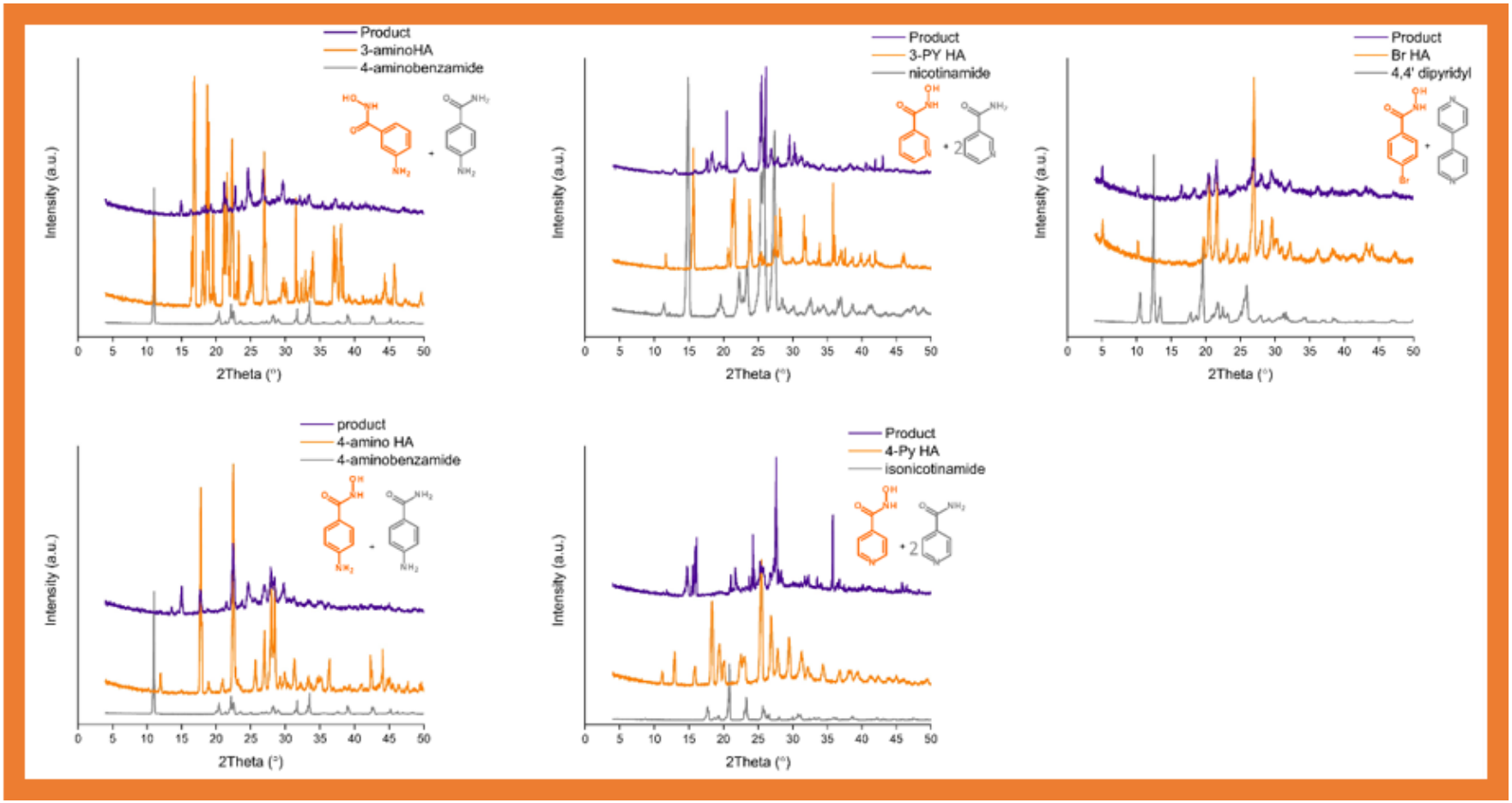

Figure 2.11 shows the chemical structures and pXRD of the co-crystal starting materials, the hydroxamic acid in orange and the co-former in grey. Also shown is the pXRD of the co-crystal (indigo) obtained through ball milling stoichiometric quantities of the two starting reagents.

As previously stated, the melting point of a co-crystal is typically different to that of its starting reagents. Table 2.2, shows the phase changes (decomposition or melting point) of the co-crystal and those of the starting materials. The five co-crystals formed have melting points/decomposition points below the lowest melt point of the two starting components. This coupled with the pXRD patterns confirms that co-crystals of hydroxamic acids have been produced. With so little known about the interactions of hydroxamic acids, it is hard to make precise predictions regarding the likely interactions. For each co-crystal, there are a number of potential interactions, for example, in the case of the 4-Bromo-benzohydroxamic acid with 4,4'-dipyridyl a halogen-bond may be formed between the Br and the N of the pyridyl. Alternatively the OH of the hydroxamic acid may hydrogen-bond to the N of the pyridyl.[6] It is not possible to be definitive about the interactions occurring within the crystal until a crystal structure of the co-crystal is obtained.

Table 2.2 comparison of the co-crystal melt point/decomposition to the melting point of the starting materials. Melt points of the hydroxamic acids and the resulting co-crystals were determined experimentally, the co-former melt point was obtained from the literature.

Starting material	Melting point (˚C)	Melt/decomposition point of co-crystal (˚C)
3-amino-benzohydroxamic acid	141-146	106-114
4-amino-benzamide	181-183	
3-pyridyl-benzohydroxamic acid	120-131	48-56
nicotinamide	128-131	
4-amino-benzohydroxamic acid	Decomposes 200^{+}	148-154
4-amino-benzamide	181-183	
4-pyridyl-hydroxamic acid	154-162	126-133
isonicotinamide	155-157	
4-bromo-hydroxamic acid	152-185	Decomposes 92-101
4,4'-dipyridyl	109-112	

To understand the interactions occurring within the crystal, a single crystal structure is desirable. Two different methods were attempted to obtain single crystals. Firstly, a stoichiometric amount of the API and co-former were dissolved in solvents the hydroxamic acids are soluble in (ethanol, methanol, DMF, DMSO) and allowed to evaporate. Antisolvent crystallisation was also attempted, using chloroform or THF as the antisolvent. Single crystals of the co-former were obtained in some cases. A second attempt, this time using the ball milled sample, was performed in a hope that the crystals would form more readily because the reaction was seeded. Both solvent evaporation and antisolvent crystallisations were again attempted, again single crystals of the co-former were obtained. Single crystals of the co-crystal remained unobserved so far.

2.4 Complexes of hydroxamic acids

2.4.1 Background and history

As mentioned in chapter 1.5.2, hydroxamic acids readily chelate to metals. Within the CSD there are a number of monotopic hydroxamic acid complexed to metals. The number of ligands involved to form the neutral complex formed is dependent upon the valency of the metal centre selected; a trivalent metal, such as Ga^{3+} or Fe^{3+} will require three ligands to charge balance, whilst tetravalent metals such as Zr^{4+} and Hf^{4+} will require four. Due to the asymmetric nature of the hydroxamic acid, the coordination of the bidentate ligand forms a five membered ring, that allows for these complexes to form a number of different isomers.[54] As early as 1899, Alfred Werner already had an insight that octahedral metal coordination complexes showed optical activity.[55,56] In 1911, Werner published work discussing the enantiomers of an octahedral cobalt complex, $[Co(en)_2X(NH_3)]^{2+}$, which was verified by their predicted optical activities.[57] In the 1920's Alexander Smirnoff was the first to report the asymmetric synthesis of a chiral octahedral metal complex by transfer of chirality from a chiral carbon to a metal centre.[54] The prevalence of octahedral complexes in the literature is high and in large thanks to Werner, the chemistry surrounding the chirality of octahedral complexes is now well understood. Within the literature on hydroxamic acid complexes, the vast majority of examples focus on octahedral complexes, where four potential isomers arise. The isomers formed can be either lambda (Λ) or delta

(Δ), as well as being facial (fac) or meridonial (mer); this provides four potential complexes, Λfac, Λmer, Δfac, Δmer. Within the CSD all four isomers can be identified within one compound, Fe(benzohydroxamate)$_3$, the four isomers are shown in Figure 2.12.

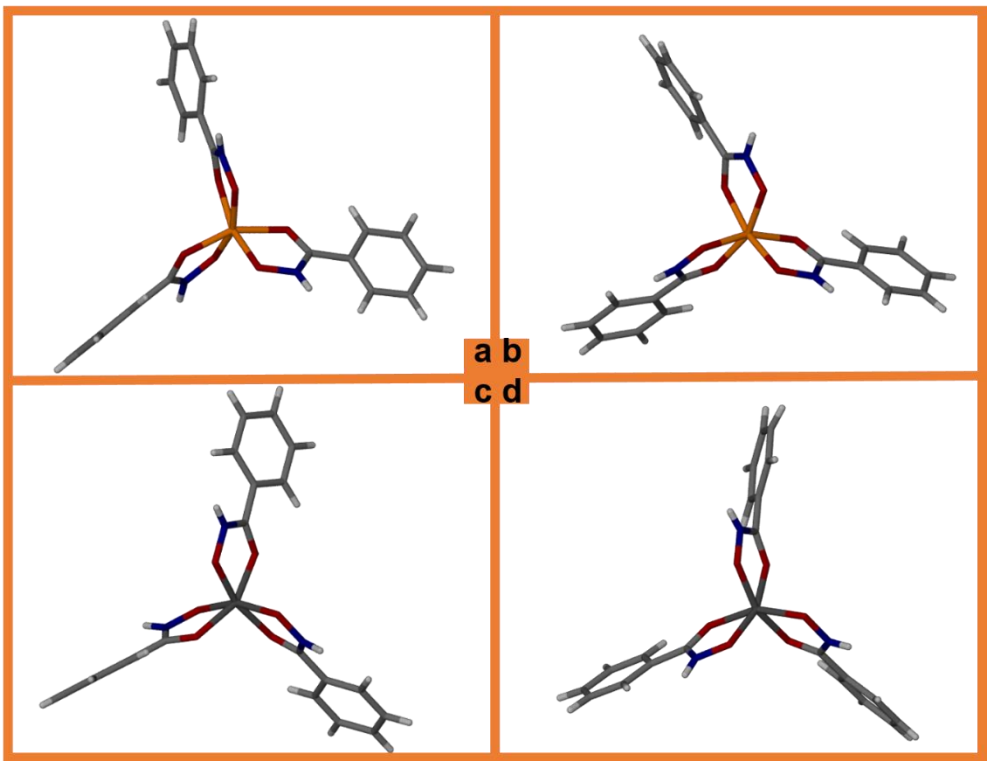

*Figure 2.12 shows images of the four octahedral complexes **a** Λmer, **b** Λfac, **c** Δmer, **d** Δfac. The NH of the propeller located at 12 o'clock is always located at the front of the complex when determining the chirality. The Δ (grey) complex shows rotating clockwise (right), the Λ (orange) shows the rotation anticlockwise (left). The facial complexes show all the NHs located to the front on all three of the ligands. A complex is considered mer if one of the NH groups is located on the back. Images created in Xseed from structures obtained from CSD Λmer and Δmer from YOLBUX Λfac FEBOAH01, Δfac FEBOAH02.*

eight coordinate complexes are formed with 4^+ metals such as zirconium. In this chapter octa-dentate refers to the metal centres having eight co-ordination bonds, (M_1L_8). The bidentate nature of the hydroxamate forms an M_1L_4 complex retaining the octa-dentate coordination. The literature surrounding octa-dentate complexes of hydroxamates with tetravalent metals is significantly less prominent.[8,58] One of the most common ways to define these octa-dentate complexes is to determine the coordination polyhedron. For eight coordinate complexes, the two possibilities are the distorted square antiprism or the distorted dodecahedron. The two structures are related, ideal D_{2d} dodecahedron can be

converted into the ideal D_{4d} square antiprism by stretching two of the vertices to form a square.[59,60]

The CSD contains five crystal structures of neutral, eight coordinate hydroxamate complexes with cerium,[7] thorium,[11] hafnium[8] and zirconium[58]. Due to their biocompatible and their potential for MOF formation, Zr and Ti were selected as metals to study in the project. It was hoped that better understanding the properties and structure of the discrete complexes would lead to a greater understanding of the chemistry and conditions required to form MOFs with hydroxamic acids. Further to this, having studied the five published structures, the molecules described here can be viewed as being excellent targets for inclusion chemistry (extrinsic porous materials) as the molecules are "awkwardly" shaped and are unlikely to pack efficiently in the solid state. The Ce and Zr structures include pyridine and water respectively, removal of these included species may allow for host:guest applications.

The medium sized, highly charged Zr^{4+} ion with an ionic radius of 0.84 Å[61] is a hard cation that shows a strong affinity for ionic oxygen donors. Titanium can display similar chemistry to zirconium and similar eight coordinate complexes would be expected to be formed. To date there are 11 single crystals structures of Ti-hydroxamate complexes, within the CSD. None of the structures show octa-dentate coordination. Two of the complexes are seven coordinate the other nine are six coordinate. This is likely due to titanium's significantly smaller ionic radius of 0.605 Å.[61] A CSD search showed that 19 of the 27 octahedral complexes formed contain benzohydroxamic acid or a derivative of it, with this in mind benzohydroxamic acid was selected as the coordination ligand.

Within the CSD there is one other eight coordinate Zr complex (TEQSAL)[58] formed of N-methyl acetohydroxamic acid. The coordination sphere of a Zr complexed to eight oxygen forms an asymmetric five member ring, with the Zr-O_N bond shorter than the Zr-O_C. Guerard[58] reports that the structure shows disorder in the ligands; the nitrogen and the carbon of the five-member ring can swap positions, causing further distortion in the bond distances. This is an example of geometric configuration in the form of cis and trans, it occurs in the ligands diagonal to each other across the metal centre (Figure 2.13).[62]

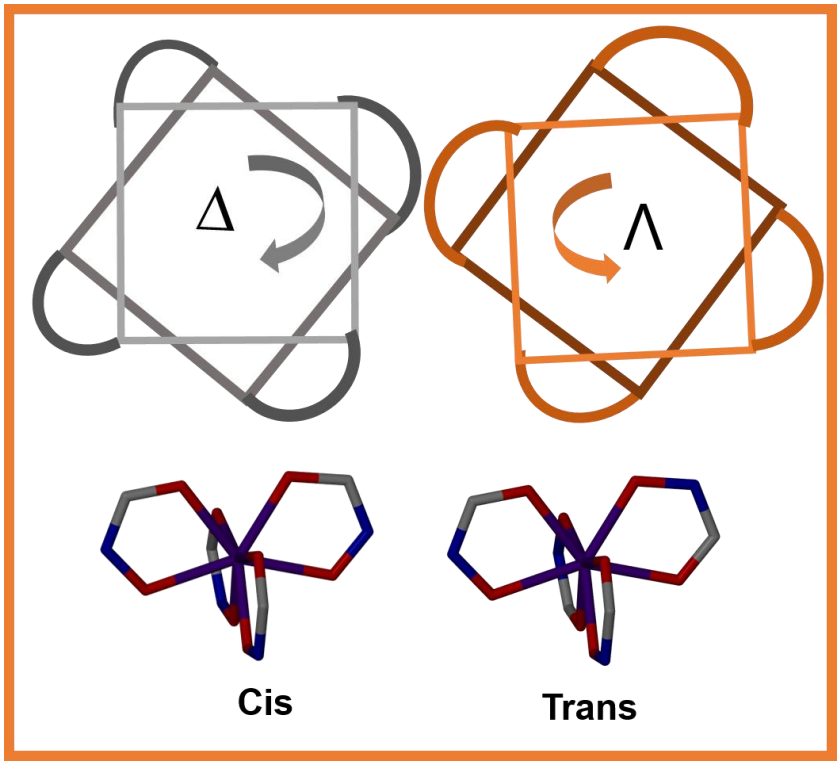

Figure 2.13 shows a representation of the Λ (orange) and Δ (grey) configuration of the square antiprism when the light-coloured square is viewed as the top face with the darker diamond shape viewed as the bottom face. The direction of the bonds connecting the top face to the bottom face indicates the chirality. Below is a representation of the cis and trans geometric configuration shown by hydroxamate complexes. In the trans complex, the nitrogen of the five-member ring are on the opposite plane to one another, one nitrogen is at the top of the 5-member ring whilst the ring diagonal to it through the metal centre it will be located on the bottom. In the cis structure, they are located on the same plane; the nitrogen diagonal through the metal can be located on the bottom of the five-member ring. The images created in X-seed are derived from the CSD TEQSAL (trans) and NAWKUU (cis) structures where just the Zr-hydroxamate coordination sphere has been displayed, all other functionality has been removed.

In the Zr_1(N-methylacetohydroxamate)$_4$ structure the disorder could simply be due to both cis and trans forms being present, alternatively it could be due to the same compound having a different orientation.

As previously stated, the octahedral complexes formed of three bidenate ligands show fac and mer geometries alongside Λ/Δ chirality. The eight coordinate complexes are also chiral; they too show Δ or Λ chirality. Further to this the eight coordinate hydroxamic acid complexes, can show cis and trans geometric configurations. Each complex is formed of four

five-member rings. Each ring has a diagonal, how the rings are orientated compared to one another leads to the cis/trans configurations. If both rings are orientated in the same way (cis), for example the C-O bond is located at the top of the complex in all four ligands. Trans would find the O-N bond located at the top of a ligand pair; therefore, a complex would have two O-N bonds and two O-C bonds at the top of each complex. The collected Zr complex crystal structures show trans configurations with both Δ/Λ isomers as a racemic mixture.

2.4.2 Results and Discussion

Two solvates of the Zr(benzohydroxamate)$_4$ complex (Figure 2.14) were obtained. The ethanol solvate crystallises in the triclinic $P\bar{1}$ space group, with an ASU of one full complex. This structure is referred to as **complex 1** ($Zr(C_7H_6NO_2)_4.4(C_2H_5OH)$). The second form, **complex 2** ($Zr(C_7H_6NO_2)_4.2(CH_3OH)$), is a methanol solvate in the tetragonal $I4_1/a$ space group, also with an ASU of one full complex. The complex in both structures is the same, it is the packing of the complex that varies significantly.

Inorganic eight coordinate complexes can form a number of different geometries; possibilities include cubic, dodecahedral and square antiprism structures. To date, only inorganic cubic geometries have been reported.[63] Coordination complexes are most commonly found in the square antiprism geometry. Although referred to as the dodecahedron the geometry can be better described as a snub bisphenoid or the bisdisphenoid. This geometry displays the D_2d point group, formed of 12 equilateral triangle faces and is one of the 92 Johnson solids.[63] The square antiprism with the D_4d point group is defined as having an even-numbered sequence of triangle sides closed by two polygon caps. In this case, it has ten faces, eight triangles surrounding two quadrilateral caps.[64]

The shape of the coordination polyhedra can be determined. To do this a number of torsion angles are collected from the crystal structure and compared to the values of the ideal polyhedra. The first value is ϕ, the torsion angle of the BAAB trapezoid, there are two per complex.[60,65] The second value is δ_{edge}, this is the dihedral angle between the faces of the polyhedron containing the edge.[60,65]

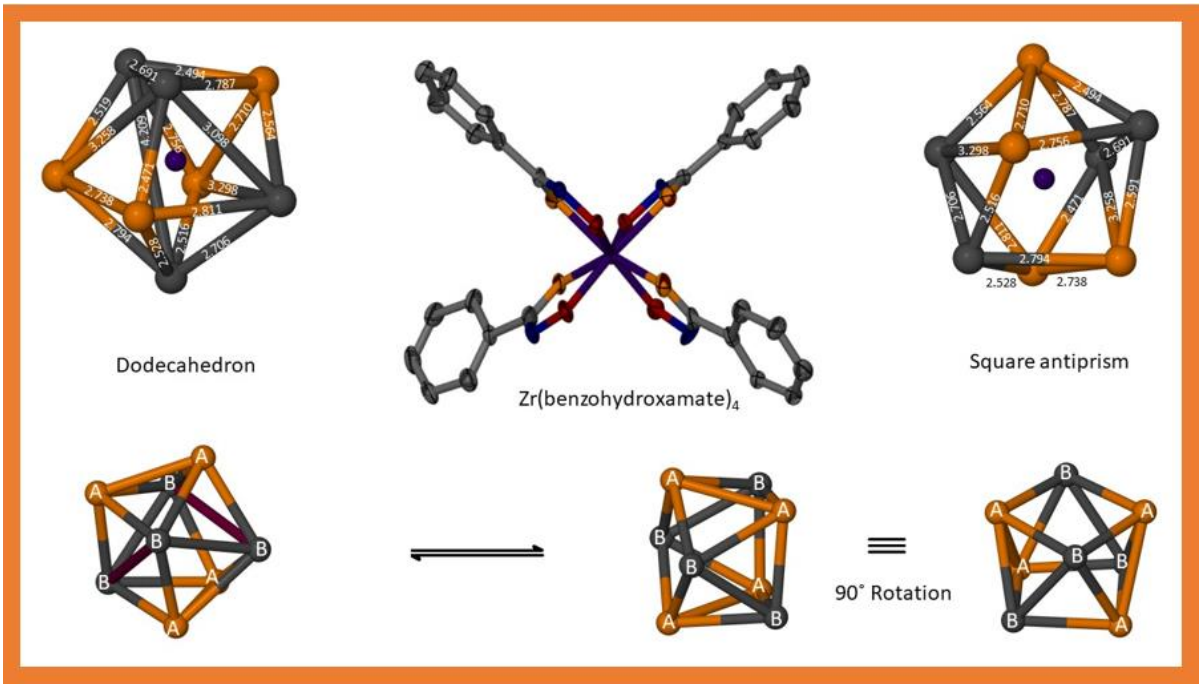

*Figure 2.14 shows a 50% ellipsoid representation of the octa-dentate Zr-benzohydromate complex. (**Complex 1** is shown but the complex is consistent for both solvates, hydrogens omitted for clarity.) The type A oxygens (the former carbonyl oxygen referred to as O_c) have been highlighted in orange, whilst the type B oxygens (oxygen next to the nitrogen O_N) remain in red, Zr is shown in indigo, the other elements are shown in standard CPK colours. Either side of the complex are the two possible polyhedra with the edge lengths shown in white along the respective edge, each distance is given in Å. The polyhedra are created in Xseed using false bonds to connect the type A (O_c shown in orange) and type B (O_N shown in grey) oxygens, the central Zr ion is shown in indigo. The images at the bottom are representations of the ideal polyhedra, with the A and B atoms represented in orange and grey. The dodecahedron (snub disphenoid) formed of 12 equilateral triangles and 18 edges, can be converted to the square antiprism. Viewed to have two squares connected via eight triangles, the squares are formed via the elongation of the two bonds highlighted in burgundy. Both images were created from a Na_3TaF_8 complex reported by Boca.*[66]

These values are collated in Table 2.3. By assigning the two oxygens of the hydroxamic acid A and B (as in Figure 2.14) where A is the carbonyl oxygen (O_C) located next to the carbon and oxygen B is the oxygen next to the nitrogen (O_N). From the values summarised in Table 2.3, it can be concluded that the Zr complexes have distorted square prismatic geometries, with an approximate D_{4d} point group symmetry. Due to the square antiprism having the possibility of enantiomeric pairs, both solvate structures crystallise as a racemate. Further

to this, the ligands diagonal to each other are always located trans to each other (Figure 2.15).

Table 2.3 where ϕ is the torsion angle of the BAAB trapezoid. δedge is the dihedral angle between the faces of the polyhedron containing the edge.

	Ideal dodecahedron	Ideal square antiprism	**Complex 1**	**Complex 2**
ϕ (˚)	0, 0	24.5, 24.5	23, 22.6	24.7, 23.9
δ_{edge} (˚)	29.5, 29.5, 29.5, 29.5	0, 0, 52.4, 52.4	56.3, 21.3, 20.6, 51.2	51.6, 46.7, 7.1, 8.9

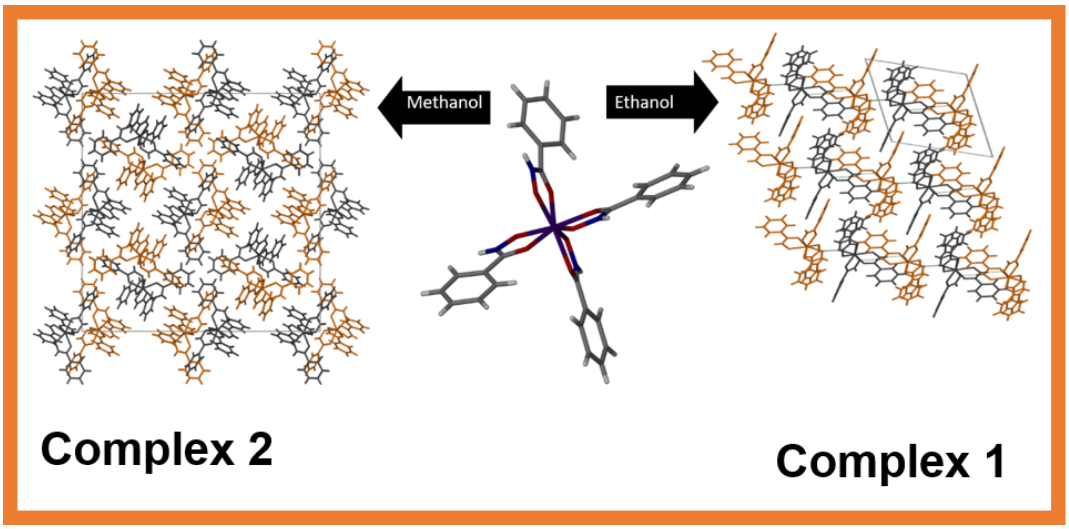

*Figure 2.15 shows the structure of the Zr complex (**complex 1**), which gives rise to two solvates. The nitrogens are shown in opposite planes giving the structure trans isomerism. The same complex then packs differently depending upon the solvent of crystallisation, the packed unit cells show the same number of molecules in each. The chirality of the complexes highlighted with Δ (grey), Λ (orange). The Zr is shown in indigo and standard CPK colours for other elements. Both crystal structures are shown down the b axis.*

In **complex 1** hydrogen-bonds are formed between two complexes of alternating chirality, forming a $C_2^2(10)$ hydrogen-bonded chain of $(\text{-}\Lambda\text{-}\Delta\text{-})_n$ complexes (Figure 2.16). A ring-type hydrogen-bond is formed through donation of the hydrogen of the NH group to the O_N

(N4···O6 = 2.902 (2) Å, N1···O2 = 2.990 (2) Å, $R_2^2(10)$). The chains stack to provide columns of one chiral form. The columns hydrogen-bond to each other via the ethanol solvent of crystallisation. N2 and N3 are hydrogen-bond donors for the ethanol (N2 ···O1D = 2.784 (9) Å, D) and (N3···O1B = 2.811 (7) Å, D). The third ethanol molecule O2 acts as a hydrogen-bond acceptor (O1C···O2 Å =2.752, D). The final ethanol molecule is disordered and found to hydrogen-bond between ethanol molecules B and C. This results in formation of a three-dimensional hydrogen-bonded network, with no π-π interactions found within this structure.

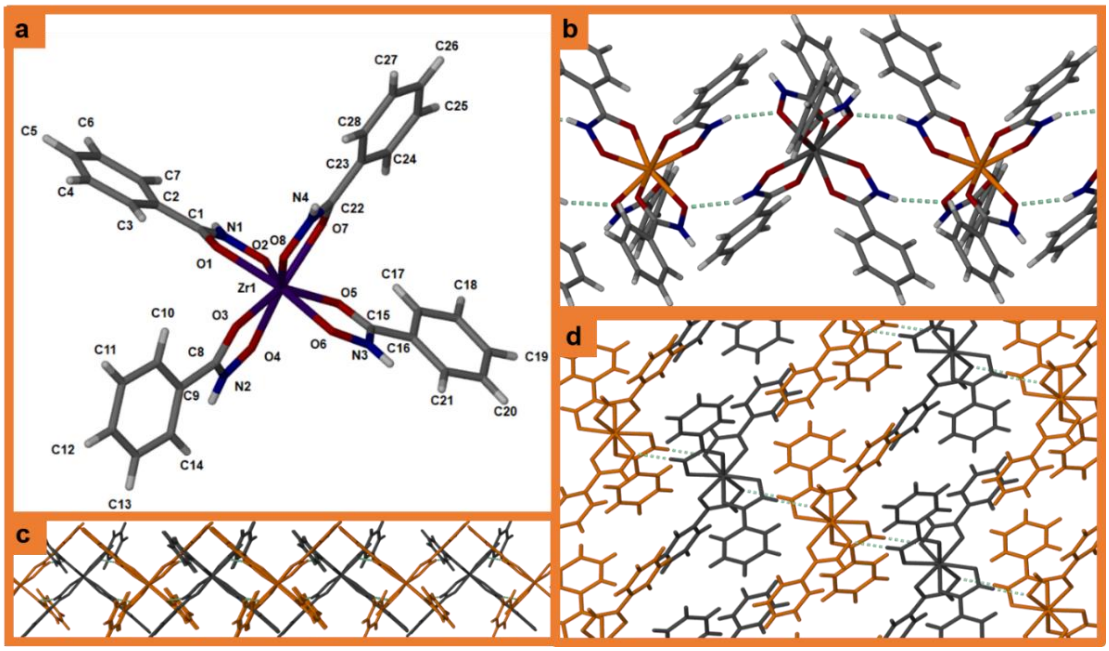

Figure 2.16 ***a*** *shows the crystallographically labelled structure of* ***complex 1****, solvent removed for clarity.* ***b*** *shows the (N_1···O_N = 2.958 Å, $R_2^2(10)$) hydrogen-bond interaction which occurs twice per complex and connects complexes of alternating chirality.* ***c*** *shows the hydrogen chains running along the page viewed down the (0 -1 -1) plane.* ***d*** *show the single chirality columns of the complex viewed down the a axis. where Δ is grey and Λ is orange.*

Complex 2 shows π-π, dispersion and hydrogen-bond interactions (Figure 2.17). The hydrogen-bond interaction shown in Figure 2.17 highlights solvent complex interactions and complex- complex interactions. The (N4···O8 = 2.769 (6) Å, N4···O1= 3.449 (7) Å $R_2^2(4)$) interaction hydrogen-bonds two complexes of alternating chirality together. Each pair of complexes is then further hydrogen-bonded via (N3···O6 = 2.747 (7) Å, $R_2^2(6)$), forming

columns. The methanol solvent of crystallisation links the columns of complexes together through the 4_1 screw axis, providing a three-dimensional hydrogen-bonded network. The $R_4^4(10)$ interaction occurs beween two methanol molecules and two complexes (N1···O1M 2.820 (8) Å), (O2···O2M 2.752 (6) Å), (O1M···O4 2.685 (7) Å), (N2···O2M 2.732 (7) Å). These hydrogen-bonds are weak, indicating that the π-π interactions are playing a major role in the packing of **complex 2**. Face-to-edge π-π interactions occur, with distances between the centroid of (C9-C14) and 27H of (C23-C28) of 3.548 Å, and the centroid of (C23-C28) to H7 of (C2-C7) at 3.519 Å.

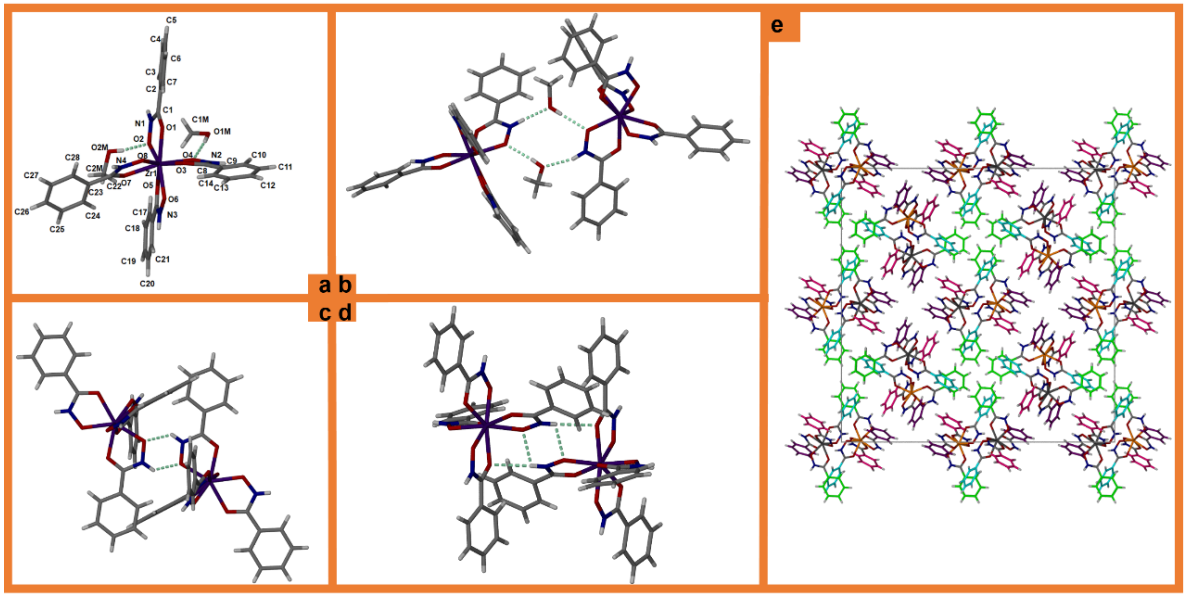

Figure 2.17 ***a*** *shows the crystallographically labelled* ***complex 2****.* ***b*** *shows the* $R_4^4(10)$ *methanol-complex hydrogen-bond interaction.* ***c*** *shows the* $R_2^2(6)$ *interaction.* ***d*** *shows the* $R_2^2(4)$ *interaction. Where the hydrogen-bond is represented as the green dashed bond. CPK colours used for other atoms with Zr in Indigo.* ***e*** *is a packed unit cell of* ***complex*** *2 viewed down the c axis, showing the π-π interactions. Where the phenyl rings are, (C2-C7) in purple, (C9-C14) green, (C16-C21) pink and (C23-C28) aqua.*

These face-to-edge π-π interactions contribute to the formation of the column. π-π interactions also occur between the columns of complexes as face-to-face, the π-π interaction distance of 3.851 Å was determined for centroid to centroid distance for the (C16-C21), (C2-C7) benzene rings.

Removing the solvent from the crystal structure, it is possible calculate the amount of solvent accessible void space in Mercury using a probe radius of 1.2 Å and an approx. grid

spacing of 0.7 Å. For **complex 1** this was determined to be 33.4%, compared to 7.6 % for **complex 2**. Figure 2.18 shows the solvent accessible void space in both structures.

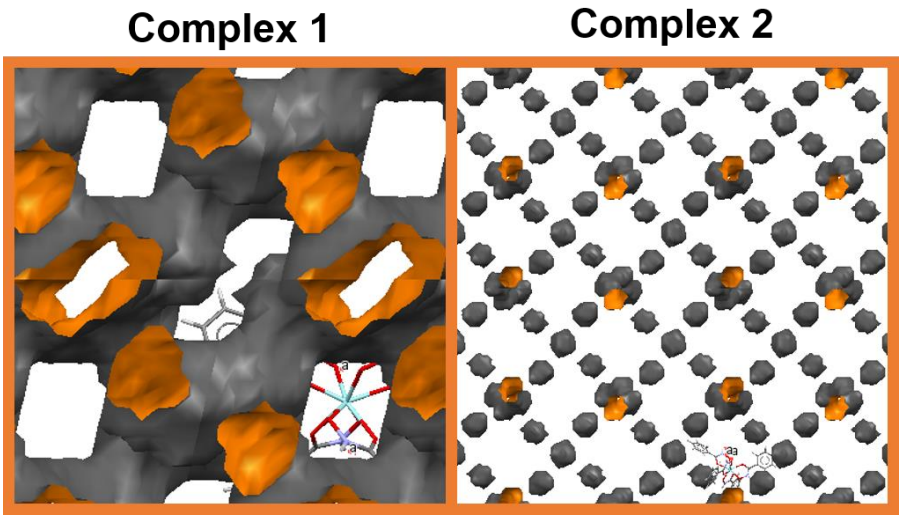

Figure 2.18 shows the calculated solvent accessible void space on the solvent free complex structures. Calculated using a probe radius of 1.2 Å and an approx. grid spacing of 0.7 Å. The orange represents the inside of the void whilst the grey represents the outside. ***Complex 1*** *shows a series of channels between the layers of complexes.* ***Complex 2*** *shows both discrete voids and channels.*

Complex 1 shows continuous channels between the layers of complex, where ethanol solvent is located. **Complex 2** shows three types of void space, a continuous channel and two discrete void spaces. The continuous channel is formed by methanol hydrogen-bonding following the 4_1 screw axis, a probe radius of 1.5 Å or more shows the void to be discrete in nature. The first discrete solvent free void space can be located between the (C23-C28) and (C9-C14) phenyl rings. The void with a volume of 15 $Å^3$ cannot be probed with a radius of greater than 1.6 Å. The second discrete void containing the C2M methanol, can be found between the four (C16-C21) phenyl rings.

2.5 Conclusion and future work

Hydroxamic acids are a complex and important area of research with a number of potential applications; some of the most important are those pertaining to pharmaceutical roles.[1] The treatment of HIV[29] and cancer[30,31] is, without doubt, a valid and important discovery but to be both safe and effective it is essential to understand how hydroxamic acids interact

not only with themselves but also metals they will meet in the body and the outside world. This thesis is just the beginning of understanding the full potential of hydroxamic acids. By understanding the supramolecular synthons these compounds favour, allows for greater chance of being able to harness the great power these molecules hold, by controlling their crystal form. The crystal form dictates many of the physical properties of the pharmaceutical compounds, including solubility, processability, stability and bioavailability.

In summary, mechanochemical synthesis has successfully produced a variety of hydroxamic acid compounds that were previously inaccessible due to their competing functionality. Mechanochemical synthesis has opened the door to a new range of compounds that were previously inaccessible via the solution state, by removing the requirement for the starting material to be soluble in water:alcohol mixtures, it is now possible to target compounds with different functionality or poor solubility. Allowing for hydroxamic acids to be produced in high yield and high purity, without the need for further purification. Attempts to control the properties and understand the favoured supramolecular synthons of the hydroxamic acids via the formation of multicomponent crystals. five multicomponent species were produced. Each showed promising variance in both their pXRD patterns and their melting/decomposition points, suggesting that a new phase has been produced. As yet single crystals of the five materials have yet to be obtained. Also produced were two solvates of a Zr(hydroxamate)$_4$ complex with distorted square antiprism geometry.

By understanding the chirality and the coordination to metals, it is possible understand how the complexes form and the geometries they favour. The strength of hydroxamate – zirconium bond is high and the biocompatibility of zirconium may open doors to their potential use as a drug delivery agent or for the incorporation of hydroxamic acids into bioactive and biocompatible MOFs.[10] The future of this project relies on the growth of single crystals of the multicomponent crystals and the analysis of the synthons favoured by these compounds. Being able to predict the interactions they favour makes the selection of the co-former a more feasible task. As yet it is not yet possible to predict the most likely interaction but this will come with the analysis of more structures. The growth of more metal-hydroxamate complexes is another area that can be exploited with the vast number of monotopic hydroxamic acids that are easily available due to mechanochemical synthesis.

The mechanochemical synthesis must also move forward by targeting multi-topic ligands and further to this the formation of asymmetric ligands, which may be better suited to the synthesis of porous materials such as MOF and MOPs. The next chapter discusses the production of MOPs from hydroxamic acids.

2.6 References

1 R. Codd, *Coord. Chem. Rev.*, 2008, **252**, 1387–1408.

2 H. L. Yale, *Chem. Rev.*, 1943, **33**, 209–256.

3 A. Yekkour, A. Meklat, C. Bijani, O. Toumatia, R. Errakhi, A. Lebrihi, F. Mathieu, A. Zitouni and N. Sabaou, *Lett. Appl. Microbiol.*, 2015, **60**, 589–596.

4 M. J. Miller, *Chem. Rev.*, 1989, **89**, 1563–1579.

5 G. R. Desiraju, *Angew. Chem. Int. Ed.*, 2007, **46**, 8342–8356.

6 G. R. Desiraju, *J. Am. Chem. Soc.*, 2013, **135**, 9952–9967.

7 H. B. Lee, J. A. Bogart, P. J. Carroll and E. J. Schelter, *Chem. Commun.*, 2014, **50**, 5361.

8 D. Tranqui, J. Laugier, P. Boyer and P. Vulliet, *Acta Crystallogr. Sect. B*, 1978, **34**, 767–773.

9 C. Puigjaner, R. Barbas, A. Portell, I. Valverde, X. Vila, X. Alcobe, M. Font-Bardia and R. Prohens, *CrystEngComm*, 2012, **14**, 362–365.

10 L. L. Tan, H. Li, Y. Zhou, Y. Zhang, X. Feng, B. Wang and Y. wei Yang, *Small*, 2015, **11**, 3807–3813.

11 W. L. Smith and K. N. Raymond, *J. Am. Chem. Soc.*, 1981, **103**, 3341–3349.

12 C. F. Pereira, A. J. Howarth, N. A. Vermeulen, F. A. Almeida Paz, J. P. C. Tomé, J. T. Hupp, O. K. Farha, G. W. Brudvig, V. S. Batista, M. Peräkylä, C. Ballatore and C. A. Schmuttenmaer, *Mater. Chem. Front.*, 2017, **1**, 1194–1199.

13 A. Porcheddu and G. Giacomelli, *J. Org. Chem.*, 2006, **71**, 7057–7059.

14 T. Beissel, R. E. Powers, T. N. Parac and K. N. Raymond, *J. Am. Chem. Soc.*, 1999, **121**, 4200–4206.

15 Ö. Almarsson, M. B. Hickey, M. Peterson, M. J. Zaworotko, B. Moulton and N. Rodriguez-Hornedo, *USF Patents*, 2011.

16 A. J. Cruz-Cabeza, S. Karki, L. Fábián, T. Friscić, G. M. Day and W. Jones, *Chem. Commun.*, 2010, **46**, 2224–2226.

17 G. R. Desiraju, *J. Chem. Sci*, 2010, **122**, 667–675.

18 G. R. Desiraju, *Angew. Chem. Int. Ed. Engl.*, 1995, **34**, 2311–2327.

19 L. R. MacGillivray, G. S. Papaefstathiou, T. Friščić, T. D. Hamilton, D. K. Bučar, Q. Chu, D. B. Varshney and I. G. Georgiev, *Acc. Chem. Res.*, 2008, **41**, 280–291.

20 A. L. A. Kala, K. Kumara, G. Pavithra, K. A. Kumar and N. K. Lokanath, *Chem. Data Collect.*, 2017, **7**–**8**, 107–115.

21 C. B. Aakeröy, S. Forbes and J. Desper, *CrystEngComm*, 2014, **16**, 5870–5877.

22 N. K. Duggirala, M. L. Perry, Ö. Almarsson and M. J. Zaworotko, *Chem. Commun.*, 2016, **52**, 640–655.

23 S. Aitipamula, R. Banerjee, A. K. Bansal, K. Biradha, M. L. Cheney, A. R. Choudhury, G. R. Desiraju, A. G. Dikundwar, R. Dubey, N. Duggirala, P. P. Ghogale, S. Ghosh, P. K. Goswami, N. R. Goud, R. R. K. R. Jetti, P. Karpinski, P. Kaushik, D. Kumar, V. Kumar, B. Moulton, A. Mukherjee, G. Mukherjee, A. S. Myerson, V. Puri, A. Ramanan, T. Rajamannar, C. M. Reddy, N. Rodriguez-Hornedo, R. D. Rogers, T. N. G. Row, P. Sanphui, N. Shan, G. Shete, A. Singh, C. C. Sun, J. A. Swift, R. Thaimattam, T. S. Thakur, R. Kumar Thaper, S. P. Thomas, S. Tothadi, V. R. Vangala, N. Variankaval, P. Vishweshwar, D. R. Weyna and M. J. Zaworotko, *Cryst. Growth Des.*, 2012, **12**, 2147–2152.

24 K. Fucke, S. A. Myz, T. P. Shakhtshneider, E. V Boldyreva and U. J. Griesser, *New J. Chem.*, 2012, **36**, 1969–1877.

25 T. Friščić, *Chem. Soc. Rev.*, 2012, **41**, 3493.

26 P. A. Wood, N. Feeder, M. Furlow, P. T. A. Galek, C. R. Groom and E. Pidcock, *CrystEngComm*, 2014, **16**, 5839.

27 A. Winston, D. V Varaprasad, J. J. Metterville and H. Rosenkrantz, *J. Pharmacol. Exp. Ther.*, 1985, **232**, 644–649.

28 S. Pepeljnjak, B. Zorc and I. Butula, *Acta Pharm.*, 2005, **55**, 401–408.

29 M. B. Lucera, C. A. Tilton, H. Mao, C. Dobrowolski, C. O. Tabler, A. A. Haqqani, J. Karn and J. C. Tilton, *J. Virol.*, 2014, **88**, 10803–12.

30 A. K. Bubna, *Indian J. Dermatol.*, 2015, **60**, 419.

31 H. J. Kim and S. C. Bae, *Am. J. Transl. Res.*, 2011, **3**, 166–79.

32 T. S. Thakur and G. R. Desiraju, *Cryst. Growth Des.*, 2008, **8**, 4031–4044.

33 D. K. Bučar and L. R. MacGillivray, *J. Am. Chem. Soc.*, 2007, **129**, 32–33.

34 D. Chopra, V. Thiruvenkatam, S. G. Manjunath and T. N. Guru Row, *Cryst. Growth Des.*, 2007, **7**, 868–874.

35 F. Fischer, D. Lubjuhn, S. Greiser, K. Rademann and F. Emmerling, *Cryst. Growth Des.*, 2016, **16**, 5843–5851.

36 M. K. Stanton and A. Bak, *Cryst. Growth Des.*, 2008, **8**, 3856–3862.

37 G. Dettori, S. Gaspa, A. Porcheddu and L. De Luca, *Adv. Synth. Catal.*, 2014, **356**, 2709–2713.

38 G. Giacomelli, A. Porcheddu and M. Salaris, *Org. Lett.*, 2003, **5**, 2715–2717.

39 A. S. Reddy, M. S. Kumar and G. R. Reddy, *Tetrahedron Lett.*, 2000, **41**, 6285–6288.

40 R. Mocci, L. De Luca, F. Delogu and A. Porcheddu, *Adv. Synth. Catal.*, 2016, **358**, 3135–3144.

41 N. Usachova, G. Leitis, A. Jirgensons and I. Kalvinsh, *Synth. Commun.*, 2010, **40**, 927–935.

42 A. V. Dushkin, *Chem. Sustain. Dev.*, 2004, **12**, 251–273.

43 A. S. Kende and J. S. Mendoza, *Tetrahedron Lett.*, 1991, **32**, 1699–1702.

44 A. Heydari and S. Aslanzadeh, *Adv. Synth. Catal.*, 2005, **347**, 1223–1225.

45 M. C. Etter, J. C. MacDonald and J. Bernstein, *Acta Crystallogr. Sect. B*, 1990, **46**, 256–262.

46 J. Bernstein, R. E. Davis, L. Shimoni and N. L. Chang, *Angew. Chem. Int. Ed. Engl.*, 1995, **34**, 1555–1573.

47 S. Ramalhete, J. S. Foster, H. R. Green, K. P. Nartowski, M. Heinrich, P. Martin, Y. Z. Khimyak and G. O. Lloyd, *Faraday Discuss.*, 2017, 423-439.

48 R. S. Cahn, C. Ingold and V. Prelog, *Angew. Chem. Int. Ed. Engl.*, 1966, **5**, 385–415.

49 M. A. Spackman and D. Jayatilaka, *CrystEngComm*, 2009, **11**, 19–32.

50 S. Madan Kumar, B. C. Manjunath, G. S. Lingaraju, M. M. M. Abdoh, M. P. Sadashiva and N. K. Lokanath, *Cryst. Struct. Theory Appl.*, 2013, **2**, 124–131.

51 G. R. Desiraju, *The crystal as a supramolecular entity*, Wiley, 1996.

52 H. Wang and W. J. Jin, *Acta Crystallogr. Sect. B*, 2017, **73**, 210–216.

53 V. Nemec and D. Cinčić, *CrystEngComm*, 2016, **18**, 7425–7429.

54 U. Knof and A. Von Zelewsky, *Angew. Chem. Int. Ed.*, 1999, **38**, 302–322.

55 A. Z. Werner, *Anorg. Chem*, 1893, **3**, 267.

56 A. Werner and A. Vilmos, *Zeitschrift für Anorg. Chemie*, 1899, **21**, 145–158.

57 K.-H. Ernst, F. R. W. P. Wild, O. Blacque and H. Berke, *Angew. Chem. Int. Ed.*, 2011, **50**, 10780–10787.

58 F. Guérard, Y. S. Lee, R. Tripier, L. P. Szajek, J. R. Deschamps and M. W. Brechbiel, *Chem. Commun.*, 2013, **49**, 1002–1004.

59 E. Psillakis, J. C. Jeffery, J. A. McCleverty and M. D. Ward, *Chem. Commun.*, 1997,

1997, 1965–1966.

60 J. L. Hoard and J. V. Silverton, *Inorg. Chem.*, 1963, **2**, 235–242.

61 R. D. Shannon, *Acta Crystallogr. Sect. A*, 1976, **32**, 751–767.

62 S. P. Gupta, *Hydroxamic Acids.Hydroxamic Acids: A Unique Family of Chemicals with Multiple Biological Activities. Springer Science & Business Media.*, Springer-Verlag, Berlin Heidelberg, 1st edn., 2013.

63 S. Alvarez, *Dalton Trans.*, 2005, **2005**, 2209–2233.

64 L. D. C. Bok, J. G. Leipoldt and S. S. Basson, *Zeitschrift für Anorg. und Allg. Chemie*, 1972, **392**, 303–315.

65 E. L. Muetterties and L. J. Guggenberger, *J. Am. Chem. Soc.*, 1974, **96**, 1748–1756.

66 V. Langer, Ľ. Smrčok and M. Boča, *Acta Crystallogr. Sect. C* , 2010, **66**, 85–86.

Chapter 3 – Molecular Cages

"Curiouser and Curiouser" Alice in Lewis Carroll's, Alice's Adventures in Wonderland

Foreword

NMR work was conducted by Scott Stinson, Cathryn Shepherd and Dr David Ellis. Mass spectroscopy was collected with Cathryn Shepherd and Logan Mackay at the University of Edinburgh. TGA data collected with Dr Kathi Edkins and Mohd-Nadzri Bin-Mohd-Najid at Queen's University, Belfast. Gas sorption data was collected at the University of Glasgow by Dr Ross Forgan and Dr Pantelis Xydias. Data collection and processing was performed by Dr Phil Chater on the xPDF (X-ray Pair Distribution Function) beamline I15-1 at Diamond Light Source, UK. The samples were sent as a part of the mail in access trial. Single crystal data collected on the Synergy, Dualflex, AtlasS2, with Dr Dyanne Cruickshank and Dr Marcus Winters at Rigaku Oxford Diffraction. Supernova, AtlasS2 with Dr Helena Shepherd at the Univeristy of Kent. Crystallographic images were created in Xseed and graphs plotted in Origin unless stated otherwise. Throughout the chapter Λ is represented by the colour orange and Δ represented in grey. Maroon represents a metal centre of either chirality. The six figure CSD recodes are included where used.

3.0 Introduction

This chapter will focus on a family of neutral M_4L_6 tetrahedral cages (Figure 3.1). These cages are based on ditopic hydroxamate ligands. Techniques such as xPDF, TGA and XRD (X-ray diffraction) have been utilised to better understand the design, crystallisation, structure and host: guest chemistry of hydroxamate MOPs.

MOPs and their potential applications; including catalysis,[1–3] molecular sensing,[4,5] drug delivery,[5–8] gas separation and storage[9–11] has progressed rapidly over recent years. These compounds with their high surface areas, increased solubility leading to improved processability and their designable structures will make them as desirable as their more illustrious cousins, MOFs, in the coming decades.[12]

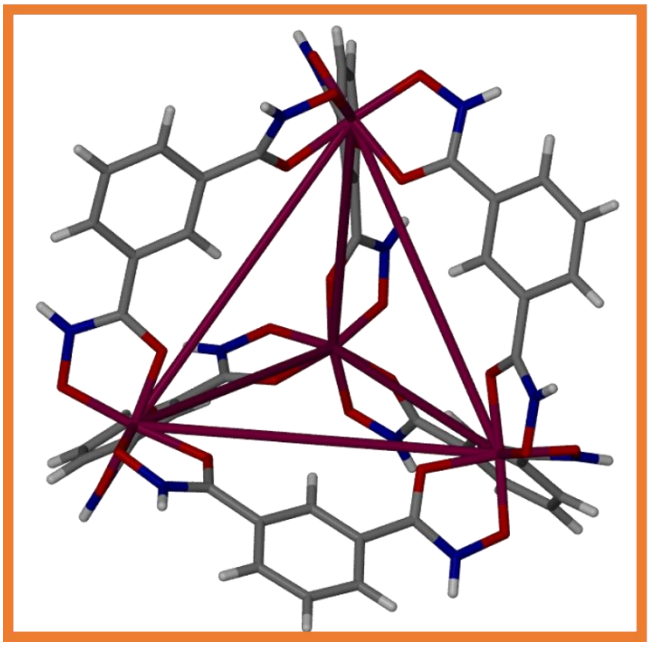

*Figure 3.1 shows a capped stick representation of a neutral M_4L_6 tetrahedra (**cage 7**) with false bonds from the metal to highlight the classical tetrahedral shape is shown in orange, where the maroon metal sites can be Fe, Ga, In or Al. Throughout the chapter standard CPK colours are used; grey for carbon, red for oxygen, blue for nitrogen and white for Hydrogen.*

At present the vast majority of cages in literature by the likes of Fujita[13–15], Nitschke[4,16–18] and Raymond[1,2,19,20] are charged species, which crystallise with a variety of charge balancing ions within their voids. The intrinsic void volume can be controlled by the size and geometry of the ligand used, this control can be exploited for many applications. Nitschke and co-workers have reported many examples of self-assembling cages for the capture of guest species[4,16–18,21], one such example is the capture of pyrophoric white phosphorus (P_4) in a tetrahedral cage[16], the void of the cage is the ideal size to contain the P_4 species. Once encapsulated P_4 is prevented from reacting because the intermediate is too large to be accommodated within the pore without significant deformation[16]. There are examples of cages used in catalysis[1,2] but possibly the most successful was the Nazarov cyclisation reported by Raymond in 2010.[2] The acid-catalysed reaction, in which a 1,4- dien-3-ol forms a cyclopentadiene, exhibited a rate increase of a million fold.[2] These charged cages show great promise in terms of application but their counter ions, though essential for charge balancing the framework, take up valuable space within the framework, which then cannot be used for guest storage.[10] Ion exchange can substitute a large bulky ion for a smaller ion

of an equal charge.[22] One way around the problem of ions in the voids is to design neutral MOPs that do not require charge-balancing ions[23,24], therefore leaving the entire void space accessible for guest species. Raymond[24,25] and Bai[23] have both reported neutral M_4L_6 tetrahedra incorporating the hydroxamic acid moiety, both host DMF (dimethyl formamide) molecules in the windows of the cage and in the extrinsic void space. Removal of the solvent guest would yield an empty framework, with extrinsic pores allowing the guest species access to the intrinsic pore.

3.0.1 xPDF

Crystalline solid materials are formed from atoms that are arranged in an ordered, periodic, three-dimensional array. If these atoms are not ordered in such a fashion the materials formed are often considered as amorphous, derived from the Greek word 'amorphos', meaning shapeless or without form.[26–28] The solid material exhibits no long-range order and show no Bragg peaks in their diffraction patterns. This, however, does not mean they are totally without order. All atoms, including liquids and gases, have a degree of local order simply due to the restrictions on how close the atoms can approach one another and molecular materials have the additional order arising from intramolecular bonds.[26,29–31] PDF (Pair Distribution Function) is a total scattering technique that can be used to determine the structure of none crystalline materials.[26–28]

3.0.1.1 PDF method

Diffraction solely focuses on the information contained within the Bragg scattering, the diffuse scattering is disregarded as part of the background.[32,33] Diffuse scattering is caused by deviations from the average structure and is typically of much lower intensity than Bragg scattering.[33,34] Total scattering data, however, takes the diffraction pattern of a material containing both the Bragg and diffuse scattering, which when Fourier transformed provides a correlation function, revealing the interatomic distances.[26,30,35] Laboratory sources with Mo or Ag sources can be used for in-house data collection, however, synchrotron X-rays or spallation source neutrons provide data of much higher quality due to their short wavelength.[26,35] To obtain the correlation function, the experimental data should be suitably corrected and normalised, for xPDF data this is performed in Gudrun. The

differential correlation function, D(r), is related by Fourier transformation to the experimental data (i(Q)) (equation (3.1)). D(r) which simplifies to equation (3.2) states the probability of finding a pair of atoms at a certain distance, r, and thus is a direct visualisation of interatomic distances in a sample.[36,37]

$$D(r) = \frac{2}{\pi}\int_{Qmin}^{Qmax} Qi(Q)M(Q)sinr(Q)dq \quad (3.1)$$

$$D(r) = 4\pi p_o G(r) \quad (3.2)$$

where ρ_o is the number density of your material (in atoms per cubic Angstrom) and Q is the scattering vector. To obtain data of a good resolution a large value of Q is essential, to obtain a large Q, a small radiation wavelength (λ) and large scattering angle (ɵ) is required.[36] Equation (3.3), shows the determination of the Q:

$$Q = 4\pi\, sin(\theta)\, /\lambda \quad (3.3)$$

Low-resolution data will more heavily damp the intensity of the peaks in the PDF than high-resolution data. The particle size, or more specifically, the size of ordered domains within the structure, also dampens the PDF, with the function tending to zero at larger distances.[26,36] In the case of the cages, each single cage can be considered a domain. D(r) is advantageous over other functions in that it does not require an accurate sample density to be obtained.[26,30,38] The detailed and complete discussions including works by Keen[36], Qiu[39] and Billinge[30,40,41] on the benefits and derivation of PDF should be viewed. More over D(r) does not weight the low-r peaks more strongly than the higher-r peaks, this allows for peaks at larger distances of r to be viewed. It is also the data format required by PDFGui.[42] Throughout this thesis, the correlation function, D(r), will be referred to as the PDF, as it is more commonly known.

3.0.1.2 PDF analysis

Analysis of total scattering data commonly includes the extraction of bond lengths and coordination numbers from fitting the first few peaks in the pattern. Coordination numbers can be obtained from the peak area of the M-O bond, for example.[30,38] This technique is mostly exploited with glasses, where there is little long range order. For more crystalline samples the analysis of PDF can be split into two distinct branches, small box analysis and

big box analysis.[30,31,38,40,43,44] The small box approach for calculating the model is to specify the smallest possible unit cell that explains the structure and to calculate the PDF from this unit cell. This approach, developed by Billinge and co-workers, is similar to Rietveld refinement, a structural model often based on a crystal structure, is refined by the minimisation of differences between the calculated PDF (a correlation function) and the measured one.[42] PDF analysis, in its simplest application, can be used to determine whether a crystallographic model adequately describes the local structure of a material. If not, the model can be further refined to more accurately describe the local area. Big box analysis works by the process of simulated annealing a large number of atoms, typically tens of thousands, are placed in a 'box'. The PDF is calculated and compared to the actual PDF obtained, the atoms are then moved slightly and the process repeated until there is no difference in the calculated and obtained PDF.[38,45] Big box analysis is significantly more computationally expensive than the small box modelling reported. Metropolis, Monte Carlo and Reverse Monte Carlo are three of the most common simulated annealing algorithms used in the structural solution of PDF.[38,45]

3.0.1.3 PDF in the literature

The analysis of total scattering patterns has become more widespread over the last decade.[43,46–48] The literature, however, is still limited but there are a small number of studies on porous materials.[49] PDF is advantageous because it allows for the study of materials that cannot be studied by conventional crystallography, materials that do not have regular long-range order, such as glasses,[48,50,51] gels[52–54] or nanoparticles.[35,55–57] I*n-situ* studies have been conducted to study the kinetics of formation of ZIFs and nanoparticles.[35,56–59] Diamond anvil cells were used to collect high-pressure amorphous phases of Fe and zeolite NaA, before PDF analysis, it was not possible to characterise these types of materials and the knowledge gained about these phases is essential to furthering materials chemistry.[59–61] Work by the Goodwin and Cheetham groups on amorphous MOFs, ZIFs and metal organic glasses shows porous structures, materials that were once disregarded, are now beginning to be understood and their structures studied.[46,47,49,51] PDF is not just for the study of the porous materials, the Billinge group and others have used PDF to determine the structure of amorphous pharmaceuticals, understanding how the

synthesis affects the local structure and how this impacts the formation of the crystalline phase.[41,55,62–66] Many potentially life-saving drugs are disregarded because of their poor solubility, the use of amorphous and nanocrystalline drug dispersions are being developed to overcome these issues, but in some cases the compound formed is unstable.[55,66] PDF can be used to monitor and understand the transformations occurring within the compound, this will lead to a better knowledge of the interactions and stabilities of these compounds which in turn will lead to better prediction of stable compounds.[55,65,66]

3.1 Project aims and overview

The self-assembling neutral M_4(hydroxamate)$_6$ tetrahedra (Figure 3.1) are dynamic in solution freely interconverting between five isomers.[23,24] Hydroxamate cages have previously been shown to be dynamic in solution; this is due to their chiral vertex converting between lambda and delta.[24,25] Bai uses the IHA ligand, reported in Figure 3.2, with iron nitrate and KOH from a DMF:methanol solution, to grow a cubic crystal in the *P2$_1$3* space group. The structure shows efficient packing, with a pseudo FCC (face centred cubic) arrangement. Within this crystal, the cages show racemic T-type symmetry.[23]

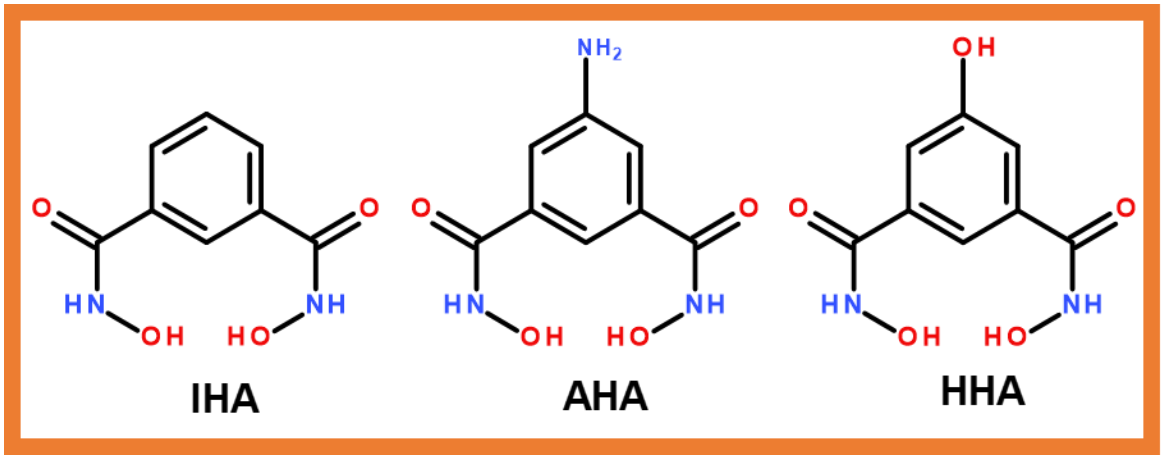

Figure 3.2 shows the structure of the three hydroxamic acid ligands. These ditopic, bidentate species form neutral tetrahedra when introduced to trivalent metals.

Crystal engineering principles were utilised. Functionalising the ligand at the five position to create a range of cages with increased solvents accessible void space was proposed. It was hypothesised that by incorporating directional hydrogen-bonding functionality an

increased extrinsic void space can be formed whilst maintaining a fixed intrinsic pore. By keeping the same isophthalic hydroxamic acid architecture it should maintain the intrinsic pore dimensions for the tetrahedra. The extrinsic porosity, however, should be different because the hydrogen-bonds will cause the cages to pack less efficiently. This will be seen by the cages packing in lower symmetry space groups.

From the three ligands (Figure 3.2), eight cages were crystallised (Table 3.1). Four of the cages form an isostructural series. The five position of the benzene ring incorporates either a hydrogen, amine or hydroxyl group. The one and three positions on the ring incorporate the hydroxamic acid moiety. The ligands are bidentate and ditopic, each ligand can coordinate at two sites and each coordination site can chelate to the metal twice, in the case of hydroxamates, this occurs through the two oxygens. Hydroxamates chelate readily to trivalent metals, this includes metals such as Fe^{3+}, Ga^{3+} and Al^{3+}.

It was hypothesised that by retaining the same basic structure, this will allow us to retain the tetrahedral cage geometry. The angle and coordination of all the ligands to the metal is retained due to the rigidity of the ligands and the 1,3-positions of the hydroxamic acid functionalities. Based on the design rule of metal organic polyhedra, it was proposed that the M_4L_6 tetrahedra geometry will be retained. Further to this, it was envisaged maintaining the same intrinsic pore dimensions when the ligands are complexed to the same metal. The incorporation of functionality at the five position provides the additional hydrogen-bonding capabilities. Allowing for the design of more extrinsically porous networks, by preventing efficient packing of the cages.

Cooper reported the use of a chiral organic molecular cage for the enantioselective separation of chiral molecules.[67] The same cage was also studied for the separation and storage of the noble gases from air.[67] The separation of guests of similar sizes and shapes is becoming ever more important, in Cooper's case the small size of the intrinsic pore at 4.4 Å provides a size match to the guest species; radon has a diameter of 4.7 Å, xenon 4.1 Å and krypton 3.96 Å. The cages showed uptake of the Nobel gases at ppm (parts per million) concentration at 40K and at 1.01 bar, a 51 wt.% uptake was recorded for Xe.

Table 3.1 representing cage formula, names, space group, lattice parameters and solvent accessible void space of the cages. Lattice parameters showing the variables using standard crystallographic settings. Solvent values (m and n) are discussed later in section 3.1.5.3.

Name	Formula	Space group	Lattice parameters	Solvent accessible void space (%)
cage 1	$Fe_4(C_8H_6N_2O_4)_6$. m(H_2O).n(DMF)	$P2_13$ Cubic	a = 27.6954 (19) Å	54.0
cage 2	$Fe_4(C_8H_7N_3O_4)_6$. m(H_2O).n(DMF)	C_2/c Monoclinic	a = 42.992(6) Å b = 31.887 (5) Å c = 30.307 (4) Å β = 91.1948 (8) ˚	63.9
cage 3	$Fe_4(C_8H_6N_2O_5)_6$. m(H_2O).n(DMF)	$P2_1/n$ Monoclinic	a = 24.5375 (12) Å b = 25.8725 (12) Å c = 25.1504 (12) Å β = 110.641 (12) ˚	68.3
cage 4	$Fe_4(C_8H_6N_2O_4)_6$. m(H_2O).n(DMF)	$R\bar{3}$ Trigonal	a = 23.3009 (19) Å c = 37.072 (4) Å	57.8
Cage 5	$Ga_4(C_8H_6N_2O_4)_6$. m(H_2O).n(DMF)	$R\bar{3}$ Trigonal	a = 22.9549 (9) Å c = 36.2162 (9) Å	56.0
cage 6	$Ga_4(C_8H_7N_3O_4)_6$. m(H_2O).n(DMF)	C_2/c Monweoclinic	a = 29.4070 (16) Å b = 40.417 (2) Å c = 16.1827 (9) Å β = 111.328 (3) ˚	74.3
cage 7	$Al_4(C_8H_6N_2O_4)_6$. m(H_2O).n(DMF)	$R\bar{3}$ Trigonal	a = 22.8281 (4) Å c = 35.8319 (8) Å	56.5
cage 8	$In_4(C_8H_6N_2O_4)_6$. m(H_2O).n(DMF)	$R\bar{3}$ Trigonal	a = 23.291 (1) Å c = 37.475 (2) Å	58.7

Attempts at separating Xe from Kr in air showed them to be highly selective and have a high capacity towards Xe compared to the current standard material. Molecular cages with a small intrinsic pore are proving themselves highly suited to a range of important industrial applications. The neutral tetrahedra reported by Bai[23] is a highly suitable candidate for exploring the separation of small molecules. The neutral nature of the cages means the void is truly accessible to the guest because no counter ion is required. The rest of this chapter will provide an in-depth description of the synthesis, structure, and properties of these compounds, aided by a range of analytical techniques; including using xPDF to understand the structural changes of the cage upon the heating and desolvation of the family of molecular cages.

The PDF data provides us with data regarding the structure of one molecular cage, from the room temperature data confirming the local structure of the cage. It can be used as a starting model for the VT-PDF study. The VT-PDF will be used to determine if the loss of crystallinity is due to decomposition of the cage, or simply the loss of the hydrogen-bonded cage network.

3.2 Cage structure

3.2.1 Coordination sphere

Within the eight cages (Table 3.1, Figure 3.3), there are a number of similarities, the most basic of which is that they are all neutral M_4L_6 tetrahedra. Each cage comprises of six ditopic, bidentate hydroxamate ligands and four trivalent metals. Each hydroxamate group bonds to the metal through its two oxygens, with each ditopic ligand connecting two metal vertices along the edges of the cage (Figure 3.3), providing each cage with four open faces. The metal vertex, formed of six metal-oxygen bonds, is a distorted octahedron. The O-N bond of the hydroxamate is always located on one face of the octahedron and consequently provides the vertex with its *fac* (facial) isomerism. Further to their isomerism the vertices are also chiral, they can display lambda (Λ), delta (Δ) chirality.

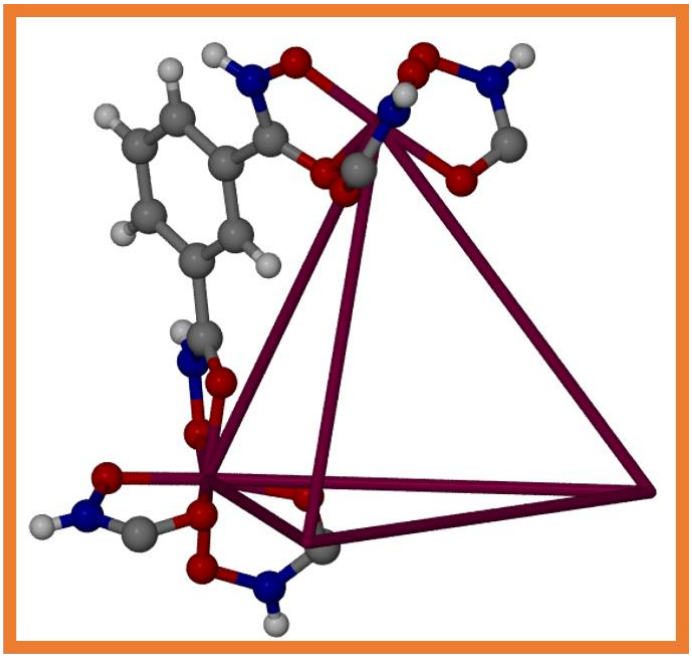

Figure 3.3 shows a capped stick representation of the M_4L_6 tetrahedra shown in maroon with a ball and stick IHA ligand connecting two metal vertex, showing its edge connectivity. Metal is shown in maroon, with other elements represented with standard CPK colours.

The distorted octahedral vertex is comprised of three bidentate hydroxamates chelating to the metal through its two oxygens. The distortion in the octahedra arises from the asymmetry in the two metal oxygen bond lengths. The longer metal – O_c (carbonyl oxygen)is always located inside the cage. The metal – O_N bond is shorter. The hydroxyl oxygen deprotonates and is located on the outside of the cage. The NH group, also located on the outside of the cage, remains protonated. The hydroxyl oxygen has a formal negative charge with each metal having three of these oxygens. The 3^+ charge of the metal is neutralised and thus the cage is neutral overall. The metal centre can have lambda (Λ) or delta (Δ) chirality, this determines which way the pitch of the propeller is orientated Λ anti-clockwise (left) or Δ clockwise (right). The two chiral centres give rise to five potential cage isomers, two T-type cages (ΛΛΛΛ or ΔΔΔΔ), two C_3 cages (ΔΛΛΛ or ΛΔΔΔ), and one S_4 cage (ΛΛΔΔ) (Figure 3.4). These names are derived from their point group symmetries and are solely related to the chirality's of the vertices. Crystallographic structures of the cages do not display these point group symmetries exactly, this is due to distortion of the ligands. The five isomers are dynamic in solution, freely interconverting between themselves; this

interconversion can be monitored on the NMR timescale. Due to the paramagnetic properties of the high spin Fe^{3+} solution state ^{1}H-NMR studies cannot be performed on samples containing this species. Diamagnetic metals such as Gallium and aluminium are, however, suitable.

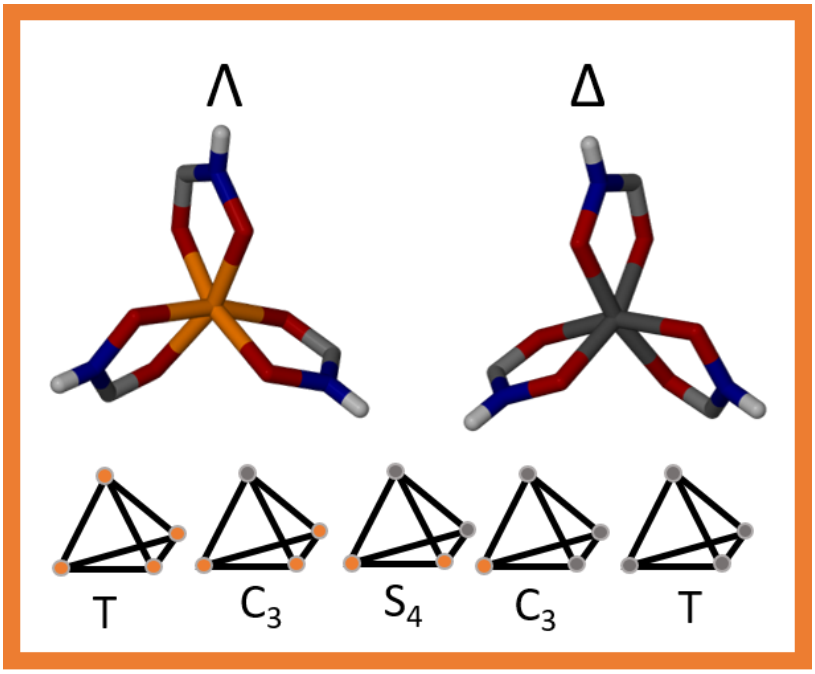

Figure 3.4 shows a capped stick representation of the octahedral hydroxamate metal vertices, which show lambda (Λ) / delta (Δ) chirality which is shown in orange and dark grey respectively, other elements shown with standard CPK colours. Below the five potential cage isomers where the orange and grey circles represent the chirality of the vertices.

The largest difference in the family produced is the packing of the cages within the unit cell. Despite each cage being of a similar geometry, an M_4L_6 cage with T-type symmetry, of a similar size, the packing and the symmetry of the space groups varies greatly between the compounds. All the crystals are packed as racemic T-type cages, both ΛΛΛΛ and ΔΔΔΔ M_4L_6 tetrahedra present. The majority are in centrosymmetric space groups, except for **Cage 1**, which packs in the *P2$_1$3* space group.

3.2.2 Literature comparison

Within the CSD there are 703 metal-hydroxamate complexes. Eighty of the structures contain octahedrally coordinated Al, Fe, Ga or In. The distorted octahedra of the vertex

(Figure 3.5) arises due to the difference in the distance between the two types of oxygen-metal bonds. The non-crystallographic labels in Figure 3.5 are used throughout this chapter for simplicity.

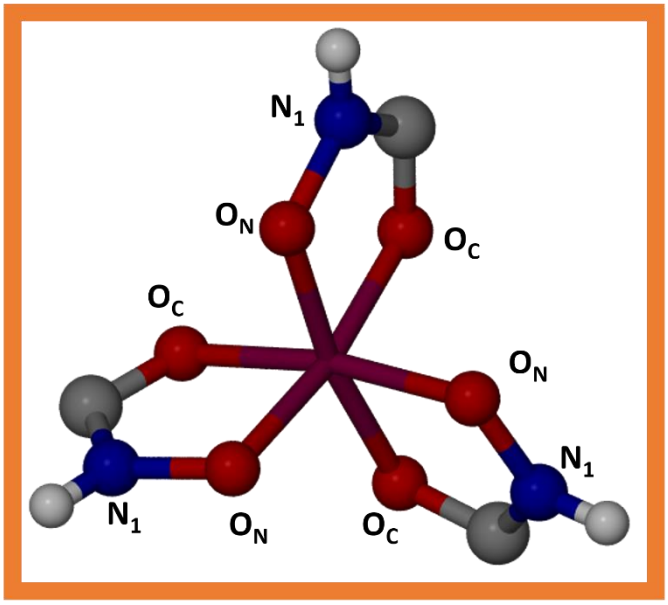

*Figure 3.5 shows a ball and stick representation of the fac metal hydroxamate octahedra (**Cage 7**). Where the metal centre is maroon in colour and CPK colours used for other elements. The displayed non-crystallographic labels are used for simplicity.*

In the case of the Al structure, there is only one reported Al hydroxamate complex in the CSD database. From the CSD structure the average carbonyl (O_C) aluminium bond length range is 1.8960-1.921 (25) Å. The aluminium based **cage 7** shows distances of Al to O_C length of 1.903 (2) Å, which falls well within the expected bond length range, is within error of the average bond length. The shorter Al-O_N length of is determined to be 1.881 (2) Å for **cage 7**. When this is compared to the literature values of 1.872-1.901 (29) Å, again it can be seen that the distances are within error of each other. When **Cage 7** is compared to the other aluminium structure, it can be concluded that both structures are similar. However, more structures are required to accurately determine what is normal for these Al hydroxamate complexes.

From these 703 structures, twelve are Ga hydroxamate complexes, the average Ga-O_N bond lengths for these structures are 1.948 (11) Å with minimum and maximum lengths of 1.913-

2.01 (97) Å. Meanwhile for Ga-O_C is 1.925-2.064 Å with an average of 1.984 (21) Å. From the two Ga cage structures, **cage 5** has a Ga-O_N length of 1.964 (3) Å, whilst the Ga-O_C length is 1.977 (3) Å. The Ga-O_N is slightly longer than the average bond length but falls comfortably within the average range. Conversely, the Ga-O_C is slightly shorter than the average, but again is well with the average range of lengths. **Cage 6** shows similar results with Ga-O_N length is 1.978 (3) Å, whilst the Ga-O_C length is 1.992 (3) Å. In the case of **cage 6**, both bond lengths are slightly above the average but again well within the average range.

There are sixty-five iron hydroxamate complexes, the average Fe-O_N bond lengths for these structures are 1.986 (21) Å, with minimum and maximum lengths of 1.805-2.106 (301) Å. Meanwhile for Fe-O_C the range is 1.906-2.153 (247) Å, with an average of 2.033 (22) Å. There are four Fe cage structures reported in this thesis, the corresponding Fe-O_n and Fe-O_c bond lengths are: **cage 1**, 1.981(3) Å; 2.065 (3) Å, **cage 2**, 1.997 (4) Å; 2.022 (4) Å, **cage 3**, 1.994 (2) Å; 2.043 (1) Å and **cage 4**, 2.004(2) Å; 2.052 (2) Å. These cages show that the carbonyl oxygen O_C is longer than the hydroxyl (Fe –O_N bond), again these values all fall comfortably within the average range.

The CSD contains one indium containing structure (JAGWUG), an octahedral, tris benzohydroxamate complex with *mer* geometry. The average In-O_N distance was determined to be 2.141 (8) Å with a range of 2.134-2.149 (15) Å, as with the other structures the In-O_c length is longer at 2.164 (4) Å with a range of 2.160-2.164 (4) Å, in comparison to **cage 8**.

Looking at the data obtained for **cage 2** (Fe-O_c 2.022 (4) Å) and **cage 3** (Fe-O_c 2.043 (1) Å), incorporation of functionality at the five position of the ring causes contraction of the Fe-O_c bond length compared to using an unsubstituted ligand (**cage 1**, Fe-O_c 2.065 (3) Å). This could be because the twist in the ligand is more pronounced, as it is bulkier, as reported by Hay.[68] Looking across the isostructural series, it is evident that the metal-oxygen bond distance contract in line with the metal radius, see section 3.4.1.2.

3.3 The solution state

3.3.1 NMR

3.3.1.1 Dynamics

Previous work by Raymond has shown hydroxamate tetrahedra are dynamic in solution.[24,25] Due to the similarities in cage structure the use of ^{1}H-NMR studies was used to better understand the dynamic properties of cages. With the aim of better understanding why the crystallisation process is unpredictable in nature.

The five cage isomers (Figure 3.6) can be observed and identified on the NMR timescale.[24,25] The chemical environment on the outside of the cage is similar to that of the free ligand, resulting in no significant change in chemical shift. However, the proton inside the cage is shifted from 7 ppm to 13 ppm. Conversion between the Δ and Λ isomers can occur via two mechanisms, the Bailar twist or the Ray-Dutt twist.[69–71] The mechanism and intermediates formed are different between the two. The Ray-Dutt twist forms an intermediate with C_2v point group symmetry. The Bailar twist intermediate is trigonal prismatic with the D_3h point group symmetry.[71] Raymond states that the Bailer Twist is preferred in tetrahedra due to the Ray-Dutt twist intermediate's symmetry enacting a metal-ligand bond breakage.

Figure 3.6 shows the five tetrahedra isomers and the ligand geometries required to form them. Distinguishing between the five isomers can be done using ^{1}H-NMR integration based on the ligand geometries. The symmetric T-type cage will contain six ΔRΔR or six ΛSΛS ligands, dependent on its metal based chirality. The two enantiomers are equivalent in NMR experiments, so one singlet will be seen because all the ligands are equivalent. A S_4 cage contains one ΔRΔR ligand, one ΛSΛS ligand and four ΛSΔR ligands, from the NMR two singlets with an integration ratio of 2:4 were expected because the ΔRΔR and ΛSΛS are magnetically equivalent. The final C_3 isomer will contain three ΛSΔR and three ΔRΔR/ΛSΛS, so this time two singlets with an integration ratio of 3:3 are expected.

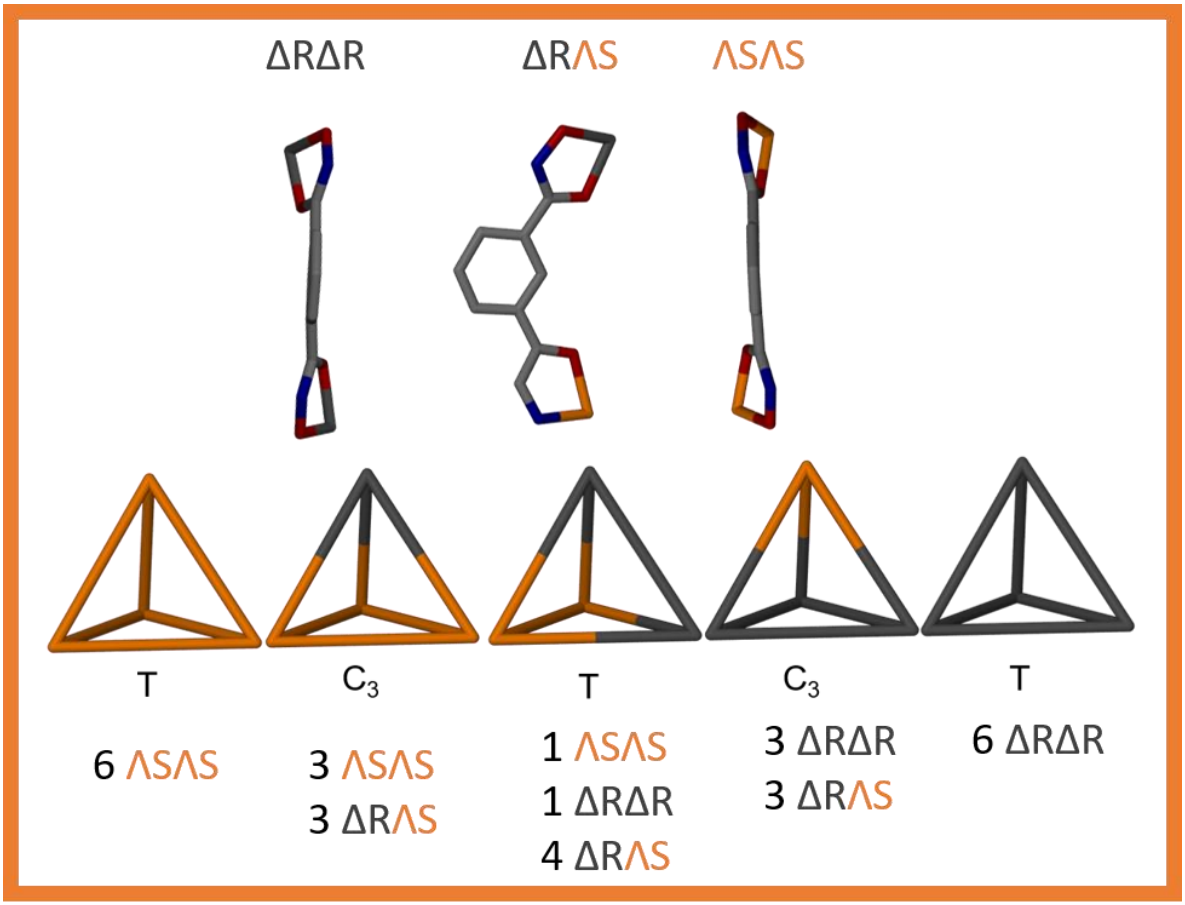

Figure 3.6 shows the capped stick structure of the three ligands geometries required to produce the various tetrahedra. Shown without hydrogens for simplicity. Standard CPK colours used, with orange or grey representing the metal centre to highlight the lambda/delta chirality. The capped stick tetrahedra along the bottom showing the breakdown of ligand conformation required for each cage isomer. Solid colour represents the homo chiral ligands and the split colour representing the hetero chiral ligand.

3.3.1.2 Axial chirality

The ligands are chemically identical, but their geometries vary to form the five isomers. In the solid state, these can be viewed as being crystallographically independent. This is due to the direction of the torsion angles, around the aromatic linker and the carbonyl group, of each ligand arm being free to rotate. The ligands can be viewed has having induced axial chirality.[72] Induced axial chirality occurs in a molecule that does not possess a chiral centre but displays an axis of chirality: about which a set of substituents are held in a non-super imposable arrangement with its mirror image.[72] In the case of the hydroxamates this is the C-C bond highlighted in Figure 3.7.

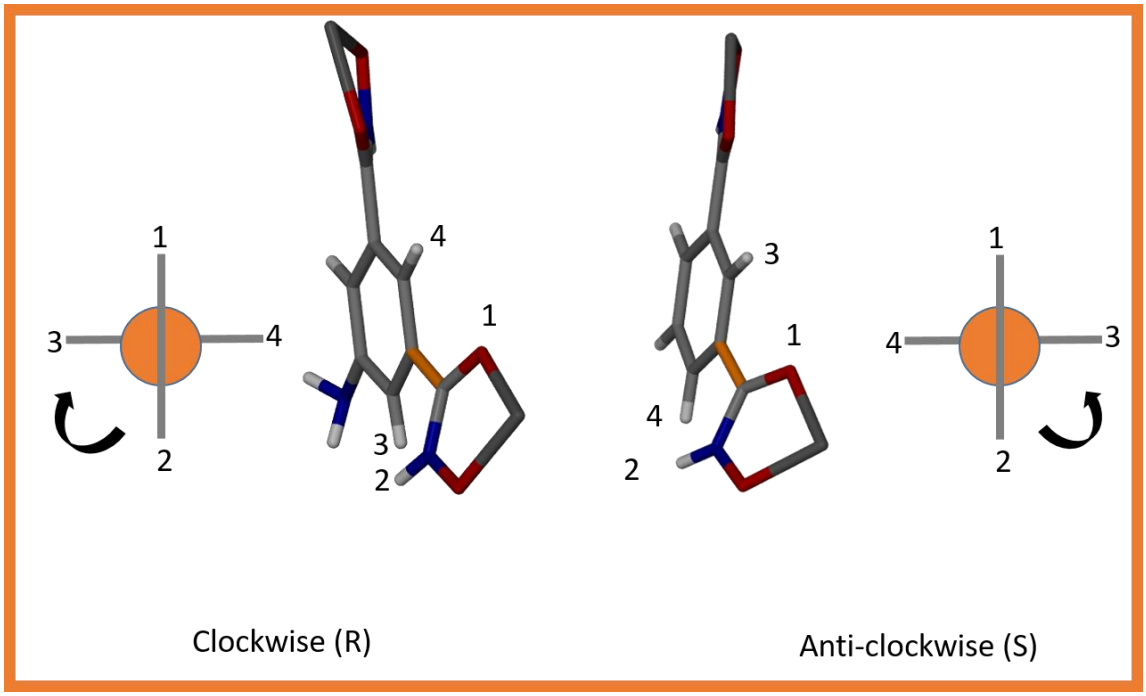

Figure 3.7 shows how a substitution at the five position can invert the chirality assignment. The image contains both Fischer-like projections and the crystallographic ligands with their substituents labelled in order of priority. The metal-ligand complex are both delta (Δ) chirality. This is shown in dark grey and the axially chiral C-C bond is represented in orange. The numbers surrounding the ligands show the priority of the substituents. The Fischer-like projections simplify the rotation to show that the incorporation of the NH_2 functionality at the five position inverts the axial chirality.

The naming (R/S) of the ligand is determined by the substituent on the five position. The assignment utilised the CIP rules[72] and as such the assignment can be inverted whilst the torsion angle is still in the same orientation/direction. Figure 3.7 shows the Λ IHA and AHA complexes. The AHA ligand with an NH_2 at the five position, is referred to as (ΛRΛR), whilst the IHA, with a hydrogen at the five position, is assigned (ΛSΛS). Both ligands have the same conformation; the chiral naming is solely due to the priority of substituents. This is confirmed by the crystallography; the solved structures show that induced axial chirality of the ligand is dependent upon the metal chirality. The rotation around the C-C axially chiral bond is not free within a tetrahedral cage.

3.3.1.3 Isomer ratio and barrier height

If the distribution between the isomers were purely statistical, the relative amounts of T:C_3:S_4 are expected to be 12.5:50:37.5%. This is determined solely by the number of potential pathway to form each isomer, if the barrier height is equal and the minima energies the same for each isomer.[24] Raymond reported the statistical distribution for their hydroxamate tetrahedra to be 4:58:38%, similar to the statistical ratio but showing the T component to be significantly smaller than predicted.[24,25] A ratio for the C_3:S_4 was determined to be 45:55 %, with a small amount of T also being present, for **cage 6**. The peak cohesion within the sample prevents an exact value for T being determined. The use of VT-NMR allows for the energy barrier between the isomers to be calculated. In the case of **cage 6**, the barrier height was determined to have an average C_3:S_4 isomer conversion energy of 88 ± 2 KJ mol^{-1}, which is slightly higher than the barrier height values reported by Raymond of 58 KJ mol^{-1} for the transition between their T:C_3:S_4 tetrahedral isomers.[24,25]

The T-type cages have the lowest abundance in solution. From the crystal structures collected it was determined that all eight cages show racemic T-type symmetry. The crystallisation is self-selecting for the T-type cage. The crystallisation of these materials can be highly unpredictable, in part, because the crystallisation is attempting to select and crystallise out the least abundant component in a solution.

3.3.2 Mass spectrometry

To better understand complexes within the solution state, a mass spectroscopy (MS) study was conducted. The stable isotopes of Ga, Fe and Al provide a distinct isotope signature; these signatures can be predicted and used as additional conformation to the M^+ ion peaks. Electron Ionization (EI) MS uses electrons to produce the detectable ions, it also causes fragmentation of the molecules, these daughter ions can also aid structural determination. The neutral M_4L_6 tetrahedra can be fragmented in a number of ways. Typically, it would be expected to see the molecular ion peak of the cage $[M_4L_6]^{n+}$, this not visible which leads to two possibilities. The $[M_2L_3]^+$ recorded at 637 m/z is simply the fragment corresponding to half the cage, alternatively it could be the helicate structure. Fragments smaller than the mother ion are expected; therefore, if the helicate were the only species present in the

solution the m/z peak at 1025 relating to the $[M_2L_5]^+$ fragment, would not be observed. These larger fragments would not be formed if the M_4L_6 tetrahedra were not present in solution. There are a number of possibilities as to why there is no visible $[M_4L_6]^+$ ion peak, the most likely is that the cages are extremely unstable at the high temperatures required for the MS and they decompose into fragments instantly. Another plausible explanation is that due to their large size they may not 'fly' and therefore do not reach the detector. From the MS it is possible to confirm that the cages self-assemble in a methanol solution and that DMF is not required for the formation of the cages. The cage formation was also confirmed using ^{1}H-NMR using DMSO as a solvent.

3.4 The solid state

3.4.1 Results and discussion

From the initial paper by Bai,[23] the cage crystallisation was repeated using methanol, DMF and potassium hydroxide to crystallise the cages, this gave highly unpredictable crystallisation with a time scale varying from around a couple of weeks to a few months. Methanol was not included within the crystals but water, which was not part of Bai's original synthesis, is included. Therefore, methanol was removed and replaced it with water. It was ultimately established that DMF and water are essential for the crystallisation of the cages. The crystallisation process, however, remains unpredictable. Despite systematically investigating the crystallisation process with a good statistical number of attempts to produce reproducible results, after over 3000 crystallisations, no pattern of crystallisation was observed. From this the only conclusion that can be drawn is that the crystallisation is unpredictable and stochastic in nature for these particular samples. The stochastic nature of the crystallisation maybe due to the dynamic nature of the cages. The interconversion of the cage isomers may prevent crystal growth, because of the difficulty obtaining the correct isomer for the crystal.

Various DMF: water mixtures were attempted to find the most effective method of crystallisation. Solvent ratio schemes, where mixtures of 0:10 DMF: water through to 10:0 DMF: water were created. It was found that the exact ratio required is highly dependent

upon the metal and ligand combination used, typically ratios of 8:2 and 6:4 DMF: water are most favourable. A selection of 3^+ metals was attempted (Cr, Fe, Al, Ga and In) with Ga, Al, In and Fe successfully providing crystals suitable for single crystal analysis. From MS and NMR studies it was concluded that the cages self-assemble freely in a range of solvents, including DMF, DMSO and methanol. DMF however, appears to be essential for the crystallisation of the cage. For the cages tested, good quality materials could only be obtained from DMF solutions.

In further efforts to better understand and improve the crystallisation other solvents, including chloroform, ethanol, DMSO (dimethyl sulfoxide), THF (tetrahydrafuran), DEF (diethylformamide), DMA (dimethylacetamide) and acetone, were also attempted with no success. This is potentially due to the poor solubility of the ligand and the dynamic nature of the cages. Solvents such as DEF, DMSO and Acetone contain a methyl group that can be located in the window of the cage. It was expected that they would be suitable alternatives for the crystallisation of the cage, but attempts at crystallisation using these compounds did not succeed, suggesting that DMF may act as a templating agent and not just a solvent. As well as displaying DMF within the windows, water molecules can also be found, hydrogen-bonded to the NH groups and to the oxygen atoms coordinated to the metal located on the outside of the cage. It is common throughout all of the structures that these water molecules form chains of hydrogen-bonded water. The solvent also shows positional disorder, in that some of the positions are sometimes water and sometimes DMF.

The intrinsic pore volume is consistent throughout the cage family providing a fixed amount of porosity, this means that when the structures are compared any increase in volume is solely due to the increase in the extrinsic void. Table 3.1 shows that, as predicted, the incorporation of functionality at the five position leads to the formation of more extrinsically porous networks. It follows that the cages with a larger void space are in less symmetric space groups due to the cages packing less efficiently. The cubic $P2_13$ space group has a void space of 54%, this increases with the next most symmetric space group, trigonal $R\bar{3}$ at 57.8%, before going to the monoclinic C_2/c and $P2_1/n$, both with more than 60% void space. **Cages 4**, **5**, **7** and **8** form an isostructural series they have the same packing, but due to the variance in their metal centres they display a decreasing intrinsic void space.

Cage 4 was only successfully crystallised once, in all other cases **cage 1** was obtained. Seeding crystals of **cages 5** and **7** failed to yield the desired phase.

From the crystallisation attempts and the NMR study it is possible to conclude that the dynamic nature of the cages in solution probably hinders the crystallisation process. In the future, rather than attempting to crystallise out the minor component of solution it may be more effective to produce a solution that is isomerically pure. One potential way of doing this is to sterically hinder the hydroxamate ligand by incorporating bulky functionality on the nitrogen. The axial chirality would be fixed in position, preventing the conversion of the cage isomers via the Bailar twist mechanism.[69,70]

3.4.2 Crystal structure analysis

3.4.2.1 Asymmetric unit

It was hypothesised that incorporating additional functionality to the five position of the phenyl ring would allow for the more directional hydrogen-bonds to form, causing an increase in extrinsic void space caused by the less efficient packing of the cages. This inefficiency should be recognisable by the packing of the cages in a lower symmetry space group because of the nature of the $P2_13$ and $R\bar{3}$ structures being FCC and HCP (hexagonal close packed), respectively. Figure 3.8 shows the asymmetric unit (ASU) of all the cages.

Cage 1 shows racemic T-type cages packed in the enantiomorphic cubic $P2_13$ space group. The lack of inversion centre within $P2_13$ means that both chiral forms need to be present within the ASU. The ASU shows two one-thirds of the T-type cage, one of these thirds relates to the Λ cage, the other relates to the Δ cage. The two cages are bound by a hydrogen-bond between the hydrogen of the NH to O_N of the hydroxamate. ($N_1 \cdots O_N$ = 2.828 (5) Å, D).

Cage 2 and **Cage 6** are both T-type tetrahedra that crystallise as a racemic pair like the others in the series. Formed of the AHA ligand incorporating the NH_2 functionality both in the *C* centred monoclinic *C*2/*c* space group. **Cage 2** has an ASU of one complete cage and one-half cage, whilst **cage 6** has an ASU of just half a cage. Despite being in the same space group, the ASU and subsequent packing of the cages is very different, these two cages are

not isostructural. **Cage 3** formed of the HHA ligand has an OH group at the five position; it packs in the $P2_1/n$ space group, with an ASU of one complete T-type cage.

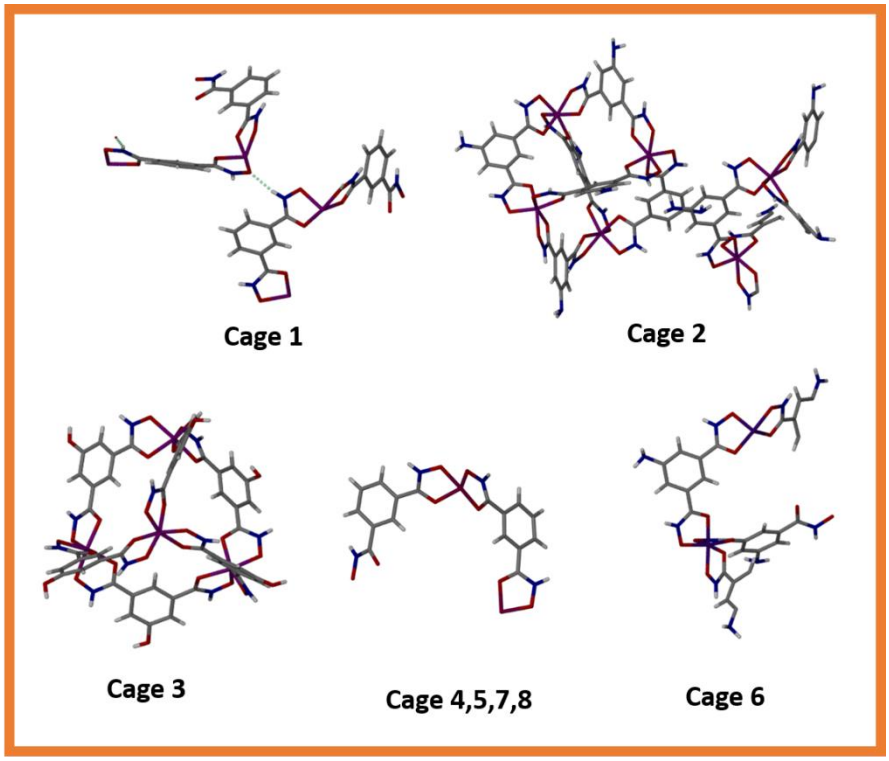

*Figure 3.8 shows capped stick representations of the solvent free ASU for all the cages. The ASU is the same for **cages 4**, **5**, **7** and **8** due to the isostructural nature of the series and are represented by one-third of a cage. **Cage 1** has an ASU of two, one-third cages. **Cage 2** ASU shows one complete cage and one-half cage. **Cage 3** ASU shows a single complete cage. **Cage 6** ASU is represented with half of a cage.*

Cage 4, **5**, **7** and **8** are isostructural, the ASU and subsequent packing of these cages is identical, to prevent repetitions, they shall be discussed as one, because the trends are common throughout the family. The isostructural series are represented by an ASU of one-third of the T-type cage, this comprises of two complete ligands and 1.333 metals, arising due to the metal atom sitting on the threefold symmetry element. The rest of the cage and the inversion of chirality occurs through the symmetry elements of the trigonal centrosymmetric $R\bar{3}$ space group. Despite the cages and their packing being isostructural the solvents of crystallisation, DMF and water, are different between the members of the isostructural series.

All the crystal structures show T-type M_4L_6 tetrahedra. They are water:DMF solvates. Each cage contains four metal-hydroxamate octahedra, where there are 12 NH groups located on the outside of the cage. In every crystal structure collected each of the 12 NH groups are always found to hydrogen-bond to other cages or the solvent of crystallisation. A discussion regarding the solvent of crystallisation for all the cages can be found in section 3.5.3

3.4.2.2 The unit cell

The packing of the cages will be discussed herein. It was hypothesised that incorporating additional functionality at the five position would produce less efficient packing and increase the amount of extrinsic void space. Figure 3.9 illustrates a single unit cell of each of these cages and shows the location of the cages within them.

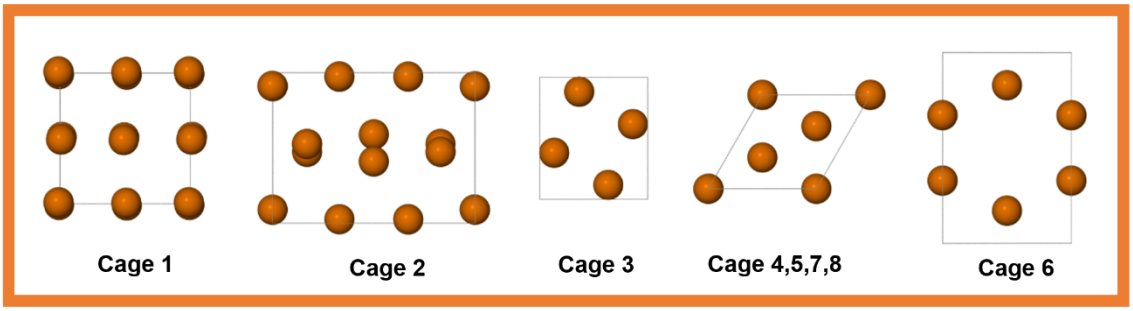

*Figure 3.9 Illustrating how the packing is less efficient in **cages 2**, **3** and **6**. Where the cages are represented as orange spheres, packed into one unit cell, viewed down the c axis.*

Cage 1

Cage 1 is packed in the cubic enantiomorphic $P2_13$ space group. The structure shows a pseudo FCC (face-centred cubic) packing with one cage located at each corner of the unit cell and one in the centre of every face, shown in Figure 3.9. Each cage has twelve NH donor groups. A single cage is hydrogen-bonded to six other cages of the alternate chirality through direct cage-cage hydrogen-bonds. The cage-cage hydrogen-bond occurs through the NH donating to the hydroxyl oxygen ($N_1 \cdots O_N$ = 2.828 (5) Å, D). Each cage provides three donor hydrogen-bonds and three acceptor hydrogen-bonds. After taking into account these hydrogen-bonds there are now nine NH groups per cage available to hydrogen-bond with

the solvent of crystallisation. Six hydrogen-bonds form with DMF and three occur with water molecules. These hydrogen-bonding interactions are summarised in Figure 3.10.

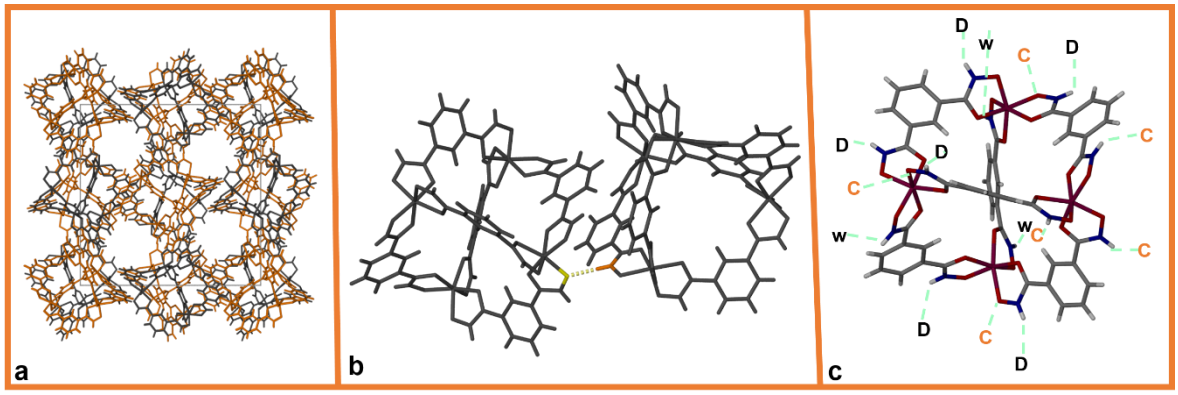

Figure 3.10 ***a*** *shows the packed unit cell of* ***cage 1****. Six cages of the alternate chirality surround each cage, forming a 3D hydrogen-bonded network along all three axes, with both intrinsic and extrinsic porosity.* ***b*** *shows the hydrogen-bonding connectivity, where cage-cage acceptor sites are shown in yellow, cage-cage donor sites in orange, image c shows the D interaction.* ***c*** *shows all the cage-solvent hydrogen-bond interactions. Where* ***D*** *represents DMF,* ***W*** *represents water, and* ***C*** *represents cage-cage interactions.*

There is no evidence of π-π interactions between any of the cages. The hydrogen-bonds between the cages create a hydrogen-bonded network of cages. This leads to discrete channels of intrinsic void space, alternating between Δ/Λ along the three principle axes and the larger extrinsic void between the cages. (Figure 3.10). The extrinsic pore is filled with the DMF and water molecules, with DMF being located within all four windows of the cage. This is representative of the entire cage family and as such is discussed in depth in section 3.5.3.

The symmetry elements (threefold axis) of the cage mean that there are three identical metal vertices, each providing an acceptor for the surround cages, the donors interacting with two DMFs and a water molecule. The preference for water may be due to the lack of available space, due to the steric bulk of the surrounding region. The final vertex however, is unique. It acts as the donor for three of the surrounding cages. In this case O_N is unable to act as an acceptor due to the steric bulk of the three surrounding cages.

Cage 2

Cage 2 shows the same direct hydrogen-bond interaction, previously seen in **cage 1**. The direct interaction occurs between the NH of one cage and O_N of the neighbouring cage ($N_1 \cdots O_N$ =2.914 (6), 2.672 (6) Å D). This time there are two of these interactions which can be combined to give a ring system, $R_2^2(10)$. The cage acts once as a donor and once as an acceptor for this hydrogen-bond. A further hydrogen-bond incorporates the additional functionality on the five position, O_N accepting the H from the NH_2 group (N_2) ($N_2 \cdots O_N$ =2.989 (7), 3.916 (4) Å, D). There are always two of these interactions present, which when combined give a ring system $R_2^2(18)$. The cage interactions are summarised in Figure 3.11. This leaves eleven NH groups of **cage 2** to form hydrogen-bonds. Ten of the NH groups form hydrogen-bonds to water and the final hydrogen-bond occurring to DMF. Each cage also acts as an acceptor to two water molecules. Each cage is hydrogen-bonded to six others, two of the same chirality and four of the opposing chirality, which differs from **cage 1**. The structures show discrete layers of intrinsic and extrinsic porosity (Figure 3.17), where the cages alternate chirality, with a lambda cage located directly above, below left and right of a delta cage, and vice versa.

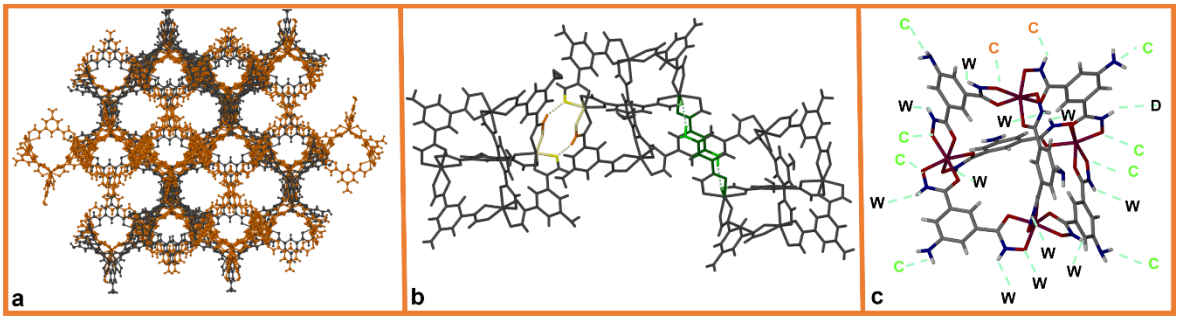

Figure 3.11 ***a*** *shows the packed cage, where layers of intrinsic and extrinsic porosity can be seen, formed by the alternating cage chirality (Λ in grey, Δ in orange).* ***b*** *shows the hydrogen-bonding interactions of* ***cage 2****. The (D/* $R_2^2(10)$*) the yellow shows the acceptor site for this interaction; the orange represents the donor site. The (D)/* $R_2^2(18)$*)) system is shown in green, the lime green representing the four donor atoms and the pale green showing the four.* ***c*** *shows all the cage-solvent hydrogen-bonds interactions. Where D represents DMF, W represents water and C represents cage-cage interactions, the orange C represents the* $R_2^2(10)$ *interaction and the green C the* $R_2^2(18)$*.*

Cage 3

Cage 3 has adopted the monoclinic $P2_1/n$ space group. As seen previously with **cages 1** and **2**, each cage is hydrogen-bonded to six others. The twelve NH groups per cage show different interactions compared to both **cages 1** and **2.** These are four cage-to-cage interactions, five water interactions and three to DMF (Figure 3.12).

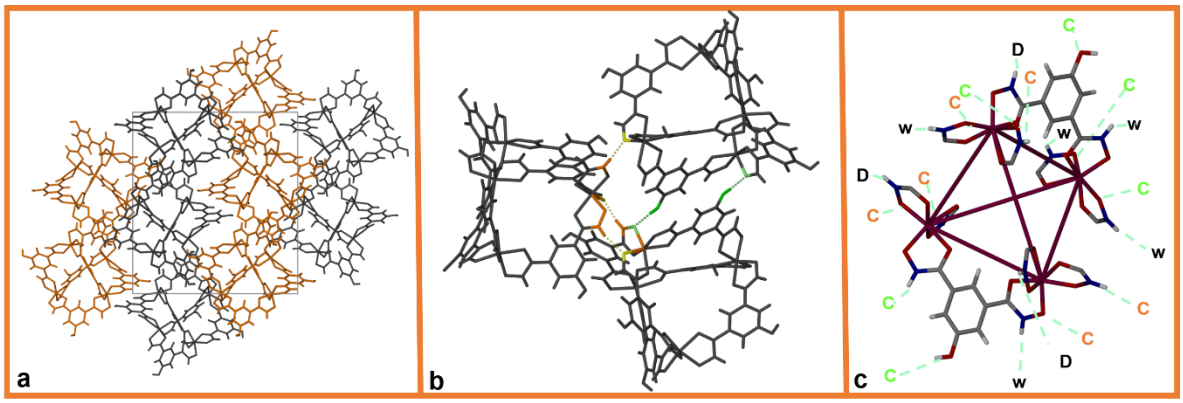

Figure 3.12 ***a*** *shows the packed unit cell of cage 3 down the axis, the cages shows chain of one chirality (Δ grey, Λ orange) viewed down the c axis.* ***b*** *represents the cage-to-cage hydrogen-bond interactions, with the* $(R_2^2(18)/D)$ *hydrogen-bond shown in lime green when the cage acts as the donor and pale green when it acts as the acceptor. The* $(R_2^2(10))$ *shown in orange when the donor and yellow when the acceptor.* ***c*** *shows all the cage-solvent hydrogen-bonds interactions. Where* ***D*** *represents DMF, W represents water and C represents cage-cage interactions, the orange C represents the* $R_2^2(10)$ *interaction and the green C the* $D/R_2^2(18)$*. The tetrahedra has been created by connecting the metal centres. For clarity only ligands E and F are shown.*

The increased number of water interactions indicates that there is more steric bulk surrounding the cage, which prevents the DMF from being able to locate itself close to the cage. **Cage 3** forms three different hydrogen-bonds to form the cage network. Each cage has twelve of these O_N groups, of which six are used in hydrogen-bonding, for this reason crystallographic labels will be used in the graph set analysis. The hydroxyl group at the five position (O_3), donates its hydrogen to one of the O_N groups, (O3F ··· O1A = 2.592 (3) Å; O4B··· O3E = 2.675 (2) Å; $R_2^2(18)$) and (O3A···O1B = 2.714 (3) Å, D). The three other cage hydrogen-bonds occur via the NH group of the hydroxamate acting as a donor to O_N. (N2F···O1F) = 2.794 (3) Å, $R_2^2(10)$ is the same interaction/synthon seen in **cage 2**. The (N2B···O4C 2.707 (2) Å, N1D···O1C = 2.910 (2) Å, $R_2^2(10)$) occurs twice per cage. These $R_2^2(10)$ are formed of

D interactions, as seen in **cages 1** and **2**. The metal vertices are crystallographically independent, each show different donor and acceptor hydrogen-bonding, represented in Figure 3.12. This independence also manifests in the four DMFs found in each of the cage windows, each one being crystallographically unique. The cages interact through the above-mentioned hydrogen-bonding, each cage is connected to two cages of the same chirality and four of the opposing chirality, as seen with **cage 2**. Thus, when the crystal is viewed down the *a* axis the cages appear to form chains of one chirality (Figure 3.12), perpendicular to the plane, with the extrinsic void space located between the chains of alternating chirality.

Cage 6

Despite **cages 2** and **6** being in the same monoclinic C centred space group, C_2/c, they show very different packing, this can be seen in Figure 3.9. **Cage 6** shows a pseudo-diamondoid framework (Figure 3.13), when viewed down the *a* axis the cages can be seen to layer, with an AB packing: in that the cage from the top layer sits in the space left by the two cages of the bottom layer. The arrangement of the cages leaves the largest solvent accessible void space seen within this family of tetrahedral cages. Each cage is connected via two hydrogen-bonds forming a ring system, ($N_1 \cdots O_N$ (*O3*) = 2.799 (5) Å, $R_2^2(10)$), this is in effect a dimer of the D hydrogen-bond typical of this family (Figure 3.13). A second hydrogen-bond incorporating the additional functionality (NH_2) can also be seen (N1= $N_2 \cdots O_N$ (*O1*) =3.018 (2) Å, *D*, N2= $R_2^2(18)$). These interactions are shown in Figure 3.13. The interactions give rise to chains of hydrogen-bonded cages, with each cage having the alternate chirality to its neighbour. The chains show an AB packing and when viewed down the *c* axis the cage chirality alternates; a Δ cage is always directly above and below Λ cages. The two-one screw axis gives rise to the chains having a 'zigzag' pattern, with one cage high on the plane and the other low. When the AB packing and the 'zigzag' chain match, for example, the high Δ cage matching up to a low Λ cage, a resultant large pore is formed.

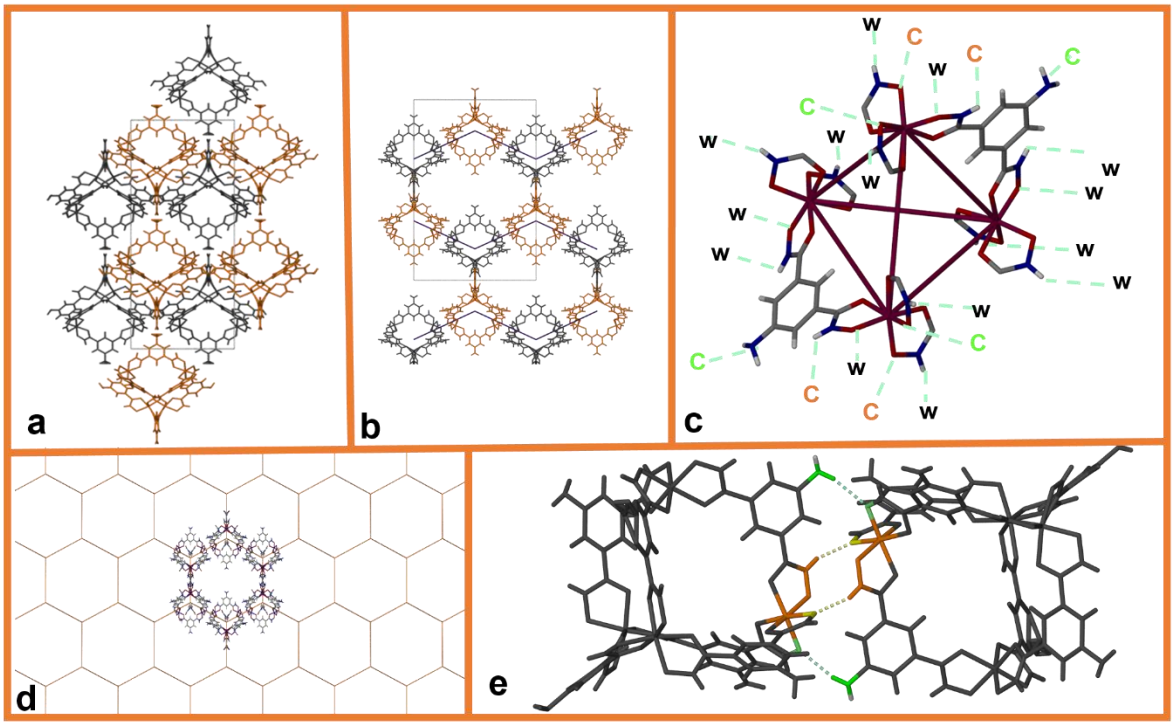

Figure 3.13 ***a*** *shows the unit cell viewed down the a axis,* ***b*** *shows the packed unit cell showing the chains of viewed down the c axis, with an alternating AB stacking of the chains, the zigzag (two-one screw axis) is highlighted with the use of indigo lines showing how the chains coupled with the AB stacking gives rise to the large extrinsic pore.* ***c*** *shows the cage-solvent hydrogen-bond interactions of one cage. Where* ***D*** *represents DMF, W represents water and C represents cage-cage interactions, the orange C represents the* $R_2^2(10)$ *interaction and the green C the D/* $R_2^2(18)$ *hydrogen-bond interactions. The tetrahedra has been created by connecting the metal centres. For simplicity, only ligands that provide hydrogen-bond interactions have been included in the image.* ***d*** *shows the pseudo-diamondoid network (in orange), with one hexagon showing the cage (in CPK colours) location within the network formed by* ***Cage 6.*** *The network was created by placing centroids at the centre of each cage and connecting them.* ***e*** *shows the cage-cage interactions for* ***cage 6*** *where the (*$N_1\cdots O_1$ *=2.799 (5) Å* $R_2^2(10)$*) hydrogen-bond pattern which is shown in orange, with the hydrogen-bond coloured yellow. This is the dimer of the (*$N_1\cdots O_N$, D*) that is seen to connect all the cages into chains of alternating chirality. Shown in green is the (*$N_2\cdots O_N$ *=3.018 (2) Å, D/*$R_2^2(18)$*) hydrogen-bond.*

The isostructural series

The isostructural **cages 4, 5, 7** and **8** show unit cells that contract in line with the ionic radii of their metal.[73] The cage diameter (measured by selecting the two furthest most non-hydrogen atoms located at the furthest distance apart) decreases from 16.062 (4) Å for In,

15.948 (4) Å Fe, 15.626 (9) Å Ga, and 15.484 (3) Å Al. This decrease in diameter correlates with the decrease in the ionic radii of the metals where the octahedral 3^+ radius for In 0.800 Å, Fe is 0.645 Å, Ga 0.620 Å and Al 0.535 Å.[73] The cages do not show any direct cage-cage interactions (no hydrogen-bonds or π-π interactions), and the solvent of crystallisation dominates their interactions. The DMF and water molecules form hydrogen-bonds between the cages and other solvent molecules forming a hydrogen-bonded network.

The difference in solvent between **cages 4** and **7** can be related to Rebek's rule of optimum occupancy of a void space of a host.[74] The rule states that 55% is the idea packing efficiency. Table 3.1 shows the values of the solvent accessible volume for the cages. **Cage 4** and **5** are at 57.8% and 56%, respectively. If this trend were to continue with the Al structure (**cage 7**), it would end up with a value below 55%, meaning the DMF and water guests would be incredibly well packed. To avoid this, the Al structure does not include as much DMF, in that it substitutes the DMF out with the cage windows for water. This results in a structure that is slightly more open at 56.5% than would be expected for the size of the cage.

Figure 3.14 shows the isostructural packing of the cages and how the hydrogen-bonding between the cages is dependent upon the solvation. In these cages, as with the others in the series, all twelve NH groups act as hydrogen-bond donors. **Cages 4** and **8** show similar hydrogen-bond interactions, these however differ from **cages 5** and **7**. In the twelve NH groups of **cages 4** and **8,** nine hydrogen-bonds are to water, the other three NH groups interact with DMF. Both cages also act as an acceptor for water, this occurs three times for **cage 4** and nine times for **cage 8**. In the case of **cages 5** and **7** all twelve NH groups act as hydrogen-bond donors to twelve water molecules. Both cages also act as an acceptor for water, this occurs four times per cage through one O_N from each vertex. **Cages 5** and **7** only have DMF in their windows, whereas **cages 4** and **8** contain additional DMF in the extrinsic pore that allows for hydrogen-bonding.

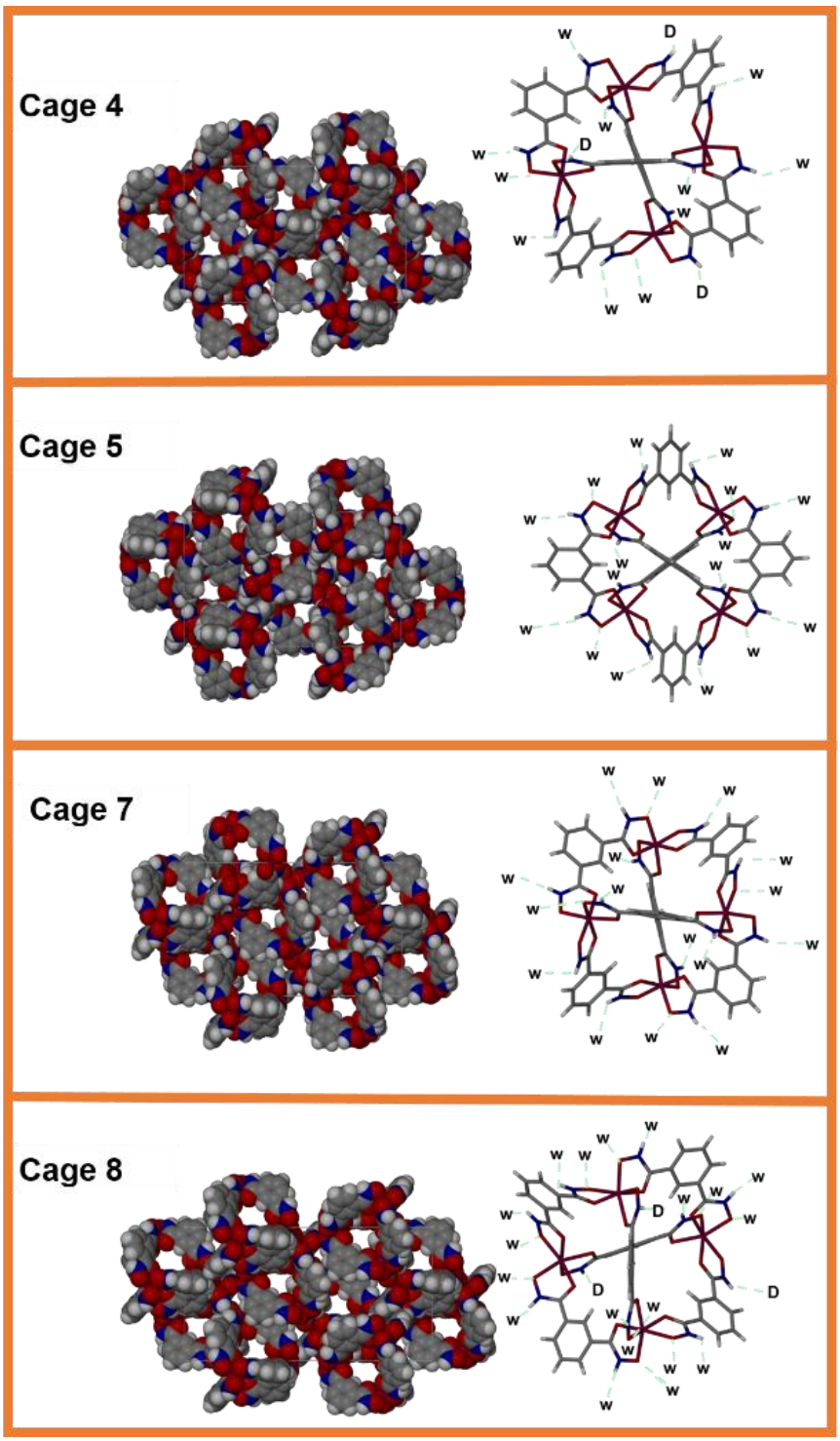

*Figure 3.14 shows a unit cell of the space filled isostructural cage series, highlighting how their packing is identical. The cage pack so their intrinsic pores form channels of intrinsic porosity shows the cage-solvent hydrogen-bond interactions of one cage. Where **D** represents DMF, W represents water. Due to the symmetry elements of the cage, there is one unique vertex and three the same. **cages 7** and **8** are shifted by ½ a unit cell compared to **cages 4** and **5**.*

Packing a single unit cell of cages without solvent and viewing it down the *c* axis shows the typical trigonal close packing, depicted in Figure 3.15, with each cage being surrounded by six of the alternate chirality. Figure 3.16 shows the cage structures viewed down the *a* axis, there are layers of cages with alternating chirality, with the extrinsic pore between them.

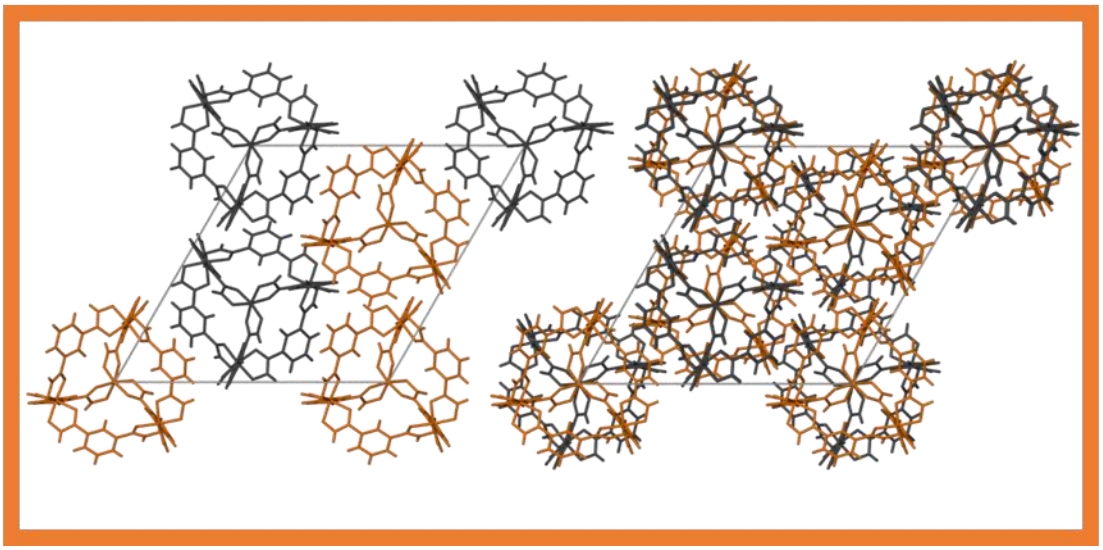

Figure 3.15 a packed $R\bar{3}$ unit cell of capped stick cages, viewed down the c axis. To highlight the trigonal packing of the cages. Solvent omitted for clarity. Λ cages in orange, Δ in dark grey ***cage 4*** *shown.*

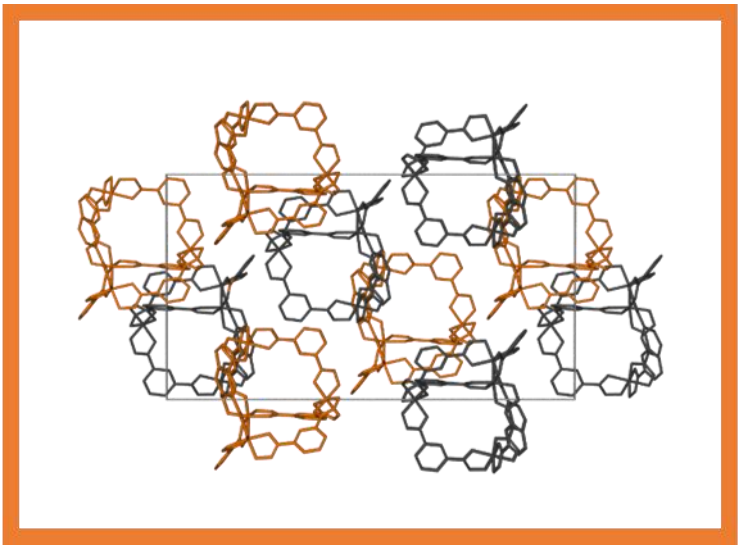

Figure 3.16 a packed $R\bar{3}$ unit cell of capped stick cages, viewed down the a axis. Highlighting the chiral layers of the cage. Solvent and hydrogens are omitted for clarity. Λ cages in orange, Δ dark grey, ***cage 4*** *shown.*

3.4.2.3 Summary

All the cages in the series form hydrogen-bonded networks incorperating DMF and water. **Cages 1, 2, 3** and **6** also display hydrogen-bonds directly between cages, unlike the isostructural series (**cages 4**, **5**, **7** and **8**). When looking at the cage-cage interactions, there is a hydrogen-bond common between all four systems. The donation of the NH hydrogen of the hydroxamate to the hydroxyl oxygen (O_N) of the hydroxamate on the neighbouring cage could be termed a *D* using graph set terminology[75]. **Cages 2**, **3** and **6** form more complex hydrogen-bonding patterns using multiples of the *D* interaction. As a result ring-type hydrogen-bonds form to the neighbouring cage, thus theoretically creating a more complex network. Also seen are additional cage-cage hydrogen-bonds that include the additional functionality on the ligand in **cages 2**, **3** and **6**. From the crystal structures all twelve of the NH's on the outside of the cage form hydrogen-bonds, be this to other cages or the solvent of crystallisation. The solvents themselves hydrogen-bond to each other forming chains of hydrogen-bonds which stabilise the crystal network. All the crystals show that the cages are T-type isomers with both steroisomers being present in a 50:50 ratio.

3.4.3 Intrinsic pore

One of the founding principles of the project was the crystal engineering of the extrinsic void space whilst retaining the same intrinsic pore. To do this it was essential that the same ligand geometry was used. The IHA ligand (Figure 3.2) has hydroxamic acid functionalities at the one and three position of the benzene ring. Chelating with trivalent metals produces distorted octahedral metal complexes which are connected together by the ligands to produce a tetrahedra. The intrinsic pore is unaffected by the addition of functionality at the five position of the phenyl ring because, as previously stated, it is located on the outside of the cage. The controlled nature of the intrinsic void means that the trends it shows are constant throughout the entire family. From the crystallography one of the most noticeable features is that the methyl of a DMF molecule is found located within each window, indicating that the intrinsic pore itself is hydrophobic in comparison to the more hydrophilic extrinsic pore.

Table 3.2 shows how the intrinsic void space is affected by the variance in metals and ligands. To compare the intrinsic void space of the cages a number of distances were determined. Firstly, by creating a centroid of the metal atoms at the centre of the intrinsic void within X-Seed and measuring the metal to centroid distance determining the radius of the intrinsic void. Due to the distortion of the ligands within each cage there is a slight variance in the metal-centroid distance between crystallographically independent metal centres; due to this an average metal to centroid distance is quoted. The free sphere radius is determined by locating the nearest atom to the centroid, which determines the largest sphere that can be situated inside the intrinsic void. The cage diameter is determined by selecting the two furthest most non-hydrogen atoms located at the furthest distance apart.

Table 3.2 shows the variation in cage size and dimensions. Values account for van der Waals.

Cage	Centroid to Metal Distance (Å)*	Largest free sphere radius (Å)	Cage Diameter (Å)	Solvent accessible void space (%)
cage 1	5.421 (119)	2.945	15.803 (8)	54.0
cage 2	5.450 (287)	2.813	18.069 (9)	63.9
cage 3	5.413 (155)	2.911	18.107 (3)	68.3
cage 4	5.445 (300)	2.984	15.948 (4)	57.8
cage 5	5.354 (233)	2.871	15.626 (9)	56.0
cage 6	5.364 (14)	2.809	18.424 (14)	74.3
cage 7	5.312 (220)	2.809	15.484 (3)	56.5
cage 8	5.526 (272)	3.079	16.062 (4)	58.7

** The metal – centroid distance is the average of the four metal centres, hence the large SD.*

Solvent accessible void space was determined from the crystal structures that had been processed using the "Squeeze" algorithm in Platon. This removes the solvent guests allowing for determination of the solvent accessible volume of the cage structures. The solvent accessible volume was calculated in Mercury with a probe radius of 1.2 Å and a grid spacing of approximately 0.7 Å.

As predicted, the intrinsic pore between cages of the same metal is maintained. With the indium cages having the largest centroid to metal distance of *ca.* 5.5 Å, decreasing to *ca*. 5.4 Å for Fe, to *ca.* 5.35 Å for Ga, and *ca.* 5.31Å for Al. This contraction can be explained by the decreasing radius of the metal. The cage diameter increases, as expected, due to the incorporation of additional functionality. The consistency of the intrinsic void volume means that any increase in the solvent accessible void space is solely due to the extrinsic porosity of the cage. The cages pack less efficiently within the unit cell, directed by the hydrogen-bonds between the cages. The size of the intrinsic pore is quite compact, in terms of host:guest chemistry this can be viewed as both a blessing and a curse. The potentially small size means it should be suited to the separation of small molecules and atoms, similar to the work reported by Cooper.[67] The small size however, means it is not suited to the storage of larger guest species. If selectivity is not sufficient, the potential storage capacity may be adversely affected, because the small nature of the pore means that only one or two molecules can be located within the intrinsic pore. If the pore is not selective, it could be filled with the wrong guest species, therefore preventing further adsorption of the desired guest.

3.4.4 The Extrinsic pore and crystal engineering

The cages all display both intrinsic and extrinsic pores. The extrinsic pores of all of the cages are hydrophilic by nature; they host water and DMF molecules within them. The extrinsic pores are seen to form continuous channels within all the collected crystal structures. By using crystal-engineering principles the aim was to increase the amount of extrinsic porosity displayed by the cages.

The largest free sphere radius between cages of the same metal are similar (Table 3.2). This means that the intrinsic void space of the cages is constant through the cages of the same metal. By maintaining the same intrinsic void volume an increase in the solvent accessible void space must be due to an increase in the extrinsic void space. In the case of the iron cages (**cages 1, 2, 3** and **4**) the extrinsic void space increases by 9.9 % for **cage 2,** 14.3 % for **cage 3** and 3.8 % for **cage 4** when compared to **cage 1**. The Ga cages (**cages 5** and **6)** where **cage 6** sees its solvent accessible void space increase by 18.3 % compared to **cage 5**. Table

3.3 shows the amount of extrinsic porosity per unit cell for each cage. As expected the CCP (**cage 1)** and HCP structures (**cages 4, 5, 7** and **8**) show the smallest amounts of extrinsic porosity, showing that as the packing of the cages becomes less efficient the amount of extrinsic porosity increases (Appendix, Chapter 3, porosity values).

Table 3.3 shows the amount of extrinsic porosity per unit cell of each cage.

Name	Extrinsic porosity (%)
cage 1	74.0
cage 2	86.6
cage 3	85.8
cage 4	81.2
cage 5	81.7
cage 6	90.1
cage 7	82.9
cage 8	79.8

Figure 3.17 shows the intrinsic and extrinsic pores of the cages. The cages are orientated so that the window of one cage is facing the window of its neighbour. Cooper defines this as window-to-window packing.[76,77] This arrangement means that the intrinsic pores of the cages are directly accessible, be that via the intrinsic pore of a neighbouring cage or from the extrinsic pore. All the cages form channels of extrinsic porosity. The intrinsic void space of the cages connects to the extrinsic void space via the windows of the cages. This forms a network of interconnected intrinsic and extrinsic porosity. A way of viewing this porosity network is using the void function in Mercury to produce a map of how the pore space is connected.

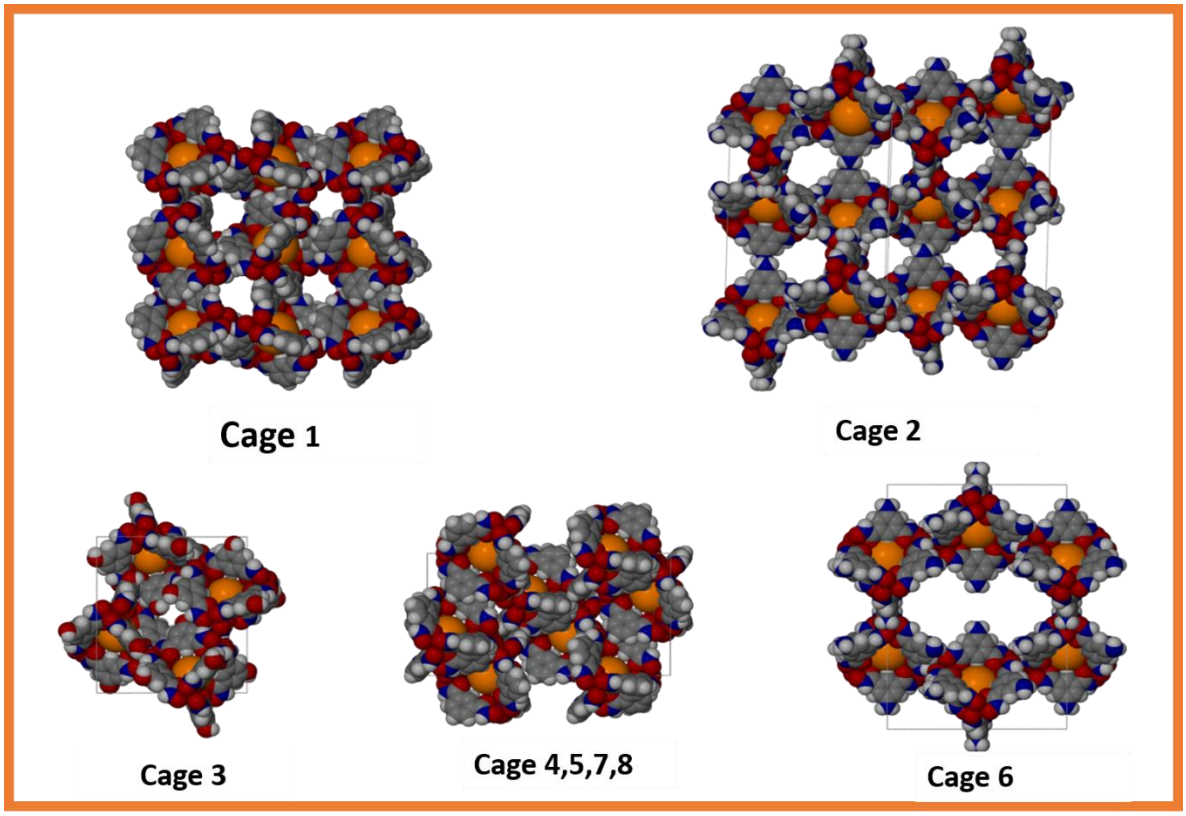

Figure 3.17 shows a set of space filled cages in CPK colours where the intrinsic void space is shown filled with an orange sphere for clarity. The extrinsic void is left unfilled. All images were taken from a perspective of 10 and are therefore comparable. ***Cage 1.*** *Fe IHA $P2_13$ down the, a axis.* ***Cage 2*** *Fe AHA viewed down [101] plane.* ***Cage 3*** *viewed down the c axis.* ***Cages 4, 5, 7, 8*** *the $R\bar{3}$ isostructural series viewed down the b axis,* ***cage 4*** *shown. Cage 6 Ga AHA viewed down the c axis.*

Figure 3.18 shows a single unit cell under the same orientation as the images above, here the inside of the pore is coloured orange and the outside in grey. From these images, it is clear to see that there are channels connecting the intrinsic pore to the extrinsic pores. Alternating layers of intrinsic and extrinsic porosity are formed. The image shows that intrinsic void space forms channels from cage to cage which are connected via the extrinsic void. As expected **cage 6** shows the largest extrinsic void. The extrinsic void shows a narrowing at the centre point due to this void being formed from six cages. In the other cages, each extrinsic void channel is formed from four cages.

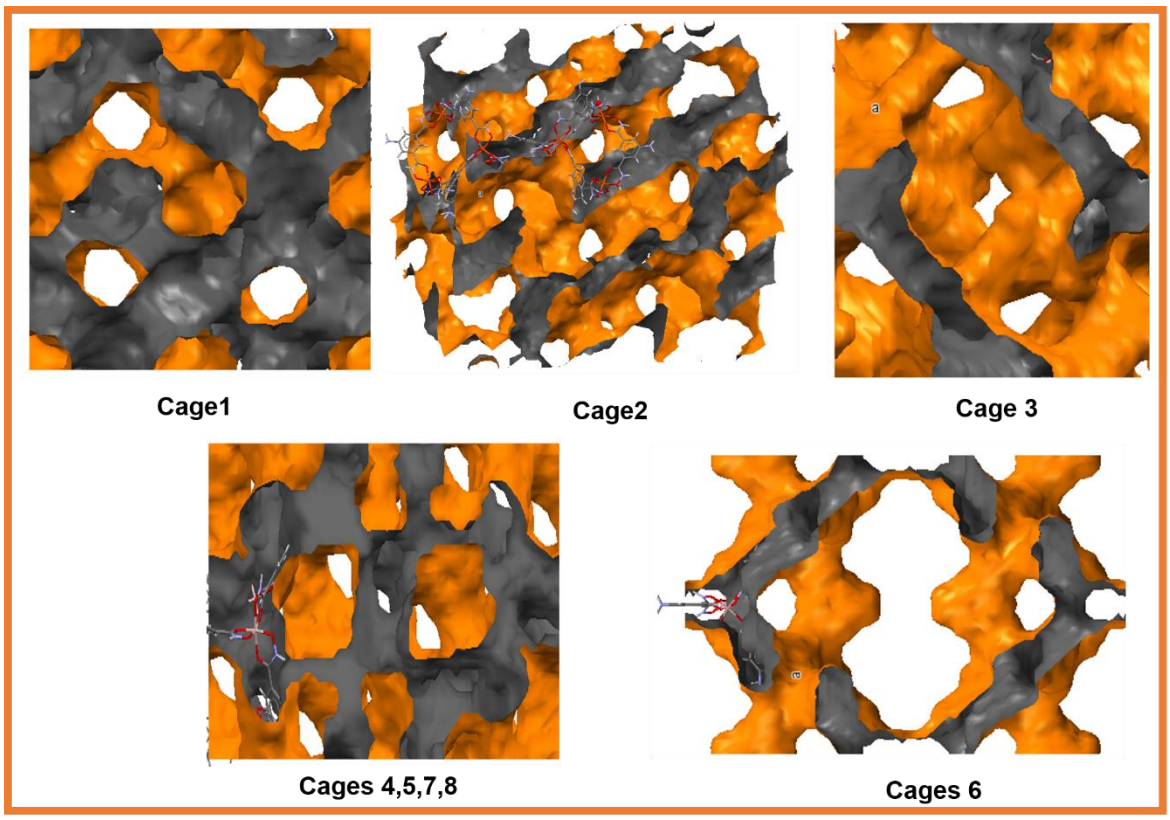

Figure 3.18 Mercury images displaying the void space of the cages. Where the inside of the pore is coloured orange and the outside in grey. ***Cage 1*** *viewed down the a axis,* ***Cages 4,5*** *and* ***7*** *are viewed down the b axis and* ***cages 3*** *and* ***6*** *down the c axis, as with the previous image.*

In summary, it has been possible to maintain the same intrinsic pore size of the cages by using the IHA ligand. By incorporating additional functionality on to the outside of the ligand, crystal engineering has been used to form more extrinsically porous materials, caused by the less efficient packing of the cages. The materials form networks of continuous porosity that incorporate both intrinsic and extrinsic porosity. All eight materials are DMF:water solvates, with the solvent of crystallisation found in the extrinsic pore. The solvent and its role shall be discussed herein.

3.4.5 Solvent disorder

Within all the crystal structures there are DMF and water solvent molecules. These solvent molecules are disordered which causes diffuse scattering, lowering the resolution of the data. Modelling disorder can be readily performed using the crystallographic software. In this case Olex2 was used with the SHELX restraints and constraints. If the solvent is clear

and the disorder model is meaningful, then this is the preferred option. In some cases the modelling of the solvent is not possible. Platon's 'SQUEEZE' program can be used to provide an approximate electron count for the residual electron density. This electron count, combined with TGA, can be used to determine the number of solvent molecules within a system.

By slowly cooling the crystal it may be possible to limit the amount of disorder seen. Flash cooling is where the crystal is placed under a flowing stream of liquid nitrogen at 100 K. A crystal of **cage 1** was cooled from room temperature to 100 K at 1 K per minute and a data set collected. The solvent disorder within the slowly cooled crystal was no more resolved than in the data set obtained by 'flash' cooling. This suggests that the disorder is inherent within the system.

Both SQUEEZE and solvent modelling were performed on the cages, both techniques provided insightful as the results complimented one another. SQUEEZE was used to determine an estimated electron count, which was used to estimate the total amount of solvent within the system. The solvent was also modelled using SHELX constraints and restraints using Olex2. The SHELX restraints SADI, DFIX and DANG were the three most common restraints to control the geometry of the DMF. After utilising the data available in the residual peaks, the best models of the solvent were found not to match up with the squeeze electron count. The predicted number of solvent molecules is significantly greater than the ones presently modelled within the structures.

From the solvent model established there is a DMF molecule located in the window of every cage. The DMF is always orientated so that a methyl group points into the hydrophobic intrinsic pore cavity, whilst the carbonyl group is located towards the hydrophilic extrinsic pore (Figure 3.19). This is a feature common throughout the entire cage series, including the published structures by Bai[23] and Raymond.[24,25] This in part explains the lack of crystallisation from other solvents. It is possible that DMF templates the crystallisation of the cage. However, from the NMR and MS studies there is evidence that the cages form in solution without DMF; this indicates that DMF is not a template for the cage formation but is integral to the formation of the crystals.

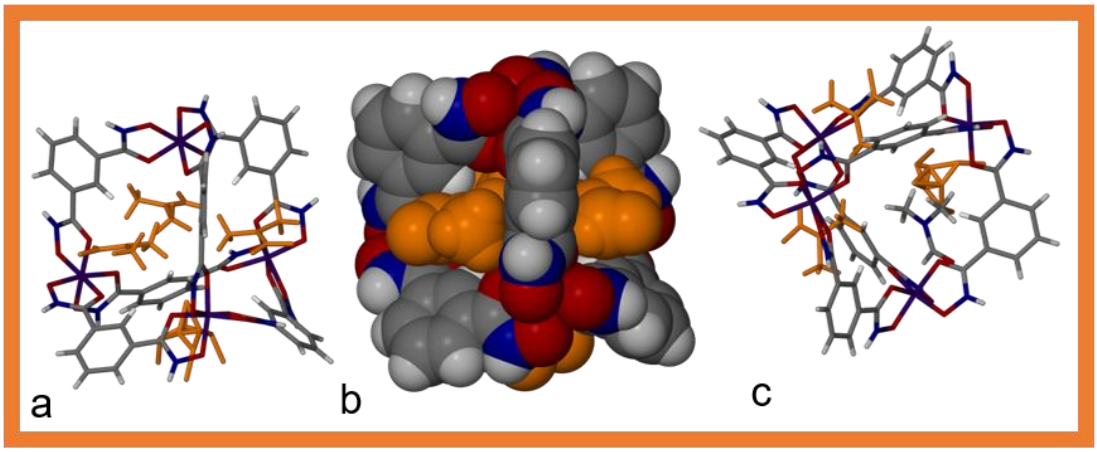

Figure 3.19 ***a Cage 1*** *in capped stick representation with DMF (orange) in every window.* ***b*** *space filled* ***cage 1*** *structure, showing space filled DMF, in orange, in the four windows of the cage,* ***c*** *capped stick representation of* ***cage 1*** *showing one DMF with CPK colours to show the DMF orientation. The DMF locates itself with a methyl in the hydrophobic intrinsic pore whilst the carbonyl is located into the hydrophilic extrinsic pore. Water molecules have been omitted for clarity. Normal CPK colours have been used to represent the cage, with the Ga centre shown in indigo.*

For the systems that have a three-fold symmetry element, **cages 1**, **4**, **5**, **7** and **8**, a DMF molecule is located on it. Figure 3.20 shows the expected DMF geometry, a nitrogen connected to two methyls and a carbonyl. The disordered DMF appears to be missing a methyl, this is not the case once the structure is grown, the carbonyl carbon is the second methyl for the second molecule. Due to being on the three fold symmetry point there are six potential sites for the DMF. Due to the data quality, it was decided to model the DMF isotropically without hydrogens. The carbon C(2Y) has an overall occupancy of 1, with all three DMF molecules sharing this one atom. The nitrogen and oxygen atoms are refined to have an occupancy of a third, whilst carbon C(1Y) has an occupancy of two-thirds due to it being both the methyl of one molecule and the carbonyl of the other. Modelling the DMF allowed me to confirm that in every window in all of the structures there is a methyl group from DMF. Within some of the crystal structures DMF and water molecules are located on the same site, although there is not enough resolution to accurately determine a ratio of DMF to water. What can be learnt from this is that the solvent acts as a donor to the O_N acceptor site of the cage. This interaction is always present but the solvent molecule can be either water or DMF. This varies from unit cell to unit cell and from crystal to crystal.

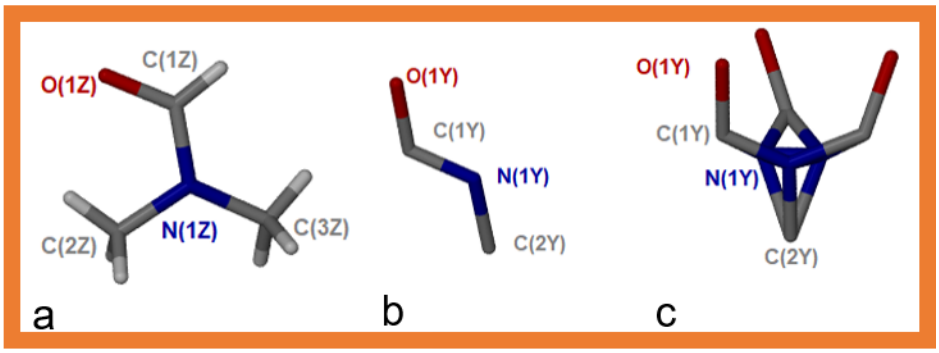

Figure 3.20 ***a*** *is a capped stick representation of the stand DMF geometry (molecule Z),* ***b*** *the ASU geometry of DMF and* ***c*** *the structure of DMF grown over the three-fold symmetry element (molecule Y).*

3.5 Cage desolvation

Cages 1, 2, 5, 6 and **7** were selected for host:guest studies, this was because the crystallisation of **Cage 4** was only successful once. **Cages 3** and **8** failed to crystallise in large enough quantities to allow for further work.

3.5.1 Solvent exchange.

With the DMF and water filling the void space, removal of these components is essential to allow for any host:guest chemistry to occur. Due to the neutral charge of the cages once the solvent species are removed the extrinsic void space will be available to allow the passage of guests into the intrinsic void. Conventionally solvent exchange is performed on materials filled with DMF, due to its high boiling point the material is soaked in low boiling point solvent, such as methanol, prior to desorbing the guests.[78–80] In the case of the cages attempts at solvent exchange failed. Due to the structural similarities of acetone and DMF, both have a similar geometry that contains a methyl group connected to carbonyl, it was suspected that the acetone would make a suitable exchange solvent, allowing for similar hydrogen-bonding patterns to form between the cages. Methanol and ethanol were also used as exchange media. Supercritical Carbon dioxide ($ScCO_2$) is another potential way of desolvating such materials, typically the ethanol solvate is most effective for $ScCO_2$ extraction.[78–80] Attempts to obtain the ethanol solvate were unsuccessful. Therefore, the extraction was performed on the DMF solvate.

3.5.2 TGA

The TGA curves (Figure 3.21) of the cages showed each of the materials has a unique solvent system, confirming the crystallography. Table 3.4 compares the solvent mass loss calculated from the TGA. The crystallographic solvent count forms the 'best crystallographic model'. The estimated electron count from the SQUEEZE data was also used to determine the number of DMF and water molecules.

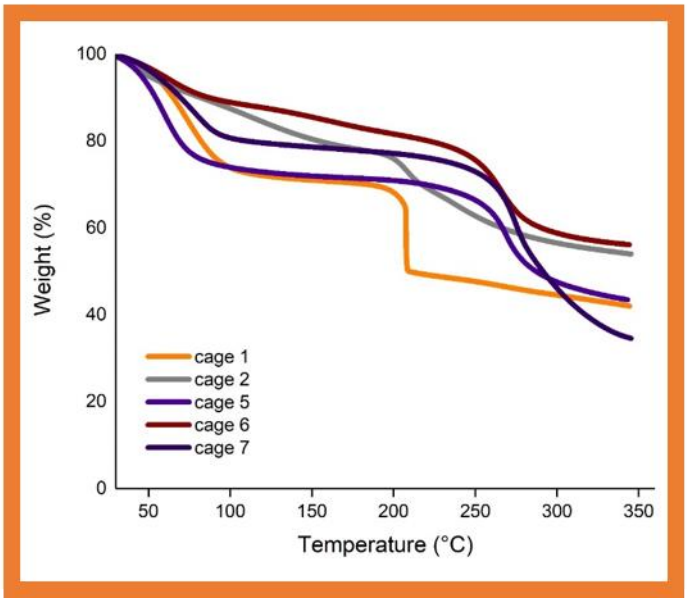

Figure 3.21 shows stacked TGA plots of the five cages. The plots show the gradual solvent loss between 30 and 100 ˚C, followed by the decomposition of the material from 180 ˚C onwards.

The SQUEEZE data in all cases shows an increased level of solvation, which is not unexpected. With the solvent being disordered within the extrinsic void it is not possible to model all the solvent it contains. The difference between the SQUEEZE values and the TGA data suggests that the cages have desolvated prior to their TGA experiment. The TGA experiment required the cages to be dry to determine an accurate weight loss. Any solvent on the surface of the crystal would skew the data obtained suggesting a greater volume of solvent than is actually contained within the structure. The larger difference between the TGA and SQUEEZE data for the more open frameworks of **cages 2**, **3** and **6** would suggest that some desolvation occurs upon removal from the mother liquor.

Table 3.4 is a comparison of the number of solvent DMF and water molecules per cage calculated from TGA, SQUEEZE and the 'best crystallographic model'.

cage	best crystallographic model	Squeeze	TGA
cage 1	7.666 DMF, 2 Water	10.5 DMF, 3 Water	7 DMF, 2 Water
cage 2	7.666 DMF, 12 Water	15.333 DMF, 13.333 Water	4 DMF, 7 Water
cage 3	8.25 DMF, 11.5 Water	16 DMF, 22 Water	N/a
cage 4	7 DMF, 15.75 Water	7 DMF, 16.5 Water	N/a
cage 5	4 DMF, 13.5 Water	4 DMF, 19.5 Water	4 DMF, 15 Water
cage 6	3 DMF, 16 Water	18 DMF, 36 Water	3 DMF, 7 Water
cage 7	4 DMF, 14.5 Water	4 DMF, 15 Water	4 DMF, 4 Water
cage 8	7 DMF, 14.5 Water	7 DMF, 14.5 Water	N/a

The typical trend in solvation shows a larger water to DMF ratio, this is probably related to the number of hydrogen-bonds required to stabilise the cage network: the exception to this is **cage 1**, which shows a DMF heavy solvate. With only two waters and 7.666 DMF molecules per cage the ratio of DMF: water is very different from the next lowest water solvate, 8.25 DMF: 11.5 water. Within the structure the water molecules appear to play an important role in the formation of the network. They are often found forming hydrogen-bonded chains of water, which link cages together.

As stated previously, **cages 2**, **3** and **6** have larger extrinsic pores than the other cages. This coupled with the diffuse scattering makes the modelling of solvent within the centre of the voids virtually impossible at present. This explains the significant difference between the SQUEEZE/TGA values and that of the modelled structure. **Cage 6**, with its pseudo-diamonoid network, has the most open network of all the structures, this would make it easier for the solvent within the voids to evaporate and therefore leads to the skewed values reported. When the single crystals themselves are studied in the mother liquor they are clear colourless prisms. When left in the atmosphere to dry they become a beige powder of poor crystallinity, when studied by pXRD. This phenomenon is unique to **cage 6**; the other materials within the family retain their single crystal morphology upon drying.

Due to the high boiling point of DMF it would be expected that the lower boiling water would be removed from the sample first. The literature shows that it is possible to remove individual solvent components by controlling the rate and temperature of heating.[81] In the case of the cages, DMF and water were removed together. **Cages 1**, **5** and **7** with their less open networks typically show a more resolved, stepped TGA when compared to the pattern shown by **cages 2** and **6**. These show a slow continuous desorption until the eventual decomposition of the framework, with no obvious step where the majority of the solvent is removed from the framework. The tempearature of desolvation is dependent upon the composition of the cage with the total desolvation of the cages typically occurring after heating at 120 ˚C for 20 minutes (Figure 3.22).

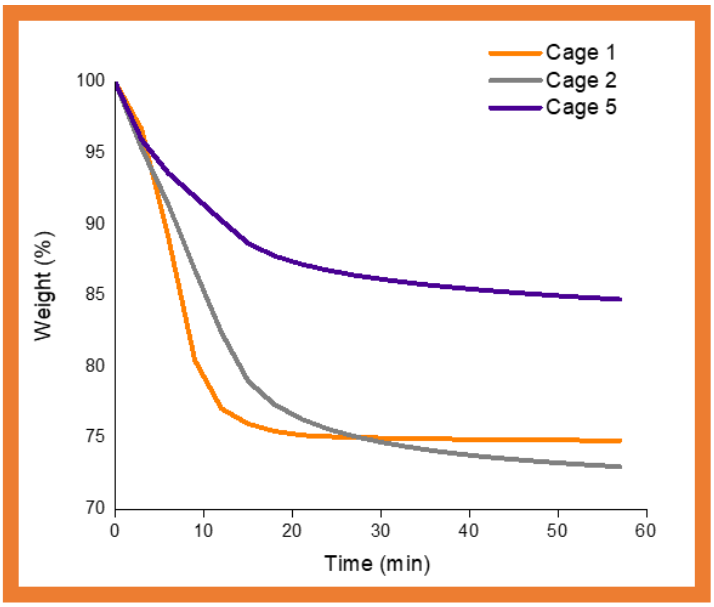

Figure 3.22 shows stacked TGA plots showing the cage desorption when heated isothermally at 120 ˚C.

To ensure that the solvent of crystallisation is removed entirely the cages were heated isothermally at 120 ˚C for 45 minutes. The decomposition point of the cages was also determined by TGA (Figure 3.21). **Cages 1** and **2** have the lowest decomposition ranges at 184 -210 ˚C and 190-215 ˚C respectively. The decomposition points of **cage 5** at 236-284 ˚C, **cage 6** at 245 – 281 ˚C and **cage 7** at 253-287 ˚C, suggesting that the iron cages are less thermally stable than their aluminium and gallium counterparts. If the Al and Ga cages are more thermally stable, they may be better suited to desolvation by heating.

3.5.3 DSC

DSC's were collected on a TA DSC Q20, V24.1 and analysed in the TA universal analysis software, V4.5A. Figure 3.23 shows the overlaid DSC curves of the cage family. The cages show a broad endothermic event between 60 – 100 ˚C, this suggests that there is desolvation of the compound and potentially a phase change occurring alongside the desolvation. For **cage 1** and **2**, there is an exothermic event at 223 ˚C and 219 ˚C corresponding to the decomposition point recorded in the TGA. The exothermic event for **cage 5** and **7** is higher at 277 ˚C and 285 ˚C, again corresponding to the TGA decomposition point.

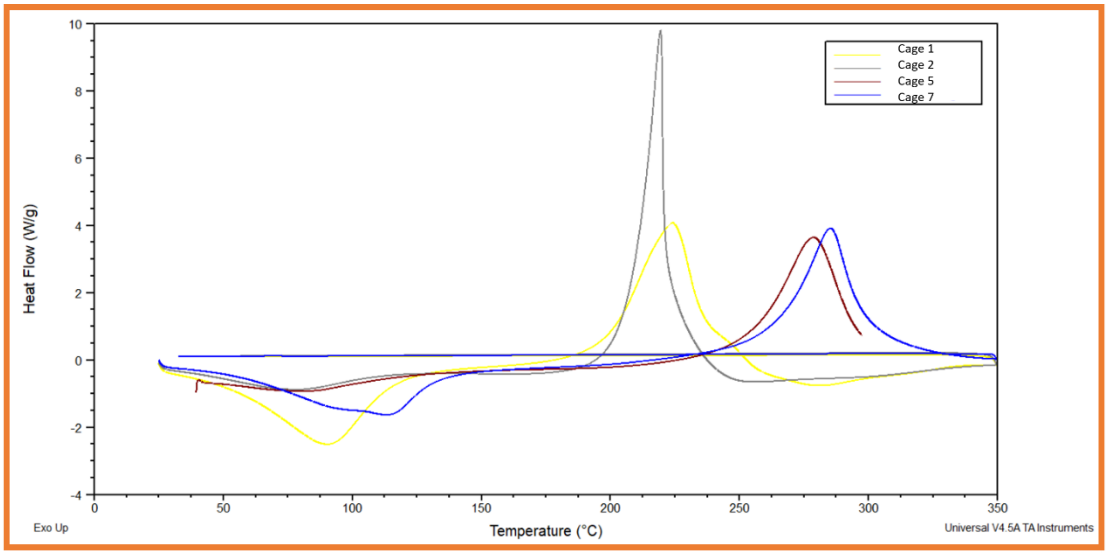

Figure 3.23 shows overlays of the cage DSC curves. Image produced using TA universal analysis software V4.5.

These are the only two events recorded, this suggests that any phase change arising in the structure is directed by and occurs simultaneously to the loss of solvent. VT-pXRD (variable temperature pXRD) was used to study these potential phase changes upon desolvation.

3.5.4 Powder X-ray diffraction

In-situ powder X-ray diffraction was conducted on a Panalytical x'pert pro with Cu radiation between 30 and 200 ˚C in a spinning open capillary at 10 ˚C intervals to ascertain the point at which crystallinity is lost upon heating. Copper radiation is known to cause fluorescence with iron containing samples, causing the background of the pattern to be significantly

higher than expected. To counteract this the diffractometers fluorescence setting was used with the appropriate samples. The single crystals of these materials have been shown to weakly diffract and the powder diffraction is continuing with this trend.

Room temperature pXRD patterns were obtained of **Cages 1, 2**, **5** and **7**. The patterns confirm the phase purity of the bulk sample. **Cage 6** shows an amorphous diffraction pattern at room temperature. This may be due to cages desolvating due to the removal of the crystals from their mother liquor. The Ga and Al samples do not suffer from Cu fluorescence. Therefore, VT-XRD was collected for **cages 5** and **7**. Figure 3.24 shows the normalised stacked pXRD data for both cages.

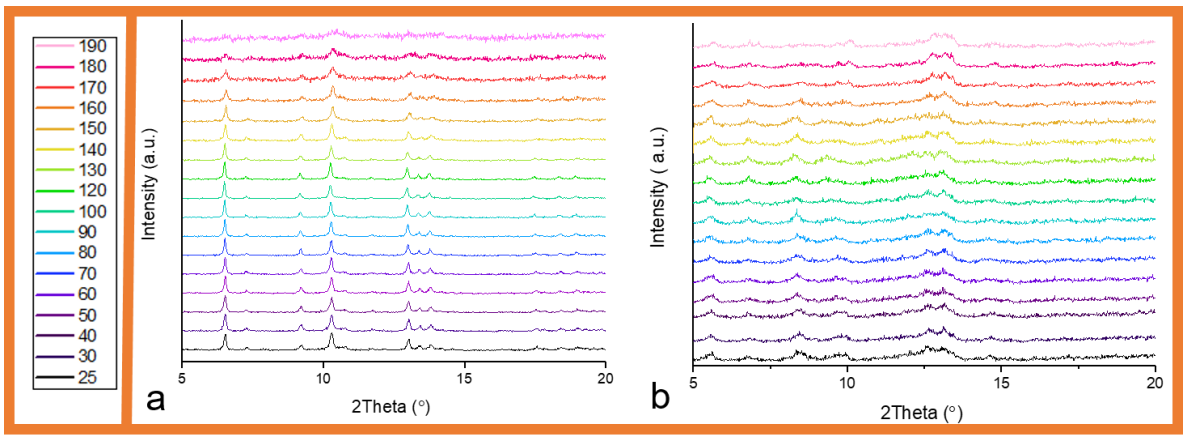

*Figure 3.24 shows stacked VT-pXRD shown between 25 and 190˚C. Image **a** shows **cage 5** and **b** shows **cage 7**.*

The pXRD patterns of **cages 5** and **7** do not show any indication of a significant phase change until they become amorphous with heating. No new peaks appear in the spectrum and there is no significant shift in any of the main peaks, this suggests that the cages do not undergo a phase change. **Cage 5** shows the onset of loss of crystallinity at 160 ˚C, with total loss of crystallinity at 180 ˚C. In summary **cages 5** and **7** show no structural change due to the removal of solvent. The solvent is crystallisation is removed by 150 ˚C, with cage decomposition occurring above 250 ˚C.

This loss of crystallinity could be due to decomposition upon heating, causing the loss of the intrinsic and extrinsic void space. Alternatively, the hydrogen-bonds holding the cages into an organised network have broken, allowing the cages to pack in such a way that they had no long-range order. If this were the case the cages would still contain intrinsic void space,

which may potentially be accessible to guest species. Conventional crystallography cannot tell us about the structure of the cages in the amorphous state. Pair distribution function allows the user to study the local structure of the cages.

3.6 xPDF

Utilising the xPDF beamline I15-1 variable temperature pair distribution function (VT-PDF) has been used to study the structural changes in the local structure of the cages, with the aim of determining whether the cage retains its intrinsic cavity when heated.

3.6.1 Experimental

The PDF technique is suited to the study of amorphous, semi-crystalline materials and nanomaterials where there is a lack of long-range order beyond 10 nm (100 Å). The high Q-range data required for the Fourier transform to provide reliable PDFs were collected on beamline I15-1, Diamond Light Source, UK. Synchrotron radiation, with a wavelength of 0.158246 Å (78 KeV), provides a Q_{max} of 79.4 $Å^{-1}$ for the data. The cage crystals are packed in 0.5 mm borosilicate glass capillary tubes. A total of five samples were collected by remote access, including two room temperature structures (**cages 5** and **7**). A further three VT data sets were collected. **Cages 1** and **6** were collected between 30 ˚C – 200 ˚C at 10 ˚C intervals. The data set for **cage 2** was collected between 30 ˚C – 100 ˚C due to loss of the beam and the sample moving during the experiment. For each sample, the data was processed in Gudrun, the PDF, D(r), was obtained by Fourier transform of the reduced structure function. Structural refinement was performed using small box modelling in PDFGui.

3.6.2 Results and discussion

3.6.2.1 Room temperature study

Analysis of the cage structures from the single crystal model gives a list of interatomic distances that can be matched with peaks in the PDF (Figure 3.25). Due to the difference in collection temperature, single crystal collection at 100 K and PDF at room temperature, there may be a variation in the bond length between the two models.

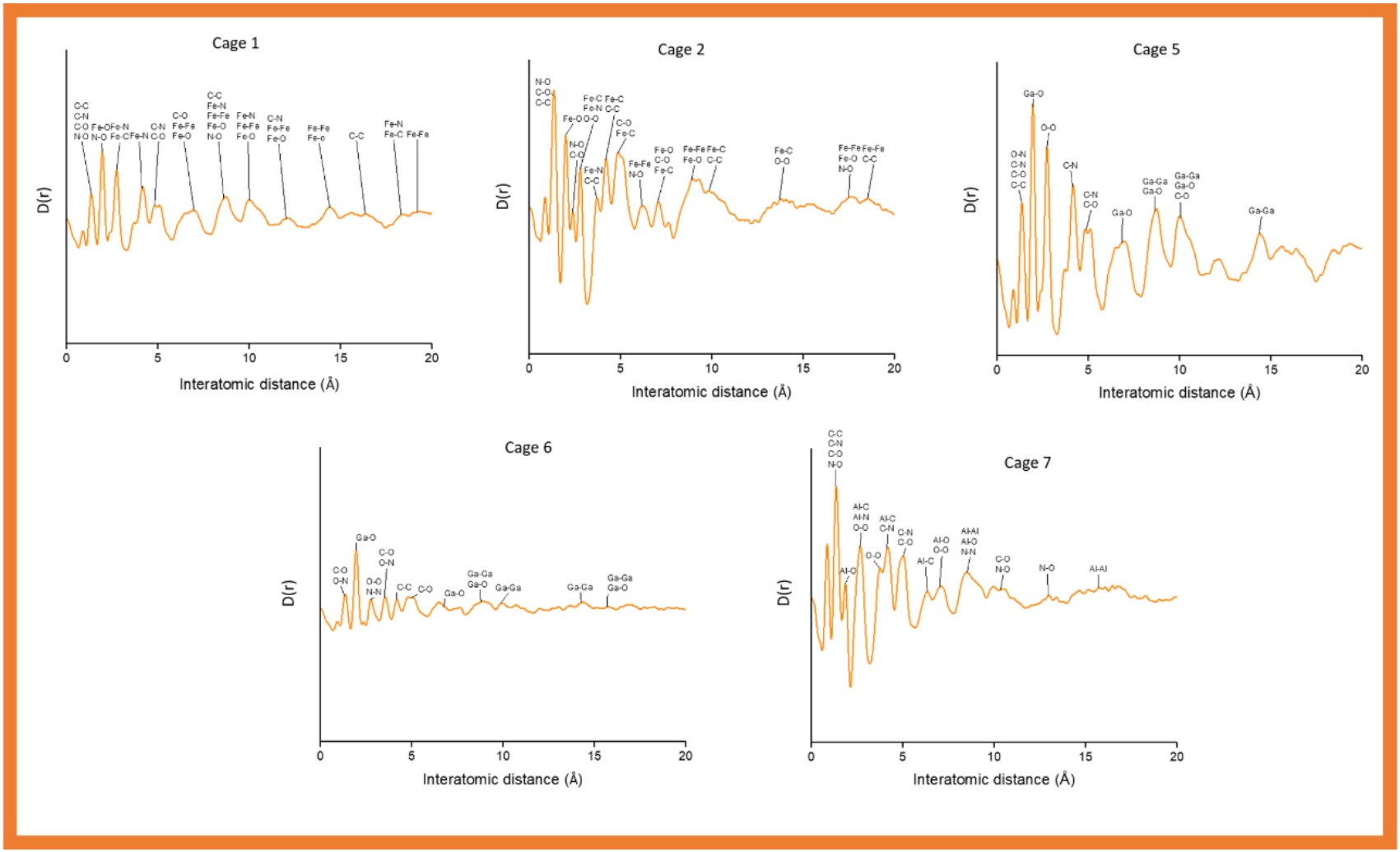

*Figure 3.25 shows the room temperature xPDF patterns of **cages 1, 2, 5, 6** and **7**. Labelled with interatomic distances.*

The designed similarities arising from the ligand and coordination sphere means the only physical bond to vary significantly are the metal-oxygen bonds. From the single crystal model it is possible to determine the interatomic distances of the cage structure, which can be directly compared to the peaks of the PDF. Further to this, PDFGui[42] was used to predict the peak position and pattern for any two atom pairs within the structure, for example, Ga-O or Ga-Ga. Overlaying the predicted pattern with the real data allows for more accurate confirmation of the peak identity. The peaks and troughs of different atoms pairs overlay causing an averaging effect in the peaks. Due to the similarities in many of the bond lengths the peaks in the PDF are related to more than one pair of atoms. The patterns are annotated with selected interatomic bond distances (Figure 3.25). These show good correlation between the peak position and interatomic distance obtained from the single crystal data and PDF data, confirming the single crystal model fits the PDF.

The spectra all display a peak at ~0.9 Å, which so far, has not assigned, it could be an artefact of processing, because at ~0.9 Å the distance is much too short to be a meaningful interaction. During their C_{60} Buckminster fullerene work, Proffen[43] reported that before 7.1 Å the PDF displays sharp peaks due to the intramolecular structure from the C-C pairs. After 7.1 Å, the PDF is broad and featureless; this is due to the intermolecular structure of the ball-ball correlations.[43] At ca. 18 Å, there is a sharp drop in resolution and the PDF becomes significantly broader, this can be contributed to the fact that we have extended beyond the cage and are now looking at the cage packing interactions. From the crystallography the cage diameter was determined to be ca. 18 Å, from this point onwards the majority of interactions would be due to the cage-cage or cage-solvent correlations as reported by Proffen.[43]

The cages also show metal-metal distances, these interactions occur between metals within the cages and from metals of different cages. From the crystallography, is it possible to calculate the average metal-metal distance within the cage, which can be compared directly to the PDF, shown in Table 3.5. The metal-metal distances of the cage can be used to help confirm that the structure of the cage is maintained when crystallinity is lost. The metal-oxygen bonds of the cage could potentially remain unchanged, especially if the octahedral metal coordination sphere is not lost. Due to the strength of the hydroxamate to metal

chelation, it is possible that the metal-oxygen bond is retained even upon cage decomposition. If the cage decomposes it is highly unlikely that the metal-metal distance would be retained; the loss of the strained ligand means the metal centres would not be constrained to their current distance, which is dependent on the ligand. Loss of the ligand would make it likely that the metal-metal distance would be much shorter as structure packs more densely.

Table 3.5 comparing the metal-metal distances from the obtain PDF and single crystal data.

Cage	Crystallographic M-M	PDF M-M
cage 1	8.9247 (13)	8.81
cage 2	8.9683(15)	8.86
cage 5	8.8771(7)	8.74
cage 6	8.8307(8)	8.81
cage 7	8.7958(15)	8.51

3.6.2.2 Variable temperature study

The pXRD data collected on the cage family showed that many of the structures lose crystallinity. This loss of crystallinity is due to the removal of solvent from the framework, be this by removal of the crystals from their mother liquor as is the case for **cage 6**, or by intentional heating of the framework leading to an amorphous phase. The hydrogen-bonded nature of the cage networks means the loss of crystallinity could be due to the loss of long-range order in the packing of the cages. Alternatively, it could be due to cage decomposition. In the case of decomposition both the intrinsic and extrinsic void of the cage would be lost and the material would likely form a non-porous phase. Having seen that the hydroxamic acids in the solution state appear to have poor heat stability, this coupled with the poor mechanical stability of the cages, has to allow for the possibility that the cages themselves decompose when crystallinity is lost, and it is not solely due to the loss of framework order. The formation of an amorphous phase due to the loss of ordered packing is potentially less serious, whilst the structure of the framework would be nearly impossible to determine, it still has the potential to be porous.[82] The intrinsic void of the cage would

be maintained and potentially still accessible for guest species. The loss of Bragg diffraction associated with amorphous compounds means that structural determination through conventional means is not possible. It was hypothesised that PDF could be used to determine the structure of the cage once in an amorphous phase because it is one of few techniques that allows for the structural determination of non-crystalline compounds. Utilising *in-situ* heating studies it was possible to follow the transformation and any phase changes undergone by the cages between 30 and 200 ˚C.

The TGA study confirmed that heating the cages removes the solvent from the network. With the solvent forming an integral part of the network and forming a significant amount of the network hydrogen-bonds. The *in-situ* PDF was collected on **cages 1, 2** and **6**, initially the data is stacked in much the same way as the pXRD data. Generally, there is no change in the pattern; this suggests that the materials are unaffected by the heating process. If there were large structural changes in the compound, differences in interatomic distances would be expected. As discussed earlier, if the cages have decomposed you would expect to see the M-M peaks disappear. If the ligand decomposed there would be no interactions connecting the two metal centres, this in turn would lead to the loss of the metal-metal peak relating to the cage commonly seen around 8 Å. Figure 3.26 show there is no significant difference between the patterns.

The peak at *ca*. 8 Å that relates to the metal-metal distance of the **cages 1** and **6** is still present up to 200 ˚C, this is indicative of the cages not decomposing. This means that the intrinsic pore of the cage is intact and potentially available for guest capture. Due to the stacked nature of the plots the data resolution looks poorer in comparison to the single plots; this is due to the scaling. What can be seen in Figure 3.26 is that as the temperature increases there is a slight increase in the metal-oxygen bond distance, as it is shifted slightly to the right. The data resolution beyond the domain of the cage is not good enough to study the cage packing. The cages could be packed so that the edge of one cage packs into the window of the neighbouring cage, preventing access to the intrinsic void. Alternatively, the cages could be packed window to window allowing for the channels of intrinsic void space to be formed allowing for the formation of a porous phase.

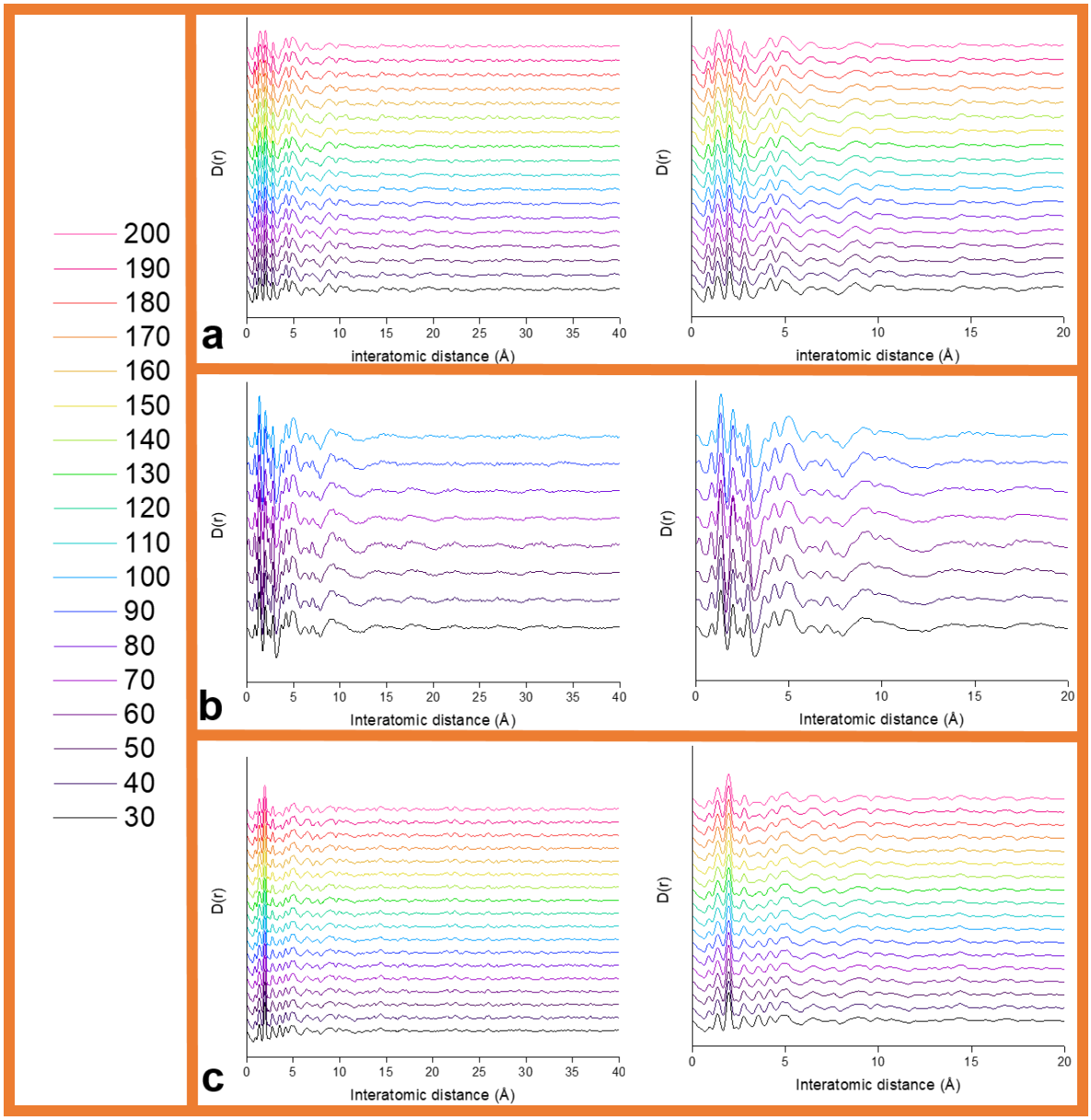

Figure 3.26 shows stacked plot of the VT-PDF study of ***a cage 1, b cage 2*** *and* ***c cage 6****.*

3.7 Host:guest chemistry

3.7.1 Water sorption

Desiccants have been used as dehumidifiers for decades and recently interest has grown in the use of water stable MOFs and molecular materials for low temperature heat transformation applications.[83–86] Thermally driven adsorption chillers (TDCs) and adsorption heat pumps (AHPs) work by cycling the absorbed or desorption of a liquid into a

porous material producing a heating or cooling effect.[83–85] With the rise of global warming leading to increased temperatures, air conditioning use is predicted to increase rapidly the problem with this is the increased electricity consumption associated with it. It is predicted that TDCs and AHPs could be used in place of electricity-expensive air conditioning and refrigerants.[83] With this in mind attempts to understand the cages desiccant, water absorbing properties were conducted.

Environments of known relative humidity (RH) can be produced using slurries of metal salts.[87–89] Three chambers were produced with relative humidities of 9 %, 55 % and 98 %. **Cages 1**, **5** and **7** were tested for their water uptake (Figure 3.27).

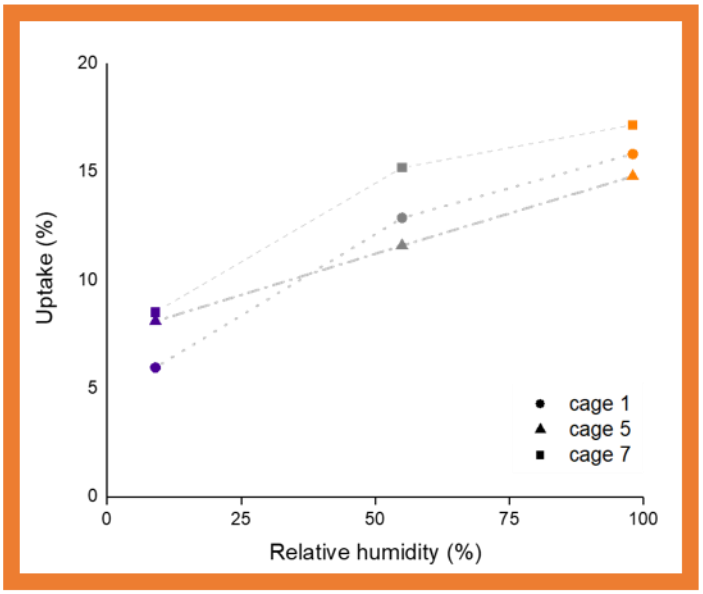

*Figure 3.27 the TGA curves showing water uptake of **cage 1**(circle), **cage 5** (triangle) and **cage 7** (square) at a relative humidity of 9 % (indigo), 55 % (grey) and 98 % (orange).*

Table 3.6 shows the amount of water absorbed per cage at 9 %, 55 % and 98 % RH. The results show that water uptake increases in line with RH. **Cage 7** has the largest solvent accessible void space of 56.5 % and also shows the largest % uptake of water across all three RH's. When looking at the number of water molecules absorbed per cage, **cage 5** (solvent accessible void space 56%) is the most effective at RH 9 % showing an additional 2 % uptake, which is equivalent to three times as many water molecules, compared to **cage 1** (solvent accessible void space of 54 %). **Cage 1** contained more DMF and less water in its original

solvate form than seen in **cages 5** and **7**. **Cage 1** originally showed nine solvent of crystallisation molecules, two of which were water. This means that across all humidities it absorbed more water than was originally present and at a RH of 55 % it is more solvated than shown by the original DMF:water phase. The mass loss of the water molecules per cage for **cages 5** and **7** at RH of 55 % and 98 % are equivalent to the original (DMF and water) solvent of crystallisation mass loss. In the original DMF:water solvate 23 solvent of crystallisation molecules were present in **cage 5** and 19 molecules in **cage 7.** This indicates that the materials have reached saturation point and cannot absorb more guest species.

Table 3.6 shows the number of absorbed water molecules per cage during the RH experiments.

Relative humidity	**Cage 1** (water molecules per cage)	**Cage 5** (water molecules per cage)	**Cage 7** (water molecules per cage)
9%	5.6	18.7	15.2
55%	10.5	21.4	22.6
98%	12.5	22.6	22.7

In summary, the materials can be desolvated, removing the solvent of crystallisation. Once desolvated the materials will reabsorb water across a range of relative humidities. **Cages 5** and **7**, show an improved water sorption capacity per cage when compared to **cage 1**. To further understand the host:guest chemistry of the cages CO_2 isotherms of **cages 1** and **2** were also obtained.

3.7.2 CO_2 sorption

Work published by Sholl and Lively[90] stated that separations and distillations account for 10-15 % of the world's energy consumption. Membrane-based separations would use 90 % less energy than distillations.[90] It was proposed that by making American petroleum and chemical separations more efficient, it could prevent a hundred million tonnes of CO_2 emissions a year, whilst saving $4 billion dollars a year.[90] The cages with their two types of void space make them ideal candidates, for the separations of CO_2. The small hydrophobic

intrinsic void should allow the linear CO_2 molecule to enter the intrinsic pore separating it from other components in the gas stream by size or electrostatics (dipole moment).

Figure 3.28 shows that at a pressure of 750 Torr (one barr) **cage 1** absorbs 0.95 mmol/g of CO_2, this is equal to 0.69 CO_2 molecules per **cage 1**. **Cage 1** absorbs more CO_2 than **cage 2**, which absorbs 0.26 mmol/g or 0.18 CO_2 molecules per **cage 2**.

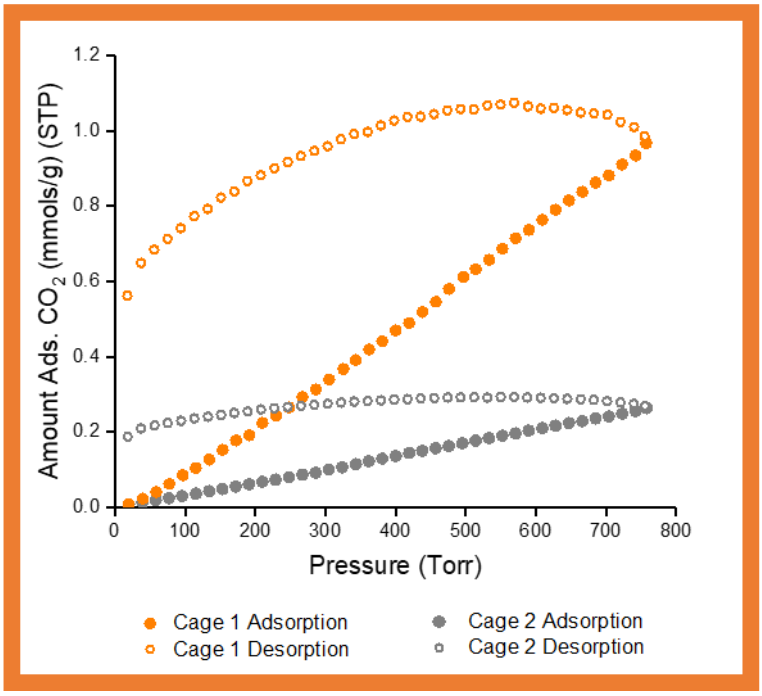

*Figure 3.28 showing the CO_2 adsorption and desorption isotherms for **cages 1** and **2**.*

Cages 1 and **2** do not show full desorption of CO_2 at a pressure of 20 Torr (26 mbarr) 0.56 mmol/g or 0.40 molecules of CO_2 per **cage 1** are still present in the sample. For **Cage 2** 0.19 mmol/g or 0.13 molecules per **cage 2** are retained. This indicates that once the CO_2 molecules have been absorbed they are bound relatively strongly to the cages; this may prove to be a useful feature if the materials were to be used for CO_2 storage.

In summary, the M_4L_6 tetrahedra are capable of absorbing water and CO_2. The cages show an increased capacity for water sorption compared to CO_2. Once absorbed the CO_2 appears to bind relatively strongly to the cages and is not fully desorbed at pressures of 20 Torr. The number of absorbed water molecules is typically better than or in line with the number of molecules seen within the original DMF:water solvate.

3.8 Conclusions and future work

This Chapter has discussed the solid and solution state structure and properties of a family of neutral M_4L_6 tetrahedra, incorporating ditopic hydroxamic acids and Fe^{3+}, Ga^{3+} Al^{3+} and In^{3+} metals. Materials crystallised out as the racemic T-type cages, with the same basic ligand geometry retained, this ensured the intrinsic pore was comparable between cages. By incorporating additional functionality on the outside of the cage at the five position of the phenyl ring, has allowed for crystal engineering of the extrinsic pore of the cage. The increased number of directional hydrogen-bonds has allowed us to design more extrinsically porous materials. Channels of porosity can be seen within all the crystal structures, typically the larger extrinsic pores, which were initially filled with solvent molecules. By studying and understanding their desorption properties, the materials produced are capable of absorbing water and CO_2. The desiccant properties of these materials require further work to fully understand their true applications. With further host:guest work the intrinsic pore can potentially be used to separated small molecules based on size or chemistry. Computational work can be conducted to understand the most suitable small molecule guests for the cage.

The amorphous nature of the desolvated crystals raised questions about the cages that conventional crystallography could not answer. By using xPDF the local structure of the [M_4hydroxamate$_6$] molecular cage has been confirmed. Using small box modelling program PDFGui,[42] and the crystallographic models obtained from the single crystal data, good correlation was seen between the predicted and actual interatomic distances. The PDF data confirms the cage diameter by showing a large drop in data resolution past *ca.* 18 Å, the cage diameter. Using VT-PDF it was possible to study the desolvation of the molecular cages and determine that the loss of cage crystallinity was due to the loss of long range order between the cages and not down to the decomposition of the cage. The data resolution is not good enough to study the cage packing, so how the cages pack in their non-crystalline phase is not yet determined.

By understanding the axial chirality of the ligand, it may be possible to make the crystallisation more predictable and controlled by designing ligands that can influence the

chirality of metal centre, preventing the dynamics seen in the solution state. Further to this, incorporation of a chiral functionality off nitrogen position may allow for further ligand control allowing only one ligand to be produced; if this were the case both the cages and there packing would be chiral. Potentially opening up a world of applications, including chiral separations.

This study has successfully crystal engineered a family of porous molecular cages to have an increased extrinsic pore. It is possible to control their structure and work has started to understand their potential as desiccants and for the separation of small molecules. The neutral tetrahedra formed display a small intrinsic pore limiting its potential application, the next step of this project is to develop cages with a larger intrinsic pore space, and this can potentially be combined with the control of the ligands axial chirality, producing large chirally pure cages suitable for catalysis and the separation of large or chiral guest species.

3.9 References

1 D. H. Leung, R. G. Bergman and K. N. Raymond, *J. Am. Chem. Soc.*, 2007, **129**, 2746–2747.

2 C. J. Hastings, M. D. Pluth, R. G. Bergman and K. N. Raymond, *J. Am. Chem. Soc.*, 2010, **132**, 6938–6940.

3 Z. J. Wang, C. J. Brown, R. G. Bergman, K. N. Raymond and F. D. Toste, *J. Am. Chem. Soc.*, 2011, **133**, 7358–7360.

4 T. K. Ronson, S. Zarra, S. P. Black and J. R. Nitschke, *Chem. Commun.*, 2013, **49**, 2476–2490.

5 N. Ahmad, H. A. Younus, A. H. Chughtai and F. Verpoort, *Chem. Soc. Rev.*, 2015, **44**, 9–25.

6 F. Kaiser, A. Schmidt, W. Heydenreuter, P. J. Altmann, A. Casini, S. A. Sieber and F. E. Kühn, *Eur. J. Inorg. Chem.*, 2016, **2016**, 5189–5196.

7 D. X. Zhang, H. X. Zhang, H. Y. Li, T. Wen and J. Zhang, *Cryst. Growth Des.*, 2015, **15**, 2433–2436.

8 H. N. Wang, X. Meng, G. S. Yang, X. L. Wang, K. Z. Shao, Z. M. Su and C. G. Wang, *Chem. Commun.*, 2011, **47**, 7128–7130.

9 E. V. Perez, K. J. Balkus, J. P. Ferraris and I. H. Musselman, *J. Memb. Sci.*, 2014, **463**, 82–93.

10 J. D. Crowley, D. Preston, R. A. S. Vasdev, K. F. White, J. E. M. Lewis and B. F. Abrahams, *Chem. - A Eur. J.*, 2017, **23**, 10559–10567.

11 M. Mastalerz, *Chem. - A Eur. J.*, 2012, **18**, 10082–10091.

12 H. R. Green and G. O. Lloyd, in *Chapter 9. Porous Metal Organic Polygons and Polyhedra - Intrinsic vs. Extrinsic Porosity in Functional Supramolecular Materials : From Surfaces to MOFs*, ed. R. Banerjee, The Royal Society of Chemistry, Cambridge, 1st edn., 2017, pp. 297–324.

13 Q. F. Sun, S. Sato and M. Fujita, *Nature Chem.*, 2012, **4**, 330–333.

14 Y. Fang, T. Murase, S. Sato and M. Fujita, *J. Am. Chem. Soc.*, 2013, **135**, 613–615.

15 Y. Inokuma, M. Kawano and M. Fujita, *Nature Chem.*, 2011, **3**, 349–358.

16 P. Mal, B. Breiner, K. Rissanen and J. R. Nitschke, *Science*, 2009, **324**, 1697–1699.

17 T. K. Ronson, W. Meng and J. R. Nitschke, *J. Am. Chem. Soc.*, 2017, **139**, 9698–9707.

18 T. K. Ronson, C. Giri, N. Kodiah Beyeh, A. Minkkinen, F. Topić, J. J. Holstein, K. Rissanen and J. R. Nitschke, *Chem. - A Eur. J.*, 2013, **19**, 3374–3382.

19 A. V. Davis, D. Fiedler, G. Seeber, A. Zahl, R. Van Eldik and K. N. Raymond, *J. Am. Chem. Soc.*, 2006, **128**, 1324–1333.

20 D. L. Caulder and K. N. Raymond, *J. Chem. Soc. Dalt. Trans.*, 1999, 1185–1200.

21 S. M. Jansze, G. Cecot, M. D. Wise, K. O. Zhurov, T. K. Ronson, A. M. Castilla, A. Finelli, P. Pattison, E. Solari, R. Scopelliti, G. E. Zelinskii, A. V. Vologzhanina, Y. Z. Voloshin, J. R. Nitschke and K. Severin, *J. Am. Chem. Soc.*, 2016, **138**, 2046–2054.

22 S. Ma, M. M. J. Smulders, Y. R. Hristova, J. K. Clegg, T. K. Ronson, S. Zarra and J. R.

Nitschke, *J. Am. Chem. Soc.*, 2013, **135**, 5678–5684.

23 Y. Bai, D. Guo, C. Y. Duan, D. Bin Dang, K. L. Pang and Q. J. Meng, *Chem. Commun.*, 2004, 186–187.

24 T. Beissel, R. E. Powers, T. N. Parac and K. N. Raymond, *J. Am. Chem. Soc.*, 1999, **121**, 4200–4206.

25 T. Beissel, R. E. Powers and K. N. Raymond, *Angew. Chem. Int. Ed. Engl.*, 1996, **35**, 1084–1085.

26 E. Takeshi and S. J. L. Billinge, in *Underneath the Bragg Peaks, Structural Analysis of Complex Materials*, Pergamon Materials Series, Oxford, 2012, vol. 16, pp. 1–25.

27 E. Takeshi and S. J. L. Billinge, in *Underneath the Bragg Peaks, Structural Analysis of Complex Materials*, Pergamon Materials Series, Oxford, 2012, vol. 16, pp. 455–465.

28 Z. H. Stachurski, *Materials*, 2011, **4**, 1564–1598.

29 E. Takeshi and S. J. L. Billinge, in *Underneath the Bragg Peaks, Structural Analysis of Complex Materials*, Pergamon Materials Series, Oxford, 2012, vol. 16, pp. 27–54.

30 E. Takeshi and S. J. L. Billinge, in *Underneath the Bragg Peaks, Structural Analysis of Complex Materials*, Pergamon Materials Series, Oxford, 2012, vol. 16, pp. 55–111.

31 E. Takeshi and S. J. L. Billinge, in *Underneath the Bragg Peaks, Structural Analysis of Complex Materials*, Pergamon Materials Series, Oxford, 2012, vol. 16, pp. 159–257.

32 R. A. Young, Ed., *The Rietveld Method*, Oxford University Press, New York, 1989.

33 R. Jenkins and R. L. Snyder, *Introduction to X-ray Powder Diffractometry*, John Wiley & Sons, New York, 1996.

34 P. M. Ossi, *Disordered Materials*, Springer, New York, 2006.

35 E. Takeshi and S. J. L. Billinge, in *Underneath the Bragg Peaks, Structural Analysis of Complex Materials*, Pergamon Materials Series, Oxford, 2012, vol. 16, pp. 407–439.

36 D. A. Keen, M. R. Ibberson, P. Day, E. J. Enderby, S. Kycia and S. J. L. Billinge, *J. Appl.*

Crystallogr., 2001, **34**, 172–177.

37 B. H. Toby and T. Egami, *Acta Crystallogr. Sect. A*, 1992, **48**, 336–346.

38 E. Takeshi and S. J. L. Billinge, in *Underneath the Bragg Peaks, Structural Analysis of Complex Materials*, Pergamon Materials Series, Oxford, 2012, vol. 16, pp. 259–295.

39 X. Qiu, E. S. Božin, P. Juhas, T. Proffen and S. J. L. Billinge, *J. Appl. Crystallogr.*, 2004, **37**, 110–116.

40 S. J. L. Billinge, *Z. Krist.*, 2004, **219**, 117–121.

41 T. E. Gorelik, M. U. Schmidt, U. Kolb and S. J. L. Billinge, *Microsc. Microanal.*, 2015, **21**, 459–471.

42 C. L. Farrow, P. Juhas, J. W. Liu, D. Bryndin, E. S. Božin, J. Bloch, T. Proffen and S. J. L. Billinge, *J. Phys. Condens. Matter*, 2007, **19**, 335219.

43 T. Proffen, S. J. L. Billinge, T. Egami and D. Louca, *Z. Krist.*, 2003, **218**, 132–143.

44 E. Takeshi and S. J. L. Billinge, in *Underneath the Bragg Peaks, Structural Analysis of Complex Materials*, Pergamon Materials Series, Oxford, 2012, vol. 16, pp. 113–158.

45 E. Takeshi and S. J. L. Billinge, in *Underneath the Bragg Peaks, Structural Analysis of Complex Materials*, Pergamon Materials Series, Oxford, 2012, vol. 16, pp. 325–369.

46 T. D. Bennett, A. L. Goodwin, M. T. Dove, D. A. Keen, M. G. Tucker, E. R. Barney, A. K. Soper, E. G. Bithell, J. C. Tan and A. K. Cheetham, *PhysRevLetts*, 2010, **104**, 115503.

47 T. D. Bennett and A. K. Cheetham, *Acc. Chem. Res.*, 2014, **47**, 1555–1562.

48 T. Proffen, K. L. Page, S. E. McLain, B. I. Clausen, T. W. Darling, J. A. TenCate, S. Y. I. Lee and E. V Ustundag, *Z. Krist.*, 2005, **220**, 1002–1008.

49 T. D. Bennett, A. L. Goodwin, M. T. Dove, D. A. Keen, M. G. Tucker, E. R. Barney, A. K. Soper, E. G. Bithell, J.-C. Tan and A. K. Cheetham, *PhysRevLetts*, 2010, **104**, 115503.

50 E. Takeshi and S. J. L. Billinge, in *Underneath the Bragg Peaks, Structural Analysis of Complex Materials*, Pergamon Materials Series, Oxford, 2012, vol. 16, pp. 371–405.

51 T. D. Bennett, Y. Yue, P. Li, A. Qiao, H. Tao, N. G. Greaves, T. Richards, G. I. Lampronti, S. A. T. Redfern, F. Blanc, O. K. Farha, J. T. Hupp, A. K. Cheetham and D. A. Keen, *J. Am. Chem. Soc.*, 2016, **138**, 3484–3492.

52 C. E. White, J. L. Provis, B. Bloomer, N. J. Henson, K. Page, J. Bloch, T. Proffen, S. J. L. Billinge, A. Llobet and J. S. J. van Deventer, *Phys. Chem. Chem. Phys.*, 2013, **15**, 8573.

53 A. E. Morandeau, C. E. White, J. Feng, B. L. Phillips, L. Ehm, C. Tarabrella, J. B. Parise, R. J. Reeder and J. J. D. Yoreo, *J. Mater. Chem. A*, 2015, **3**, 8597–8605.

54 C. J. Benmore and P. J. M. Monteiro, *Cem. Concr. Res.*, 2010, **40**, 892–897.

55 S. J. L. Billinge, T. Dykhne, P. Juhás, E. Božin, R. Taylor, A. J. Florence and K. Shankland, *CrystEngComm*, 2010, **12**, 1366–1368.

56 D. Saha, K. M. Ø. Jensen, C. Tyrsted, E. D. Bøjesen, A. H. Mamakhel, A. C. Dippel, M. Christensen and B. B. Iversen, *Angew. Chem. Int. Ed.*, 2014, **53**, 3667–3670.

57 J. L. Mi, K. M. Ø. Jensen, C. Tyrsted, M. Bremholm, B. B. Iversen, L. Sø, B. B. Iversen, S. J. L. Billinge, E. Lægsgaard, I. Stensgaard, B. Hammer and F. Besenbacher, *CrystEngComm*, 2015, **17**, 6868–6877.

58 T. D. Bennett and A. K. Cheetham, *Acc. Chem. Res.*, 2014, 47, 1555–1562.

59 K. M. Ø. Jensen, H. L. Andersen, C. Tyrsted, E. D. Bøjesen, A. C. Dippel, N. Lock, S. J. L. Billinge, B. B. Iversen and M. Christensen, *ACS Nano*, 2014, **8**, 10704–10714.

60 V. A. Burnell, J. E. Readman, C. C. Tang, J. E. Parker, S. P. Thompson and J. A. Hriljac, *J. Solid State Chem.*, 2010, **183**, 2196–2204.

61 J. E. Readman, P. M. Forster, K. W. Chapman, P. J. Chupas, J. B. Parise and J. A. Hriljac, *Chem. Comm.*, 2009, **2**, 3383–3385.

62 M. D. Moore, A. M. Steinbach, I. S. Buckner and P. L. D. Wildfong, *Pharm. Res.*, 2009, **26**, 2429–2437.

63 Y. Nguyen Thi, K. Rademann and F. Emmerling, *CrystEngComm*, 2015, **17**, 9029–9036.

64 M. W. Terban, E. Y. Cheung, P. Krolikowski and S. J. L. Billinge, *Cryst. Growth Des.*,

2016, **16**, 210–220.

65 E. Takeshi and S. J. L. Billinge, in *Underneath the Bragg Peaks, Structural Analysis of Complex Materials*, Pergamon Materials Series, Oxford, 2012, vol. 16, pp. 441–453.

66 S. J. L. Billinge, *Nanomedicine*, 2015, **10**, 2473–2475.

67 L. Chen, P. S. Reiss, S. Y. Chong, D. Holden, K. E. Jelfs, T. Hasell, M. A. Little, A. Kewley, M. E. Briggs, A. Stephenson, K. M. Thomas, J. A. Armstrong, J. Bell, J. Busto, R. Noel, J. Liu, D. M. Strachan, P. K. Thallapally and A. I. Cooper, *Nat. Mater.*, 2014, **13**, 954–960.

68 N. J. Young and B. P. Hay, *Chem. Commun.*, 2013, **49**, 1354–1379.

69 D. Seebach, A. K. Beck and A. Heckel, *Angew. Chem. Int. Ed.*, 2001, **40**, 92–138.

70 D. L. Caulder and K. N. Raymond, *J. Chem. Soc. Dalt. Trans.*, 1999, **0**, 1185–1200.

71 H. S. Rzepa and M. E. Cass, *Inorg. Chem.*, 2007, **46**, 451–457.

72 R. S. Cahn, C. Ingold and V. Prelog, *Angew. Chem. Int. Ed. Engl.*, 1966, **5**, 385–415.

73 R. D. Shannon, *Acta Crystallogr. Sect. A*, 1976, **32**, 751–767.

74 S. Mecozzi and J. . J. Rebek, *Chem. - A Eur. J.*, 1998, **4**, 1016–1022.

75 M. C. Etter, J. C. MacDonald and J. Bernstein, *Acta Crystallogr. Sect. B*, 1990, **46**, 256–262.

76 A. G. Slater, M. A. Little, A. Pulido, S. Y. Chong, D. Holden, L. Chen, C. Morgan, X. Wu, G. Cheng, R. Clowes, M. E. Briggs, T. Hasell, K. E. Jelfs, G. M. Day and A. I. Cooper, *Nature Chem.*, 2016, **9**, 1–9.

77 T. Hasell, X. Wu, J. T. A. Jones, J. Bacsa, A. Steiner, T. Mitra, A. Trewin, D. J. Adams and A. I. Cooper, *Nature Chem.*, 2010, **2**, 750–755.

78 D. J. Tranchemontagne, J. R. Hunt and O. M. Yaghi, *Tetrahedron*, 2008, **64**, 8553–8557.

79 J. E. Mondloch, O. Karagiaridi, O. K. Farha and J. T. Hupp, *CrystEngComm*, 2013, **15**,

9258.

80 A. P. Nelson, O. K. Farha, K. L. Mulfort and J. T. Hupp, *J. Am. Chem. Soc.*, 2009, **131**, 458–460.

81 Z.-R. Tang, S. a. Kondrat, C. Dickinson, J. K. Bartley, a. F. Carley, S. H. Taylor, T. E. Davies, M. Allix, M. J. Rosseinsky, J. B. Claridge, Z. Xu, S. Romani, M. J. Crudace and G. J. Hutchings, *Catal. Sci. Technol.*, 2011, **1**, 740.

82 J. Tian, P. K. Thallapally and B. P. McGrail, *CrystEngComm*, 2012, **14**, 1909–1919.

83 C. Janiak and S. K. Henninger, *Chimia.*, 2013, **67**, 419–424.

84 F. Jeremias, V. Lozan, S. K. Henninger and C. Janiak, *Dalton Trans.*, 2013, **42**, 15967.

85 F. Jeremias, D. Fröhlich, C. Janiak and S. K. Henninger, *New J. Chem.*, 2014, **38**, 1846–1852.

86 A. Khutia, H. U. Rammelberg, T. Schmidt, S. Henninger and C. Janiak, *Chem. Mater.*, 2013, **25**, 790–798.

87 A. Wexler and S. Hasegawa, *J. Res. Natl. Bur. Stand.*, 1954, **53**, 19–26.

88 L. Greenspan, *J. Res. Natl. Bur. Stand. Sect. A Phys. Chem.*, 1977, **81A**, 89–96.

89 J. Young, *J. Appl. Chem.*, 1967, **17**, 241–245.

90 D. S. Sholl and R. P. Lively, *Nature*, 2016, **532**, 435–437.

Chapter 4 – Co-ordination Polymers

"You must not let anyone define your limits because of where you come from. Your only limit is your soul." Ratatouille

Foreword

Void space diagrams were created in Mercury where the inside of the void is coloured orange, the outside is coloured grey. All other images were produced in X-Seed using CPK colours unless stated otherwise. The CoI_2 coordination polymer was grown by José Miguel Luque Alled. Gas sorption data was collected at the University of Glasgow by Dr Ross Forgan and Dr Pantelis Xydias.

4.0 Introduction

Materials with porosity typically can be classified as either extrinsic or intrinsic, but rarely both.[1–3] Intrinsic porosity is seen within the molecule, for example, the void space within the macrocycle is an intrinsic void.[2] Extrinsic porosity is that found between the molecules.[4–6] Materials displaying both intrinsic and extrinsic porosity have become more common since the rise of the molecular cage.[1,2,7,8] Once intrinsic or extrinsic porosity has been determined the void space can also be further viewed as continuous or discrete. Continuous is where the voids are connected to form channels that can potentially allow for solvent and other guest species to freely move throughout the system[9] and discrete is where the voids are not connected.[10,11] Discrete voids are typically non-porous, but in some special cases they do allow for porosity.[3] Guest inclusion within discrete voids can occur through single-crystal-to-single-crystal tranformations, where the host structure deforms allowing for the guest to be included.[3,9,11]

The dipyridyldiamide ligand, **ligand 1** (Figure 4.1a), has previously been reported to produce a range of porous macrocycles, supramolecular isomers and coordination polymers (CPs).[12–

[15] A macrocycle (Figure 4.1b) is defined by IUPAC as a "cyclic macromolecule or a macromolecular cyclic portion of a molecule."[16,17] The IUPAC definition of a coordination polymer (Figure 4.1c) is “a coordination compound with repeating coordination entities extending in 1, 2 or 3 dimensions.”[16,18,19] Supramolecular isomers comprise network structures that have identical chemical compositions but differ from one another in their structure.[15,20] The literature on this ligand shows the formation of a series of materials, dependent upon the guest species (organic solvent) used.[13] These materials show a vast array of intrinsic, extrinsic, discrete and continuous porosity.[12–14,21] These materials can be viewed as β phases as discussed in chapter 1.0, Figure 1.1.[2,22]

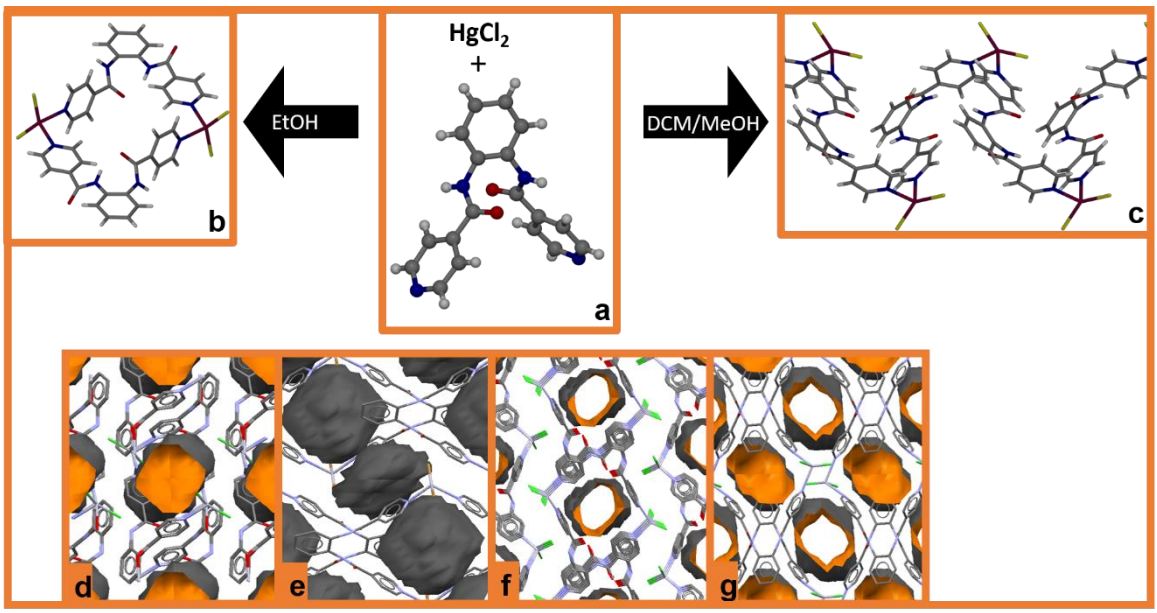

*Figure 4.1 **a** shows a ball and stick diagram of **ligand 1** (BAXNIY). **b** shows a capped stick example of the 2x2 $HgCl_2$ macrocycle (KATGET) and **c** shows the capped stick 1D $HgCl_2$ coordination polymer (KATGUJ). Where Hg is shown in burgundy, chlorine in yellow and CPK used for all other atoms. Figures **d-g** shows the variance in void spaces shown between some of the complexes formed by **ligand 1**. **d** (XAHRUU) shows a discrete void located at the centre of each macrocycle. **e** (XAHSAB) shows discrete voids at both the intrinsic and extrinsic space. **f** shows channels of continuous intrinsic porosity (KATGET). **g** shows the discrete intrinsic void and the continuous channel of the extrinsic void space (XAHROO).*

Previously reported literature includes Puddephatt and co-workers paper on **ligand 1** with mercury (II), halides (HgX_2) forming 2x2 macrocycles (2 metal atoms to two ligands).[13] The

mercury centre is found to be '*roughly tetrahedral*' [13] with each macrocycle containing an intrinsic void at its centre. Puddephatt used tetrahydrofuran (THF) as the solvent of crystallisation forming an 'isostrucural' series of $HgCl_2$, $HgBr_2$ and HgI_2 2x2 macrocycles. The crystal structures of the three β phase materials shows that there are two discrete void spaces; the intrinsic pore of the macrocycle and the second is the extrinsic void space located between the macrocycles.[13] A disordered THF guest molecule can be located in both the intrinsic and extrinsic pores of all three materials. By computationally removing the solvent from the crystal structure and assuming that the βo phase is retained after solvation, further analysis on the structures. It was established that the voids and the packing of the $HgCl_2$ structure are different to that of the $HgBr_2$ and HgI_2 (Figure 4.2). The $HgBr_2$ and HgI_2 structures are isostructural, whilst the $HgCl_2$ is a supramolecular isomer, showing a different structure and packing (Figure 4.2).

The Br and I structure show two discrete void spaces; one located at the intrinsic pore and one located at the extrinsic pore. Meanwhile the Cl structure shows a continuous channel at the extrinsic pore and a discrete intrinsic pore. Puddephatt noted that by varying the solvent of crystallisation, from THF to 1,2-dichloroethane, a different crystal form was obtained for the $HgCl_2$ macrocycle. This time with a discrete void located at the centre of each macrocycle (Figure 4.2).[13] This supports the view that the solvent inclusion determines the macrocyclic structure.[13] These inclusion compounds can be viewed as β phases, removal of the included solvent may therefore result in the formation of the βo phase or form an α phase. These phases may show different host:guest properties.[2,22]

Lloyd and co-workers also produced different β phases of 2x2 macrocycles.[12] This time focusing on HgX_2, $CoCl_2$ and $ZnCl_2$ crystallised from ethanol and methanol, this gave rise to 2X2 macrocycles but with a different packing (supramolecular isomers). This time the macrocycles were found to stack in such a way that the intrinsic pores formed continuous channels through the crystal and no extrinsic pores were formed.

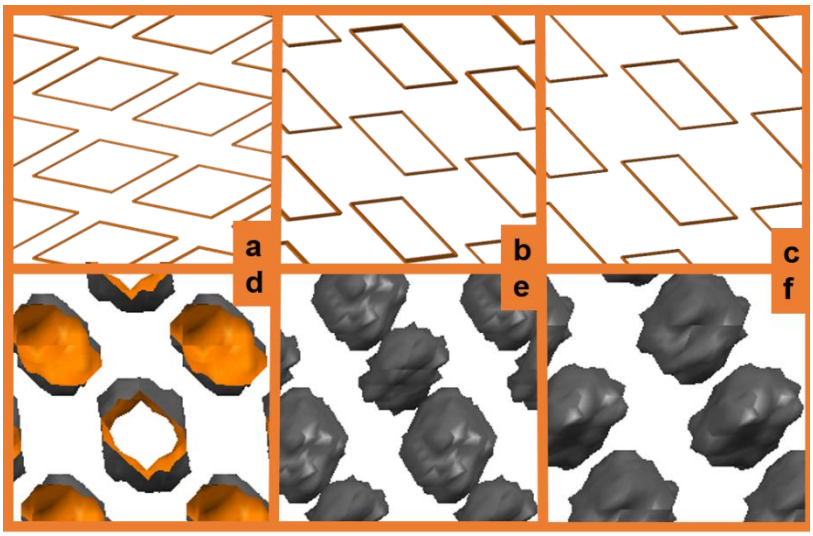

Figure 4.2 shows the variation in the packing of the HgX_2 macrocycles, ***a,d*** *show $HgCl_2$,* ***b,e*** *show $HgBr_2$ and* ***c,f*** *show HgI_2.* Images **a**-**c** *are shown down the b axis where the macrocycle has been produced by creating a centroid at the centre of the phenyl ring which is then bonded to the metal centre showing the macrocycle as a quadrilateral. The packing of the Cl macrocycle is not isostructural to the Br and I species. Images* ***d-f*** *are all viewed down the a axis, they show the void space in the crystal structure, which in the case of the Cl structure the extrinsic void is a channel and the intrinsic pore a discrete void, compared to discrete voids for both intrinsic and extrinsic pores of the Br and I structures.*

$HgBr_2$ crystallised from methanol was found to produce a 4x4 macrocycle that displays discrete intrinsic voids, that are larger than those seen in the HgX_2 2x2 macrocycle.[12] Lloyd and co-workers report that a DCM:methanol mixture causes the formation of a 1D CP with $HgCl_2$.[12,23] They also report that the macrocycles are capable of guest uptake, guests include I_2, CO_2 and CS_2.[12] After desolvating the macrocycles and producing the βo phase, a new guest species is introduced forming the δ phase.[2] From these examples, the porosity within these materials is rich and varied when crystallised from solution (Figure 4.1). The macrocycles highlight the fact that the included solvent within controls the porosity, both in terms of discrete or continuous, and as to whether the phenomena of both intrinsic and extrinsic porosity is experienced within the same material (Figure 4.1).

Porous materials such as MOFs and macrocycles are conventionally synthesised via solution state synthesis, this makes large scale synthesis of the compounds difficult.[24] One potential way around this is the use of mechanochemistry. Mechanochemistry is the means of

conducting chemical reactions using grinding or extrusion; reducing the amount of solvent and time required.[25,26] The benefits of mechanochemistry includes making the synthesis route scalable and environmentally friendly in conjunction with being atom and energy efficient.[25] Mechanochemical synthesis of porous materials allows the user to avoid thermally sensitive, toxic and often expensive organic solvents.[27,28] Safer and less expensive precursors such as metal sulphates and oxides can also be employed because their poor solubility in solvent is no longer a factor in mechanochemical synthesis.[25]

In 2016, the first commercial use for MOFs was established.[29] Ethylene is essential for the ripening of fruit and vegetables, however, its presence is detrimental to the storage and transport of the fresh produce.[29–31] Ethylene allows the continuation of ripening, potentially leading to over-ripened goods. By removing the ethylene, the fruit cannot continue to ripen at the same rate allowing for prolonged shelf life. The MOF, synthesised via mechanochemistry, contains 1-methylcyclopropene: which is a used commercially to slow the ripening of fruit.[32,33] The 1-methylcyclopropene, acts as a competitive inhibitor, binding tightly to the ethylene receptor in the plant thus preventing the ethylene from ripening the fruit.[32,33] Due to its mechanochemical synthesis, the MOF is produced rapidly and in high quantity with very little solvent present.[29,30] This example shows that mechanochemistry is extremely useful in the production of bulk samples.

Mechanochemistry has proven itself extremely useful for the bulk synthesis of porous materials such as MOFs.[25,28,34,35] The complexes of **ligand 1** provides an interesting study for mechanochemical bulk synthesis, due to the dynamic self-assembly of the ligand with metals, the varied topologies of the materials produced and the difficulty of producing bulk sample from the solution state.[12,13] The solvent of crystallisation plays a large role in the structure and porosity of the materials obtained from the solution state.[12,13] The ultimate aim was to understand how the mechanochemical synthesis affects the structure and properties of the compounds, in comparison to the conventional solution state synthesis.

Herein the formation of a series of metal nitrate-containing complexes incorporating **ligand 1** from solution state synthesis is reported. Also studied was how the method of synthesis

affects the material properties of the compounds. Mechanochemical synthesis was used for the bulk preparation of the transition metal halide macrocycles ($CoCl_2$/$ZnCl_2$).

4.1 Results and Discussion

Many structures have been reported based around **ligand 1**, whose synthesis has been previously reported.[12,13] In the last decade, the ligand has given rise to discrete 2x2 and 4x4 macrocycles, supramolecular isomers and 1D CPs.[12,13,21] What links these materials is their porosity; these materials can be referred to as porosity topological isomers. The materials always show intrinsic porosity but by varying the topology, the intrinsic pores can be connected together in a variety of ways and it is also possible to create extrinsic porosity in the materials.

4.1.1 Solution state synthesis

A variety of metal halides have been reported to produce macrocycles and CPs, however, there is no data on the use of other metal salts such as metal nitrates.[12–14,21,23] Using solution state synthesis to further probe the crystallisation landscape of these compounds, three CP with octahedral coordination spheres and 2:1 ligand:metal ratios were produced. These materials differ from the previously reported 1D CP [12] which showed a 1:1 ligand to metal ratio and tetrahedrally coordinated metal.

Crystallising $Co(NO_3)_2$ with **ligand 1** from ethanol produces a 2D coordination polymer with an octahedral cobalt coordination sphere (Figure 4.3). This structure will be referred to as **CP1** ($[Co(H_2O)_2\text{-}(\mu\text{-}C_{18}H_{14}N_4O_2)_2]_n$, where μ denotes a bridging ligand between the metal centres).[36] The Cd metal centre is coordinated to four pyridyl functionalities at the equatorial positions and two water molecules coordinated to the apical positions. The chains of **ligand 1** and metal form a 2D CP through the symmetry elements (2_1 screw axis down the [1 0 0] and the C glide) of the C_2/c space group. As seen with the other reported 1D CP there is no ligand based intramolecular hydrogen-bond.[12] Instead a *C17* intermolecular hydrogen-bond between the amide nitrogen and the oxygen of the carbonyl of the neighbouring molecule occurs. This interaction occurs twice; once between (N5···O3=

2.966 (4) Å, *C17* these can combine to form a second network $R_2^2(14)$). The same interactions occur between N6···O3 = 2.955 (4) Å, *C17*, $R_2^2(14)$. The CP forms types of discrete void spaces where the disordered charge balancing nitrate anion can be located, hydrogen-bonded to the apical waters.

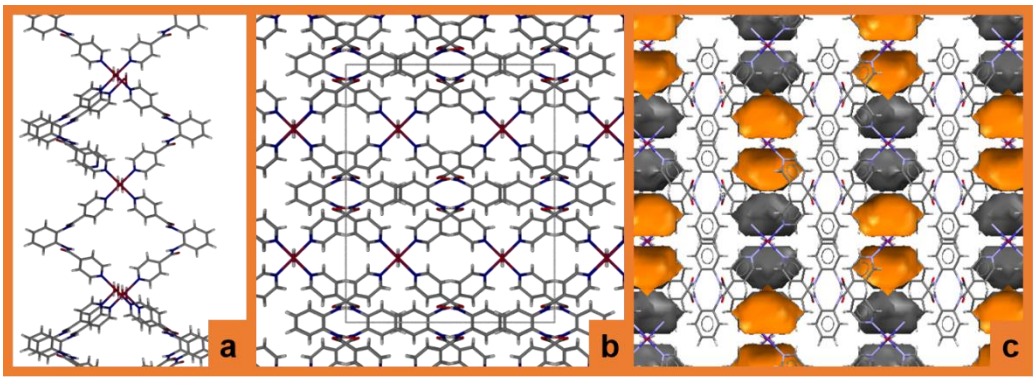

*Figure 4.3 shows **a** the structure of the 2D **CP1**. **b** the packed unit cell of **CP1**. **c** the void spaces of **CP1**, image created in Mercury where orange represents the inside of the void and grey the outside. All images are shown down the a axis. CPK colours used.*

CP2, $[Cd(NO_3)_2\text{-}(\mu\text{-}C_{18}H_{14}N_4O_2)_2]_n$,is a 1D CP formed from two equivalents **ligand 1** and one equivalent $Cd(NO_3)_2$ with ethanol. The crystallisation process has a stochastic nature and sometimes gels prior to crystallisation; as seen with the previously reported $CoCl_2$ macrocyle.[12] **CP3**, $[Co(I)_2\text{-}(\mu\text{-}C_{18}H_{14}N_4O_2)_2]_n$, is produced from two equivalents of **ligand 1** and one equivalent CoI_2 in a 50:50 methanol:THF solution. Like **CP1** both **CP2** and **CP3** have octahedral metal centres. Each metal centre is bound to four equatorial pyridyl ligands. **CP2** has two apical nitrate groups and **CP3** two has apical iodo groups. This forms chains of continuous rings, which are similar in structure to the discrete 2x2 macrocycles (Figure 4.4). Each ring contains an intrinsic void, which has the potential to be a discrete void or to stack and form a continuous channel. The macrocycles show a 1:1 metal to ligand ratio, the CPs show a 2:1 ligand to metal ratio.

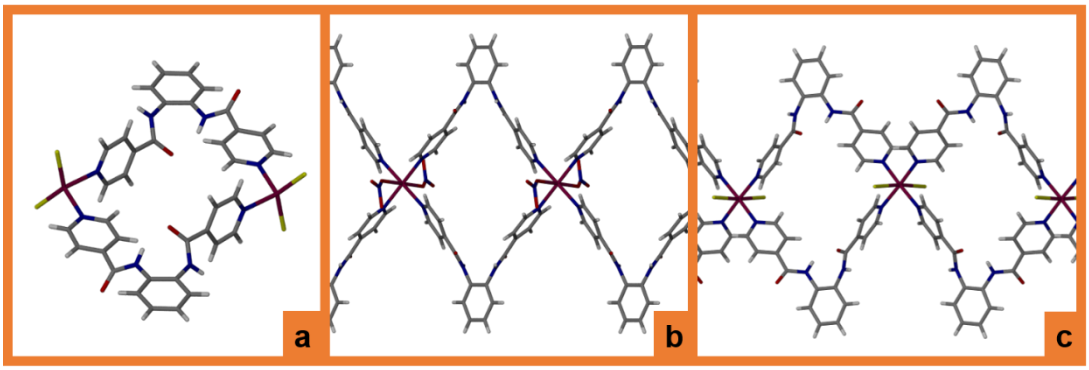

*Figure 4.4 shows **a** a 2X2 macrocycle (KATGET). **b** the ring structure of **CP2. c** the ring structure of **CP3**. CPK colours used with iodine in yellow and metal in maroon.*

CP2 and **CP3** can be viewed as supramolecular isomers. They both form chains of macrocycles formed of two metals with two bridging ligands. By changing the anion functionality from nitrate to iodine, it has caused the CP to favour different crystallisation solvents and a change in hydrogen-bonding interactions.

In the **CP2** structure (Figure 4.5), each chain of coordination polymer extends down the [1 0 1] plane following the $2_1/c$ symmetry operations. This causes a displacement of 11.375 (6) Å, which corresponds to half the width of the polymer and a shift of 4.415 (6) Å which is a (a quarter of the ac diagonal). Like **CP1** and the macrocycles reported by Puddephatt, the structure shows intermolecular hydrogen-bonds between the ligands.[13] An intermolecular hydrogen-bonded chain forms between the hydrogen of the amide and the carbonyl oxygen (N2···O5 = 2.830 (5) Å, N3···O4= 2.735 (6) Å, *C4*). This forms a structure with two void spaces, a discrete intrisic void and a continuous extrinsic channel, which is bordered by the nitrate groups. Like the literature examples,[12,13] solvent can be located within the void spaces of the structure, in this case disordered ethanol molecules. **CP2** readily desolvates at room temperature, a crystal placed under a microscope will turn from a clear crystal to an opaque mass within a few minutes.

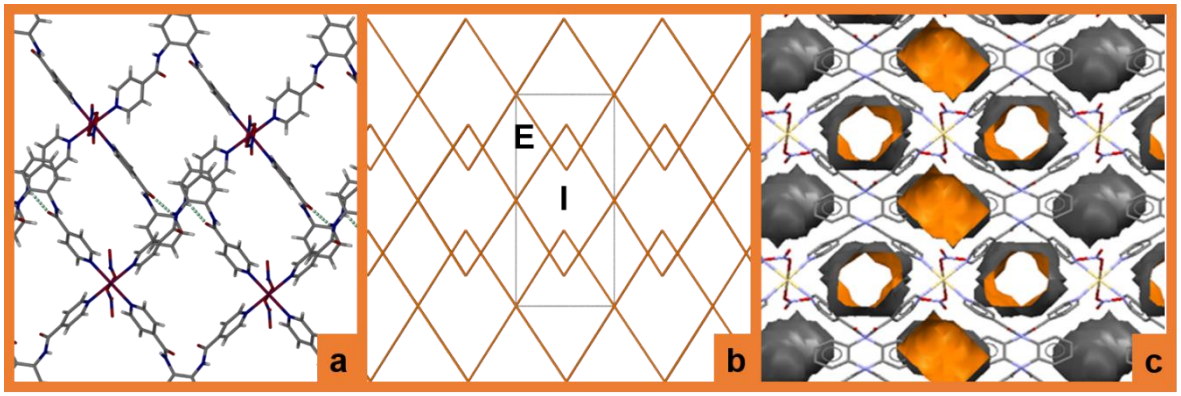

*Figure 4.5 shows **a** the C4 hydrogen-bond pattern of **CP2** is shown as the green broken bond**.** Viewed down the c axis. **b** the packed unit cell of **CP2** with extrinsic porosity (E) and intrinsic porosity (I) shown. The macrocycles are shown as simplified diamonds formed of the metal centre and a centroid of the phenyl ring viewed down the c axis. **c** the void spaces of **CP2**, down the c axis. Image created in Mercury, with a grid spacing of 0.7 Å and a probe radius of 1.2 Å. Orange represents the inside of the void and grey the outside of the void space. CPK colours used, with Cd in maroon.*

The **CP3** structure forms a 1D CP following the 2_1 screw axis and the c glide plane down the (1 0 -1) plane. Each 'macrocycle' in the chain has two *S7* intramolecular hydrogen-bonds occurring between the hydrogen of the amide and the carbonyl oxygen, (N3···O1 = 2.696 (4) Å, *S7*). Intramolecular hydrogen-bonds were reported to form in the $CoCl_2$ and $ZnCl_2$ macrocycles.[12] As seen previously with **CP1**, **CP2** and the literature[13] there is also an intermolecular $R_4^4 16$ hydrogen-bond formed (Figure 4.6). This interaction incorporates the *S7* intramolecular hydrogen-bond and a direct hydrogen-bond between the other NH and carbonyl of the ligand, (N2···O2 = 2.934 (5) Å, D). This provides the **CP3** structure with two continuous hour-glass shaped channels for both the intrinsic and extrinsic void spaces.

The Mercury void space image calculated for **CP3** uses different parameters to those typically used throughout this thesis. The grid spacing was reduced from 0.7 Å to 0.3 Å, providing a smoother and more accurate assessment of the void space. The ASU is one metal and one complete **ligand 1**. The voids are created via the symmetry of the space group, this means that the extrinsic void should be constant through both chains, i.e. it should always be a discrete void or a narrow channel. When the larger (0.7 Å) grid spacing

was used the image created formed an ABC pattern, where the extrinsic void space was shown as a continuous channel and a discrete channel (Figure 4.7).

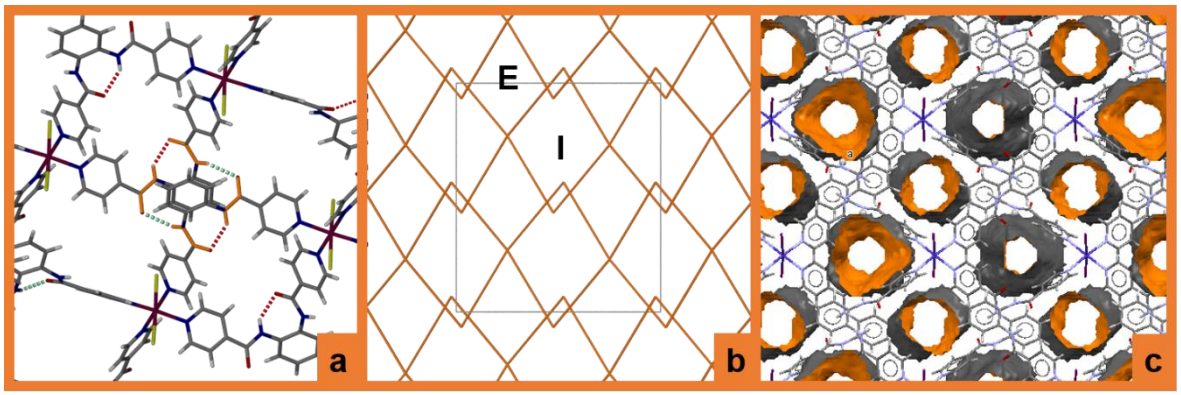

*Figure 4.6 shows **a** the hydrogen-bond interactions of **CP3**. The S7 interaction is shown in red, the D interaction is shown in green. The intermolecular $R_4^4 16$ atoms are highlighted in orange. **b** The packed unit cell of **CP3** with extrinsic porosity (E) and intrinsic porosity (I) shown. The macrocycles are shown as simplified diamonds formed of the metal centre and a centroid of the phenyl ring viewed down the b axis. **c** The void spaces of **CP3**, down the a axis. Image created in Mercury with a grid spacing of 0.3 Å and a probe radius of 1.2 Å. Orange represents the inside of the void and grey the outside of the void space. CPK colours used with Co in maroon and iodine in yellow.*

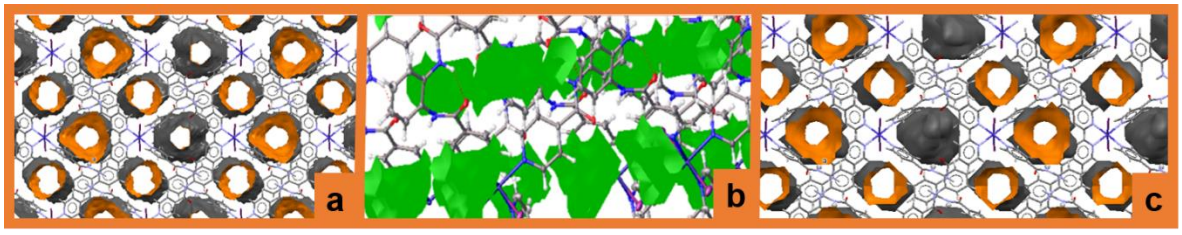

*Figure 4.7 **a** the re-analysed void space analysis of **CP3** calculated in Mercury using a grid spacing of 0.3 Å. **b** The Olex2 void space analysis, showing the ABC extrinsic void pattern. **C** The void space analysis calculated in Mercury using a grid spacing of 0.7 Å, showing the extrinsic void as both a discrete void and a continuous channel.*

By using a smaller grid spacing of 0.3 Å the image produced in Mercury provides the correct AB pattern, showing an hour glass shaped continuous channel for every extrinsic void, (Figure 4.7). Using the Olex2 void space analysis provides the same in ABC void pattern, as seen with the 0.7 Å grid spacing in Mercury. This incorrect void assignment, is a known

problem using grid based systems. The placement of the grid points along cell edges and channels with a variable cross-sectional area can be incorrect compared to the actual void space of the structure. By using a smaller grid, a more accurate void space can be calculated.

4.1.2 Mechanochemical Synthesis

Mechanochemistry is used to create bulk samples of known compounds and provide access to previously unseen structures. This project aimed to understand how mechanochemical synthesis would affect the structure and properties of the complexes of ligand 1. Solvent plays a significant role in determining the structure of these compounds.[12,13] Therefore, a variety of solvents were attempted, with the metal salts mixtures, to study the effect on the assembly process. The CoI_2·THF **CP3** structure is difficult to obtain from the solution state. The crystallisation of the **CP3** proceeds via the conversion from a CoI_2.MeOH macrocycle over the period of two months. Therefore, the formation of the **CP3** structure was one of the main targets using mechanochemical synthesis, the structure is yet to be obtained via mechanochemical synthesis, (Table 4.1).

Table 4.1 The solvents and metal salts used in mechanochemical synthesis.

Solvents	Metal salts
THF	CoI_2, $CoBr_2$, $CoCl_2$ $Co(NO_3)_2·6H_2O$, $Zn(NO_3)_2·4H_2O$, $ZnCl_2$, $CdCl_2·2.5H_2O$
Ethanol	$CdCl_2·2.5H_2O$, $CoCl_2$, $Co(NO_3)_2·6H_2O$, $Zn(NO_3)_2·4H_2O$, $ZnCl_2$, $Cd(NO_3)_2·4H_2O$
Methanol	$CoCl_2$, $Co(NO_3)_2·6H_2O$, $Zn(NO_3)_2·4H_2O$, $ZnCl_2$, $CdCl_2·2.5H_2O$, $Cd(NO_3)_2·4H_2O$
Chloroform	$CoCl_2$, $Zn(NO_3)_2·4H_2O$, $ZnCl_2$,

A typical mechanochemical synthesis was performed using 250 µL of solvent with 100 mg of ligand 1 with a 1:1 or 2:1 or 1:2 metal: ligand ratio. The mixture was ball milled in Teflon cups with one seven mm stainless steel ball at 30 Hz for 30 minutes. The CoI_2·THF CP3 structure is difficult to obtain from the solution state. The crystallisation of the CP3

proceeds via the conversion from a CoI_2.MeOH macrocycle over the period of two months. Therefore, the formation of the CP3 structure was one of the main targets using mechanochemical synthesis, the structure is yet to be obtained via this method.

From the attempted mechanochemical syntheses three structures were obtained. The pXRD patterns for the other samples showed either no conversion from the starting materials or provided an amorphous phase. Two of the obtained structures are the previously reported $CoCl_2$ and $ZnCl_2$ 2x2 macrocycles.[12] The obtained powder patterns are a match to the predicted powder pattern obtained from the single crystal structure (Figure 4.8).

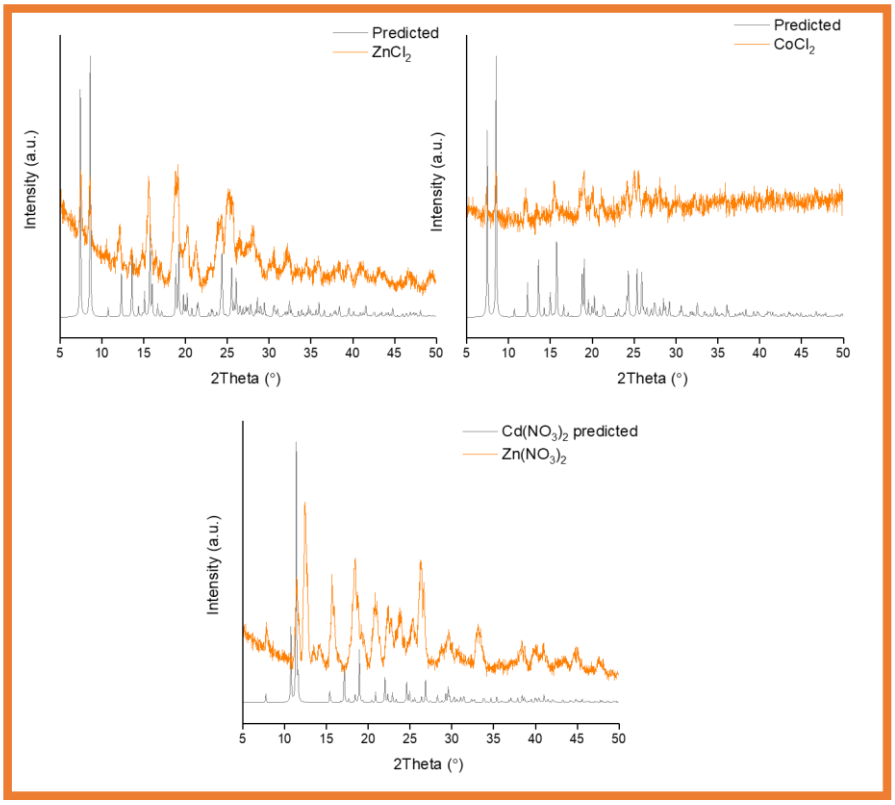

Figure 4.8 Stacked pXRD plots of the predicted powder patterns and the obtained pattern of the mechnochemically synthesised CPs and macrocycles.

The included solvent of choice for the system was ethanol with an addition of 20 µl of water, with a 1:1 metal:ligand ratio forming the macrocycle. The third structure is currently unobtained via solution state synthesis, formed from $Zn(NO_3)_2$ with ethanol. The CP formed

is isostructural to the **CP2** ($Cd(NO_3)_2$) structure reported earlier (4.1.1). The calculated pXRD pattern of **CP2** from the single crystal x-ray diffraction structure is a match for the obtained pXRD pattern of the $Zn(NO_3)_2$. The $Zn(NO_3)_2$ pXRD pattern shows the same major peaks as the predicted **CP2** pattern. Also seen in the $Zn(NO_3)_2$ pXRD pattern is a shift in the peak position and peak broadening. The peak broadening can be related to the small particle size caused by the milling process. The shift in the peak position could also be related to the height of the packed sample and indicates the lattice parameter of the two materials is different. This is expected due to the difference in the atomic radii of Cd (0.95 Å) and Zn (0.6 Å) metals.[37]

The mechanochemical synthesis proceeds via Liquid-assisted grinding (LAG).[28,38] This is the use of catalytic amounts of liquid phase to accelerate mechanochemical reactions.[28,38] By improving mobility of the reaction components, the reaction can be steered towards the formation of a particular phase.[28,34,38–40] The reaction requires ethanol as a solvent, the stoichiometry is fourteen equivalents of ethanol per one equivalent of ligand. Without the addition of ethanol, the reaction fails to proceed. In the crystallised phase, it is well reported that the included solvent plays a significant role in the structure. Ethanol is found in both void spaces of the $CoCl_2$ and $ZnCl_2$ macrocycles.[12] It would be expected that the mechanochemical structures behave in a similar way.

Water assisted grinding (WAG) is the addition of a catalytical quantity of water that facilitates the reaction process.[40–42] The non-hydrate metal salts required the incorporation of 20 µl of water (three and a half equivalents of water per metal) to successfully convert to the final compound; the metal salt hydrates did not require extra water to form the final materials. The additional amount of added water is close to that incorporated by the waters of hydration from the other metal salts. The water is not included within the structure, however, it is an essential component for the formation of the compound. If water is not present, the reaction fails to produce the final product. It appears that the water is facilitating the reaction between the metal salts and **ligand 1**. This is similar to the phenomena seen with mechanochemical synthesis of ZIFs (zeolitic imidazolate framework). ZIF synthesis through mechanochemistry is well reported.[38,41,43–49] To form a porous ZIF

from ZnO using mechanochemical synthesis, an ionic species must be present. This is referred to as ILAG (ion and liquid-assisted grinding).[43,45] The ionic species, typically ammonium salts, enabled the imidazole to react with the otherwise inert ZnO.[43,45] The anion helps to control the the formation of the framework, varying the anion allows access to different frameworks.[43] In this case the water could be acting in a similar way to the NH_4^+ cations in the mechanochemical synthesis of ZIFs, which are thought to be 'benefical' for ZIF synthesis.[43]

The $CoCl_2$ and $ZnCl_2$ macrocycles were obtained on bulk scale through both crystallisation and mechanochemical synthesis. This allows the study of how synthesis route affects the material properties of the compound. The single crystals of the compound contains one ethanol solvent molecule per void; this can be removed by heating.[12] The empty structure (βo phase) can then uptake guest species.[12] TGA was performed on the ball mill sample to determine if there were any inclusions within the voids. The $CoCl_2$ macrocycle shows 1.07 % mass loss prior to decomposition of the compound at 294 ˚C. The ball milled sample does not contain an ethanol molecule in each void as seen with the crystallised sample. The $Zn(NO_3)_2$ CP experiences a 7 % mass loss prior to decomposition at 228 ˚C. The $ZnCl_2$ macrocycle shows a 4.18 % mass loss at 68 ˚C from the loss of the ethanol solvent and a further 3 % loss of mass between 293 - 309 ˚C. This further mass loss could be unbound ligands located inside the voids of the structure.

BET surface areas were obtained for both $ZnCl_2$ macrocycles and the $CoCl_2$ macrocycle. The crystallised $ZnCl_2$ macrocycle shows a BET surface area of 224.6 m^2/g and a type 1 BET isotherm, this indicates that the material is microporous in nature.[50] The two ball milled samples show type 2 BET isotherms with a BET surface area of 105.0 m^2/g for the $CoCl_2$ macrocycle and 155.4 m^2/g for $ZnCl_2$ macrocycle. The type 2 isotherm is indicative that the materials show both microporous and mesoporous character.[50] The mesoporous character can potentially be related to the formation of lattice defects caused by the mechanochemical synthesis.[51–53] The smaller BET surface area shown by the mechanochemically synthesised compounds suggests the pores are blocked with unreacted starting materials which were not detected by pXRD.[54] CO_2 isotherms (Figure 4.9) were

collected for the three mechanochemically synthesised compounds and for the $ZnCl_2$ and $CoCl_2$ macrocycles synthesised via crystallisation. All five samples experienced the same desolvation process of isothermal heating at 150 ˚C for four hours.

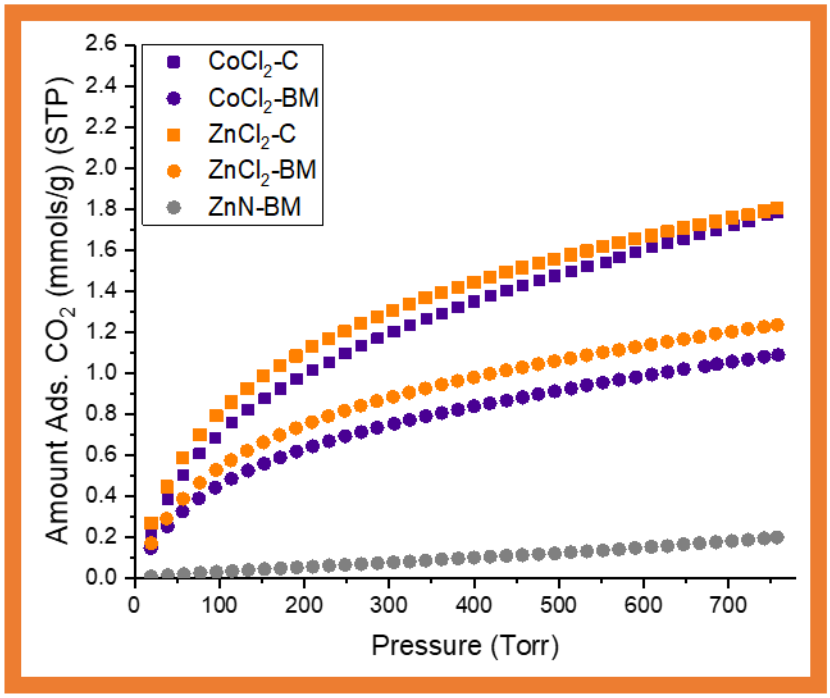

Figure 4.9 shows the CO_2 isotherms for the five compounds. Where C denotes the crystallised samples and BM mechanochemically synthesised samples.

At a pressure of 750 Torr (1 Barr) the crystallised $CoCl_2$ and $ZnCl_2$ samples contained two CO_2 molecules per macrocycle. This value indicates that the material is saturated according to the value previously reported in the literature.[12] The ball milled samples show a lower BET surface area and have a lower CO_2 adsorption. For the $CoCl_2$ – BM macrocycle sample 1.2 CO_2 molecules per macrocycle are absorbed. For the $ZnCl_2$ – BM macrocycle 1.4 CO_2 molecules per macrocycle are absorbed. The ball milled sample absorbs less CO_2 than the crystallised sample, this could be due to defects or incorporation of underreacted starting material in the void space.[54] The 1D CP formed from **ligand 1** and $Zn(NO_3)_2$ absorbs 0.2 CO_2 molecules, this is significantly less than the macrocycles. However, at 750 Torr the material is still absorbing CO_2. The material maybe better suited to adsorption at higher pressures. There is potential that the material shows a gating effect. Gating effects can be useful in the

separation of CO_2 from other gases such as C_2H_2 and CH_4.[55,56] Due to equipment limitations, studying the adsorption at higher pressures has not yet be conducted. Further work is required to understand if the samples can be processed to improve the adsorption capacity.[38,57,58] There is a literature precedence for improving the adsorption of mechanochemically synthesised materials through washing.[54] However, if further research fails to improve the adsorption capacity the mechanochemical process is significantly 'greener'.[59]

A standard crystallisation requires 15 mL of ethanol per 17 mg of ligand, compared to the mechanochemical synthesis requires 250 µl per 100 mg of **ligand 1**. Assuming 100 % conversion in both systems to form 1 kg of $CoCl_2$ macrocycle, 710 g of **ligand 1** is required. Therefore, mechanochemical synthesis requires 1.775 L of ethanol compared to 626 L for crystallisation. Mechanochemical synthesis saves over 620 L of solvent per kg of macrocycle produced, even with the slight reduction in CO_2 desorption capacity, the synthesis has to be viewed as a 'greener' and more cost effective synthesis.[59]

4.3 Conclusions

To conclude solvent plays a large role in determining the structure of CPs and macrocycles formed by **ligand 1**. In addition to the structures within the literature, a series of 1D and 2D CPs, incorporating CoI_2, $Cd(NO_3)_2$ and $Co(NO_3)_2$ have been synthesised via crystallisation. These structures show both discrete and continuous, intrinsic and extrinsic voids. Further to this, using mechanochemistry allows access to previously unobtainable structures ($Zn(NO_3)_2$), that are isostructural to compounds produced in the solution state. Mechanochemistry also provided a route to bulk synthesise compounds previously obtained via the solution state, $ZnCl_2$ and $CoCl_2$ macrocycles. It was also established that, whilst not included within the structure, the addition of water is essential to the formation of these compounds when produced via mechanochemistry. The mechanochemically synthesised compounds show less adsorption capacity at present but further work into the post synthesis modification may yield a structure that is as porous. The mechanochemically

synthesised compounds require 620 L less ethanol per kg, making them more environmentally friendly and more cost effective to synthesis.[59]

4.4 References

1 M. J. Bojdys, M. E. Briggs, J. T. A. Jones, D. J. Adams, S. Y. Chong, M. Schmidtmann and A. I. Cooper, *J. Am. Chem. Soc.*, 2011, **133**, 16566–16571.

2 H. R. Green and G. O. Lloyd, in *Chapter 9. Porous Metal Organic Polygons and Polyhedra - Intrinsic vs. Extrinsic Porosity in Functional Supramolecular Materials : From Surfaces to MOFs*, ed. R. Banerjee, The Royal Society of Chemistry, Cambridge, 1st edn., 2017, pp. 297–324.

3 L. J. Barbour, *Chem. Commun.*, 2006, 1163–1168.

4 R. M. Barrer and V. H. Shanson, *Chem. Commun.*, 1976, 333.

5 T. Jacobs, V. J. Smith, L. H. Thomas and L. J. Barbour, *Chem. Commun.*, 2014, **50**, 85–87.

6 M. Mastalerz and I. M. Oppel, *Angew. Chem. Int. Ed.*, 2012, **51**, 5252–5255.

7 Y. Bai, D. Guo, C. Y. Duan, D. Bin Dang, K. L. Pang and Q. J. Meng, *Chem. Commun.*, 2004, 186–187.

8 T. K. Ronson, C. Giri, N. Kodiah Beyeh, A. Minkkinen, F. Topić, J. J. Holstein, K. Rissanen and J. R. Nitschke, *Chem. - A Eur. J.*, 2013, **19**, 3374–3382.

9 L. Dobrzańska, G. O. Lloyd, H. G. Raubenheimer and L. J. Barbour, *J. Am. Chem. Soc.*, 2005, **127**, 13134–13135.

10 J. Tian, P. K. Thallapally and B. P. McGrail, *CrystEngComm*, 2012, **14**, 1909–1919.

11 L. Dobrzańska, G. O. Lloyd, H. G. Raubenheimer and L. J. Barbour, *J. Am. Chem. Soc.*, 2006, **128**, 698–699.

12 C. D. Jones, J. C. Tan and G. O. Lloyd, *Chem. Commun.*, 2012, **48**, 2110–2112.

13 T. J. Burchell, D. J. Eisler and R. J. Puddephatt, *Inorg. Chem.*, 2004, **43**, 5550–5557.

14 T. J. Burchell, D. J. Eisler and R. J. Puddephatt, *Chem. Commun.*, 2004, **788**, 944–945.

15 B. Moulton and M. J. Zaworotko, *Chem. Rev.*, 2001, **101**, 1629–1658.

16 A. D. McNaughty and A. Wilkinson, Eds., *IUPAC, Compendium of Chemical Terminology, (the 'Gold Book').*, Blackwell Scientific Publications, Oxford, 2nd edn., 1997.

17 J. C. Chambron, C. Dietrichbuchecker, C. Hemmert, A. K. Khemiss, D. Mitchell, J. P. Sauvage and J. Weiss, *Pure Appl. Chem.*, 1990, **62**, 1027–1034.

18 L. Öhrström, *Crystals*, 2015, **5**, 154–162.

19 S. Kitagawa and K. Uemura, *Chem. Soc. Rev.*, 2005, **34**, 109.

20 S. A. Bourne, in *Supramolecular Chemistry*, John Wiley & Sons, Ltd, Chichester, UK, 2012.

21 T. J. Burchell, D. J. Eisler and R. J. Puddephatt, *Cryst. Growth Des.*, 2006, **6**, 974–982.

22 L. R. Nassimbeni, *Acc. Chem. Res.*, 2003, **36**, 631–637.

23 T. J. Burchell, D. J. Eisler, M. C. Jennings and R. J. Puddephatt, *Chem. Commun.*, 2003, 2228–2229.

24 J. L. C. Rowsell and O. M. Yaghi, *Microporous Mesoporous Mater.*, 2004, **73**, 3–14.

25 T. Friščić, *Encycl. Inorg. Bioinorg. Chem.*, 2014, 1–19.

26 S. L. James and T. Friščić, *Chem. Commun.*, 2013, **49**, 5349.

27 A. Pichon, A. Lazuen-Garay and S. L. James, *CrystEngComm*, 2006, **8**, 211.

28 T. Friščić, *J. Mater. Chem.*, 2010, **20**, 7599.

29 Editorial, *Nature Chem.*, 2016, **8**, 987–987.

30 M. Technologies, 2016.

31 Decco, 2017.

32 S. M. Blankenship, X. Fan and J. P. Mattheis, *J. Am. Soc. Hortic. Sci.*, 1999, **124**, 690–695.

33 S. M. Blakenship and J. M. Dole, *Postharvest Biol. Technol.*, 2003, **28**, 1–25.

34 T. Friščić, *Chem. Soc. Rev.*, 2012, **41**, 3493.

35 Y. R. Lee, J. Kim and W. S. Ahn, *Korean J. Chem. Eng.*, 2013, **30**, 1667–1680.

36 M. Elie, M. D. Weber, F. Di Meo, F. Sguerra, J. F. Lohier, R. B. Pansu, J. L. Renaud, M. Hamel, M. Linares, R. D. Costa and S. Gaillard, *Chem. A Eur. JournalA Eur. J.*, 2017, **23**, 16328–16337.

37 R. D. Shannon, *Acta Crystallogr. Sect. A*, 1976, **32**, 751–767.

38 S. L. James, C. J. Adams, C. Bolm, D. Braga, P. Collier, T. Friščić, F. Grepioni, K. D. M. Harris, G. Hyett, W. Jones, A. Krebs, J. Mack, L. Maini, A. G. Orpen, I. P. Parkin, W. C. Shearouse, J. W. Steed and D. C. Waddell, *Chem. Soc. Rev.*, 2012, **41**, 413–447.

39 P. Wang, G. Li, Y. Chen, S. Chen, S. L. James and W. Yuan, *CrystEngComm*, 2012, **14**, 1994.

40 T. Friščić and L. Fábián, *CrystEngComm*, 2009, **11**, 743.

41 F. C. Strobridge, N. Judas and T. Friscić, *CrystEngComm*, 2010, **12**, 2409–2418.

42 G. A. Bowmaker, N. Chaichit, C. Pakawatchai, B. W. Skelton and A. H. White, *Dalton Trans.*, 2008, 2926.

43 P. J. Beldon, L. Fábián, R. S. Stein, A. Thirumurugan, A. K. Cheetham and T. Friščić, *Angew. Chemie - Int. Ed.*, 2010, **49**, 9640–9643.

44 A. L. Garay, A. Pichon and S. L. James, *Chem. Soc. Rev.*, 2007, **36**, 846.

45 T. Friščić, I. Halasz, P. J. Beldon, A. M. Belenguer, F. Adams, S. A. J. Kimber, V. Honkimäki and R. E. Dinnebier, *Nature Chem.*, 2012, **5**, 66–73.

46 Y. R. Lee, M. S. Jang, H. Y. Cho, H. J. Kwon, S. Kim and W. S. Ahn, *Chem. Eng. J.*, 2015, **271**, 276–280.

47 A. D. Katsenis, A. Puskaric, V. Strukil, C. Mottillo, P. A. Julien, K. Uzarevic, M. H. Pham, T. O. Do, S. A. J. Kimber, P. Lazic, O. Magdysyuk, R. E. Dinnebier, I. Halasz and T. Friščić, *Nat. Commun.*, 2015, **6**, 6662.

48 T. D. Bennett, S. Cao, J. C. Tan, D. A. Keen, E. G. Bithell, P. J. Beldon, T. Friscic and A. K. Cheetham, *J. Am. Chem. Soc.*, 2011, **133**, 14546–14549.

49 W. Yuan, T. Friščič, D. Apperley and S. L. James, *Angew. Chemie - Int. Ed.*, 2010, **49**, 3916–3919.

50 S. Storck, H. Bretinger and W. F. Maier, *Appl. Catal. A Gen.*, 1998, **174**, 137–146.

51 V. V. Boldyrev, *Mater. Sci. Forum*, 1996, **225**–**227**, 511–520.

52 P. Y. Butyagin, *Russ. Chem. Rev.*, 1984, **53**, 1025–1038.

53 U. Steinike and K. Tkáčová, *J. Mater. Synth. Process.*, 2000, **8**, 197–203.

54 W. Yuan, A. L. Garay, A. Pichon, R. Clowes, C. D. Wood, A. I. Cooper and S. L. James, *CrystEngComm*, 2010, **12**, 4063.

55 E. J. Carrington, C. A. McAnally, A. J. Fletcher, S. P. Thompson, M. Warren and L. Brammer, *Nature Chem.*, 2017, **9**, 882–889.

56 M. L. Foo, R. Matsuda, Y. Hijikata, R. Krishna, H. Sato, S. Horike, A. Hori, J. Duan, Y. Sato, Y. Kubota, M. Takata and S. Kitagawa, *J. Am. Chem. Soc.*, 2016, **138**, 3022–3030.

57 J. L. Do and T. Friščić, *ACS Cent. Sci.*, 2017, **3**, 13–19.

58 N. Stock and S. Biswas, *Chem. Rev.*, 2012, **112**, 933–969.

59 M. Gaab, N. Trukhan, S. Maurer, R. Gummaraju and U. Muller, *Microporous Mesoporous Mater.*, 2012, **157**, 131–136.

Chapter 5 – Overview and Future Work

'*Don't just fly, soar' Dumbo*

5.1 Conclusions and future work

Hydroxamic acid compounds were synthesised and studied for their solid state properties. These studies included the supramolecular packing in organic crystalline phases (pure and multi-component), and the coordination chemistry of the hydroxamates to metals, with particular focus on the development of porosity in crystalline materials. Metal-hydroxamate complexes, which displayed both intrinsic and extrinsic porosity. Produced were different solvates of a Zr_1(hydroxamate)$_4$ complex (chapter two) and a family of M_4L_6 tetrahedra[1] incorporating Fe^{3+}, Al^{3+}, Ga^{3+} and In^{3+} which were designed incorporating crystal engineering approaches (chapter three).

The aim of chapter two was to understand the synthesis and supramolecular synthons of hydroxamic acids. The mechanochemical synthesis of hydroxamic acids removes the solubility barrier enforced by the solution state synthesis, making it possible to synthesise previously inaccessible hydroxamic acids. By comparison of the crystal structures available on the CSD and those obtained through this study. Understanding has been gained into the types of interactions hydroxamic acids favour and how to create multicomponent crystals.[2–6] Hydroxamic acids play a major role in medicinal chemistry; this makes the synthesis of multicomponent co-crystals of hydroxamic acids, of great importance because it allows for better control of the properties, such as solubility of hydroxamic acids.[7–10] The future of this progress lies in synthesis of hydroxamic acids through mechanochemical synthesis, which allows for the incorporation of hydroxamic acids with other functionalities.[11] The formation and design of multicomponent crystals will also be a major area of study. With an increase in the number of hydroxamic acids and multicomponent crystals, it is likely that there will be an increase in the number of crystal structures containing these compounds. This allows

for greater understanding of the supramolecular synthons they favour, this in turn allows for multicomponent crystals to be designed and leads to a greater likelihood of success.[2,4]

Throughout this work hydroxamic acid chelation to metals has been shown to be complex due to dynamics in solution and chirality.[12–16] That said hydroxamic acids deprotonate in predictable ways forming hydroxamates.[12] Which chelate to metals with a predictable bidentate coordination.[12] A range of metal-hydroxamate complexes have been produced including discrete Zr_1L_4 complexes which show extrinsic porosity (chapter two) and a family of M_4L_6 formed from trivalent metals (Fe, Al, In and Ga) are reported in chapter three.

The hypothesis chapter three was to produce more extrinsically porous materials whilst maintaining the same intrinsic pore space and to understand the host:guest chemistry of the materials. Crystal engineering techniques were used to increase the amount of extrinic porosity seen in a family of M_4L_6 tetrahedra. These hydrogen-bonded networks were designed by controlling the cage geometry and dimesions, by retaining the same ligand geometry but incorporating additional functionality at the five position of the phenyl ring. This additional functionality prevented the CCP or HCP close packed structres seen with the unfunctionalised structure and allowed for the formation of less ordered networks. xPDF was used to confirm the structure of the tetrahedra after removal of the solvent of crystallisation, confirming that the cage structure was retained after heating.[17,18] DMF plays a major role in the crystallisation of these tetrahedra, but is not essential to their formation. The molecular cages show host:guest chemistry, absorbing water at atmospheric temperatures and pressures, and CO_2 at pressures below one barr. The cages retain CO_2 upon desorption which may prove useful for CO_2 storage in the future. Further work is required to understand the full host:guest chemistry of these materials. The promising water sorption capabilities of these structures could be further determined by DVS (Dynamic Vapour Sorption), to determine if they would be suitable as desiccants. Computational studies should be conducted to assess the suitability of potential guests. The Nobel gases could be ideal candidates for further gas sorption studies. The van der Waals radii for, Xe (2.16 Å), Kr (2.02 Å), Ar (1.88 Å), and Ne (1.54 Å), are similar,[19,20] it is difficult to separate the atoms based solely on size in materials with large voids.[20] The solution state

dynamics and chiralities of metal hydroxamate complexes has been studied but further work is required to fully understand how to design the framework topologies incorporating them.[16,21] Controlling the dynamic nature of the complexes formed in solution is the obvious next step of this process.

The aim of chapter four was to understand the effect that synthesis route plays on a family of dynamic self-assembling macrocycles and coordination polymers. In terms of their structure and material properties. By utilising mechanochemical techniques, porous molecular materials and hydroxamic acids have been synthesised. Mechanochemistry has provided a quick and convenient method for rapidly obtaining bulk quantities of CPs and macrocycles, typically obtained from the solution state (chapter four). The synthesis has reduced the amount of solvent by over 620 L per kg of material, saving money and the environment. The macrocycles produced show less absorption capacity at present but with further post synthesis purification the capacity maybe optimised.[22] Microporous and mesoporous character has been incorporated into the mechanochemically synthesised macrocycle BET isotherms.[23] The solution state isotherms are purely microporous. Mechanochemistry has also allowed access to a CP previously inaccessible through the solution state; the material shows a low CO_2 capacity at pressures of one Barr. However, it is hoped that at higher pressures it may show improved uptake properties.[24]

This thesis is just the beginning of the story for hydroxamic acids and their porous materials; this work has shown there is a wealth of underutilised and unexplored properties relating to the hydroxamic acid. By better understanding their supramolecular synthons and the chiral, dynamic nature they show when complexed it will be possible to exploit their numerous properties, in the form of cocrystal and porous materials. Over the coming years and decades, one should expect there to be an abundance of publications regarding these fascinating compounds.

5.2 References

1 Y. Bai, D. Guo, C. Y. Duan, D. Bin Dang, K. L. Pang and Q. J. Meng, *Chem. Commun.*,

2004, 186–187.

2 T. S. Thakur and G. R. Desiraju, *Cryst. Growth Des.*, 2008, **8**, 4031–4044.

3 G. R. Desiraju, *Angew. Chem. Int. Ed. Engl.*, 1995, **34**, 2311–2327.

4 G. R. Desiraju, *J. Chem. Sci*, 2010, **122**, 667–675.

5 G. R. Desiraju, *The crystal as a supramolecular entity*, Wiley, 1996.

6 P. A. Wood, N. Feeder, M. Furlow, P. T. A. Galek, C. R. Groom and E. Pidcock, *CrystEngComm*, 2014, **16**, 5839.

7 D. K. Bučar and L. R. MacGillivray, *J. Am. Chem. Soc.*, 2007, **129**, 32–33.

8 N. K. Duggirala, M. L. Perry, Ö. Almarsson and M. J. Zaworotko, *Chem. Commun.*, 2016, **52**, 640–655.

9 S. Aitipamula, R. Banerjee, A. K. Bansal, K. Biradha, M. L. Cheney, A. R. Choudhury, G. R. Desiraju, A. G. Dikundwar, R. Dubey, N. Duggirala, P. P. Ghogale, S. Ghosh, P. K. Goswami, N. R. Goud, R. R. K. R. Jetti, P. Karpinski, P. Kaushik, D. Kumar, V. Kumar, B. Moulton, A. Mukherjee, G. Mukherjee, A. S. Myerson, V. Puri, A. Ramanan, T. Rajamannar, C. M. Reddy, N. Rodriguez-Hornedo, R. D. Rogers, T. N. G. Row, P. Sanphui, N. Shan, G. Shete, A. Singh, C. C. Sun, J. A. Swift, R. Thaimattam, T. S. Thakur, R. Kumar Thaper, S. P. Thomas, S. Tothadi, V. R. Vangala, N. Variankaval, P. Vishweshwar, D. R. Weyna and M. J. Zaworotko, *Cryst. Growth Des.*, 2012, **12**, 2147–2152.

10 F. Fischer, D. Lubjuhn, S. Greiser, K. Rademann and F. Emmerling, *Cryst. Growth Des.*, 2016, **16**, 5843–5851.

11 R. Mocci, L. De Luca, F. Delogu and A. Porcheddu, *Adv. Synth. Catal.*, 2016, **358**, 3135–3144.

12 R. Codd, *Coord. Chem. Rev.*, 2008, **252**, 1387–1408.

13 C. J. Carrano, S. R. Cooper and K. N. Raymond, *J. Am. Chem. Soc.*, 1978, **101**, 599–604.

14 D. L. Caulder and K. N. Raymond, *J. Chem. Soc. Dalt. Trans.*, 1999, **0**, 1185–1200.

15 G. Seeber, B. E. F. Tiedemann and K. N. Raymond, *Top. Curr. Chem.*, 2006, **265**, 147–183.

16 T. Beissel, R. E. Powers, T. N. Parac and K. N. Raymond, *J. Am. Chem. Soc.*, 1999, **121**, 4200–4206.

17 E. Takeshi and S. J. L. Billinge, in *Underneath the Bragg Peaks, Structural Analysis of Complex Materials*, Pergamon Materials Series, Oxford, 2012, vol. 16, pp. 55–111.

18 S. J. L. Billinge, T. Dykhne, P. Juhás, E. Božin, R. Taylor, A. J. Florence and K. Shankland, *CrystEngComm*, 2010, **12**, 1366–1368.

19 R. D. Shannon, *Acta Crystallogr. Sect. A*, 1976, **32**, 751–767.

20 L. Chen, P. S. Reiss, S. Y. Chong, D. Holden, K. E. Jelfs, T. Hasell, M. A. Little, A. Kewley, M. E. Briggs, A. Stephenson, K. M. Thomas, J. A. Armstrong, J. Bell, J. Busto, R. Noel, J. Liu, D. M. Strachan, P. K. Thallapally and A. I. Cooper, *Nat. Mater.*, 2014, **13**, 954–960.

21 T. Beissel, R. E. Powers and K. N. Raymond, *Angew. Chem. Int. Ed. Engl.*, 1996, **35**, 1084–1085.

22 W. Yuan, A. L. Garay, A. Pichon, R. Clowes, C. D. Wood, A. I. Cooper and S. L. James, *CrystEngComm*, 2010, **12**, 4063.

23 S. Storck, H. Bretinger and W. F. Maier, *Appl. Catal. A Gen.*, 1998, **174**, 137–146.

24 T. Jacobs, G. O. Lloyd, J. A. Gertenbach, K. K. Müller-Nedebock, C. Esterhuysen and L. J. Barbour, *Angew. Chem. Int. Ed.*, 2012, **51**, 4913–4916.

Appendix A

"When something is too hard….there is always another way." Dory's Dad in finding Dory

A.0 Methodology

A.0.1 Chemical list

All chemicals and starting regents were bought from commercial sources (flourochem, Sigma Aldrich, TCI chemicals or Fisher Scientific). Full characterisation of all synthesised compounds can also be seen below. Distilled water was used for all experiments and crystallisations.

All solvents – Fisher Scientific. All deuterated solvents – Cambridge isotope laboratories. Halogenated benzoic acids – Flourochem. Hydroxylamine salts – Sigma Aldrich / Fisher Scientific. Metal Salts – Sigma Aldrich / Fisher Scientific. Organic esters – TCI chemicals / Sigma Aldrich.

A.1 Analytical techniques

A.1.1 NMR

^{1}H NMR spectra were recorded on a Bruker AV 300 spectrometer at 300 MHz and referenced to residual solvent. ^{13}C NMR spectra were recorded using the same spectrometers at 75 MHz. Solid state ^{13}C NMR spectra recorded on a Bruker AV 400 spectrometer at MHz. Chemical shifts (δ in ppm) were referenced to tetramethylsilane (TMS) or to residual solvent peaks (DMSO at δH 2.50 ppm, δC at 39.51 ppm or D_2O δH 4.80 ppm, δC N/a).

A.1.2 IR

IR spectra were recorded on a Nicolet is5 instrument using 24 scans at a resolution of 1 cm^{-1} and data spacing of 0.964 cm^{-1} with all samples loaded directly onto the instrument.

A.1.3 TGA

Data was collected on a TA Q500. Samples were loaded into aluminum pans and heated under a flowing nitrogen atmosphere. A standard experiment uses a ramp rate of 3 ˚C per minute between a range of 40 ˚C and 300 ˚C. Desorption experiments were temperature dependent upon the material but the sample was held isothermal at the desolvation temperature for three hours. Again the ramp rate was 3 ˚C per minute. (Stellenbosch University/Queens University Belfast)

A.1.4 DSC

DSC data was recorded on a TA Q200 using a ramp rate of 3 ˚C per minute between 40 ˚C and 300 ˚C. Samples were loaded into aluminium pans, with crimped lids. Punctured to release any pressure build up. (Stellenbosch University)

DSC data for the Co-crystals in Chapter 2 were collected on a NETZSCH STA 409PC/PG using a ramp rate of 5 ˚C per minute between 30 ˚C and 450 ˚C. Samples were loaded into open aluminium pans. (University of Kent)

A.1.5 pXRD

pXRD patterns were collected at room temperature using a Bruker D8 Advance powder diffractometer in reflectance mode. Lynxeye super speed detector was used with the radiation being monochromated Cu Kα1, with a characteristic wavelength of 1.541 Å. 15 minute scans over the range $5° \leq 2\theta \leq 40°$ (stepsize = 0.025°/counting time = 0.5 s/steps). Sample run on a flatbed sample holder.

A.1.5.1 VT-pXRD

VT-pXRD patterns were collected at 10 ˚C intervals between 30 and 200 ˚C using a Panalytical X'Pert powder diffractometer in reflectance mode. With the radiation being monochromated Cu Kα1, with a characteristic wavelength of 1.541 Å. 12 minute scans over the range 5° ≤ 2θ ≤ 40°. Sample run in an open borosilicate capillary. (Stellenbosch University)

A.1.6 Sc XRD

Single-crystal X-ray data was collected on a Bruker X8 APEX-II CCD diffractometer with a graphite monochromator, using Mo-Kα radiation, λ = 0.71073 Å, from a sealed source at 100 K. Data was collected using APEX-II software, integrated using SAINT and corrected for absorption using SADABS. Alternatively data was collected on a Synergy, Dualflex, AtlasS2, diffractometer with CuKα radiation, λ = 1.54184 Å. All structures were collected at low temperature. Data was processed using CrysAlis^{Pro} (University of Kent/Rigaku Oxford Diffraction). All the structures were solved using Olex2, with ShelXS direct methods or ShelXT. All structures were refined using least squared refinement with ShelXL. Images where created in X-Seed using pov-ray. Solvent accessible void images were created in Mercury using a grid size of 0.7 Å and a probe radius of 1.2 Å.

The SQUEEZE algorithm within Platon program was used to provides an estimated electron count. Which can be used to help determine the amount of solvent within the structure.

A.1.7 Mass spectroscopy

Mass spectrometry data were recorded using electrospray ionization (ESI) in positive mode using a Bruker microTOF instrument. Dr L. McKay ran the samples at the University of Edinburgh.

A.1.8 Mechanochemical synthesis

Standard reaction conditions reactants ground with a Retsch MM400 shaker mill in a 20 mL Teflon vessel with a 7 mm steel ball at a the specified time and frequency.

A.1.9 Gas sorption

Gas uptake: N_2 adsorption isotherms were carried out at 77 K on a Quantachrome Autosorb iQ gas sorption analyser. CO_2 adsorption measurements were carried out at 273 K. Samples were degassed using the internal turbo pump. BET surface areas were calculated from the isotherms using the Micropore BET Assistant in the Quantachrome ASiQwin operating software. Pore size distributions were calculated using the N_2 at 77 K on carbon (slit pore, QSDFT, equilibrium model) calculation model within the Quantachrome ASiQwin operating software. (University of Glasgow)

A.1.10 CrystalExplorer

Electrostatic potential Hirschfeld surfaces were calculated using CrystalExplorer with Tonto. DFT calculation was performed with 6-311G (d,p) basis set with Becke88 exchange potential and LYP correlation potential.

A.2 Chapter 2

A.2.0 Solution state monotopic ligands

3-amino-benzohydroxamic acid

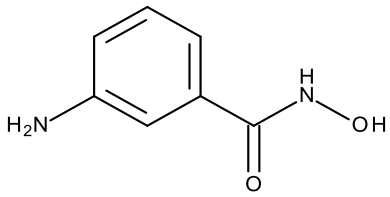

Ethyl 3-aminobenzoate (4.956g, 30mmol), was dissolved in a 50:50 ethanol:methanol solution (50mL), to which an aqueous solution (45mL) of hydroxylamine hydrochloride (6.25g, 90mmol), sodium hydroxide (7.2g, 180mmol) was added. The solution was heated to 40°C with stirring for 17 hours. The solution pH was adjusted to between pH 6.9 - 6.5 with 5% hydrochloric acid. The reaction mixture was concentrated under reduced pressure and

allowed to crystallise over a 24-hour period resulting in brown needle crystals that transform into block like crystals. (88%)

^{1}H NMR (300MHz, DMSO) δ: 5.23 (s, 2H, NH), 6.67 (d, 1H, ArH) 6.83 (d, 1H, ArH), 7.01 (t, 1H), 8.85 (bs, 1H, OH), 10.95 (bs, 1H, NH). 164.05 (**ATR**, cm-1) 3291 (NH), 3062 (Ar CH), 2736 (OH), 1665 (N-C=O), 1538 (Ar C=C bend), 710 (Ar CH bend). **MS** (ESI) m/z: 153 $[M+H]^+$. **Melting point** = 141-146 °C

Crystal data for $C_7H_8N_2O_2.H_2O$: M =170.17, clear yellow block, 0.5 x 0.5 x 0.5 mm^3, orthorhombic, space group $Pna2_1$ (No. 33), a = 9.4347(7), b = 5.6012(4), c = 15.6939(11) Å, V = 829.35(10) Å^3, Z = 4, D_c = 1.363 g cm^{-3}, F_{000} = 360, Bruker APEX-II CCD, MoKα radiation, λ= 0.71073 Å, T = 100 K, $2\Theta_{max}$ = 79.8º, 21784 reflections collected, 4597 unique (R_{int} = 0.0222). Final *GooF* = 1.049, $R1$ = 0.0344, $wR2$ = 0.0961, R indices based on 4315 reflections with $I > 2\sigma(I)$ (refinement on F^2), 114 parameters, 1 restraint. Lp and absorption corrections applied, , μ = 0.108 mm^{-1}.

4-amino-benzohydroxamic acid– Jamie Foster

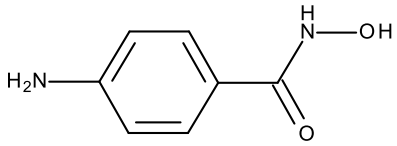

Ethyl 4-aminobenzoate (4.956g, 30mmol), was dissolved in a 50:50 ethanol:methanol solution (50mL), to which an aqueous solution (45mL) of hydroxylamine hydrochloride (6.25g, 90mmol), sodium hydroxide (7.2g, 180mmol) was added. The solution was heated to 40°C with stirring for 17 hours. The solution pH was adjusted to between pH 6.9 - 6.5 with 5% hydrochloric acid. The reaction mixture was concentrated under reduced pressure and allowed to crystallise over a 24-hour period resulting in brown needle crystals. (92 %)

^{1}H NMR (300MHz, DMSO) δ: 5.59 (s, 2H, NH_2), 6.52 (d, 2H, ArH) 7.45 (d, 2H, ArH), 8.64 (bs, 2H, OH), 10.75 (bs, 2H, NH). (**ATR**, cm-1) 3337 (NH), 3017 (Ar CH), 2781 (OH), 1629 (N-C=O), 1573 (Ar C=C bend), 691 (Ar CH bend). **MS** (ESI) m/z: 153 $[M+H]^+$. **Melting point** = decomposes above 200 °C.

Crystal data for $C_7H_8N_2O_2$: M = 152.15, orange needle, 0.5 × 0.3 × 0.05 mm^3, orthorhombic, space group $Pna2_1$ (No. 33), a = 7.8443(6), b = 16.8759(12), c = 5.0951(3) Å, V = 674.49(8) Å^3, Z = 4, D_c = 1.498 g cm^{-3}, F_{000} = 320, Bruker APEX-II CCD, MoKα radiation, λ = 0.71073 Å, T = 293(2) K, $2\theta_{max}$ = 60.0º, 5877 reflections collected, 1917 unique (R_{int} = 0.0270). Final *GooF* = 1.059, $R1$ = 0.0361, $wR2$ = 0.0910, R indices based on 1732 reflections with $I > 2\sigma(I)$ (refinement on F^2), 102 parameters, 1 restraint. Lp and absorption corrections applied, μ = 0.112 mm^{-1}.

3-pyridyl-benzohydroxamic acid

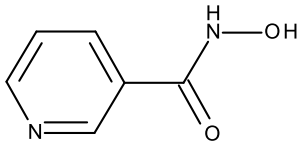

Methyl nicotinate (4.11g, 30mmol), was dissolved in methanol (50mL), to which an aqueous solution (45mL) of hydroxylamine hydrochloride (6.25g, 90mmol), sodium hydroxide (7.20g, 180mmol) was added. The solution was heated to 40°C with stirring for 17 hours. The solution pH was adjusted to between pH 6.9 - 6.5 with 5% hydrochloric acid. The reaction solution concentrated under reduced pressure allow the crystalisation of the colourless needle product, (96 %).

^{1}H NMR (300MHz, DMSO) δ: 7.48 (d, 1H, ArH), 8.21 (t, 1H) 8.75 (d, 1H, ArH) 8.97 (s, 1H, ArH), 9.30 (bs, 1H, OH), 11.27 (bs, 1H, NH). (**ATR**, cm-1) 3357 (NH), 3148 (Ar CH), 2651 (OH), 1674 (N-C=O), 1593 (Ar C=C bend), 776 (Ar CH bend). **Melting point** = 120-131 °C.

4-pyridyl-benzodroxamic acid

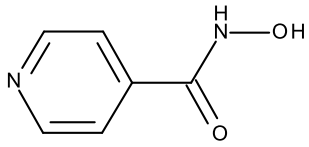

Methyl isonicotinate (4.11g, 30mmol), was dissolved in methanol (50mL), to which an aqueous solution (45mL) of hydroxylamine hydrochloride (6.25g, 90mmol), sodium hydroxide (7.20g, 180mmol) was added. The solution was heated to 40°C with stirring for 17 hours. The solution pH was adjusted to between pH 6.9 - 6.5 with 5% hydrochloric acid. The reaction solution was concentrated under reduced causing the precipitation of the white solid product.

^{1}H NMR (300MHz, DMSO) δ: 7.67 (d, 2H, ArH), 8.70 (d, 2H, ArH) 9.30 (bs, 1H, OH), 11.48 (bs, 1H, NH). (**ATR,** cm-1) 3360 (NH), 3061 (Ar CH), 2990 (OH), 1651 (N-C=O), 1545 (Ar C=C bend), 686 (Ar CH bend). **Melting point** = 154-162 °C.

A.2.1 Solution state multitopic ligands

Isophthaloyl hydroxamic acid – Jamie Foster

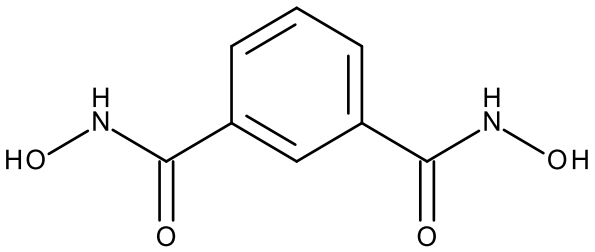

Dimethyl benzene-1,3-dicarboxylate (5.82g, 30mmol), was dissolved in methanol (50mL), to which an aqueous solution (45mL) of hydroxylamine hydrochloride (9.5g, 120mmol), sodium hydroxide (10.8g, 240mmol) was added. The solution was heated to 40°C with stirring for 17 hours. The solution pH was adjusted to between pH 6.9 - 6.5 with 5% hydrochloric acid. The white solid produced was obtained via vacuum filtration (98%).

^{1}H NMR (300MHz, DMSO) δ: 7.53 (t, 1H, ArH), 7.85 (dd, 2H, ArH) 8.16 (s, 1H, ArH), 9.18 (bs, 2H, OH), 11.27 (bs, 2H, NH). **^{13}C NMR** (75 MHz, DMSO) δ: 126.30, 128.98, 129.75, 133.52, 164.05 (**ATR**, cm^{-1}) 3309.53 (NH), 3047.30 (Ar CH), 2759.21 (OH), 1645.43 (N-C=O), 1548 (Ar C=C bend), 710 (Ar CH bend). **MS** (ESI) m/z: 197 $[M+H]^+$. **Melting point** = decomposes above 200 °C.

5-Amino-isophthaloyl Hydroxamic Acid

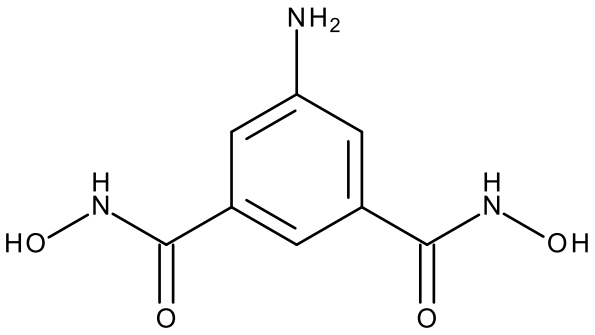

5-amino-dimethyl benzene-1,3-dicarboxylate (4.18 g, 20 mmol), was dissolved in methanol (50 mL), to which an aqueous solution (45 mL) of hydroxylamine hydrochloride (9.5 g, 120 mmol), sodium hydroxide (10.8 g, 240 mmol) was added. The solution was heated to 40 °C with stirring for 17 hours. The solution pH adjusted to ~6.8 with 5 % hydrochloric acid and reduced pressure used to obtain a solid. Purification of the product was performed by dissolving the product in deionised water and allowing it to precipitate out over several days. Vacuum filtration yields a beige solid product. (96 %).

^{1}H NMR (300MHz, DMSO) δ: 5.46 (s, 2H, NH), 7.03 (s, 2H, ArH), 7.18 (s, 1H, ArH) 8.95 (bs, 2H, OH), 11.00 (bs, 2H, NH). **^{13}C NMR** (75 MHz, DMSO) δ: 113.08, 115.12, 134.37, 149.24, 165.25 (**ATR**, cm^{-1}): 3351.55 (NH), 3262.15 (NH_2), 2845.48 (OH), 1638.72 (N-C=O), 1593.31 (Ar C=C bend), 734.31 (Ar CH bend). **MS** (ESI) m/z: 234 $[M+Na]^+$ **Melting point** = decomposes above 200 °C.

Crystal data for $C_8H_9O_4N_3$: M =211.17, clear light yellow irregular, 0.07 × 0.05 × 0.05 mm^3, monoclinic, space group $P12_1/c1$ (No. 14), a = 11.9733(10), b = 9.5273(7), c = 7.8736(7) Å, β = 106.936(5)°, V = 859.22(12) $Å^3$, Z = 2, D_c = 1.633 g cm^{-3}, F_{000} = 440, Bruker APEX-II CCD,

MoKα radiation, λ = 0.71073 Å, T = 100 K, $2\theta_{max}$ = 62.3º, 20105 reflections collected, 2738 unique (R_{int} = 0.0623). Final *GooF* = 1.036, *R*1 = 0.0577, *wR*2 = 0.1410, *R* indices based on 1904 reflections with $I > 2\sigma(I)$ (refinement on F^2), 139 parameters, 0 restraints. Lp and absorption corrections applied, μ = 0.133 mm^{-1}.

5-Hydroxy-isophthaloyl hydroxamic acid

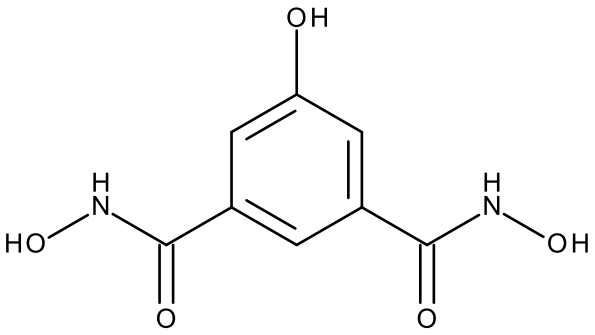

Dimethyl 5-hydroxybenzene-1,3-dicarboxylate (4.20 g, 20mmol), was dissolved in methanol (50 mL), to which an aqueous solution (45 mL) of hydroxylamine hydrochloride (9.5 g, 120 mmol), and sodium hydroxide (10.8 g, 240 mmol) was added. The solution was heated at 40 °C with stirring for 17 hours. The solution pH was adjusted to between 6.7 – 6.5 with 5 % hydrochloric acid. The white solid produced was via vacuum filtration (79 %).

^{1}H NMR (300MHz, DMSO) δ: 6.46 (bs, 1H, OH), 7.25 (s, 2H, ArH), 7.56 (s, 1H, ArH), 9.06 (bs, 2H, OH), 11.09 (bs, 2H, NH). **^{13}C NMR** (75 MHz, DMSO) δ: 116.76, 134.91, 157.14, 164.26, 176.12. (**ATR**, cm-1): 3301.49 (NH), 3065.63 (Ar CH bend) 2359.07 (OH), 1634.54 (N-C=O), 1580.48 (Ar C=C bend), 854.22 (Ar CH bend). **MS** (ESI) m/z: 213 [M+H]+. **Melting point** = decomposes above 200°C.

Terephthaloyl hydroxamic acid

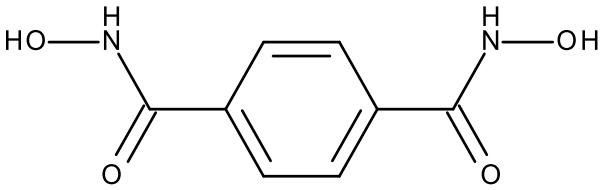

Dimethyl-benzene-1,4-dicarboxylate (5.82 g, 30 mmol), was dissolved in methanol (50 mL), to which an aqueous solution (45 mL) of hydroxylamine hydrochloride (9.5 g, 120 mmol), sodium hydroxide (10.8 g, 240 mmol) was added. The solution was heated to 40 °C with stirring for 17 hours. The solution pH was adjusted to ~6.50 with 5 % hydrochloric acid. The white solid produced was obtained via vacuum filtration (94 %).

^{1}H NMR (300MHz, DMSO) δ: 7.81 (s, 4H, ArH), 9.16 (bs, 2H, OH), 11.31 (bs, 2H, NH). ^{13}C NMR (75 MHz, DMSO) δ: 127.38, 135.51, 163.83. (**ATR**, cm-1): 3282.00 (NH), 3024.94 (Ar CH bend) 2701.10 (OH), 1643.82 (N-C=O), 1556.23 (Ar C=C bend), 887.86 (Ar CH bend). **MS** (ESI) m/z: 197 [M+H]+. Melting point =decomposes above 200 °C.

4-carboxy-benzohydroxamic acid

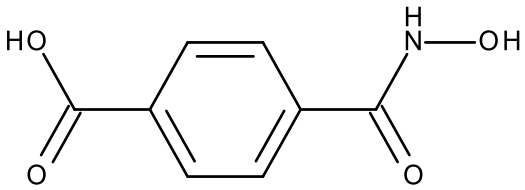

4-(methoxycarbonyl)benzoic acid (5.40 g, 30 mmol), was dissolved in methanol (50 mL). To which an aqueous solution (45 mL) of hydroxylamine hydrochloride (6.25 g, 90 mmol) and sodium hydroxide (7.20 g, 180 mmol) was added. The solution was heated at 40 °C with stirring for 17 hours. The solution pH was adjusted to between 3.5 - 3.2 with 5 % hydrochloric acid. The white solid produced was obtained via vacuum filtration (82 %).

^{1}H NMR (300MHz, DMSO) δ: 7.84 (d, 2H, ArH) 8.02 (d, 2H, ArH), 9.16 (bs, 1H, OH), 11.38 (bs, 1H, NH), 13.13 (bs, 1H, COOH). (**ATR**, cm-1): 3298.73 (NH), 2546.97 (OH), 1678.92 (N-C=O),

1557.70 (Ar C=C bend), 897.16 (Ar CH bend). **MS** (ESI) m/z: 182 [M+H]+. **Melting point** = decomposes above 200 °C.

Benzene-1,3,5-trihydroxamic acid

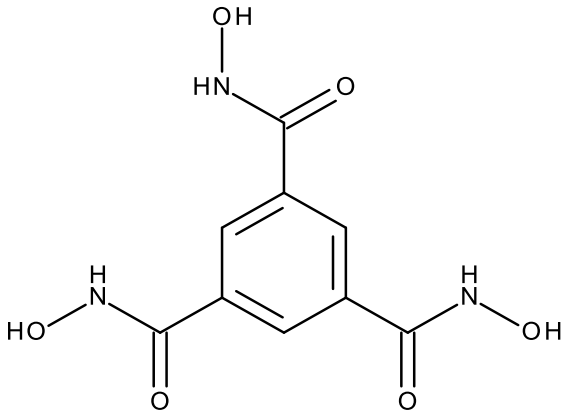

Trimethyl benzene-1,3,5-tricarboxylate (5.04 g, 20 mmol), was dissolved in methanol (50 mL), to which an aqueous solution (45 mL) of hydroxylamine hydrochloride (9.38 g, 135 mmol) and sodium hydroxide (10.8 g, 270 mmol) was added. The solution was heated to 40 °C with stirring for 17 hours. The solution was adjusted to between pH 6.5 – 6 with 5 % hydrochloric acid. The white solid produced was obtained via vacuum filtration. (3.42 g, 67 %).

^{1}H NMR (300MHz, DMSO) δ: 8.24 (s, 3H, ArH), 9.23 (bs, 3H, OH), 11.43 (bs, 3H, NH). (**ATR**, cm-1): 3365.32 (NH), 3022.69 (Ar CH bend) 2845.87 (OH), 1651.48 (N-C=O), 1538.55 (Ar C=C bend), 768.69 (Ar CH bend). **MS** (ESI) m/z: 556 $[M+H]^+$. **Melting point** = decomposes above 200 °C.

A.2.2 Mechanochemical synthesis

4-fluoro-benzohydroxamic acid

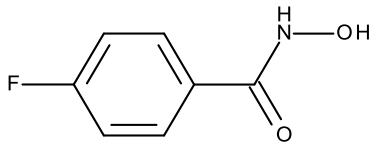

4-flourobenzoic acid (1.43 mmol, 200 mg) is added to a ball mill cup with CDI (1.86 mmol, 489 mg) and nitromethane (40 µl) this is milled at 25H_z for 10 minutes. Imidazole (2.1 mmol, 145 mg) and hydroxylamine sulphate (2.1 mmol, 351 mg) is added to the mixture and milled for a further 60 minutes. The reaction mixture is washed with basic pH 10 water, causing the precipitation of the white solid product (40 %).

^{1}H NMR (300MHz, DMSO) δ: 7.26 (dd, 2H, ArH), 7.82 (dd, 2H, ArH) 9.05 (s, 1H, NH), 11.23 (s, 1H, OH). **^{13}C NMR** (75 MHz, DMSO) δ: 113.99, 123.00, 131.05, 135.50, 156.44 (**ATR**, cm-1) 3288 (NH), 3035 (Ar CH), 2738 (OH), 1650 (N-C=O), 1563(Ar C=C bend), 750 (Ar CH bend). **MS** (ESI) m/z: 156 $[M+H]^+$. **Melting point** = 162-164 °C.

3-chloro-benzohydroxamic acid

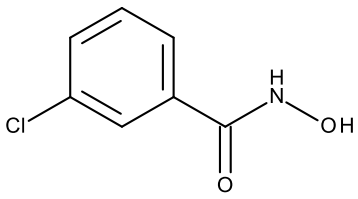

3-chlorobenzoic acid (1.27 mmol, 200 mg) is added to a ball mill cup with CDI (1.66 mmol, 269 mg) and nitromethane (40 µl) this is milled at 25H_z for 10 minutes. Imidazole (1.91 mmol, 130 mg) and hydroxylamine sulphate (1.91 mmol, 314mg) is added to the mixture

and milled for a further 60 minutes. The reaction mixture is washed with basic pH 10 water, causing the precipitation of the off white solid product (92 %).

^{1}H NMR (300MHz, DMSO) δ: 7.50 (T, 1H, ArH), 7.59 (d, 1H, ArH), 7.72 (d, 1H, ArH), 7.83 (s, 2H, ArH) 9.16 (s, 1H, NH), 11.34 (s, 1H, OH). **^{13}C NMR** (DMSO) δ: 125.56, 126.66, 130.40, 130.99, 133.18 (**ATR**, cm-1) 3291 (NH), 3072 (Ar CH), 2745 (OH), 1656 (N-C=O), 1558 (Ar C=C bend), 725 (Ar CH bend). **MS** (ESI) m/z: 217 [M+H]+. **Melting point** = 178-183 °C.

4-chloro-benzohydroxamic acid

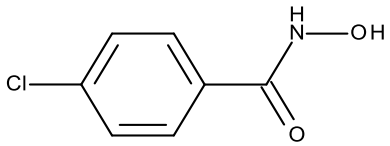

4-chlorobenzoic acid (1.27 mmol, 200 mg) is added to a ball mill cup with CDI (1.66 mmol, 269 mg) and nitromethane (40 µl) this is milled at 25H_z for 10 minutes. Imidazole (1.91 mmol, 130 mg) and hydroxylamine sulphate (1.91 mmol, 314mg) is added to the mixture and milled for a further 60 minutes. The reaction mixture is washed with basic pH 10 water, causing the precipitation of the off white solid product (96 %).

^{1}H NMR (300MHz, DMSO) δ: 7.53 (d, 2H, ArH), 7.77 (d, 2H, ArH), 9.10 (s, 1H, NH), 11.34 (s, 1H, OH). **^{13}C NMR** (300MHz, DMSO) δ: 119.56, 129.09, 128.83, 130.13, 131.42 (ATR, cm-1) 3285 (NH), 3068 (Ar CH), 2733 (OH), 1646 (N-C=O), 1558 (Ar C=C bend), 845 (Cl-C). **MS** (ESI) m/z: 217 $[M+H]^{+}$. **Melting point** = 191-196 °C.

4-bromo-benzohydroxamic acid – Gemma McMurdo

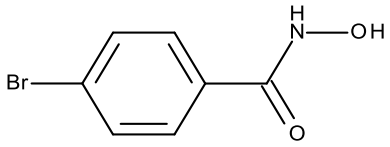

4-bromobenzoic acid (0.995 mmol, 200 mg) is added to a ball mill cup with CDI (1.3 mmol, 210 mg) and nitromethane (40 µl) this is milled at 25H_z for 10 minutes. Imidazole (1.5 mmol, 102 mg) and hydroxylamine sulphate (1.5 mmol, 245 mg) is added to the mixture and milled for a further 60 minutes. The reaction mixture is washed with basic pH 10 water, causing the precipitation of the white solid product (98 %).

^{1}H NMR (300MHz, DMSO) δ: 7.72 (d, 2H, ArH), 7.79 (d, 2H, ArH), 9.14 (s, 1H, NH), 11.34 (s, 1H, OH). **^{13}C NMR** (300MHz, DMSO) δ: 127.25, 128.09, 130.13, 135.42, 161.34 (ATR, cm-1) 3365 (NH), 3048 (Ar CH), 2742 (OH), 1652 (N-C=O), 1549 (Ar C=C bend), 851 (Br-C). **MS** (ESI) m/z: 264 $[M+H]^+$. **Melting point** =152-185 °C.

3-iodo-benzohydroxamic acid

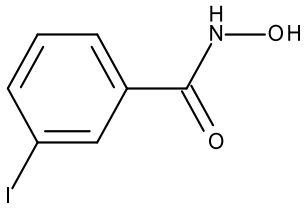

3-iodobenzoic acid (0.806 mmol, 200 mg) is added to a ball mill cup with CDI (1.05 mmol, 170 mg) and nitromethane (40 µl) this is milled at 25H_z for 10 minutes. Imidazole (1.20 mmol, 82 mg) and hydroxylamine sulphate (1.20 mmol, 198 mg) is added to the mixture and milled for a further 60 minutes. The reaction mixture is washed with basic pH 10 water, causing the precipitation of the white solid product (92 %).

^{1}H NMR (300MHz, DMSO) δ: 7.28 (t 1H, ArH), 7.76 (d, 1H, ArH), 7.89 (d, 1H, ArH), 8.08 (s 1H, ArH), 9.12 (s, 1H, NH), 11.34 (s, 1H, OH). **^{13}C NMR** (300MHz, DMSO) δ: 126.21, 126.89,

128.91, 130.56, 135.31, 139.58 162.75 (**ATR**, cm-1) 3363 (NH), 3179 (Ar CH), 2785 (OH), 1657 (N-C=O), 1551 (Ar C=C bend), 794 (Ar CH bend). **MS** (ESI) m/z: 264 $[M+H]^+$ **Melting point** = decomposes above 200 °C.

4-iodo-benzohydroxamic acid

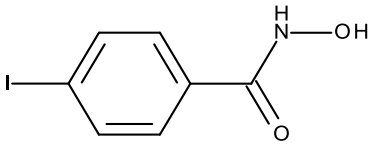

4-iodobenzoic acid (0.806 mmol, 200 mg) is added to a ball mill cup with CDI (1.05 mmol, 170 mg) and nitromethane (40 µl) this is milled at $25H_z$ for 10 minutes. Imidazole (1.20 mmol, 82 mg) and hydroxylamine sulphate (1.20 mmol, 198 mg) is added to the mixture and milled for a further 60 minutes. The reaction mixture is washed with basic pH 10 water, causing the precipitation of the white solid product (98 %).

^{1}H NMR (300MHz, DMSO) δ:7.53 (d, 2H, ArH), 7.84 (d, 2H, ArH), 9.08 (s, 1H, NH), 11.27 (s, 1H, OH). **^{13}C NMR** (300MHz, DMSO) δ: 107.51, 128.79, 132.35, 137.22, 155.15 (**ATR**, cm-1) 3364 (NH), 3176 (Ar CH), 2997 (OH), 1633 (N-C=O), 1633 (Ar C=C bend), 849 (Ar CH bend). **MS** (ESI) m/z: 264 $[M+H]^+$. **Melting point** = decomposes above 200 °C.

4-methyl-benzohydroxamic acid

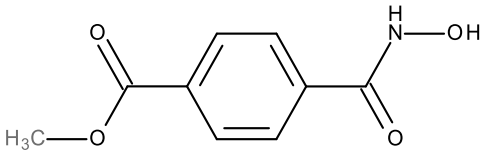

4-monomethylterepthalate (1.11 mmol, 200 mg) is added to a ball mill cup with CDI (3.33 mmol, 234 mg) and nitromethane (40 µl) this is milled at $25H_z$ for 10 minutes. Imidazole (1.67 mmol, 113 mg) and hydroxylamine sulphate (1.67 mmol, 273 mg) is added to a the

mixture and milled for a further 60 minutes. The reaction mixture is washed with basic pH 10 water, causing the precipitation of the white solid product (90 %).

^{1}H NMR (300MHz, DMSO) δ:2.72 (s 3H CH_3) 7.83 (d, 2H, ArH), 8.00 (d, 2H, ArH), 9.15 (s, 1H, NH), 11.45 (s, 1H, OH). (**ATR**, cm-1) 3459 (NH), 3028 (Ar CH), 2822 (OH), 2669 (COOH) 1660 (N-C=O), 1598 (Ar C=C bend), 770 (Ar CH bend). **MS** (ESI) m/z: 196 $[M+H]^+$.

A.2.3 CSD searches

Uncomplexed hydroxamic acids

Table 1 The CCDC refcodes for the 38 hydroxamic acid structures used.

anivoj	domqus	hitwoy	vapgol	xislan
Bidkee	evopip	kowyie	wenqem	xocfaw
bowhie	fetwum	labrov	wutwep	
canxog	fonhum	neykin	xavmem	
desbej	fulkee	ojetay	xavmow	
desbin	fulkii	rayrue	xavnaj	
desbot	fuzzab	salhxa	xavnen	
dojguf	gadyoc	satmuw	xersod	
dojham	gifkud	tibdis	xetnoa	

Search parameter were only organic structure. No powders structures, ions or disorder and not polymeric structures.

Octa-dentate Hydroxamate complexes

BPHXHF01, IPHTHA, IPHTHB, TEQSAL, YILGUX.

Search parameters, any metal complexed to 4 hydroxamates. No ions and no powder structures.

Ti-hydroxmate complexes

COPPIG, FIDQOA, FIDQUG, KACKUX, KACLAE, LOQBOJ, OJOBOF, OJOBUL, OJOCAS.

Search parameters, Ti complexed to hydroxamate, no ions and no powder structures.

A.2.4 Cocrystal DSC

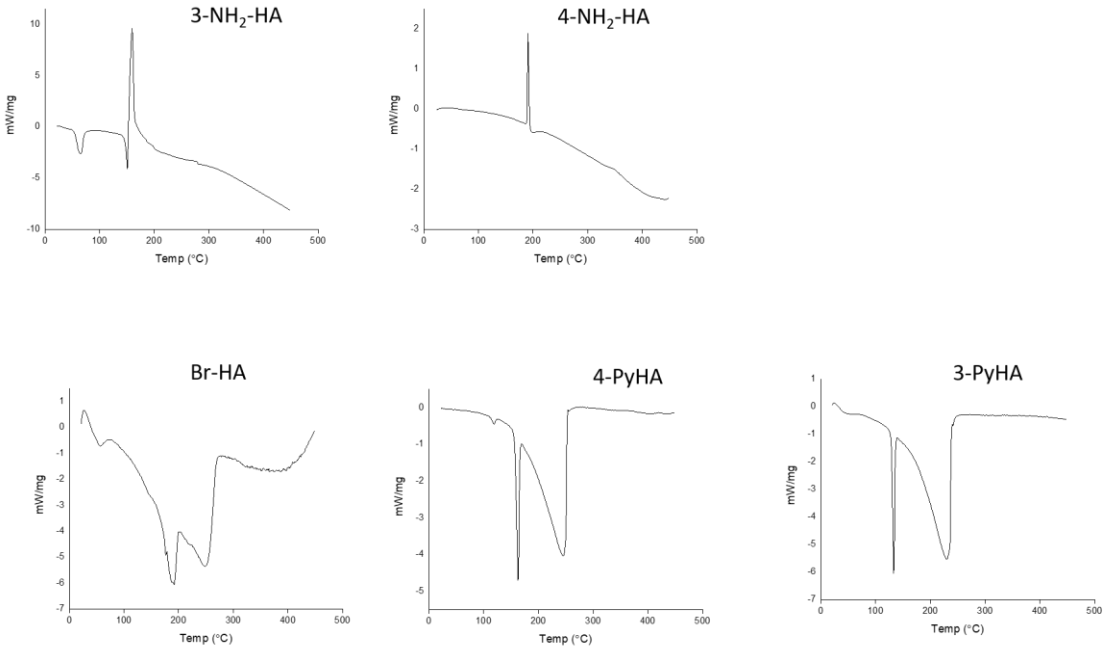

Figure A1 The DSC traces for the hydroxamic acid starting materials.

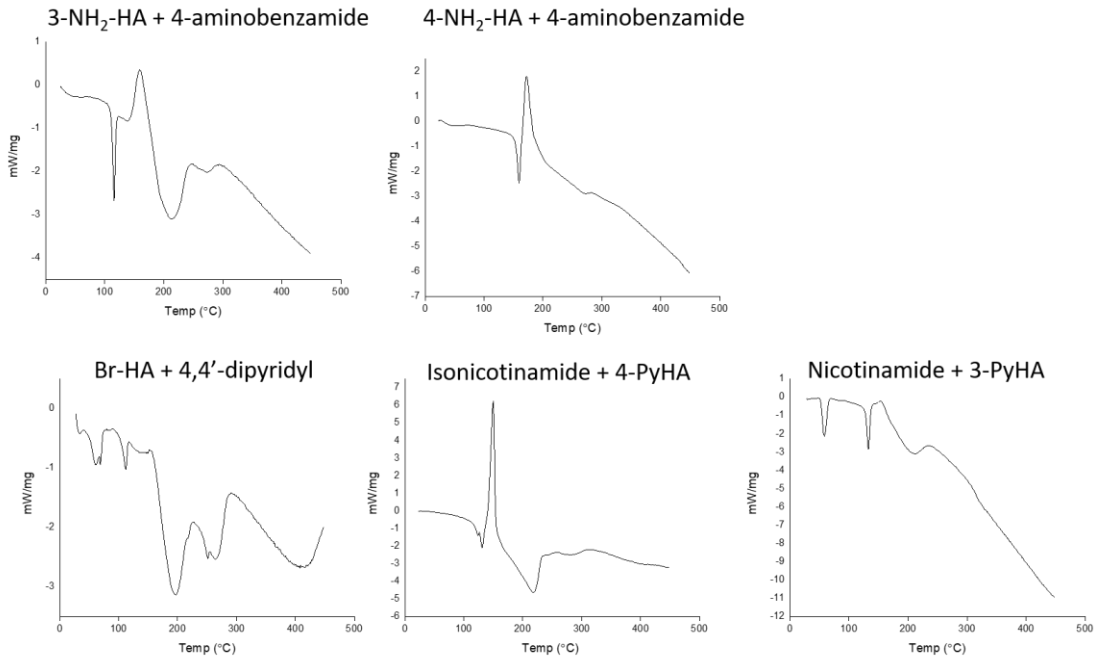

Figure A2 DSC traces of the hydroxamic acid co-crystals.

A.2.5 Zirconium(benzohydroxamate)$_4$ complex

Four equivalents of Benzohydroxamic acid were dissolved in alcohol (ethanol/methanol 3mL), to which a solution of zirconium tetrachloride (1 equivalent 2 mL). The solution was allowed to crystallise at room temperature over a period of several weeks. This results in clear colourless crystal. Both the ethanol and methanol solvate were obtained.

Crystal data for complex 1: M = 840.00, triclinic, space group P-1 (No. 2), a = 13.0745(12), b = 13.3892(12), c = 13.4768(10) Å, α = 111.699(8), β = 92.605(7), γ = 113.295(9)°, V = 1961.9(3) Å^3, Z = 2, D_c = 1.388 g cm^{-3}, F_{000} = 856, CuKα radiation, λ = 1.54184 Å, T = 293(2) K, 2θ_{max} = 147.0º, 16209 reflections collected, 7659 unique (R_{int} = 0.0648). Final *GooF* = 1.059, $R1$ = 0.1016, $wR2$ = 0.2762, R indices based on 6760 reflections with $I > 2\sigma(I)$ (refinement on F^2), 399 parameters, 0 restraints. Lp and absorption corrections applied, μ = 2.845 mm^{-1}.

Crystal data for Complex 2: M = 719.84, clear colourless plate, 0.186 × 0.061 × 0.028 mm^3, tetragonal, space group $I4_1/a$ (No. 88), a = b = 35.2341(15), c = 10.1095(5) Å, V = 12550.3(12) Å^3, Z = 18, D_c = 1.435 g cm^{-3}, F_{000} = 5526, SuperNova, Dual, Cu at home/near, AtlasS2, CuKα radiation, λ = 1.54184 Å, T = 99.9(5) K, 2Θmax = 147.4º, 62675 reflections collected, 6266 unique (Rint = 0.1045). Final GooF = 1.246, R1 = 0.0779, wR2 = 0.1534, R indices based on 5605 reflections with $I > 2\sigma(I)$ (refinement on F2), 413 parameters, 0 restraints. Lp and absorption corrections applied, μ = 3.636 mm-1.

A.3 Chapter 3

A.3.1 NMR

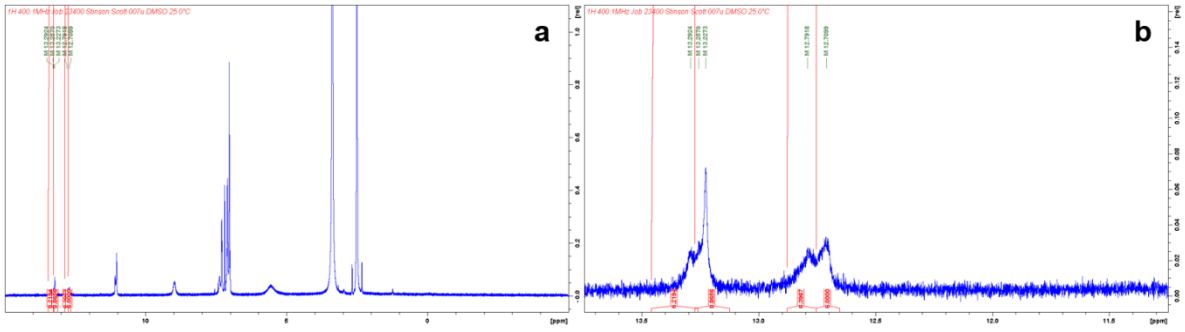

*Figure A3 ^{1}H-NMR spectrum of **Cage 6** analysed using Bruker topspin 3.5 pl 7. Where **a** shows the spectrum of the cage and **b** is narrowed to highlight the 11-14 ppm region where the proton located within the intrinsic pore of the cage is situated on the spectrum.*

A.3.2 Mass spectroscopy

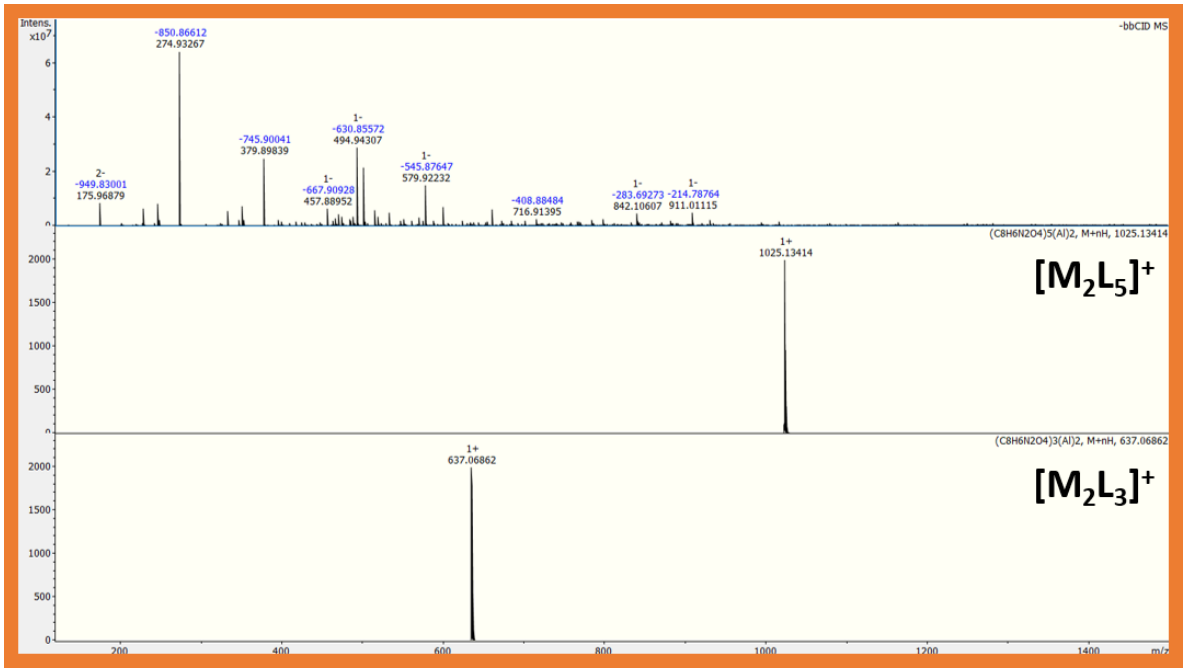

*Figure A4 **Cage 7** mass spectrum. Showing the predicted $[M_2L_5]^+$ and $[M_2L_3]^+$ m/z peaks and the corresponding collected peaks.*

A.3.3 Cage data

A.3.3.1 Cage 1

Synthesis

The crystallisation of cage 1 uses the standard crystallisation method where by Ligand IHA (0.1 mmol, 19.6 g) is dissolved in 6 mL of DMF to this solution 4 mL of an aqueous iron nitrate nonahydrate (0.1 mmol, 40.4 mg) solution is added forming a deep purple solution. The glass vial is sealed and left to crystallise for up to 6 weeks at room temperature, dark purple cubes are formed.

Single Crystal

Crystal data for: $C_{48}H_{36}Fe_4N_{12}O_{24}$, M = 1388.30, red cube, 0.2 × 0.2 × 0.2 mm^3, cubic, space group $P2_13$ (No. 198), a = 27.6954(19), V = 21243(4) Å^3, Z = 7.99992, D_c = 0.868 g cm^{-3}, F_{000} = 5632, Bruker SMART X8, MoKα radiation, λ = 0.71073 Å, T = 173.15 K, $2\theta_{max}$ = 52.7º, 187554 reflections collected, 14504 unique (R_{int} = 0.1438). Final *GooF* = 0.898, $R1$ = 0.0471, $wR2$ = 0.0940, R indices based on 10039 reflections with $I > 2\sigma(I)$ (refinement on F^2), 524 parameters, 0 restraints. Lp and absorption corrections applied, μ = 0.586 mm^{-1}.

pXRD

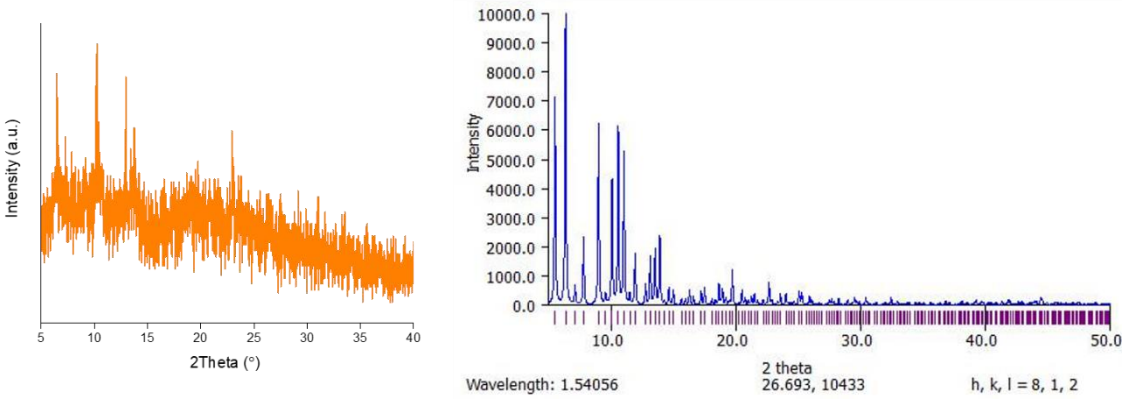

Figure A5 the collected pXRD pattern of cage 1 in orange. The predicted Cage 1 pXRD pattern in blue. Predicted pattern calculated in Mercury.

TGA and DSC

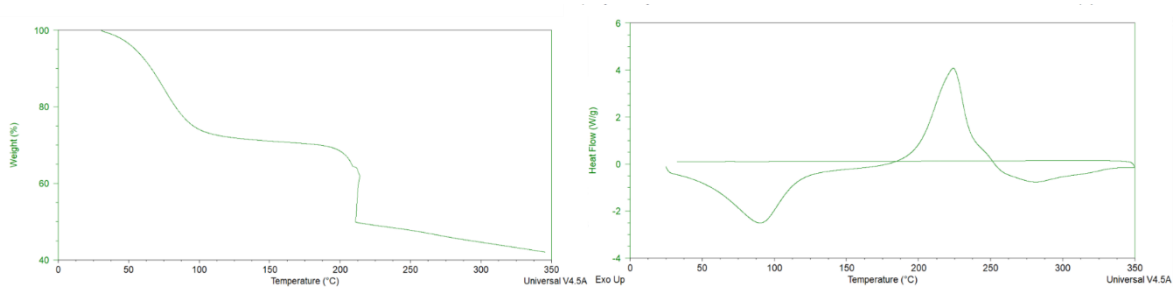

Figure A6 The TGA showing the DMF:water solvent mass loss of Cage 1 on the left. The DSC of Cage 1 on the right.

Water sorption TGA

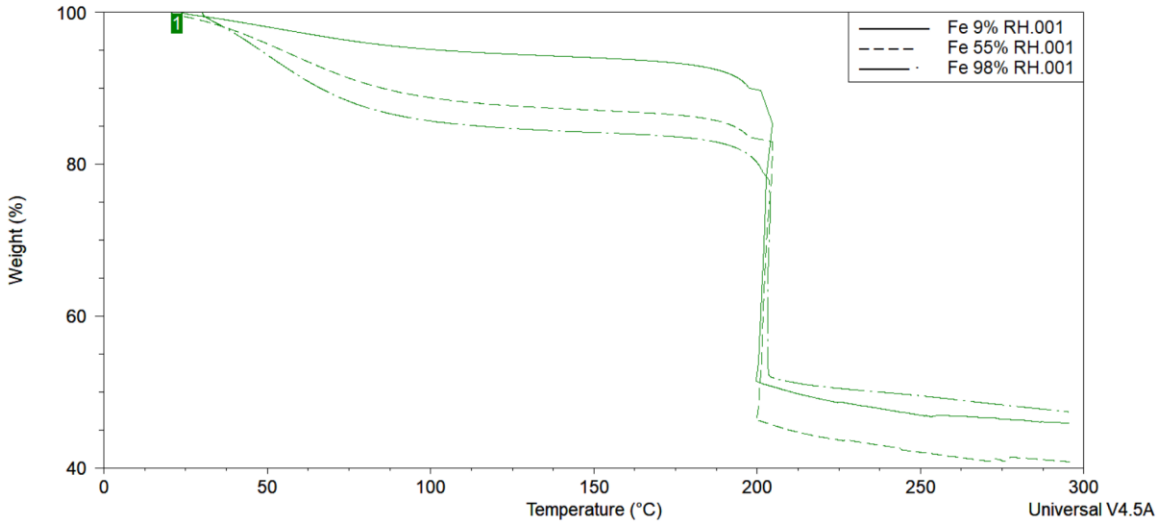

Figure A7 shows the TGA of Cage 1, after it has been exposed to three different relative humidity chambers.

A.3.3.2 Cage 2

Synthesis

The crystallisation of cage 2 uses the standard crystallisation method where by Ligand AHA (0.1 mmol, 21.1 mg) is dissolved in 7 mL of DMF to this solution 3 mL of an aqueous iron nitrate nonahydrate (0.1 mmol, 40.4 mg) solution is added forming a deep purple solution. The glass vial is sealed and left to crystallise for up to 6 weeks at room temperature, dark purple needles are formed. A second morphology of this species can be obtained; this material is collected as a crunchy purple solid that failed to provide a crystalline pXRD pattern.

Single crystal

Crystal data for: $C_{48}H_{42.67}Fe_4N_{18}O_{24}$, M = 2248.20, dark red needle, 1 × 0.4 × 0.1 mm^3, monoclinic, space group $C12/c1$ (No. 15), a = 42.992(6), b = 31.887(5), c = 30.307(4) Å, β = 91.194(8)°, V = 41539(10) Å^3, Z = 12, D_c = 1.078 g cm^{-3}, F_{000} = 14108, Bruker SMART X8, MoKα radiation, λ = 0.71073 Å, T = 173.15 K, $2\theta_{max}$ = 49.9º, 96304 reflections collected, 35047 unique (R_{int} = 0.0646). Final *GooF* = 1.282, $R1$ = 0.1058, $wR2$ = 0.3128, R indices based on 19921 reflections with $I > 2\sigma(I)$ (refinement on F^2), 2056 parameters, 24 restraints. Lp and absorption corrections applied, μ = 0.484 mm^{-1}.

pXRD

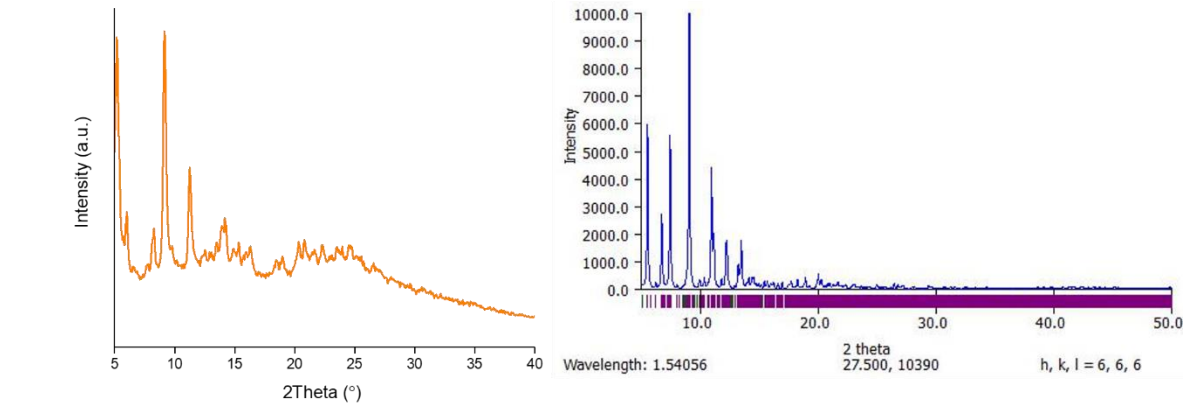

Figure A8 the collected pXRD pattern of cage 2 in orange. The predicted Cage 2 pXRD pattern in blue. Predicted pattern calculated in Mercury.

TGA and DSC

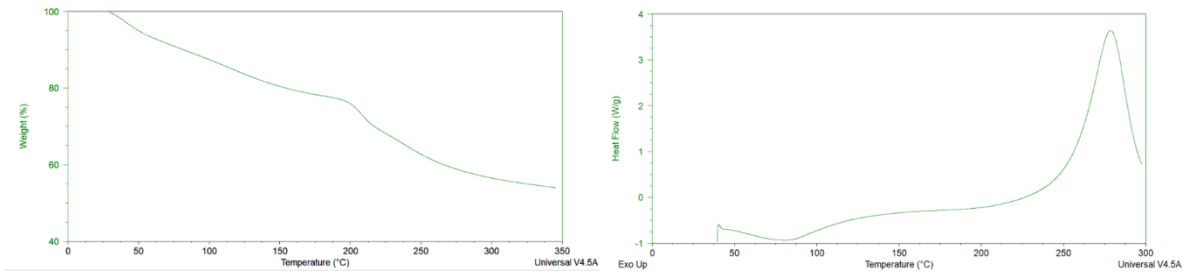

Figure A9 The TGA showing the DMF:water solvent mass loss of Cage 2 on the left. The DSC of Cage 2 on the right.

A.3.3.3 Cage 3

Synthesis

The crystallisation of cage 3 uses the standard crystallisation method where by Ligand HHA (0.1mmol, 21.2 mg) is dissolved in 6 mL of DMF to this solution 4 mL of an aqueous iron nitrate nonahydrate (0.1mmol, 40.4 mg) solution is added forming a deep purple solution. The glass vial is sealed and left to crystallise for up to 6 weeks at room temperature, red plates are formed.

Single crystal

Crystal data for: $\mathbf{C_{48}H_{36}Fe_4N_{12}O_{30}}$, M = 1484.29, dark red plate, 0.3 × 0.3 × 0.01 mm^3, monoclinic, space group $P12_1/n1$ (No. 14), a = 24.5375(12), b = 25.8725(12), c = 25.1504(12) Å, β = 110.641(2)°, V = 14941.7(12) Å^3, Z = 4, D_c = 0.660 g cm^{-3}, F_{000} = 3008, Bruker SMART X8, MoKα radiation, λ = 0.71073 Å, T = 100.15 K, 2θ_{max} = 65.3º, 375290 reflections collected, 53893 unique (R_{int} = 0.0859). Final *GooF* = 0.969, $R1$ = 0.0662, $wR2$ = 0.1881, R indices based on 26391 reflections with $I > 2\sigma(I)$ (refinement on F^2), 853 parameters, 0 restraints. Lp and absorption corrections applied, μ = 0.421 mm^{-1}.

A.3.3.4 Cage 4

Synthesis

A second form of cage 1 was isolated and its crystal structure collected. The structure proved to be isostructural to cage 5 having the *R*-3 space group. This crystal form was only obtained once and further attempts to attain this form have proved unsuccessful. Attempts at using cage 5 as seeding crystals were also made again this failed to yield the correct form. The crystals where more red in colour than form i and less cubic in shape.

Single crystal

Crystal data for: $\mathbf{C_{48}H_{36}Fe_4N_{12}O_{24}}$, M =1388.30, dark red cube, 0.2 × 0.2 × 0.2 mm^3, trigonal, space group *R*-3 (No. 148), a = b = 23.3009(19), c = 37.072(4) Å, V = 17431(3) Å^3, Z = 5.99994,

D_c = 0.794 g cm^{-3}, F_{000} = 4224, Bruker SMART X8, MoKα radiation, λ = 0.71073 Å, *T* = 173.15 K, 2θ_{max} = 64.6º, 98545 reflections collected, 13731 unique (R_{int} = 0.0411). Final *GooF* = 0.997, *R*1 = 0.0700, *wR*2 = 0.2144, *R* indices based on 10131 reflections with $I > 2\sigma(I)$ (refinement on F^2), 265 parameters, 0 restraints. Lp and absorption corrections applied, μ = 0.535 mm^{-1}.

A.3.3.5 Cage 5

Synthesis

The crystallisation of cage 5 uses the standard crystallisation method where by Ligand IHA (0.1 mmol, 19.6 mg) is dissolved in 8 mL of DMF to this solution 2 mL of an aqueous gallium nitrate hydrate (0.1mmol, 30 mg) solution is added forming a colourless solution. The glass vial is sealed and left to crystallise for up to 6 weeks at room temperature, colourless prisms are formed.

Single crystal

Crystal data for: $C_{48}H_{36}Ga_4N_{12}O_{24}$, M = 1443.78 , yellow prism, 0.282 × 0.206 × 0.142 mm^3, trigonal, space group R-3 (No. 148), a = b = 22.9549(6), c = 36.2162(9) Å, V = 16526.7(9) Å^3, Z = 5.99994, D_c = 0.870 g cm^{-3}, F_{000} = 4344, Synergy, Dualflex, AtlasS2, CuKα radiation, λ = 1.54184 Å, T = 100.01(10) K, 2θ_{max} = 154.4º, 20806 reflections collected, 7431 unique (R_{int} = 0.0321). Final *GooF* = 1.099, *R*1 = 0.0649, *wR*2 = 0.2082, *R* indices based on 6290 reflections with $I > 2\sigma(I)$ (refinement on F^2), 265 parameters, 0 restraints. Lp and absorption corrections applied, μ = 1.542 mm^{-1}.

pXRD

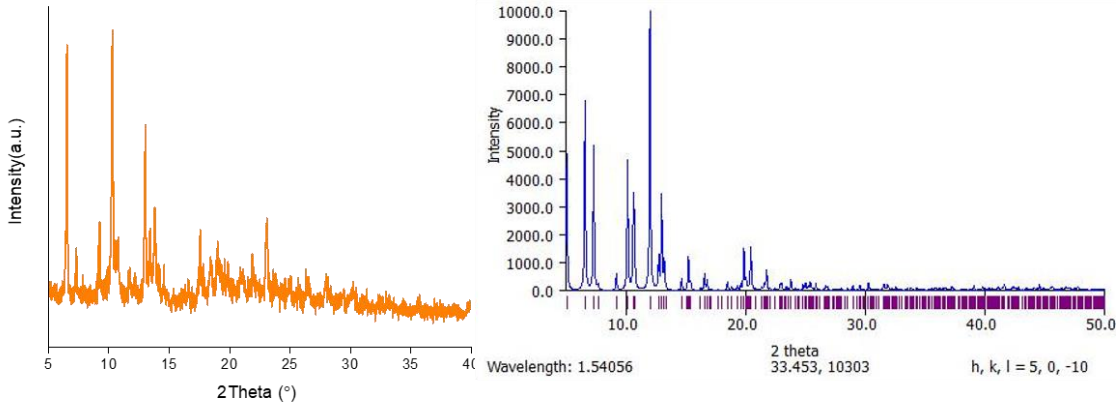

Figure A10 the collected pXRD pattern of cage 5 in orange. The predicted Cage 5 pXRD pattern in blue. Predicted pattern calculated in Mercury

TGA and DSC

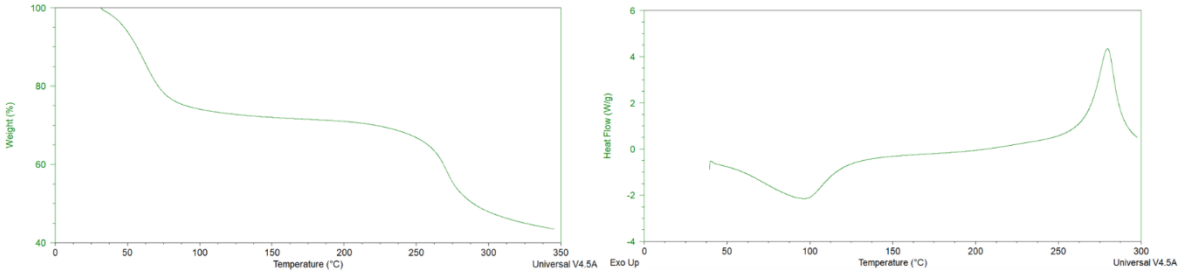

Figure A11 The TGA showing the DMF:water solvent mass loss of Cage 5 on the left. The DSC of Cage 5 on the right.

Water sorption TGA

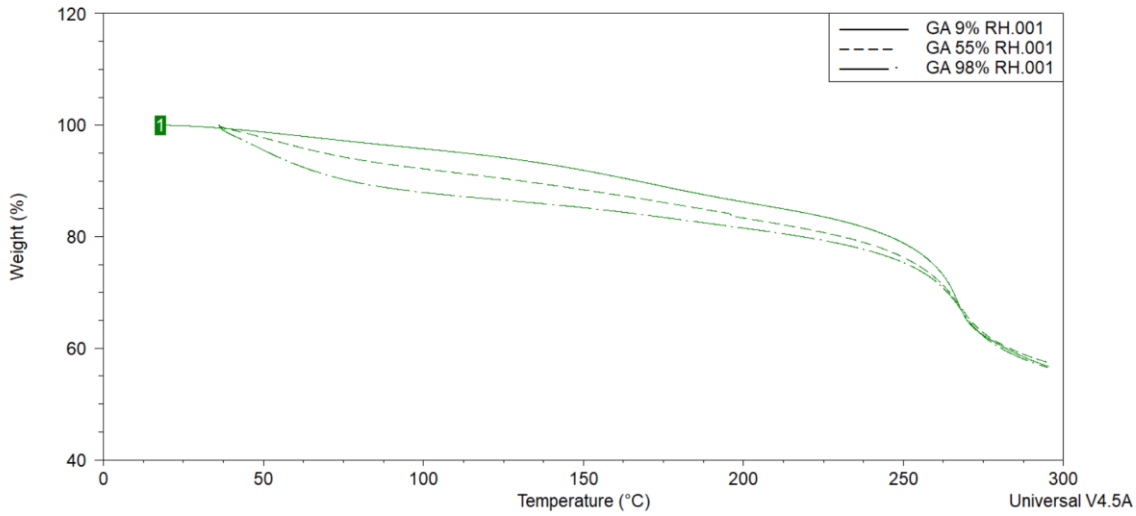

Figure A12 shows the TGA of Cage 5, after it has been exposed to three different relative humidity chambers

A.3.3.6 Cage 6

Synthesis

The crystallisation of cage 6 uses the standard crystallisation method where by Ligand AHA (0.1 mmol, 21.1 mg) is dissolved in 8 mL of DMF to this solution 2 mL of an aqueous gallium nitrate hydrate (0.1 mmol, 30 mg) solution is added forming a clear pale yellow solution. The glass vial is sealed and left to crystallise for up to 6 weeks at room temperature, beige prisms are formed.

Single crystal

Crystal data for $C_{48}H_{42}Ga_4N_{18}O_{24}$, M = 1533.87,, colourless plate, 0.06 × 0.04 × 0.02 mm^3, monoclinic, space group $C12/c1$ (No. 15), a = 29.4070(16), b = 40.417(2), c = 16.1827(9) Å, β = 111.328(3)°, V = 17916.7(18) Å^3, Z = 4, D_c = 0.569 g cm^{-3}, F_{000} = 3088, Bruker SMART X8, MoKα radiation, λ = 0.71073 Å, T = 173.15 K, $2\theta_{max}$ = 54.5º, 148999 reflections collected, 19802 unique (R_{int} = 0.1570). Final *GooF* = 0.961, $R1$ = 0.0695, $wR2$ = 0.1902, R indices based on 8949 reflections with $I > 2\sigma(I)$ (refinement on F^2), 430 parameters, 0 restraints. Lp and absorption corrections applied, μ = 0.628 mm^{-1}.

TGA and DSC

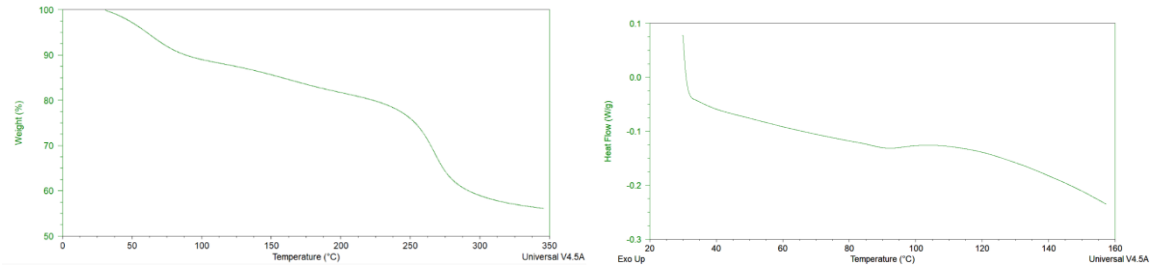

Figure A13 The TGA showing the DMF:water solvent mass loss of Cage 6 on the left. The DSC of Cage 6 on the right.

A.3.3.7 Cage 7

Synthesis

The crystallisation of cage 7 uses the standard crystallisation method where by Ligand IHA (0.1 mmol, 19.6 mg) is dissolved in 8 mL of DMF to this solution 2 mL of an aqueous aluminium nitrate nonahydrate (0.1 mmol, 37.5 mg) solution is added forming a colourless solution. The glass vial is sealed and left to crystallise for up to 6 weeks at room temperature, pale yellow prisms are formed.

Single crystal

Crystal data for: $C_{48}H_{36}Al_4N_{12}O_{24}$, M =1272.93 , yellow prism, 0.4 × 0.2 × 0.2 mm^3, trigonal, space group R-3 (No. 148), a = b = 22.8281(4), c = 35.8319(8) Å, V = 16171.1(7) Å^3, Z = 5.9994, D_c = 0.784 g cm^{-3}, F_{000} = 3912, Synergy, Dualflex, AtlasS2, Cu Kα radiation, λ = 1.54184 Å, T = 100.01(10) K, $2\theta_{max}$ = 147.9º, 26496 reflections collected, 7017 unique (R_{int} = 0.0453). Final *GooF* = 1.032, $R1$ = 0.0858, $wR2$ = 0.2662, R indices based on 5721 reflections with $I > 2\sigma(I)$ (refinement on F^2), 265 parameters, 0 restraints. Lp and absorption corrections applied, μ = 0.838 mm^{-1}.

pXRD

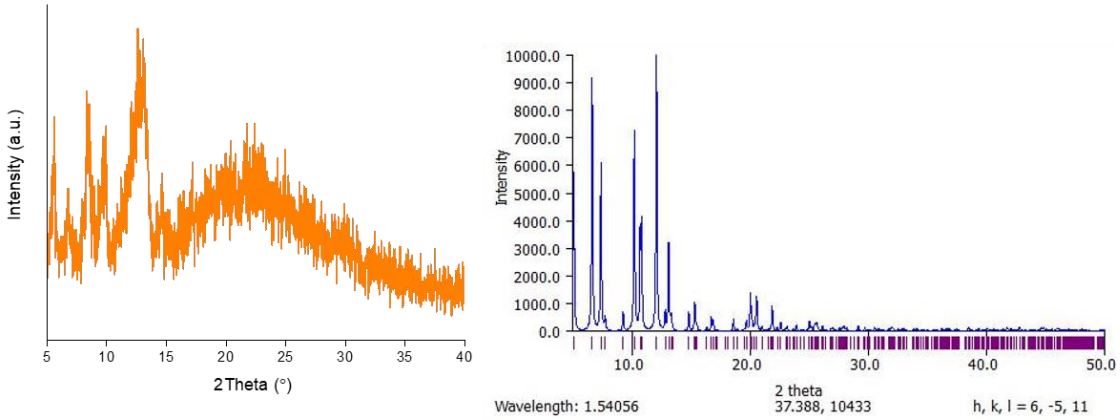

Figure A14 the collected pXRD pattern of cage 7 in orange. The predicted Cage 7 pXRD pattern in blue. Predicted pattern calculated in Mercury

TGA and DSC

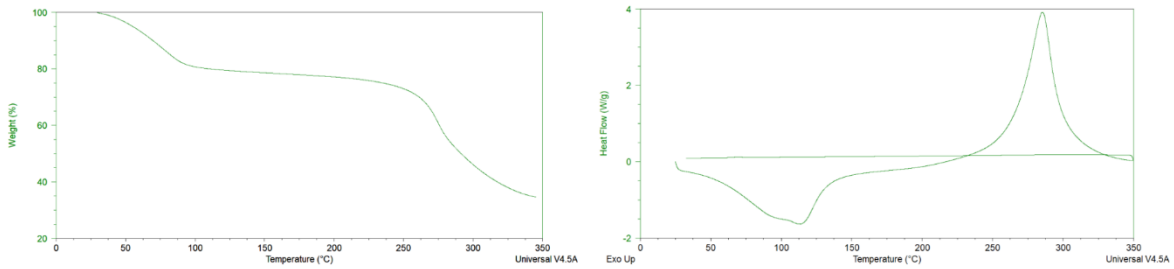

Figure A15 The TGA showing the DMF:water solvent mass loss of Cage 7 on the left. The DSC of Cage 7 on the right.

Water sorption TGA

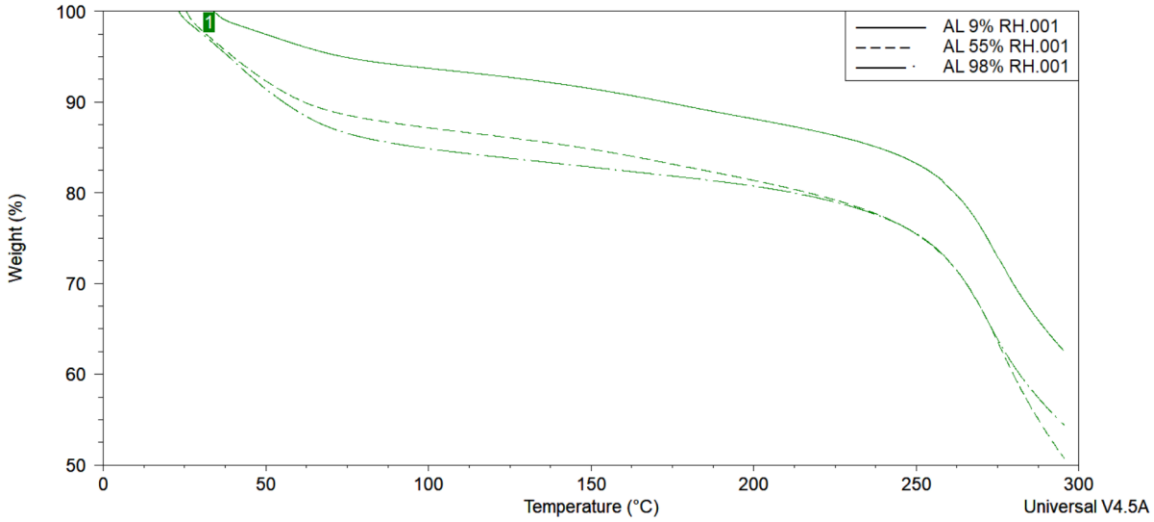

Figure A16 shows the TGA of Cage 7, after it has been exposed to three different relative humidity chambers

A.3.3.8 Cage 8

Synthesis

The crystallisation of cage 8 uses the standard crystallisation method where by Ligand IHA (0.1mmol, 0.018g) is dissolved in 3 mL of DMF to this solution 7 mL of an aqueous indium nitrate hydrate (0.1mmol, 0.03g) solution is added forming a colourless solution. The glass vial is capped and left to crystallise for up to 15 weeks at room temperature, colourless blocks are formed.

Single crystal

Crystal data for $C_{48}H_{36}In_4N_{12}O_{24}$: M = 1625.79, clear colourless block, 0.5 × 0.5 × 0.25 mm^3, trigonal, space group R-3 (No. 148), a = b = 23.2917(10), c = 37.475(2) Å, V = 17606.6(18) Å^3, Z = 5.994, D_c = 0.919 g cm^{-3}, F_{000} = 4776, Bruker APEX-II CCD, MoKα radiation, λ = 0.71073 Å, T = 273.15 K, 2θ_{max} = 67.4º, 221894 reflections collected, 15451 unique (R_{int} = 0.0403). Final *GooF* = 1.037, $R1$ = 0.0339, $wR2$ = 0.1010, R indices based on 12023 reflections with $I > 2\sigma(I)$ (refinement on F^2), 265 parameters, 0 restraints. Lp and absorption corrections applied, μ = 0.822 mm^{-1}.

A.3.4 Water uptake studies

Relative humidity (RH) chambers are a seal vial filled with a slurry of distilled water and pure metal salt, at a fixed temperature. The RH chamber produced were RH 98 % - K_2SO_4, RH 55 % -$Mg(NO_3)_2$, RH 9 % - KOH at 20 ˚C.

A vial containing a sample of the desolvated cage is placed inside the RH chamber and the system is allowed to equilibrate for 24 hours. After which time, the sample is removed from the chamber and subjected to a TGA experiment to remove and quantify the amount of water absorbed. The desorption value was taken at 150 ˚C for all nine samples.

A.3.5 Porosity values

The free sphere radius value was used to determine the volume of the intrinsic void space for one cage. This value was used to determine the total intrinsic void volume. By multiplying by the number of cages per unit cell. This value was subtracted from the total solvent accessible void volume (calculated in Mercury), providing the amount of extrinsic void space per unit cell.

A.4 Chapter 4

Ligand 1 - N,N'-(1,2-phenylene)diisonicotinamide.

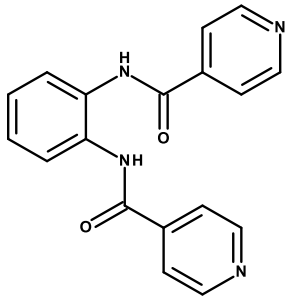

Ligand 1 synthesis is the same as reported by Jones and co-workers.[1] Isonicotinyl chloride hydrochloride (1.70 g, 9.6 mmol) was added to a stirred solution of o-phenylenediamine

(0.52 g, 4.8 mmol) and triethylamine (3 g, 29.6 mmol) in THF (50 ml) at 0 ˚C. The suspension was heated under nitrogen at 80 ˚C for 48 h. The resulting off-white precipitate is then recrystallized from ethanol.

A.4.0 Macrocycle and coordination polymer synthesis

A.4.0.1 CP1

Ligand 1 (17 mg, 53 µmol) is added to a screw top glass vial and is dissolved in boiling ethanol (15 ml) once cooled an ethanol solution (2 mL) of colbalt nitrate hexahydrate (30.8mg, 106 µmol) is added and the vial sealed. Single crystal structure determination, Squeeze was used due to the disordered nature of the solvent and anion.

Crystal data: M =585.30, monoclinic, space group $C12/c1$ (No. 15), a = 9.112(3), b = 22.529(6), c = 18.265(10) Å, β = 90.36(4)°, V = 3749(3) Å^3, Z = 5, D_c = 1.296 g cm^{-3}, F_{000} = 1516, CuKα radiation, λ = 1.54184 Å, T = 293(2) K, $2\theta_{max}$ = 146.2º, 7998 reflections collected, 3380 unique (R_{int} = 0.0605). Final *GooF* = 1.104, $R1$= 0.0765, $wR2$ = 0.2181, R indices based on 2927 reflections with $I > 2\sigma(I)$ (refinement on F^2), 104 parameters, 0 restraints. Lp and absorption corrections applied, μ = 4.040 mm^{-1}.

A.4.0.2 CP2

Ligand 1 (17 mg, 53 µmol) is added to a screw top glass vial and is dissolved in boiling ethanol (15 ml) once cooled an ethanol solution (2 mL) of Cadmium nitrate tetrahydrate (193mg, 106 µmol) is added and the vial sealed. Crystallisation occurs within 72 hour sometimes via a gel state. Single crystal structure determination and TGA analysis. Squeeze was used due to the disordered nature of the solvent.

Crystal data: M = 436.54 , clear colourless irregular, 0.2 × 0.08 × 0.08 mm^3, monoclinic, space group $P12_1/c1$ (No. 14), a = 11.1278(6), b = 22.7534(9), c = 9.2320(3) Å, β = 107.517(5)°, V = 2229.10(18) Å^3, Z = 4, D_c = 1.301 g cm^{-3}, F_{000} = 884, Synergy, Dualflex, AtlasS2, CuKα radiation, λ = 1.54184 Å, T = 100.00(10) K, $2\theta_{max}$ = 152.6º, 17519 reflections collected, 4545 unique (R_{int} = 0.0402). Final *GooF* = 1.064, $R1$ = 0.0845, $wR2$ = 0.2379, R

indices based on 3997 reflections with $I > 2\sigma(I)$ (refinement on F^2), 259 parameters, 0 restraints. Lp and absorption corrections applied, $\mu = 4.443$ mm^{-1}.

A.4.0.3 CP3

Ligand 1 (17 mg, 53 µmol) is added to a screw top glass vial and is dissolved in boiling THF (7.5 ml) once cooled an methanol solution (7.5 mL) of Cobalt iodide (33mg, 106 µmol) is added and the vial sealed. Crystallisation occurs over a three month period via the co-ordination polymer.

Crystal data: M = 1093.60, yellow-green block, 0.31 × 0.29 × 0.08 mm^3, monoclinic, space group $C12/c1$ (No. 15), a = 8.1181(5), b = 24.6486(13), c = 22.3166(12) Å, β = 98.290(2)°, V = 4418.9(4) Å^3, Z = 4, D_c = 1.644 g cm^{-3}, F_{000} = 2180, Bruker APEX-II CCD, MoKα radiation, λ = 0.71073 Å, T = 100.15 K, $2\theta_{max}$ = 52.8º, 29100 reflections collected, 4252 unique (R_{int} = 0.0637). Final *GooF* = 1.069, $R1$ = 0.0415, $wR2$ = 0.0724, R indices based on 3264 reflections with $I > 2\sigma(I)$ (refinement on F^2), 325 parameters, 0 restraints. Lp and absorption corrections applied, μ = 1.843 mm^{-1}.

A.4.1 Mechanochemical synthesis

A.4.1.1 Zn Nitrate CP

Synthesis

Ligand 1 (100 mg, 0.3 mmol) is added to a ball mill cup, to which zinc nitrate hexahydrate (188 mg, 0.6 mmol) is added along with 250 µL of ethanol and ball milled at 30 Hz for 30 minutes.

TGA

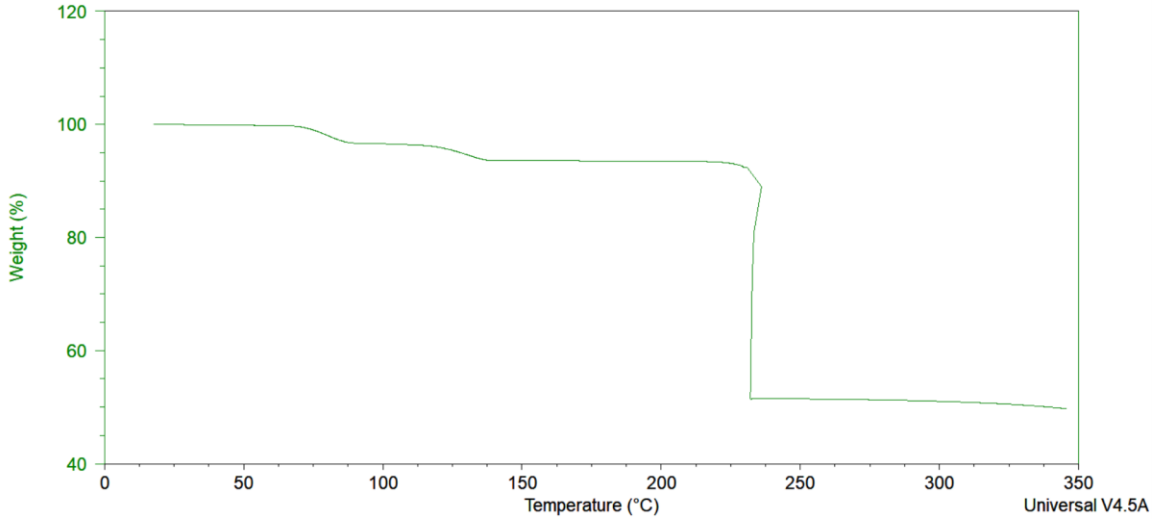

Figure A17 TGA plot of the $Zn(NO_3)_2$ CP.

A.4.1.2 $CoCl_2$ Macrocycle

Synthesis

Ligand 1 (100 mg, 0.3 mmol) is added to a ball mill cup, to which cobalt chloride (38.7 mg, 0.3 mmol) is added along with 250 µL of ethanol and 20 µL of water. The mixture is ball milled at 30 Hz for 30 minutes.

TGA

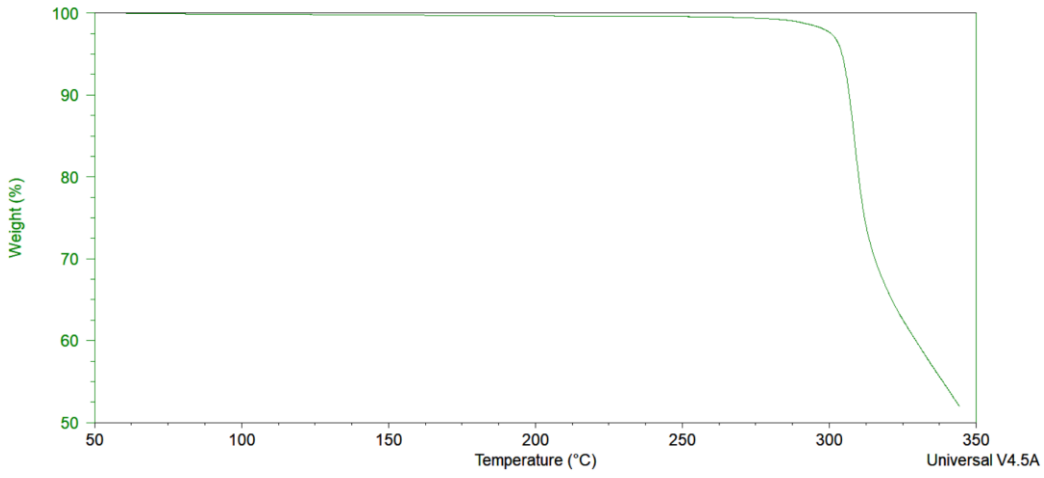

Figure A18 TGA plot of the $CoCl_2$ macrocycle synthesised via mechanochemistry.

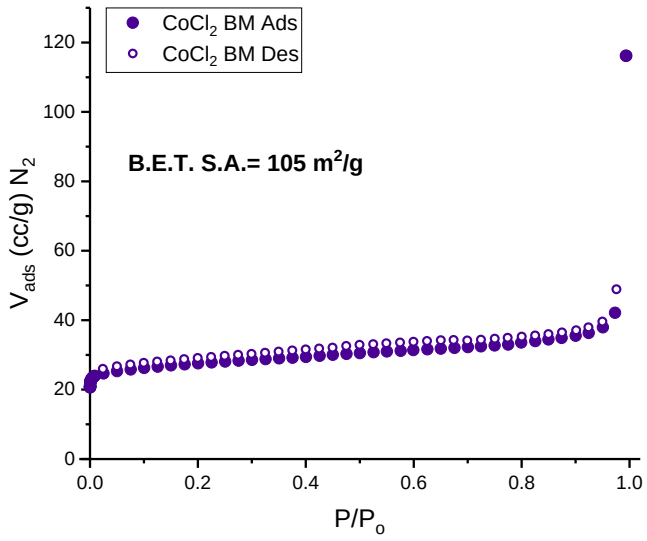

Figure A19 BET surface area isotherm of the ball milled $CoCl_2$ macrocycle. Shwoing microporous and mesoporous character.

A.4.1.3 $ZnCl_2$ Macrocycle

Synthesis

Ligand 1 (100 mg, 0.3 mmol) is added to a ball mill cup, to which cobalt chloride (40 mg, 0.3mmol) is added along with 250 µL of ethanol and 20 µL of water. The mixture is ball milled at 30 Hz for 30 minutes.

TGA

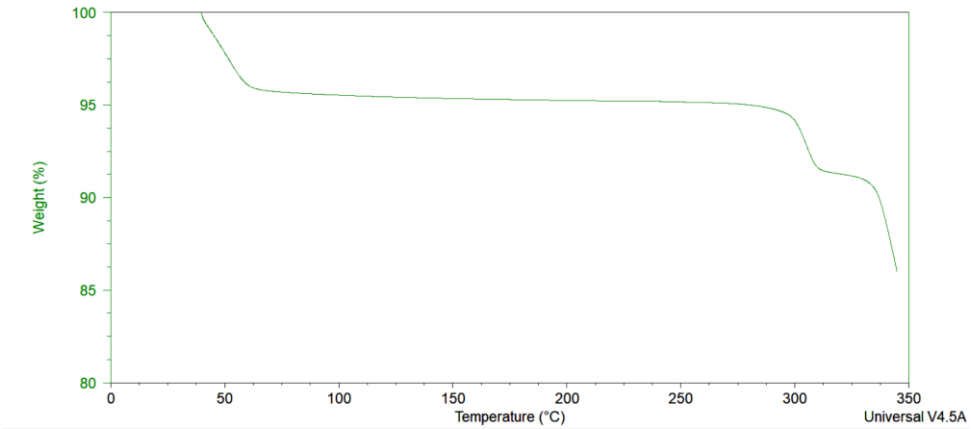

Figure A20 TGA plot for the ball milled $ZnCl_2$ Macrocycle.

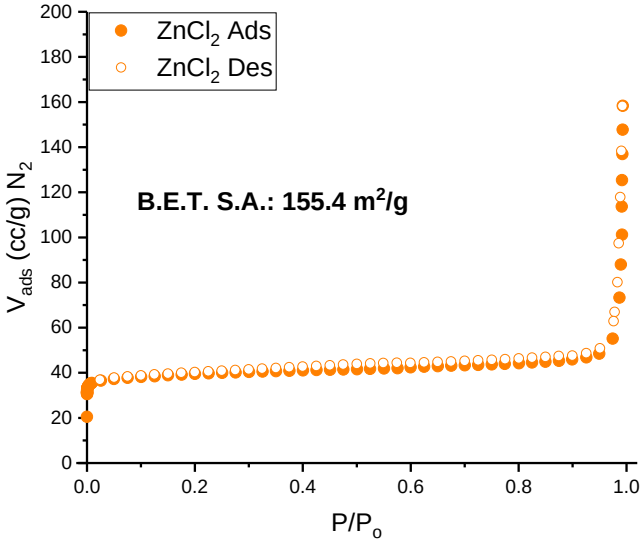

Figure A21. BET surface area isotherm of the ball milled $ZnCl_2$ macrocycle. Showing microporous and mesoporous character.[2]

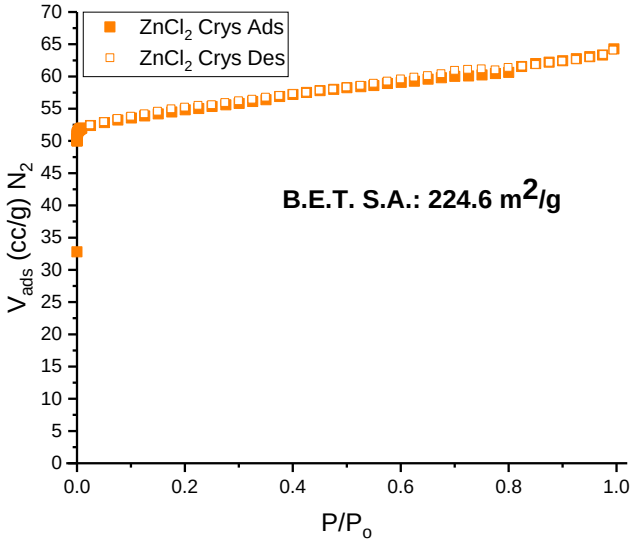

Figure A22. BET surface area isotherm of the crystallised $ZnCl_2$ macrocycle. Showing only microporous character.

A.5 References

1 C. D. Jones, J. C. Tan and G. O. Lloyd, *Chem. Commun.*, 2012, **48**, 2110–2112.

2 S. Storck, H. Bretinger and W. F. Maier, *Appl. Catal. A Gen.*, 1998, **174**, 137–146.